Studies of

Light Scalar Particles and

Dressed Gauge Propagators in QCD

A thesis submitted for the degree of

Doctor of Philosophy

by

David Wilson

Institute for Particle Physics Phenomenology

Durham University

September 2010

Abstract

The equations of QCD are widely believed to describe the properties of mesons, baryons and their hadronisation after hard interactions at particle accelerators such as the LHC. However, the theoretical framework linking the fundamental Lagrangian of QCD to the mesons and baryons observed in experiment is still in development. The states observed by experiments can be investigated using a variety of other theoretical methods. We consider here two methods, Chiral Perturbation Theory and carefully considering the poles in a scattering amplitude. In chapters 2 and 3 we apply these methods to determine the composition of the $\sigma(600)$ and $f_0(980)$ scalar resonances observed in $\pi\pi$ scattering.

In chapter 4 we turn to make the connection between the fundamental Lagrangian and the observed physics. The first step here is to solve the Schwinger-Dyson equations for the gluons, ghosts and quarks which describe how a Green's function behaves non-perturbatively. We primarily investigate the coupled gluon and ghost system without quarks. We find that non–trivial vertices are required to obtain self–consistent solutions in the simplest truncation and that a solution with a finite ghost dressing function appears to be preferred.

Declaration

I declare that no material presented in this thesis has been submitted by myself for a degree at this or any other university.

The research presented in this thesis has been carried out in collaboration with M.R. Pennington.

The research presented in Chapter 2 was also carried out in collaboration with J.R. Pelaez, M.R. Pennington, and J.R. Ruiz de Elvira and is in preparation for publication, it currently available as an e-print, arXiv:1009.6204,
'Chiral Perturbation Theory, the $1/N_c$ *expansion and Regge behaviour determine the structure of the lightest scalar meson.'*

The research presented in Chapter 3 was carried out in collaboration with M.R. Pennington, and is in preparation for publication,
'New data from Babar and the pole structure of the $f_0(980)$*'*

Acknowledgements

Firstly I would like to thank my supervisor, Mike Pennington for the invaluable support and guidance he has offered over the past four years. Although busy improving the education of all of the school-children in County Durham, and most of those in North-East England, whilst simultaneously staging a coup to take over a theory group at an American national laboratory, you still found time to answer my questions and suggest ways out of my problems. Thank you.

I would also like to thank the students and staff at the IPPP, in particular Aoife Bharucha, Eimear O'Callaghan, Jesus Javier Cobos-Martinez, James Currie, Alison Fowler, Nigel Glover, Mark Goodsell, Frank Krauss, Tracey Li, Luis Matos, Katy Morgan, Andrew Papanastasiou, Joao Pires, Adrian Signer, Philip '*Flip*' Tanedo, Jamie Tattersall, Ciaran Williams, Karina Williams and Richard Williams, for numerous invaluable discussions about maths, physics, numerics, and most recently, "how to do 'X' using LaTex". I am particularly indebted to Jacobo Ruiz de Elvira for his advice and programs regarding the Chiral Perturbation Theory section of this thesis in chapter 2. I am also indebted to Marco Pappagallo for an early look at some preliminary data.

I would like to thank Sophie Harris for always being positive, supportive and for many happy weekends together.

Finally I would like to thank my parents, Nick and Sue Wilson for giving me a perfect start in life. More recently, to my father, Nick, for being strong and positive in the most difficult circumstances and to my mother, Sue, for having the determination and motivation to make the most of some very difficult times.

Contents

List of figures

List of tables

Chapter 1.

Introduction

In a world primarily informed by human perception the world described by the fundamental equations of physics is often counter-intuitive. The developments in 20^{th} Century physics were nothing but remarkable, starting with the theory of special relativity that puts space and time, energy and mass, on equal footing and combining this with quantum mechanics that describes so well the peculiar properties of individual atoms has led to a single unifying picture capable of describing almost all aspects of nature we are capable of measuring.

There are four known fundamental forces in nature, the Electromagnetic force, the Weak force, the Strong force and Gravity, as decribed by Einstein's General Relativity. The first three forces are well described by the Standard Model of Particle Physics as a relativistic quantum field theory that satisfies both the theory of special relativity and generalises the non-relativistic quantum mechanics of the 1920s and 1930s. The unifying picture is of matter fields, quarks and leptons, interacting via force-carrying fields for each of the fundamental forces. The simplest of these is the electromagnetic force, which is well described by the prototype theory of the standard model, Quantum Electrodynamics, or QED. In QED we find the theory describes the interaction of charged particles such as electrons, muons and protons, interacting with the quantum of the electromagnetic field known as the photon, essentially a 'particle' of light if you like. Remarkably, we find that simple symmetry considerations lead to this description, and the only starting point required is the Lagrangian for fermionic particles. The symmetry is known as a gauge symmetry and is a consequence of the absolute phase of the electron or photon being unobservable; the theory being symmetric with respect to changes in phase.

1.1. Gauge Symmetry

The classical Langrangian density for spin-1/2 particles is found from the Dirac equation and is given by,

$$\mathcal{L} = \overline{\psi}\left(i\gamma^{\mu}\partial_{\mu} - m\right)\psi \tag{1.1}$$

where the matrices γ^{μ} satisfy the Clifford algebra $\{\gamma^{\mu}, \gamma^{\nu}\} = 2g^{\mu\nu}$. The symmetry transformation for the matter fields is,

$$\psi(x) \rightarrow \psi'(x) = U\psi(x) = e^{i\phi}\psi(x). \tag{1.2}$$

The real magic happens when the phase symmetry is promoted from a global symmetry acting over the whole of space to a local symmetry acting separately at each space-time point,

$$\psi(x) \rightarrow \psi'(x) = U(x)\psi(x) = e^{i\phi(x)}\psi(x). \tag{1.3}$$

The partial derivative in eq. (1.1) now acts on the phase $\phi(x)$ giving rise to a new term if this symmetry is to be satisfied,

$$\mathcal{L} \rightarrow \mathcal{L}' = \overline{\psi}(x)\left(i\gamma^{\mu}\partial_{\mu} - m\right)\psi(x) \; - \; \overline{\psi}(x)\left(\gamma^{\mu}\partial_{\mu}\phi(x)\right)\psi(x). \tag{1.4}$$

This new term has the correct Lorentz structure to represent a fermion-photon interaction, for which we also have to add a kinetic term giving the Lagrangian of QED,

$$\mathcal{L} = \overline{\psi}\left(i\gamma^{\mu}\partial_{\mu} - m\right)\psi \; + \; ig\overline{\psi}\gamma^{\mu}A_{\mu}\psi \; - \; \frac{1}{4}F^{\mu\nu}F_{\mu\nu}, \tag{1.5}$$

where $F_{\mu\nu} = \partial_{\mu}A_{\nu} - \partial_{\nu}A_{\mu}$, where A_{μ} is the photon field. The consequences of each term in this equation can be read off, the first term gives rise to the fermion propagator, that describes the propagation of fermions between two positions or points in momentum space. The second term describes a three-point interation between a fermion and photon. The final term gives rise to a massless propagator for the photon field.

Following the same principles with enlarged symmetry groups leads to the theory of the strong interations known as Quantum Chromodynamics and considering a spontaneously broken gauge symmetry leads to the massive gauge bosons observed in weak interaction processes at high energies. The method for breaking this gauge symmetry is the Higgs

mechanism that the LHC at CERN hopes to investigate. The Higgs boson is required to produce the masses observed for the W and Z weak bosons and is also proposed as the mechanism of mass generation for all of the massive particles of the Standard Model. An unfortunate feature of this theory is that none of the fermionic masses, or indeed, the mass of the Higgs itself are predicted; they are simply free parameters that must be measured by experiment. Certainly, this is a very exciting time for particle physics and only now is the LHC beginning to take its first steps into the unknown. It may take many years to accumulate the data required to reveal the new physics present at the TeV scale.

In order to make theoretical predictions from the fundamental standard model, typically we must use a special expansion called perturbation theory. This is the only systematic way to obtain predictions from the fundamental Lagrangian where the errors are under control. A perturbative expansion can be applied in a number of ways, but the most generally applicable is to expand in the coupling constant g. This is a parameter that is usually small and describes the strength of the interactions between the different particles in the Lagrangian. A series may be constructed of the form $\# + \#g^2 + \#g^4 + ...$ where higher powers of g may be neglected if g is small enough. This is highly successful for all parts of the standard model, except QCD.

In QCD at high energies g is small and the perturbative series works reasonably well, provided a sufficient number of orders can be calculated for the process of interest. However as the interaction energy is reduced g becomes large and the perturbative series loses any meaning since all the terms of the series are of comparable magnitude. Some other method must then be used to obtain predictions and this will be the primary subject of this thesis.

1.2. The Quark Model

The discovery of mesons came from the earliest experiments that exposed photographic plates to cosmic rays. Before long, a whole spectrum of states were discovered that could be classified in a similar manner to atomic systems with spin, parity and charge-conjugation quantum numbers, J^{PC}. The lightest observed hadronic particles are the pseudoscalars with $J^P = 0^-$, these are the π's discovered by Powell and K's discovered by Rochester in the 1940s. In the 1960s Gell-Mann and Zweig independently suggested a method of classification, sometimes referred to as the *Eightfold Way*. An example of this

is depicted in fig. 1.1, where we plot the particle positions in a plane defined by specific combinations of their observable quantum numbers,

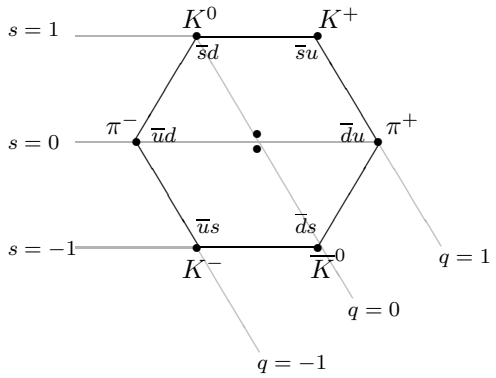

Figure 1.1.: The octet of pseudoscalars. In the centre the we have the combinations $\pi^0 = \frac{1}{\sqrt{2}}\left(\overline{u}u - \overline{d}d\right)$ and $\eta = \frac{1}{\sqrt{6}}\left(\overline{u}u + \overline{d}d - 2\overline{s}s\right)$. There is also a singlet that forms the final state in the nonet, $\eta' = \frac{1}{\sqrt{3}}\left(\overline{u}u + \overline{d}d + \overline{s}s\right)$. Note that convention states that the strange quark has strangeness $s = -1$.

Similar nonets may be formed for other J^{PC} states, where J is the total spin, P is parity and C is charge conjugation. An interesting problem occurs for the scalar sector, $J^P = 0^+$, where there appear to be enough resonances for two nonets. Chapters 2 and 3 are dedicated to investigating the particle composition of two of the lightest scalar resonances observed in QCD.

The arrangement depicted from fig. 1.1 is suggestive of an $SU(3)$ symmetry between a particle and anti-particle which leads to the decomposition,

$$\mathbf{3} \otimes \overline{\mathbf{3}} = \mathbf{8} \oplus \mathbf{1} \tag{1.6}$$

where we now understand the left hand side of the equation to represent how three symmetric light quarks, carrying colour but neglecting mass, u, d, s and their antiparticles combine to form an octet and singlet of colourless states. The quark model then led to the theory of Quantum Chromodynamics in the early 1970s as a gauge theory similar to the $U(1)$ QED theory already in existence, but now based around an $SU(3)$ *colour* symmetry, where the quarks themselves interact with a different force-carrier called the gluon, each carrying a new charge called colour.

1.3. Quantum Chromodynamics

It is widely believed that Quantum Chromodynamics (QCD) is the correct theory to describe the strong interactions that give rise to a plethora of particles containing quarks and gluons ranging in masses from the neutral pion at 135 MeV to bound states containing b-quarks around and above 10 GeV. Asymptotic states bound by the strong interactions are observed to be colour-neutral, this is closely related to the confinement of coloured particles and is a fundamental problem yet to be fully understood. It is closely related to the running of the coupling between interactions of the fields of the Lagrangian,

$$\mathcal{L} = \bar{\psi}^a \left(i\not{D} - m \right) \psi^a - \frac{1}{4} F^a_{\mu\nu} F^{\mu\nu}_a - \frac{1}{2\xi} \left(\partial_\mu A^\mu_a \right)^2 + \left(\partial^\mu \bar{c}_a \right) D^{ab}_\mu c_b \tag{1.7}$$

$$F^a_{\mu\nu} = \partial_\mu A^a_\nu - \partial_\nu A^a_\mu + g f^{abc} A^b_\mu A^c_\nu \tag{1.8}$$

$$D_\mu = \partial_\mu - ig\tau^a A^a_\mu \tag{1.9}$$

where g is the bare coupling, ψ denotes quark fields, A_μ is the gluon field, τ^a is a generator of the $SU(3)$ group in the fundamental representation, c is the Fadeev-Popov ghost field and ξ is the gauge parameter.

QCD is an $SU(3)$ gauge theory which implies that the ψ and A fields in the above equations have an additional index, due to the colour quantum number. Colour is always hidden from experiment by confinement but is crucial in the structure of the theory. The $SU(3)$ group has two representations that appear in the Lagrangian of QCD, the matter fields live in the fundamental representation which may be given as the Gell-Mann matrices, whilst the gluon field lives in the adjoint representation which may be defined by the antisymmetric structure constant, f^{abc},

$$\tau^a_{ij} = i f^a_{ij} \tag{1.10}$$

where τ^a_{ij} is in the adjoint representation.

The generators of the group τ^a are related to the structure constants by the commutation relation,

$$[\tau^a, \tau^b] = i f^{abc} \tau^c \tag{1.11}$$

where a, b and c are the colour indices. The transformation property of ψ with the operation of the group element $U \in SU(3)$,

$$U = \exp(i\tau^a \phi^a) \tag{1.12}$$

is defined as,

$$\psi \to \psi' = U\,\psi\,. \tag{1.13}$$

Local gauge invariance is imposed in QCD, as in QED, where gauge invariance is enforced at each spacetime point. The term $\bar{\psi}\not{D}\psi$ is then invariant under $SU(3)$ gauge transformations.

Using the Lagrangian, we may derive the Feynman rules of the theory which are used to construct scattering amplitudes. The most straightforward method is to adopt the path integral approach found in numerous standard references [1–3], we begin by making the connection with the action S, completely analogous to the classical quantity of the same name,

$$S[\psi, \bar{\psi}, A, c, \bar{c}] = \int d^4x\ \mathcal{L}_{QCD}[\psi, \bar{\psi}, A, c, \bar{c}]\,. \tag{1.14}$$

In analogy to statistical mechanics we then write down a partition function $\mathcal{Z}$ and add a source term for each field,

$$\begin{aligned}\mathcal{Z}[\eta, \overline{\eta}, J, \sigma, \overline{\sigma}] = &\int \mathcal{D}\left[\psi, \overline{\psi}, A, c, \overline{c}\right] \times \\ &\exp\left(i \int d^4x\ \mathcal{L}_{QCD}[\psi, \overline{\psi}, A, c, \overline{c}] + \overline{\eta}\psi + \overline{\psi}\eta + J^\mu A_\mu + \overline{\sigma}c + \overline{c}\sigma\right)\,.\end{aligned} \tag{1.15}$$

The functional derivative with respect to the sources may then be used to derive the Greens functions, symbolically for a generic source j and a generic propagator $\Delta(x_1 - x_2)$ may be found by performing two functional derivatives,

$$\frac{1}{Z[0]}\frac{i\delta}{\delta j(x_1)}\frac{i\delta}{\delta j(x_2)}Z[j] = \Delta(x_1 - x_2) \tag{1.16}$$

and normalising with $\frac{1}{Z[0]}$. The functional $Z[j]$ generates both connected and disconnected Green's functions. In particle theory we are only really interested in the connected Green's functions that are required to construct scattering amplitudes, these are simply related

to $Z[j]$ by,

$$Z[j] = e^{iW[j]} \tag{1.17}$$

where $W[j]$ is the generating functional of the connected Green's functions [4]. It is then straightforward to derive the Feynman rule for a connected n-point Green's function by taking functional derivatives and setting the sources to zero,

$$G_n^c(x_1, ..., x_n) = (-i)^{n-1} \frac{\partial^n W[j]}{\partial j(x_1)...\partial j(x_n)}\Big|_{j=0}. \tag{1.18}$$

The Feynman rules that we apply, in momentum space, are given in appendix B. These are obtained using a Fourier transform from coordinate space. The Feynman rules are only of real importance in chapters 4 and 5 where they are used in the derivation of the integration kernels for the Schwinger–Dyson Equations.

1.4. Outline

First we consider two scalar resonances seen in low-energy QCD, the $\sigma(600)$ and the $f_0(980)$ using two completely different methods, we investigate the poles and quark composition of each with clear conclusions. These methods are phenomenological in that they are applied to the data in order to understand the physics.

Secondly we consider the Schwinger-Dyson Equations of QCD, which are fundamental equations from field theory and are a natural first step in deriving observable quantities in low-energy QCD from the fundamental Lagrangian.

Chapter 2.

The structure of the $\sigma(600)$ from Regge Theory and its N_c-dependence in Chiral Perturbation theory

Understanding the composition of mesons has proven to be a difficult task. Mesons such as the π's and the K's have long been understood as simple bound states of a light quark and an antiquark. In any hadron however there will be other contributions, particularly from other strongly interacting particles such as gluons and valence quarks not necessary in the simple $\bar{q}q$ picture. These quantum effects will no doubt give rise to important properties that may be observed in production, scattering or decay processes. There are other resonances whose composition is much less clear. Beginning with a state that spends most of its time as $\bar{q}q$ such as the lightest spin-1 meson, the, $\rho(770)$ which has $J^{PC} = 1^{--}$. We know that this decays predominantly to $\pi\pi$ and therefore must spend a significant amount of its time in a $\bar{q}q\bar{q}q$ configuration, which clouds the simple $\overline{q}q$ picture. A similar argument must of course be true of all particles that couple strongly to decay channels. There are many resonances in QCD whose composition is unknown or poorly understood, a relatively recent example is the $X(3872)$ which lies close to the $\overline{D}D^*$ threshold, has a narrow width, and has no expected candidate from quark potential models. It appears that the strong coupling to decay channels can pull a bare $\overline{c}c$ state downwards in mass, significantly changing its properties in the process [5–9].

A class of particles of particular interest are the light scalar mesons. Whilst the LHC searches the TeV scale for the long-sought fundamental scalar responsible for breaking the SU(2) symmetry of the standard model, QCD at strong coupling already breaks the symmetry of the vacuum at the MeV level through quark and gluon condensates. The

lightest unflavoured scalar mesons, the $\sigma(600)$ and the $f_0(980)$ feel the effects of the vacuum greater than most since they are unimpeded by an angular momentum factor between their constituents. The production threshold opens sharply with a cusp that goes like $(1 - s_{\rm th}/s)^{1/2}$, rather than some higher power if there were angular momentum present. In the language of quantum mechanics, this would describe a state with a non-zero wavefunction at the origin which, in the language of quantum mechanics, would increase the probability of decay over a higher-spin state. The point is that scalars feel the effects of the vacuum and coupling decay to channels more strongly than their higher-spin counterparts, and it is this that often makes understanding their composition so much more challenging.

In this chapter we combine a range of techniques to investigate the composition of the lightest scalar enchancement in QCD, the $\sigma(600)$. This meson decays predominantly to $\pi\pi$ and has a width of similar size to its mass. We first present chiral perturbation theory and its unitarisation that allows meson scattering amplitudes below 2 GeV^2 to be obtained. The behaviour of these amplitudes, particularly the σ and ρ resonances with increasing N_c is then presented [10]. Finite Energy Sum Rules are then considered in conjunction with Regge Theory and Semi-Local Duality and if these are to be satisfied for all N_c then we find a natural explanation arises at $\mathcal{O}(p^6)$ in chiral perturbation theory.

2.1. Chiral Perturbation Theory

Chiral perturbation theory (χPT) provides an excellent theoretical description of the interactions of the π and K mesons in low-energy QCD. It has SU(2) and SU(3) variants which utilise the small quark masses for u, d and u, d, s quarks respectively, relative to the hadronic scale, to invoke approximate chiral symmetry. In group theory language, starting with the massless u, d and s quarks we have $SU(3)_L \times SU(3)_R \to SU(3)_{L+R}$ after spontaneous symmetry breaking, the lightest pseudoscalar mesons correspond to the pseudo-goldstone bosons of the symmetry breaking. In the limit of vanishing light quark masses, the low-energy expansion would be exact, instead however, the quark masses are introduced as a perturbation. This allows an expansion in external momenta, derivatives and quark masses. The number of terms in the Lagrangian grows order by order, but the number remains finite and the theory is renormalisable and predictive, at least up to $\mathcal{O}(p^6)$.

At first order in p^2, the effective theory depends on just one low-energy constant, f_π, the pion decay constant. At $\mathcal{O}(p^4)$ there are 10 additional parameters, but only 8 of these contribute to scattering processes, denoted $L_{i=1\to 8}$. Theoretically these must be fixed at some renormalisation scale μ, this is usually taken in the region of m_ρ, we use $\mu = 770$ MeV. The number of parameters grows rapidly order-by-order.

The truncated chiral expansion up to second order is valid typically up to around 500 MeV, extrapolation further usually leads to amplitudes that violate unitarity. Explicitly imposing unitarity as a constraint has recently been used as a method to extend the range of validity of the chiral expansion above 1 GeV, to great success. Chiral perturbation theory combined with unitarity is able to predict key features in the low-energy spectrum, most notably the $\sigma(600)$, the $\rho(770)$, and the $K^*(892)$.

In $\pi\pi$ scattering only the σ and the ρ are important below $K\overline{K}$ threshold. The σ is a scalar resonance, seen in the $I = 0$ channel. It is very broad spanning the entire region between the $\pi\pi$ and $K\overline{K}$ thresholds. The ρ is a vector state seen in $I = 1$ currents that is very narrow compared to the σ.

2.1.1. Chiral Lagrangian

Chiral perturbation theory is best described by an effective Lagrangian that is an expansion in powers of momentum. The Lagrangian for SU(3) χPT, where the masses of the u, d and s quarks are initially assumed massless, is constructed such that is respects the symmetries of QCD and exact chiral symmetry $SU(3)_L \times SU(3)_R$ is initially assumed that is spontaneously broken. Since the masses are small they may be introduced as a perturbation, that also breaks the chiral symmetry. In order to respect the symmetries, the first order that contributes is $\mathcal{O}(p^2)$ and only even orders contribute. If we write the chiral Lagrangian in the form,

$$\mathcal{L} = \mathcal{L}^{(2)} + \mathcal{L}^{(4)} + \mathcal{L}^{(6)} + ... \tag{2.1}$$

then the first term is,

$$\mathcal{L}^{(2)} = \frac{f^2}{4}\mathrm{Tr}\left(\partial_\mu U \partial^\mu U^\dagger + \mathcal{M}^\dagger U + \mathcal{M} U^\dagger\right) \tag{2.2}$$

the second term is,

$$\begin{aligned}\mathcal{L}^{(4)} &= L_1 \mathrm{Tr}\left(\left(\partial_\mu U \partial^\mu U^\dagger\right)^2\right) + L_2 \mathrm{Tr}\left(\partial_\mu U \partial_\nu U^\dagger\right) \mathrm{Tr}\left(\partial^\mu U \partial^\nu U^\dagger\right) \\ &+ L_3 \mathrm{Tr}\left(\partial_\mu U \partial^\mu U^\dagger \partial_\nu U \partial^\nu U^\dagger\right) + L_4 \mathrm{Tr}\left(\partial_\mu U \partial^\mu U^\dagger\right) \mathrm{Tr}\left(\mathcal{M}^\dagger U + \mathcal{M} U^\dagger\right) \\ &+ L_5 \mathrm{Tr}\left(\partial_\mu U \partial^\mu U^\dagger \left(\mathcal{M}^\dagger U + \mathcal{M} U^\dagger\right)\right) + L_6 \mathrm{Tr}\left(\left(\mathcal{M}^\dagger U + \mathcal{M} U^\dagger\right)^2\right) \\ &+ L_7 \mathrm{Tr}\left(\left(U^\dagger \mathcal{M} - \mathcal{M}^\dagger U\right)^2\right) + L_8 \mathrm{Tr}\left(\mathcal{M}^\dagger U \mathcal{M}^\dagger U + U^\dagger \mathcal{M} U^\dagger \mathcal{M}\right) \end{aligned} \tag{2.3}$$

where U collects the goldstone fields and is different for the SU(2) and SU(3) variants of χPT. $\mathcal{M}$ is the quark mass matrix, which for SU(2) is given by $m_\pi^2 \mathbb{1}$ and f is the unrenormalised pion decay constant. The L_i's are the unrenormalised Wilson coefficients for the SU(3) effective theory at $\mathcal{O}(p^4)$, in χPT these are not at present calculable by matching to full QCD, so they are determined by fitting to experiment. In χPT the Wilson coefficients are often referred to as the low-energy constants or LECs. For SU(3) we have,

$$U = \exp \frac{i\sqrt{2}}{f} \begin{pmatrix} \frac{1}{\sqrt{2}}\pi^0 + \frac{1}{\sqrt{6}}\eta & \pi^+ & K^+ \\ \pi^- & \frac{-1}{\sqrt{2}}\pi^0 + \frac{1}{\sqrt{6}}\eta & K^0 \\ K^- & \bar{K}^0 & \frac{-2}{\sqrt{6}}\eta \end{pmatrix} \tag{2.4}$$

where $\mathcal{M} = \mathrm{diag}(m_{0,\pi}^2, m_{0,\pi}^2, 2m_{0,K}^2 - m_{0,\pi}^2)$. The π's, K's and η's are the fields in the chiral theory and their bare masses, which are simply related to their physical masses are the respective $m_{0,i}$ terms in $\mathcal{M}$. For SU(2) the situation is a little different since there are only four Wilson coeffecients which are denoted $l_{i=1\to4}$, in this case the matrix U becomes,

$$U = \exp \frac{i\sqrt{2}}{f} \begin{pmatrix} \frac{1}{\sqrt{2}}\pi^0 & \pi^+ \\ \pi^- & \frac{-1}{\sqrt{2}}\pi^0 \end{pmatrix}, \tag{2.5}$$

the chiral Lagrangian at $\mathcal{O}(p^6)$ for SU(2) is given ref. [11]. An important test of the stability of the χPT expansion is that the SU(2) and SU(3) forms give similar predictions for their regions of validity; this has been verified. In this study we will first use SU(3) χPT at one-loop [10], $\mathcal{O}(p^4)$, initially to provide our $\pi\pi$ amplitude and in a coupled channel system where we must diagonalise,

$$\mathbf{A} = \begin{pmatrix} A_{\pi\pi} & A_{\pi K} \\ A_{K\pi} & A_{KK} \end{pmatrix}, \tag{2.6}$$

when above $K\overline{K}$ threshold in order to obtain the physical $\pi\pi$ scattering amplitude. The matrix elements A_{ij} are calculable from standard chiral perturbation theory, as an example $A_{\pi\pi}$ is given below in eq. (2.7). This and the other components A_{ij} are obtained from ref. [10]. This mixing matrix is only relevant for the $J = 0$ channel because we only consider amplitudes up to 2 GeV^2 where no significant decay channels are open for higher spins. Later we use the SU(2) variant at two-loops $\mathcal{O}(p^6)$ [11], since this provides a greater range of validity and digs deeper into the full theory. This is represents the highest order amplitudes that are currently available in the literature.

2.1.2. The χPT $\pi\pi$ Amplitude at one-loop and two-loop order

There is only one process relevant to $\pi\pi$ scattering below 1 GeV, which has been calculated most recently at one-loop order by *Peláez and Gómez-Nicola* [10] in a study that combines data on many different channels to simultaneously fit the low-energy constants. References to previous calculations may be found in their paper. The relevant amplitude is $\pi^0\pi^0 \to \pi^+\pi^-$, which is denoted $A_{\pi\pi}(s,t,u)$, this may be used to construct processes with distinct isospin using symmetry crossing relations,

$$
\begin{aligned}
A_{\pi\pi}(s,t,u) = {} & \frac{s-M_\pi^2}{f_\pi^2} - \frac{\mu_\pi}{3f_\pi^2 M_\pi^2}\left\{4s^2 - 4tu - 4sM_\pi^2 + 9M_\pi^4\right\} \\
& - \frac{\mu_K}{6f_\pi^2 M_K^2}\left\{s^2 - tu + 2sM_\pi^2\right\} - \frac{\mu_\eta M_\pi^4}{9f_\pi^2 M_\eta^2} \\
& + \frac{4}{f_\pi^4}\left\{(2L_1^r + L_3)(s-2M_\pi^2)^2 + L_2^r[(t-2M_\pi^2)^2 + (u-2M_\pi^2)^2]\right\} \\
& + \frac{8M_\pi^2}{f_\pi^4}\left\{(2L_4^r + L_5^r)s + 2(2L_6^r + L_8^r - 2L_4^r - L_5^r)M_\pi^2\right\} \\
& + \frac{1}{576\pi^2 f_\pi^4}\left\{30(M_\pi^2 - s)s + 21tu - 56M_\pi^4\right\} \\
& + \frac{1}{2f_\pi^4}\left\{\frac{s^2\bar{J}_{KK}(s)}{4} + \frac{M_\pi^4\bar{J}_{\eta\eta}(s)}{9} + (s^2 - M_\pi^4)\bar{J}_{\pi\pi}(s)\right\} \\
& + \frac{1}{6f_\pi^4}\Bigg\{\frac{(t-4M_K^2)(2s+t-4M_\pi^2)\bar{J}_{KK}(t)}{4} \\
& + \left[t(t-u) - 2M_\pi^2(t-2u+M_\pi^2)\right]\bar{J}_{\pi\pi}(t) + [t \leftrightarrow u]\Bigg\},
\end{aligned}
$$

where the L_i^r terms are the renormalised Wilson coeffecients of the effective theory. The $\overline{J_i}$'s are loop integral results that have a simple algebraic form given by ref. [10], along with a full description of the construction of the amplitudes and renormalisation procedure.

The terms s, t, u are the usual Mandelstam variables and the M_i's are the physical meson masses. The first term is the tree level, $\mathcal{O}(p^2)$ contribution, the terms μ_i, where $i = \pi, K, \eta$ arise due to the renormalisation procedure. They are given by,

$$\mu_i = \frac{M_i}{32\pi^2 f_\pi^2} \log \frac{M_i}{\mu}. \tag{2.7}$$

The entire amplitude is $t \leftrightarrow u$ symmetric, which is a useful consistency check. Given the amplitude $A(s,t,u)$ and a set of renormalised low-energy constants L_i^r, then the distinct s-channel isospin processes, A^{sI}, may be constructed as,

$$A^{s0}(s,t,u) = 3A(s,t,u) + A(t,s,u) + A(u,t,s), \tag{2.8}$$

$$A^{s1}(s,t,u) = A(t,s,u) + A(u,t,s), \tag{2.9}$$

$$A^{s2}(s,t,u) = A(t,s,u) - A(u,t,s), \tag{2.10}$$

this alone does not produce any resonances. However, eq. (2.7) can be improved by going by beyond fixed order in χPT using the unitarity of the S-matrix.

In order to apply the unitarity condition, the partial waves of these must be projected out, since each partial wave must respect unitarity alone. The partial waves, f_{IJ} can be obtained via,

$$[f_{IJ}(s)]^{(n)} = \frac{1}{64\pi} \int_{-1}^{1} dx P_J(x) A^{I\,(n)}(s, t(x), u(x)) \tag{2.11}$$

where $A^{I\,(n)}$ denotes the contribution at the order n in χPT amplitude given in eq. (2.7), and a factor $1/2$ has been included in the normalisation, to account for identical particles and the $P_J(x)$ are the Legendre polynomials, $P_J(x) = 1\ , x\ , \frac{1}{2}(3x^2 - 1)$ for $J = 1, 2, 3$ respectively. The constants f_π and L_i are fitted from experiment and critically depend on N_c. Their leading order N_c behaviour is known and these are the parameters that enable the large-N_c limit to be investigated.

Above $K\overline{K}$ threshold, as we will see in chapter 3, the $\pi\pi$ channel couples to $K\overline{K}$, particularly for $I = 0$, $J = 0$ where the $\sigma(600)$ resides. These effects should be included and the method is outlined in ref. [10]. In addition to the $\pi^0\pi^0 \to \pi^+\pi^-$ amplitude, the $\pi\pi \to KK$ and $KK \to KK$ amplitudes are also required and the unitarisation procedure must be generalised to a 2×2 matrix, where this contribution becomes important. Diagonalisation then leads to important contributions due to the mixing from the off-diagonal components.

The two-loop $\mathcal{O}(p^6)$ amplitude is given in ref. [11]. Its unitarisation procedure is described below.

2.1.3. Unitarity and the Inverse Amplitude Method

Unitarity is a property of the S-matrix, $\mathbf{S}^\dagger\mathbf{S} = \mathbb{1}$ that is necessary for CPT symmetry to hold. A simple relation can be derived for a general T-matrix element, which we define from the S matrix in usual way,

$$S_{ij} = \delta_{ij} + 2i\sqrt{\rho_i\rho_j}\,T_{ij} \tag{2.12}$$

where S is the S-matrix, T is the T-matrix and ρ_i is a phase space factor that will appear frequently during this chapter and the next, given by $\rho_i(s) = (1-4m_i^2/s)^{1/2}$. The unitarity of the S-matrix leads to the condition,

$$\mathrm{Im}T_{ij} = T_{ik}\rho_k T^*_{kj}, \tag{2.13}$$

or alternatively we may write,

$$\mathrm{Im}(T^{-1})_{ij} = -\delta_{ij}\rho_i \quad \text{(no summation)}. \tag{2.14}$$

This is an incredibly useful result that gives us a tight restriction on the behaviour of T. This result allows us to write down the manifestly real K-matrix to represent our T-matrix elements, where some $K = \mathrm{Re}\,T$ would be valid for the exact amplitude,

$$T = \left(\frac{1}{K} - i\rho\right)^{-1}. \tag{2.15}$$

In QCD at low energies the ρ and σ saturate the unitarity limit well below the scale of 1 GeV where χPT is typically valid. The amplitudes T satisfy unitarity, but only up to their perturbative order, if we expand T in a perturbative series as in χPT,

$$T = T^{(2)} + T^{(4)} + T^{(6)} + T^{(8)} + ... \tag{2.16}$$

then the unitarity condition eq. (2.13) will only be satisfied up to its perturbative order. Since the unitarity relation eq. 2.13 is linear in T on the left and quadratic on the right

then,

$$\mathrm{Im}T^{(2)} = 0 \tag{2.17}$$

$$\mathrm{Im}T^{(4)} = T^{(2)*}\rho T^{(2)} \tag{2.18}$$

$$\mathrm{Im}T^{(6)} = T^{(4)*}\rho T^{(2)} + T^{(2)*}\rho T^{(4)} \ . \tag{2.19}$$

Since the unitarity limit is reached at such low energies in $\pi\pi$ scattering then convergence can be improved since the imaginary part of the inverse amplitude is known. The Inverse Amplitude Method (IAM) applied to χPT [10, 12, 13] is essentially a strict enforcement of eq. (2.15) using the χPT amplitude to give $K = \mathrm{Re}T$. The form was originally derived by a dispersion relation analysis,

$$T \simeq \frac{\left(T^{(2)}\right)^2}{T^{(2)} - T^{(4)}} \, . \tag{2.20}$$

A binomial expansion of this expression yields the same series as in eq. (2.16), so they are equivalent order by order, but the IAM resums the series in such a way that the expansion goes beyond perturbative unitarity.

Unitarity must be respected for each partial wave so then the expressions that are applied are, for NLO $\mathcal{O}(p^4)$,

$$f_{IJ} \simeq \frac{\left([f_{IJ}]^{(2)}\right)^2}{[f_{IJ}]^{(2)} - [f_{IJ}]^{(4)}} \tag{2.21}$$

and at NNLO $\mathcal{O}(p^6)$,

$$f_{IJ} \simeq \frac{\left([f_{IJ}]^{(2)}\right)^2}{[f_{IJ}]^{(2)} - [f_{IJ}]^{(4)} - [f_{IJ}]^{(6)} + \left([f_{IJ}]^{(4)}\right)^2/[f_{IJ}]^{(2)}} \tag{2.22}$$

it is this that is used to unitarise the amplitudes. In $\pi\pi$ scattering below $K\overline{K}$ threshold then all of the above equations are just simple scalar equations, above threshold in the $J = 0$ channel we diagonalise a 2×2 matrix as outlined in [10]. This unitarisation procedure allows χPT to correctly reproduce the poles required for the ρ and σ resonances from first principles given a standard set of low-energy constants fixed from scattering processes.

After this step the amplitude with distinct isospin in the s-channel may then constructed by doing the sum to invert the decompostion in eq. (2.11),

$$\mathrm{Im}A^{sI}(s,t) = \sum_J (2J+1)\,\mathrm{Im}f_{IJ}(s)P_J(z(s,t)) \tag{2.23}$$

where,

$$z(s,t) = 1 + \frac{2t}{s - s_{th}} \tag{2.24}$$

and $P_J(z(s,t))$ are Legendre polynomials in z. The advantage is that the partial waves f_{IJ} now respect unitarity exactly, not just perturbatively. The sum may be truncated for small momenta since only the first few partial waves will contribute. We depict the unitarisation procedure in fig. 2.1.

2.2. Local Duality, Regge Theory and Finite Energy Sum Rules

Local Duality is a feature observed in many experimental scattering processes that as energy increases from threshold distinct narrow resonances appear first as sharp peaks close to threshold, which the higher energy partners become increasingly wider until a smooth Regge behaviour is observed far from threshold. The low-energy region behaves much like a sum of narrow resonances, with a background, whilst the large phase space for higher poles results in increasing decay widths until they begin to overlap and are indistinguishable from each other, and the background. This smooth behaviour of the scattering amplitude far from threshold may be thought of as a sum of many resonances in the direct (s-) channel but is most readily described by a small number of crossed (t-) channel exchanges [14, 15]. Semi-local duality [16, 17] is the observation that whilst the smooth Regge behaviour closely matches the amplitude at higher energies, it also matches at low energies towards the threshold region if a *local average* is considered.

Regge exchanges must also be built from the quarks and gluons described by QCD; there must be $\overline{q}q$ and multiquark components present. In the isospin-2 channel in $\pi\pi$ scattering there are no regular $\overline{q}q$ resonances so any exchanges in this channel must be of a more complicated nature. From experiment it is known that at $N_c = 3$, $\overline{q}q$ exchanges dominate.

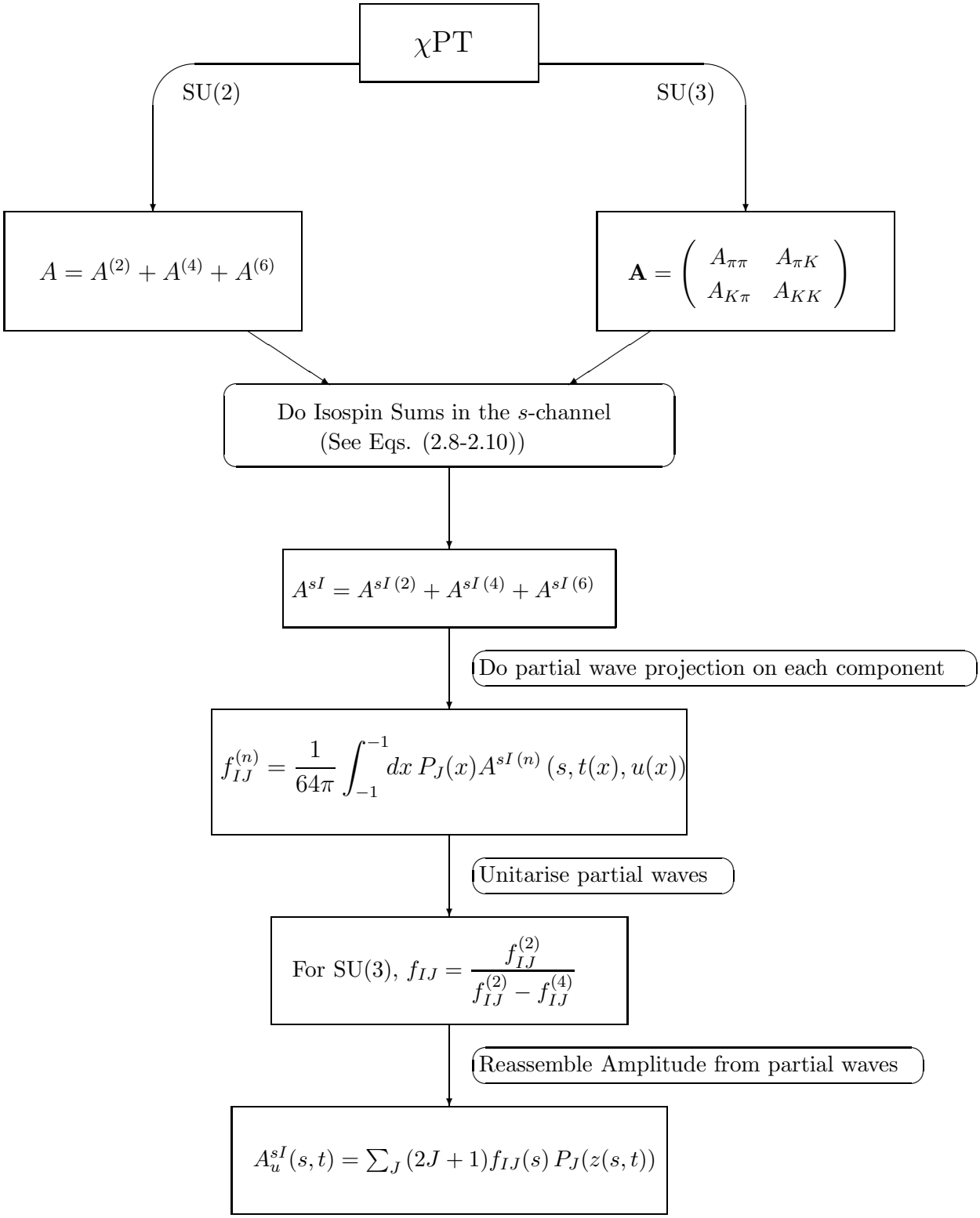

Figure 2.1.: The unitarisation of χPT partial wave amplitudes using the IAM method. A_u^{sI} denotes the unitarised version of A^{sI} which is a $\pi\pi$ amplitude with distinct isospin I in the s-channel.

In the process $\pi^+\pi^- \to \pi^-\pi^+$ which is an isospin-2 process in the t-channel then the low-energy resonances must have contributions that, on the average, cancel [18].

In $\pi\pi$ scattering there are two resonances at low-energies that have been observed by experiment and have been readily reproduced by the χPT amplitudes given above. The $\rho(770)$ is the narrow vector state and has $I = J = 1$, whilst the $\sigma(600)$ is a broad scalar state with $I = J = 0$. The contributions of these components in $\pi^+\pi^-$ scattering do cancel when averaged over a suitable region defined with the Finite Energy Sum Rules (FESR), which we describe below for the $I = 2$ $t-$channel process. How this relation is upheld with increasing N_c may not be immediately obvious since the σ is believed to be a multiquark state that we expect to disappear with increasing N_c, whilst the ρ is expected to remain due to its predominantly $\overline{q}q$ composition, it tends to a δ-function for large-N_c. If the σ melts away completely then there is nothing for the ρ to cancel against, which would lead to the conclusion that semi-local duality and the Regge behaviour of scattering amplitudes can only be a feature of the physical world with $N_c = 3$. However, theoretically this is not what is expected since multiquark Regge exchanges should be increasingly suppressed with increasing N_c. This apparent contradiction will be investigated using FESR and χPT and we show that an answer may be found at $\mathcal{O}(p^6)$ in χPT, when we consider the amplitudes up to 2 GeV^2.

2.2.1. The *t*-channel Amplitudes

The unitarised s-channel $\pi\pi$ scattering amplitudes with definite isospin are referred to now as $A^{sI}(s,t)$ dropping the u from fig 2.1, we may relate these to the t-channel exchange with definite isospin using crossing relations,

$$A^{t0}(s,t) = \frac{1}{3}A^{s0}(s,t) + \quad A^{s1}(s,t) + \frac{5}{3}A^{s2}(s,t), \tag{2.25}$$

$$A^{t1}(s,t) = \frac{1}{3}A^{s0}(s,t) + \frac{1}{2}A^{s1}(s,t) - \frac{5}{6}A^{s2}(s,t), \tag{2.26}$$

$$A^{t2}(s,t) = \frac{1}{3}A^{s0}(s,t) - \frac{1}{2}A^{s1}(s,t) + \frac{1}{6}A^{s2}(s,t). \tag{2.27}$$

The inputs A^{sI} for these are calculable from unitarised χPT as sums of partial waves as defined by eq. (2.11), and outlined above. At fixed t and large ν the imaginary parts of

these amplitudes are related to their Regge counterparts,

$$\mathrm{Im}A^{tI}(\nu,t) = \sum_R \beta_R(t)\left[\alpha'(\nu-\nu_{th})\right]^{\alpha_R(t)}, \tag{2.28}$$

where $\alpha_R(t)$ is the Regge trajectory, $\beta_R(t)$ is the Regge coupling and α' is the universal gradient of $\overline{q}q$ trajectories, $\beta_R(t) \simeq 0.9$ GeV^{-2}, and $\nu_{th} = (s_{th}+t)/2$.

The *local average* used for the semi-local duality between Regge amplitudes and the resonance region may be expressed as a FESR,

$$\int_{\nu_1}^{\nu_2} d\nu\ \nu^{-n}\mathrm{Im}A^{tI}_{\mathrm{res}}(\nu,t) \simeq \int_{\nu_1}^{\nu_2} d\nu\ \nu^{-n}\mathrm{Im}A^{tI}_{\mathrm{Regge}}(\nu,t) \tag{2.29}$$

where $\nu = (s-u)/2$ is used due to the symmetry of the amplitudes under $s \to u$, $\nu = s = -u$ along the line $t = t_{th} = 4m_\pi^2$. The region over which these are matched should be some integer multiple of the separation of resonances which is conveniently given by $1/\alpha'$. We consider two ranges, from threshold, ν_{th} to $\nu = 1$ GeV^2 and from ν_{th} to $\nu = 2$ GeV^2, where $\nu_{th} = (s_{th}+t)/2$.

2.2.2. Comparing the FESR relation with experiment

In order to understand how well the relation eq. (2.29) is satisfied at higher values of N_c it is important to understand how well it works for the physical amplitudes at $N_c = 3$. In order to represent physical reality we use a partial wave parameterisation given by *Kaminski, Peláez and Yndurain* [19]. This represents the results of a thorough analysis of the available $\pi\pi$ scattering data up to 2 GeV^2 covering the S, P and D partial waves. We investigate the ratio,

$$R_n^I = \frac{\int_{\nu_1}^{\nu_2} d\nu\ \nu^{-n}\mathrm{Im}A^{tI}(\nu,t)}{\int_{\nu_1}^{\nu_3} d\nu\ \nu^{-n}\mathrm{Im}A^{tI}(\nu,t)} \tag{2.30}$$

where we consider the first two regions that are valid, with $\nu_1 = \nu_{th}$ and up to $\nu_2 = 1$ GeV^2 and $\nu_3 = 2$ GeV^2, eq. (2.29) is well satisfied when the ratio $R_n^I \simeq 1$. We consider only the leading Regge behaviour because then the coupling β_R cancels in this ratio. For $\mathrm{Im}A^{t0}$ the Pomeron Regge trajectory gives the dominant contribution, and for $\mathrm{Im}A^{t1}$ it is the $\rho(770)$ that gives the dominant contribution, the leading contribution to these amplitudes

from Regge theory may be given as,

$$\mathrm{Im}A^{t0}_{\mathrm{Regge}} = 1.08 + 0.25t \tag{2.31}$$

$$\mathrm{Im}A^{t1}_{\mathrm{Regge}} = 0.47 + 0.89t \tag{2.32}$$

where eq. (2.32) is calculated by fitting the linear trajectory through the $\rho(770)$ and $\rho_3(1680)$ resonances listed in the PDG data tables [20], when plotted as in figure 2.2. This Regge trajectory is degenerate with another given by the $f_2(1270)$ and $f_4(2050)$, also shown in figure 2.2. The pomeron trajectory is obtained from ref. [21]. Using eq. (2.30) we find the results given in table 2.1. The amplitudes from χPT are represented by a sum of the lowest partial waves, it is important also to check the range of validity. For higher values of n in eq. (2.30) then the lowest partial waves should dominate since this adds extra weight to the low-energy region. Higher waves are suppressed close to the threshold by factors of $(1 - s_{th}/s)^{2J+1}$, so for increasing J, they are increasingly suppressed. Hence, a sum of the first few partial waves should be sufficient, however it is important to check whether it is appropriate to include upto J=1, 2 or 3. Using the KPY parameterisation of the experimental data this is straightforward.

We conclude that from table 2.1, we should include up to the D wave in order to obtain a good agreement and that for $n = 0$, eq. (2.30) does not give good agreement, presumably higher partial waves are responsible. So we restrict our investigation to $1 \leq n \leq 3$ and include the S, P and D partial waves in the sum. Higher values of n put too much emphasis on the region close to threshold which is far from the poles of these resonances so is not a measure of the cancellation between $\sigma(600)$ and $\rho(770)$ which we intend to investigate.

2.3. N_c Dependence and resonance structure

The physical world in which our experiments are performed is restricted to QCD with three colours. Since we have the fundamental theory we can of course vary N_c and calculate various quantities with $N_c \neq 3$. It is useful to consider $N_c > 3$ since this can elucidate some of the inner workings of the mesons χPT is capable of producing [22, 23].

Increasing N_c results in a reduced coupling of $q\overline{q}$ states to decay channels and hence their widths decrease. The same effect also causes states made of four quarks or exotic combinations of quarks and gluons to become increasingly wide, thus their poles move

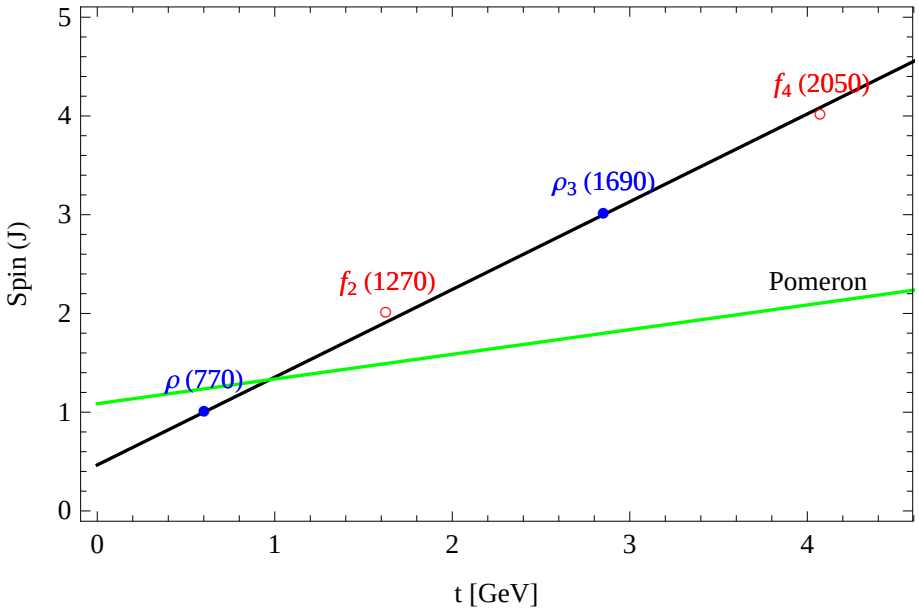

Figure 2.2.: A plot of the two dominant Regge trajectories used for isospin−0 and isospin−1 in the $t-$channel.

		$\mathbf{R_n^{I=0}}$		$\mathbf{R_n^{I=1}}$	
	n	$t = t_{th}$	$t = 0$	$t = t_{th}$	$t = 0$
Regge	0	0.213	0.226	0.324	0.351
	1	0.403	0.436	0.586	0.647
	2	0.678	0.743	0.856	0.919
	3	0.902	0.951	0.974	0.993
KPY S, P, D waves	0	0.337 ± 0.093	0.342 ± 0.083	0.479 ± 0.213	0.492 ± 0.191
	1	0.567 ± 0.095	0.582 ± 0.082	0.725 ± 0.157	0.741 ± 0.131
	2	0.788 ± 0.061	0.815 ± 0.047	0.894 ± 0.072	0.911 ± 0.052
	3	0.927 ± 0.023	0.953 ± 0.013	0.971 ± 0.022	0.982 ± 0.011
KPY S and P waves	0	0.615 ± 0.169	0.572 ± 0.133	0.743 ± 0.187	0.709 ± 0.103
	1	0.796 ± 0.145	0.771 ± 0.120	0.874 ± 0.123	0.861 ± 0.064
	2	0.912 ± 0.088	0.909 ± 0.068	0.950 ± 0.062	0.950 ± 0.026
	3	0.971 ± 0.038	0.977 ± 0.021	0.984 ± 0.023	0.989 ± 0.006

Table 2.1.: The R_n^I ratios from Regge Theory and the KPY parameterisation of $\pi\pi$ scattering, with and without D-waves.

away from the real axis in the E Argand plane, and the resonances disappear into the background. These behaviours are seen in low-energy unitarised χPT; the ρ becomes narrower and the σ enhancement subsides, as shown in the fig. 2.4 for the case given by SU(3) $\mathcal{O}(p^4)$ χPT. The precise behaviour depends on the LECs that are used, in this case we use the LECs given by ref. [24] and reproduced in table 2.2. These LECs give a ρ mass that moves to very slowly to lower energies with increasing N_c, for other choices the ρ mass can move to higher energies. The behaviour of the imaginary part of the pole in E however is always the same; with increasing N_c the imaginary part becomes smaller. Conversely, the opposite happens for the σ, as N_c increases, the imaginary part becomes larger until no obvious structure is visible. The behaviour of the dominant pole in E on the unphysical sheet is shown in figure 2.3, the position of the pole in E is related to the mass and width by,

$$E = M - i\Gamma/2 \tag{2.33}$$

where M corresponds to the particle mass and Γ to its width. In figure 2.4 we plot the $\pi\pi$ amplitude from SU(3) χPT for a range of values of N_c.

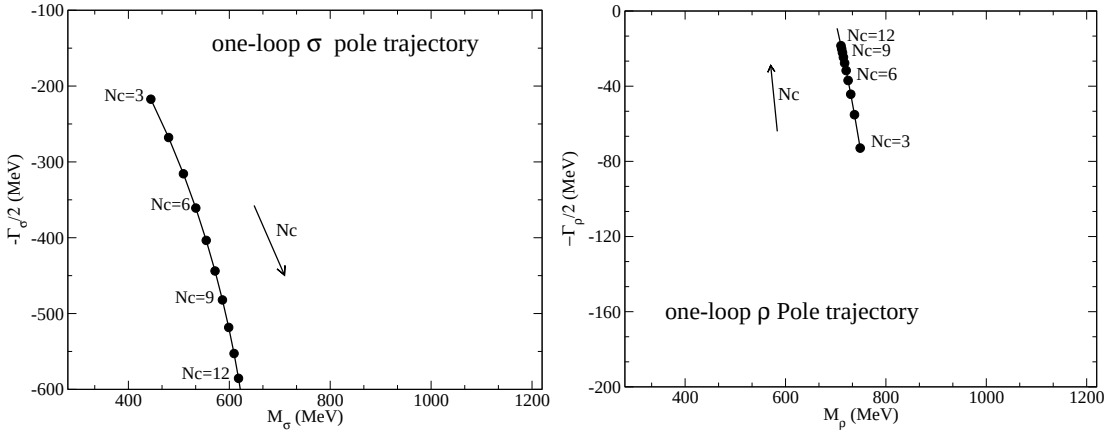

Figure 2.3.: The motion of the σ and ρ poles at $\mathcal{O}(p^4)$, from [25–27].

Coeff.	$N_c = 3$ Value [24]	$\mathcal{O}(N_c)$ scaling [28]
$f_\pi(N_c)$	92.4 MeV	$\sqrt{N_c/3} f_\pi(N_c = 3)$
$L_1(N_c)$	$(0.60 \pm 0.09) \times 10^{-3}$	$L_1(N_c = 3) - \frac{1}{2}\left(L_2(N_c) - L_2(N_c = 3)\right)$
$L_2(N_c)$	$(1.22 \pm 0.08) \times 10^{-3}$	$(N_c/3)\, L_2(N_c = 3)$
$L_3(N_c)$	$(-3.02 \pm 0.06) \times 10^{-3}$	$(N_c/3)\, L_3(N_c = 3)$
$L_4(N_c)$	0 (fixed)	$L_4(N_c = 3)$
$L_5(N_c)$	$(1.90 \pm 0.03) \times 10^{-3}$	$(N_c/3)\ L_5(N_c = 3)$
$L_6(N_c)$	$(-0.07 \pm 0.20) \times 10^{-3}$	$L_6(N_c = 3)$
$L_7(N_c)$	$(-0.25 \pm 0.18) \times 10^{-3}$	$L_7(N_c = 3)$
$L_8(N_c)$	$(0.84 \pm 0.23) \times 10^{-3}$	$(N_c/3)\ L_8(N_c = 3)$

Table 2.2.: The Wilson coefficients and their leading order N_c behaviour. These are renormalised at the scale $\mu = 770\,\text{MeV} \simeq m_\rho$. Note that the combination $2L_1(N_c) - L_2(N_c)$ is assumed constant for all N_c, which implies the L_1 behaviour above. An alternative is to assume $N_c/3$ scaling for L_1 as for the other N_c dependent L_i's.

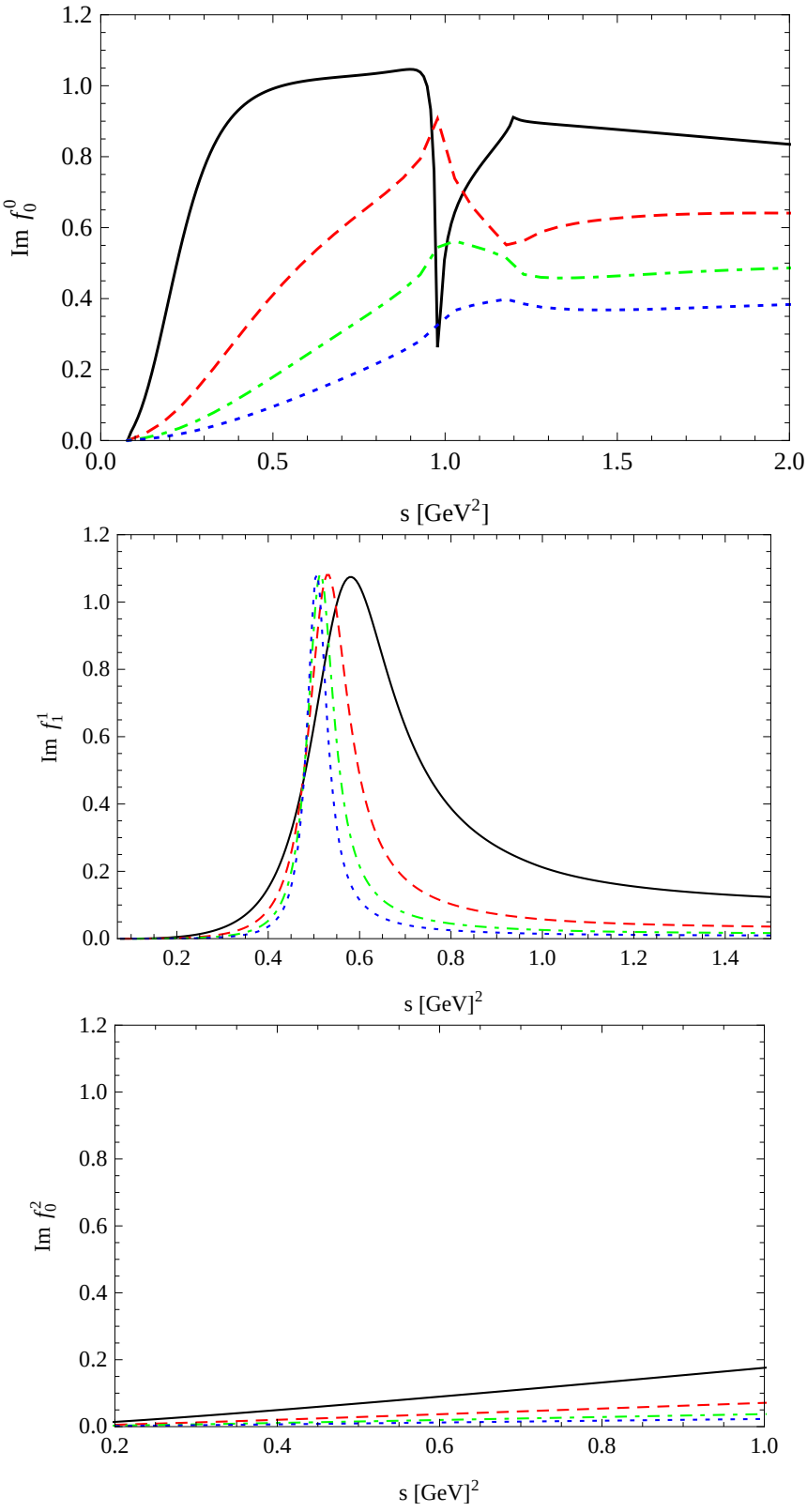

Figure 2.4.: The amplitudes Imf_{IJ} as defined in Eq. (2.21) from SU(3) χPT at $\mathcal{O}(p^4)$. Top: The σ enhancement as a function of N_c. Middle: The ρ resonance as a function of N_c. Bottom: The $I = 2$ scalar channel as a function of N_c (N_c=[3(Black, Solid), 6(Red, Dashed), 9(Green, Dot-dashed), 12(Blue, Dotted)]).

2.4. Chiral Perturbation Theory at $\mathcal{O}(p^4)$ and Semi-Local Duality

Now that we have verified that semi-local duality between resonances and Regge exchange is satisfied at $N_c = 3$ we intend to investigate what happens when this is increased. As visible in fig. 2.4, increasing N_c has the effect of making $\overline{q}q$ resonances narrower as they decouple from their decay channels, whilst four-quark or exotic states subside into the vacuum. For $\mathrm{Im}f_0^0$ we note that the $\sigma(600)$ appears to fade away at $\mathcal{O}(p^4)$, whilst in $\mathrm{Im}f_1^1$ the $\rho(770)$ becomes narrower.

In this section we consider the partial wave amplitudes represented in figure 2.4 and combine them in the appropriate ways given in eqs. (2.25–2.27) in order to obtain the A^{tI} amplitudes for $I = 0$, 1 and 2. The $I = 2$ channel is of particular importance because no $\overline{q}q$ states exist there.

To quantify the N_c-dependence at different orders in χPT and with different choices of LECs, we calculate the value of Finite Energy Sum Rules ratios,

$$F(t, N_c)_n^{I\,I'} = \frac{\int_{\nu_{\rm th}}^{\nu_{\rm max}} d\nu\ \mathrm{Im}\ A^{tI}(\nu, t, N_{\rm c})/\nu^n}{\int_{\nu_{\rm th}}^{\nu_{\rm max}} d\nu\ \mathrm{Im}\ A^{tI'}(\nu, t, N_{\rm c})/\nu^n}, \tag{2.34}$$

for different values of $n = 0{-}3$, $N_{\rm c} < 12$, t, $\nu_{\rm max}$, and isospin t-channels I, I'. The ratio F^{10} compares the amplitude given by ρ Regge-exchange with that controlled by the Pomeron, while the ratio F^{21} compares the 'exotic' four quark exchange with $\overline{q}q$ ρ-exchange.

We show the results in Table 2.3, and plot the data in fig. 2.6. The integrands used to calculate the ratios plotted in fig. 2.6 are themselves plotted in fig. 2.5. If the Regge expectations were valid at one-loop order, we would expect F^{10} to tend to 0.66 and for F^{21} to be very small in magnitude, just as they are at $N_c = 3$, particularly for a cutoff of 2 GeV^2. However, as N_c increases we find that the ratio F^{10} tends to 0.5, while that for F^{21} tends to -1. This is in accord with the $n = 1, 2$ sum rules becoming increasingly dominated by the ρ with very little scalar contribution. This difference is a consequence of the apparent four quark nature of the σ being incompatible with Regge expectations.

The t-channel amplitudes for $\mathrm{Im}A^{tI}$ with $I = 1$ and $I = 2$ from $\mathcal{O}(p^4)$ χPT including the first three partial waves are plotted in figure 2.5, including the weights with s^{-n}. These form the integrands for the FESR.

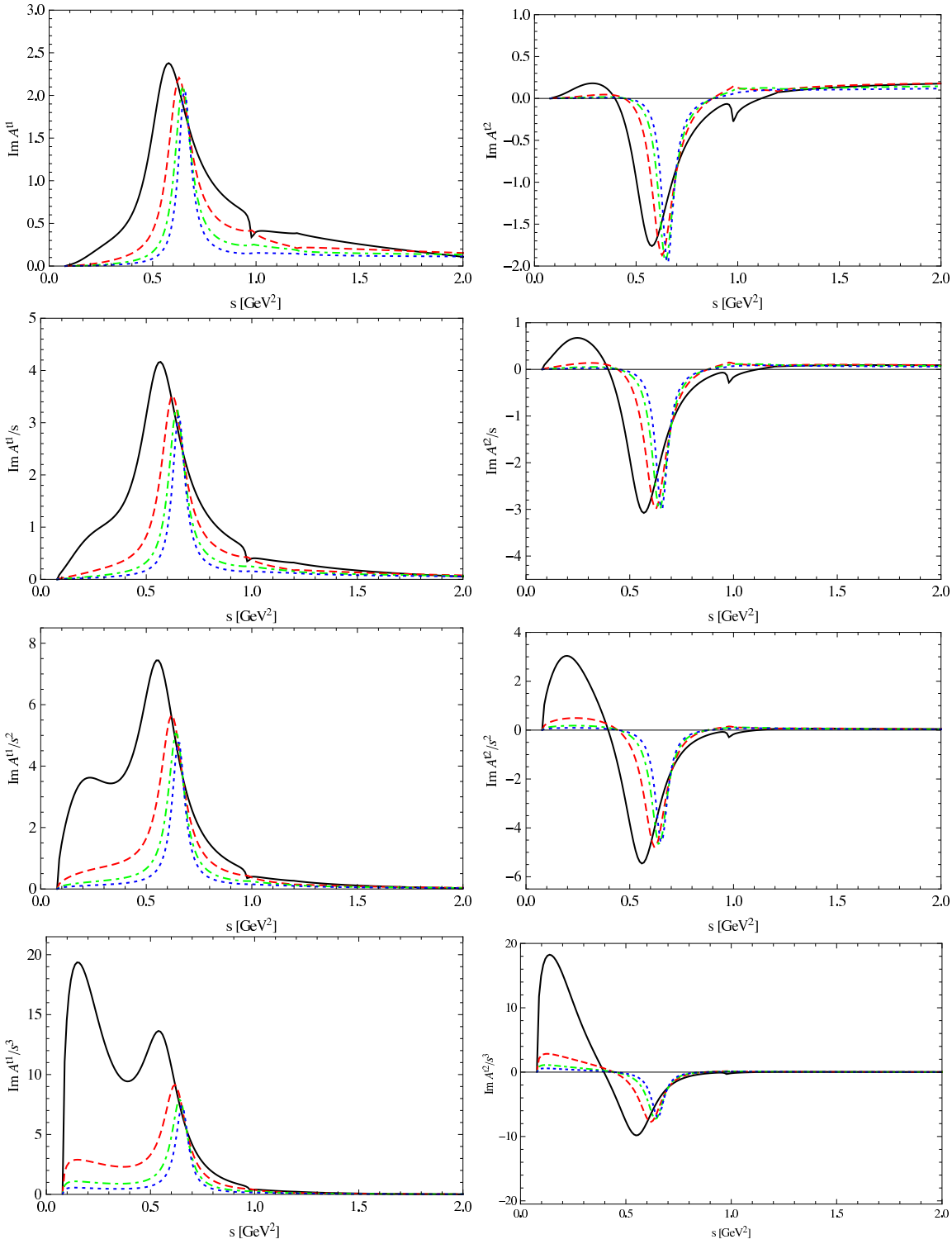

Figure 2.5.: The $\mathrm{Im}A^{tI}(s, t = 4m_\pi^2)/s^n$ amplitudes which form the integrands for the FESR. Black, solid curve $N_c = 3$. Red, Dashed curve $N_c = 6$, Green, Dot-dashed curve $N_c = 9$. Blue, Dotted $N_c = 12$

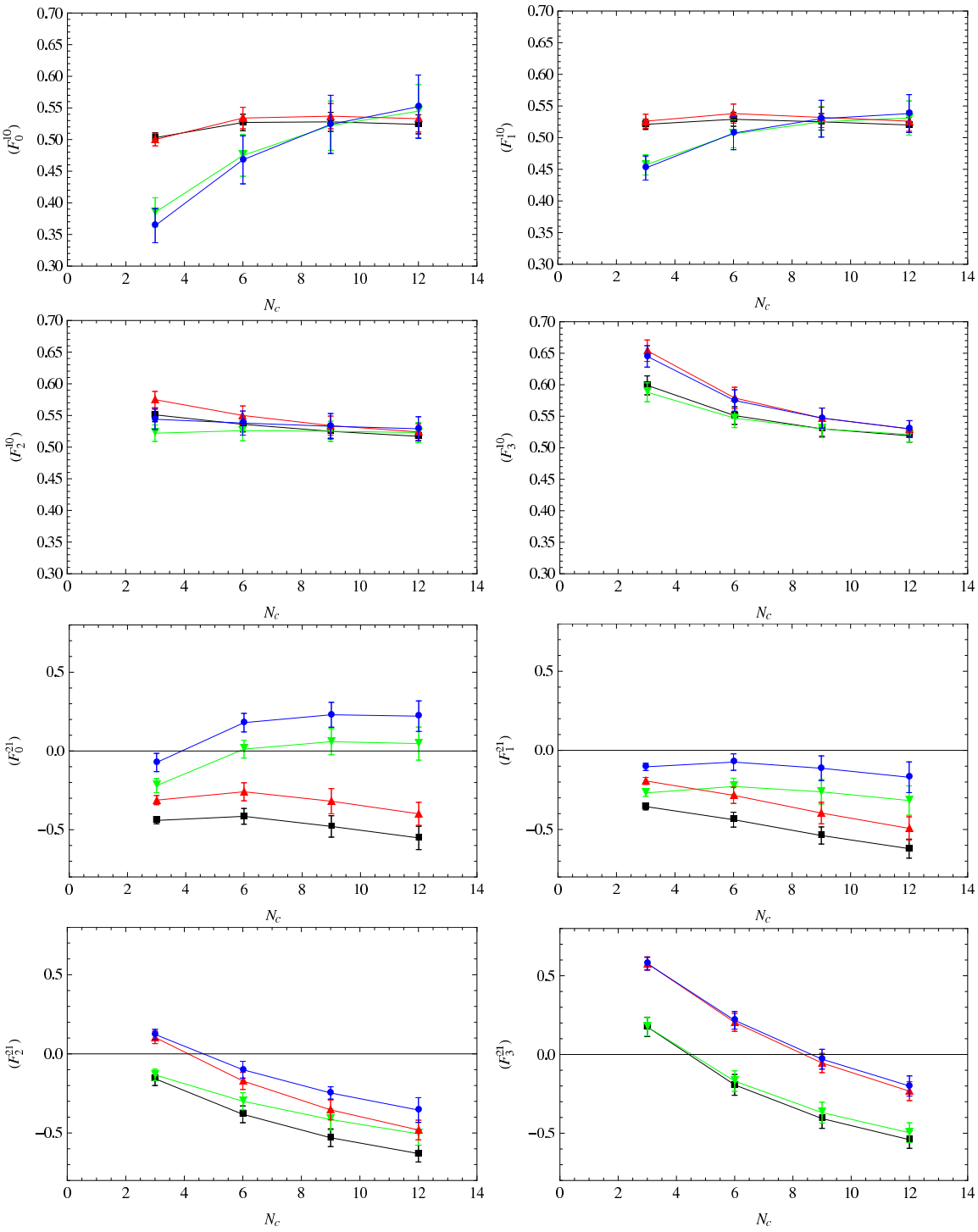

Figure 2.6.: The Ratios F_n^{IJ} at $\mathcal{O}(p^4)$. Black squares: $\nu_{\max} = 1$, $t = 4m_\pi^2$. Red up-triangles: $\nu_{\max} = 1$, $t = 0$. Green down-triangles: $\nu_{\max} = 2$, $t = 4m_\pi^2$. Blue circles: $\nu_{\max} = 2$, $t = 0$

			1-loop SU(3) χPT IAM			
			$t = 4m_\pi^2$		**$t = 0$**	
	n	N_c	ν_{max}=1 GeV^2	ν_{max}=2 GeV^2	ν_{max}=1 GeV^2	ν_{max}=2 GeV^2
F^{10}	0	3	0.503 ± 0.008	0.385 ± 0.023	0.500 ± 0.010	0.364 ± 0.027
		6	0.527 ± 0.013	0.475 ± 0.033	0.534 ± 0.017	0.468 ± 0.038
		9	0.528 ± 0.015	0.522 ± 0.039	0.537 ± 0.020	0.524 ± 0.046
		12	0.524 ± 0.015	0.545 ± 0.042	0.533 ± 0.021	0.552 ± 0.050
	1	3	0.521 ± 0.008	0.457 ± 0.016	0.526 ± 0.011	0.452 ± 0.019
		6	0.529 ± 0.011	0.506 ± 0.022	0.538 ± 0.015	0.507 ± 0.026
		9	0.525 ± 0.013	0.525 ± 0.024	0.532 ± 0.016	0.530 ± 0.029
		12	0.520 ± 0.012	0.531 ± 0.027	0.526 ± 0.016	0.538 ± 0.030
	2	3	0.551 ± 0.011	0.522 ± 0.013	0.575 ± 0.013	0.544 ± 0.016
		6	0.536 ± 0.012	0.526 ± 0.016	0.550 ± 0.015	0.538 ± 0.019
		9	0.525 ± 0.011	0.525 ± 0.016	0.534 ± 0.015	0.533 ± 0.020
		12	0.517 ± 0.010	0.523 ± 0.016	0.524 ± 0.013	0.529 ± 0.019
	3	3	0.599 ± 0.015	0.588 ± 0.015	0.654 ± 0.017	0.645 ± 0.017
		6	0.551 ± 0.014	0.547 ± 0.015	0.579 ± 0.017	0.575 ± 0.018
		9	0.530 ± 0.012	0.530 ± 0.014	0.547 ± 0.016	0.547 ± 0.017
		12	0.519 ± 0.010	0.521 ± 0.012	0.530 ± 0.013	0.532 ± 0.015
F^{21}	0	3	-0.441 ± 0.021	-0.220 ± 0.045	-0.312 ± 0.029	-0.073 ± 0.058
		6	-0.415 ± 0.050	0.012 ± 0.057	-0.259 ± 0.057	0.180 ± 0.059
		9	-0.479 ± 0.068	0.059 ± 0.083	-0.319 ± 0.080	0.230 ± 0.079
		12	-0.552 ± 0.074	0.047 ± 0.105	-0.399 ± 0.073	0.221 ± 0.097
	1	3	-0.355 ± 0.021	-0.269 ± 0.021	-0.193 ± 0.022	-0.104 ± 0.023
		6	-0.438 ± 0.047	-0.228 ± 0.052	-0.284 ± 0.051	-0.074 ± 0.052
		9	-0.538 ± 0.054	-0.262 ± 0.077	-0.396 ± 0.068	-0.113 ± 0.078
		12	-0.621 ± 0.060	-0.317 ± 0.093	-0.493 ± 0.073	-0.170 ± 0.097
	2	3	-0.157 ± 0.043	-0.133 ± 0.036	0.107 ± 0.039	0.123 ± 0.032
		6	-0.382 ± 0.053	-0.299 ± 0.054	-0.171 ± 0.054	-0.100 ± 0.053
		9	-0.530 ± 0.056	-0.415 ± 0.066	-0.354 ± 0.063	-0.247 ± 0.069
		12	-0.630 ± 0.053	-0.505 ± 0.072	-0.481 ± 0.062	-0.355 ± 0.078
	3	3	0.175 ± 0.062	0.176 ± 0.058	0.578 ± 0.042	0.577 ± 0.040
		6	-0.193 ± 0.066	-0.169 ± 0.065	0.204 ± 0.057	0.217 ± 0.056
		9	-0.407 ± 0.062	-0.369 ± 0.066	-0.054 ± 0.061	-0.030 ± 0.063
		12	-0.541 ± 0.055	-0.497 ± 0.063	-0.233 ± 0.060	-0.200 ± 0.064

Table 2.3.: Ratios for 1 loop UChPT using LECs from a single channel fit

2.5. Chiral Perturbation Theory at $\mathcal{O}(p^6)$ and Semi-Local Duality

The case for SU(2) $\mathcal{O}(p^6)$ χPT is a little different, there are eleven low-energy constants which must be constrained for the $\pi\pi$ amplitude, one at $\mathcal{O}(p^2)$, four at $\mathcal{O}(p^4)$ and six at $\mathcal{O}(p^6)$, examples of these are given in table 2.5. There are larger uncertainties regarding the values to use and different values that give similar results at $N_c = 3$ may give quite different results at larger values of N_c. In ref. [25] the possible behaviours of the ρ and σ were incorporated as artificial constraints on the LECs and fits were produced for the following cases, where in each a minimisation is first performed at $N_c = 3$ to data and then a model is applied as described below at higher values of N_c depending on the desired behaviour. This is added to the χ^2 for data in the minimisation and different parameters are found in each case. The cases we consider are:

- Case A: ρ as $\overline{q}q$, σ only from data.
- Case B: ρ and σ as $\overline{q}q$.
- Case C: σ as $\overline{q}q$, ρ only from data.

A model is then proposed in ref. [25] to test each of the cases, such that if a state is $\overline{q}q$ in composition, its mass and width should have the following behaviours,

$$M^{\overline{q}q}(N_c) = M_0 \left(1 + \frac{\epsilon_M}{N_c}\right) \tag{2.35}$$

for the mass, and for the width of the state we have,

$$\Gamma^{\overline{q}q}(N_c) = \frac{\Gamma_0}{N_c} \left(1 + \frac{\epsilon_\Gamma}{N_c}\right) \tag{2.36}$$

where M_0 and Γ_0 are N_c-independent quantities and these equations give the familiar property that the mass is roughly constant $M \sim \mathcal{O}(1)$ and the width becomes narrower with N_c, $\Gamma \sim \mathcal{O}(1/N_c)$.

For a $\overline{q}q$ state the expected M_{N_c} and Γ_{N_c} can be obtained from the IAM amplitudes,

$$M_{N_c}^{\overline{q}q} \simeq M_{N_c-1}\left[1+\epsilon_M\left(\frac{1}{N_c}-\frac{1}{N_c-1}\right)\right] \;=\; M_{N_c-1} \;+\; \Delta M_{N_c}^{\overline{q}q}, \qquad (2.37)$$

$$\Gamma_{N_c}^{\overline{q}q} \simeq \frac{N_c-1}{N_c}\,\Gamma_{N_c-1}\left[1+\epsilon_\Gamma\left(\frac{1}{N_c}-\frac{1}{N_c-1}\right)\right] \;=\; \frac{N_c-1}{N_c}\,\Gamma_{N_c-1} \;+\; \Delta\Gamma_{N_c}^{\overline{q}q}. \qquad (2.38)$$

We therefore define an averaged $\chi^2_{\overline{q}q}$ to measure how close a resonance is to a $\overline{q}q$ behaviour, using as uncertainty the $\Delta M_{N_c}^{\overline{q}q}$ and $\Delta\Gamma_{N_c}^{\overline{q}q}$

$$\chi^2_{\overline{q}q} \;=\; \frac{1}{2n}\sum_{N_c=4}^{n}\left[\left(\frac{M_{N_c}^{\overline{q}q}-M_{N_c}}{\Delta M_{N_c}^{\overline{q}q}}\right)^2+\left(\frac{\Gamma_{N_c}^{\overline{q}q}-\Gamma_{N_c}}{\Delta\Gamma_{N_c}^{\overline{q}q}}\right)^2\right]. \qquad (2.39)$$

This $\chi^2_{\overline{q}q}$ is added to $\chi^2_{\rm data}$ and the sum is minimised. Case A is where the data are fitted assuming that the ρ is a $\overline{q}q$ meson as N_c is increased, while Case B assumes that both the σ and the ρ are $\overline{q}q$ states with increasing N_c. Lastly, Case C is where we minimise $\chi^2_{\rm data}$ and just $\chi^2_{\overline{q}q}$ for the σ.

Case A returns the best fit to data, as would be expected from χPT at $\mathcal{O}(p^4)$, but even this contains a subleading $\overline{q}q$ component apparently of the σ above 1 GeV as can be seen in the plot for $\mathrm{Im}f_0^0$ in fig. 2.8. As may already be apparent, this subleading component will be vital later when we consider whether the Finite Energy Sum Rules and Semi-Local Duality are satisfied as N_c changes.

In Table 2.4 the values of the χ^2 contributions for each case are given, where N_c is summed from 3 to 12. We see that constraining the ρ to be a $\overline{q}q$ state by including eq. (2.39) in the minimisation is completely compatible with data at $N_c = 3$. In contrast, imposing a $\overline{q}q$ configuration for the σ gives a much poorer agreement with data and can distort the simple structure for the ρ. It is interesting to point out that, the lower energy at which the σ $\overline{q}q$ behaviour emerges, the higher energy at which the ρ pole moves with N_c. Therefore, as much as we try to force the σ to behave as a $\overline{q}q$ meson, less the ρ meson does. However, requiring a $\overline{q}q$ composition for the σ for larger N_c causes no such incompatibility with the physical world at $N_c = 3$.

We can follow the position of the poles in the complex E-plane which is performed in fig. 2.7, here we see the physical σ pole at $N_c = 3$ first begin to move away from the real axis

IAM Fit	$\chi^2_{\rm data}$	$\chi^2_{\rho,\overline{q}q}$	$\chi^2_{\sigma,\overline{q}q}$	$\chi^2_{\sigma,\overline{q}q,N_c=9}$	$\chi^2_{\sigma,\overline{q}q,N_c=12}$
Case A: ρ as $\overline{q}q$	1.1	0.9	15.0	4.8	3.4
Case B: ρ and σ as $\overline{q}q$	1.5	1.3	4.0	0.8	0.5
Case C: σ as $\overline{q}q$	1.4	2.0	3.5	0.6	0.5

Table 2.4.: Values of the χ^2 for the different SU(2) fits.

as is seen in the SU(3) calculation, however now extra effects from the additional terms in the chiral expansion cause the pole to turn back towards the real axis at energies in the region of 1 GeV^2 signalling the presence of a $q\overline{q}$ component in its Fock space. Figure 2.7 is directly comparable to fig. 2.3 for the $\mathcal{O}(p^4)$ version of the calculation. The pole motion is completely smooth for both the ρ and the σ suggesting that this really is a property of these states as seen as N_c increases. The effect is also visible when we look at the imaginary parts of the amplitudes, see fig. 2.8. There, a peak is seen in the $I = J = 0$ channel that arises around $N_c = 9$. This behaviour may be related to the existence of another $q\overline{q}$ nonet above 1 GeV [29–38].

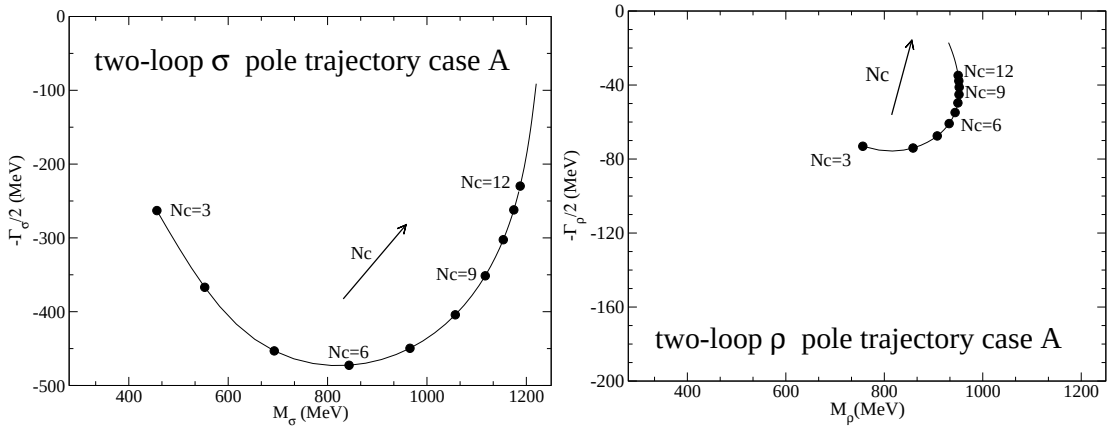

Figure 2.7.: The motion of the σ and ρ poles at $\mathcal{O}(p^6)$ for Case A [25–27].

These new effects come towards the edge of the region of validity of the single channel unitarised chiral theory, at around 1 GeV. As N_c is increased beyond 12 then the effects of coupled channels should be taken into account. In order to do this would require the SU(3) $\mathcal{O}(p^6)$ amplitudes which are at present unknown. This serves as a caveat to the conclusions of this analysis, particularly for a σ pole much above 1 GeV, that coupled channel effects could be important.

Coeff	Case A	Case B	Case C	$\mathcal{O}(N_c)$ scaling.
l_1^r	-5.4×10^{-3}	-5.7×10^{-3}	-5.7×10^{-3}	$(N_c/3)$
l_2^r	1.8×10^{-3}	2.5×10^{-3}	2.6×10^{-3}	$(N_c/3)$
l_3^r	1.5×10^{-3}	0.39×10^{-3}	-1.7×10^{-3}	$(N_c/3)$
l_4^r	9.0×10^{-3}	3.5×10^{-3}	1.7×10^{-3}	$(N_c/3)$
r_1	-0.6×10^{-4}	-0.58×10^{-4}	-0.60×10^{-4}	$(N_c/3)^2$
r_2	1.5×10^{-4}	1.5×10^{-4}	1.3×10^{-4}	$(N_c/3)^2$
r_3	-1.4×10^{-4}	-3.2×10^{-4}	-4.4×10^{-4}	$(N_c/3)^2$
r_4	1.4×10^{-4}	-0.49×10^{-4}	-0.03×10^{-4}	$(N_c/3)^2$
r_5	2.4×10^{-4}	2.7×10^{-4}	2.7×10^{-4}	$(N_c/3)^2$
r_6	-0.6×10^{-4}	0.62×10^{-4}	-0.7×10^{-4}	$(N_c/3)^2$

Table 2.5.: The SU(2) at $\mathcal{O}(p^6)$ low-energy constants from ref. [25].

Applying the low-energy constants from Case A above we perform the same analysis as for the $\mathcal{O}(p^4)$ SU(3) calculation given above now using the SU(2) $\mathcal{O}(p^6)$ theory. The motion of the σ pole has an important effect on the outcome, particularly if we integrate the FESR up to 2 GeV^2. First we show in fig. 2.9 the integrands for calculating the ratio F_n^{IJ}, then we give the numerical values for the ratios again in table 2.6. The behaviour is best visualised in fig. 2.10 where we see in particular for F_1^{21} and F_2^{21} for the curves where $\nu_{max} = 2\text{GeV}^2$, then the t-channel amplitude is always small, as is expected if local duality is to be upheld with increasing N_c.

This leads us to the conclusion, notwithstanding the caveat given above regarding the unknown coupled channel effects above 1 GeV, that in this framework, local duality can be a feature of the theory as described by $\mathcal{O}(p^6)$ SU(2) unitarised chiral perturbation theory. Local duality however is not apparent in the standard LECs which we have applied for the $\mathcal{O}(p^4)$ SU(3) version of the calculation. This difference happens at $\mathcal{O}(p^6)$ because the pole associated with the resonance referred as the σ does not continue to move away from the real axis in the complex E plane as N_c becomes larger, as is seen in $\mathcal{O}(p^4)$ SU(3) unitarised chiral perturbation theory. Instead, the pole moves smoothly away to begin with, consistent with a dominant four-quark structure, but around $N_c = 6$ the pole begins to move back towards the real axis, signalling an emerging $\overline{q}q$ structure. This then provides the necessary contribution to keep the $I = 2$ t-channel exchanges small, as is expected from local duality, particularly when the integration region encompasses this pole, as can be seen from fig. 2.10.

			2-loop SU(2) χPT (ρ as $\bar{q}q$)			
			$t = 4m_\pi^2$		**$t = 0$**	
	n	N_c	ν_{max}=1 GeV^2	ν_{max}=2 GeV^2	ν_{max}=1 GeV^2	ν_{max}=2 GeV^2
F^{10}	0	3	0.493	0.359	0.488	0.334
		6	0.494	0.370	0.492	0.349
		9	0.491	0.395	0.490	0.376
		12	0.489	0.422	0.488	0.404
	1	3	0.508	0.442	0.511	0.434
		6	0.496	0.419	0.494	0.407
		9	0.488	0.430	0.487	0.418
		12	0.485	0.447	0.483	0.436
	2	3	0.533	0.505	0.551	0.522
		6	0.498	0.467	0.498	0.454
		9	0.482	0.452	0.479	0.445
		12	0.477	0.460	0.472	0.452
	3	3	0.572	0.563	0.618	0.611
		6	0.503	0.485	0.511	0.495
		9	0.472	0.460	0.468	0.456
		12	0.461	0.457	0.451	0.447
F^{21}	0	3	-0.421	-0.060	-0.280	0.135
		6	-0.536	-0.086	-0.454	0.058
		9	-0.648	-0.061	-0.579	0.073
		12	-0.748	-0.038	-0.686	0.090
	1	3	-0.351	-0.202	-0.183	-0.028
		6	-0.438	-0.196	-0.335	-0.069
		9	-0.578	-0.215	-0.497	-0.102
		12	-0.699	-0.227	-0.629	-0.121
	2	3	-0.173	-0.123	0.097	0.139
		6	-0.249	-0.152	-0.069	0.027
		9	-0.435	-0.248	-0.294	-0.105
		12	-0.594	-0.314	-0.477	-0.192
	3	3	0.146	0.156	0.570	0.575
		6	0.102	0.112	0.485	0.488
		9	-0.121	-0.073	0.249	0.275
		12	-0.332	-0.216	0.012	0.092

Table 2.6.: Ratios for 2 loops UChPT using the ρ as $\bar{q}q$ LECS fit.

2.6. Conclusions

The N_c dependence of the unitarised chiral amplitudes at one loop order poses a problem for the concept of semi-local duality between resonances and Regge exchanges. However, at two loop order this is no longer the case. Semi-local duality is then satisfied at all N_c where the IAM unitarisation procedure is valid, typically where $N_c < 30$. This is because at one loop order the ρ and σ resonances have quite distinct structures, it is shown that the ρ is a $\overline{q}q$ state, whilst the σ is not. Their behaviour with increasing N_c makes these distinguishable. In contrast, at higher order in the chiral expansion, the σ has a $\overline{q}q$ component in its Fock space, which though sub-dominant at $N_c = 3$, becomes increasingly important as N_c increases. This is critical, as we have shown here, in ensuring semi-local duality is fulfilled as N_c increases. Thus the chiral expansion contains the solution to the apparent paradox of how the distinctive natures of the ρ and σ resonances are reconciled with semi-local duality as N_c is increased. Indeed, despite the additional freedom brought about by the extra Low Energy Constants at two loop order, fixing these from experiment at $N_c = 3$ automatically brings this compatibility with semi-local duality as N_c increases. This is a most satisfying result.

It has been investigated whether the one loop chiral amplitudes could also reproduce this behaviour. Explicitly imposing the behaviour as N_c is increased as we do here for the $\mathcal{O}(p^6)$ amplitudes, however it does not appear possible to simultaneously satisfy a subleading $\overline{q}q$ component in the σ, and the $\pi\pi$ scattering data. The additional freedom that arises in the $\mathcal{O}(p^6)$ amplitudes reaches further into the fundamental theory to give rise to this behaviour [27].

We consider further implications combined with the results of chapter 3 in our final conclusion.

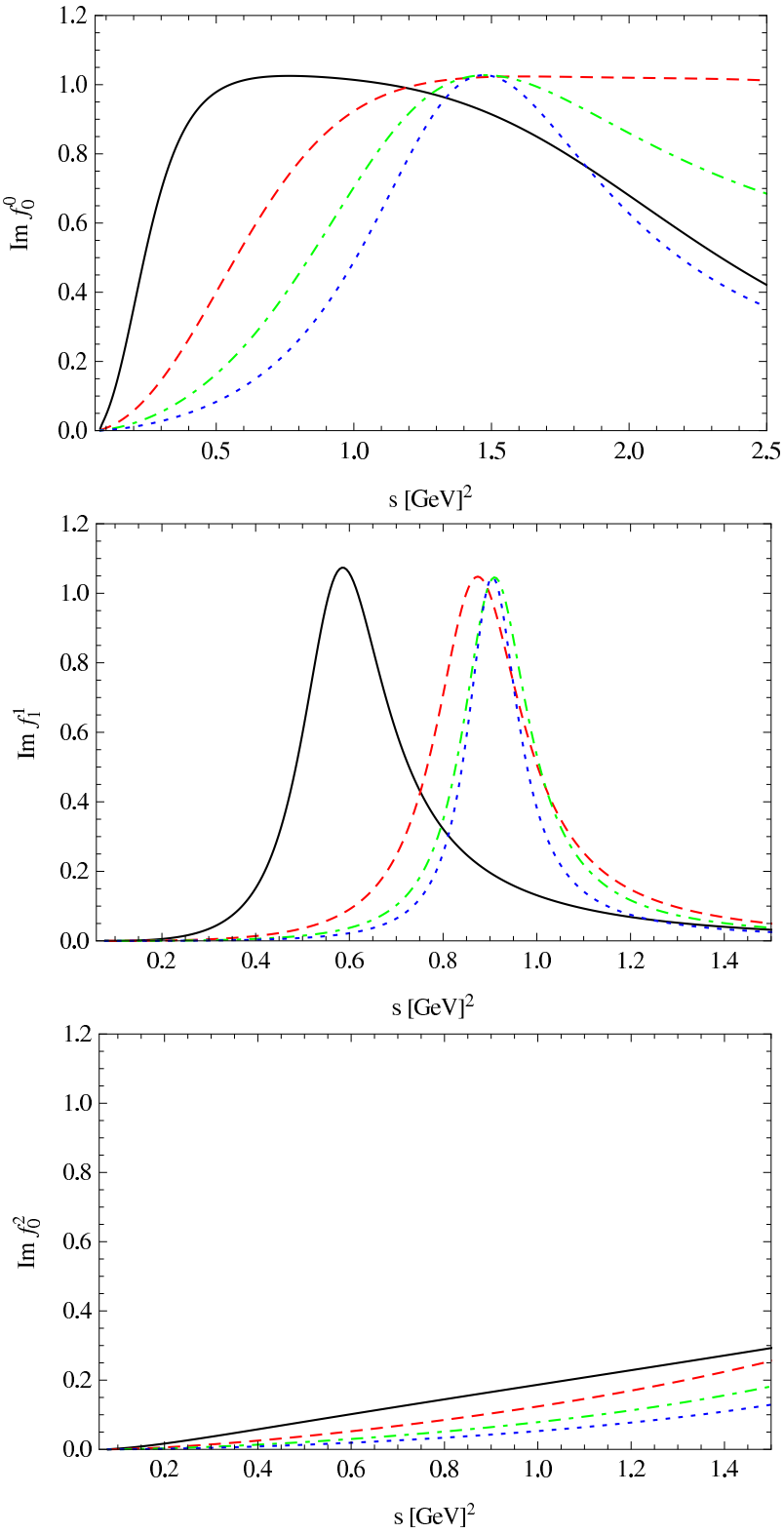

Figure 2.8.: The amplitudes Imf_{IJ} as defined in Eq. (2.21) from SU(2) χPT at $\mathcal{O}(p^6)$ for Case A in table 2.5. Top: The σ enhancement as a function of N_c. Middle: The ρ resonance as a function of N_c. Bottom: The $I = 2$ scalar channel as a function of N_c (N_c=[3(Black, Solid), 6(Red, Dashed), 9(Green, Dot-dashed), 12(Blue, Dotted)]).

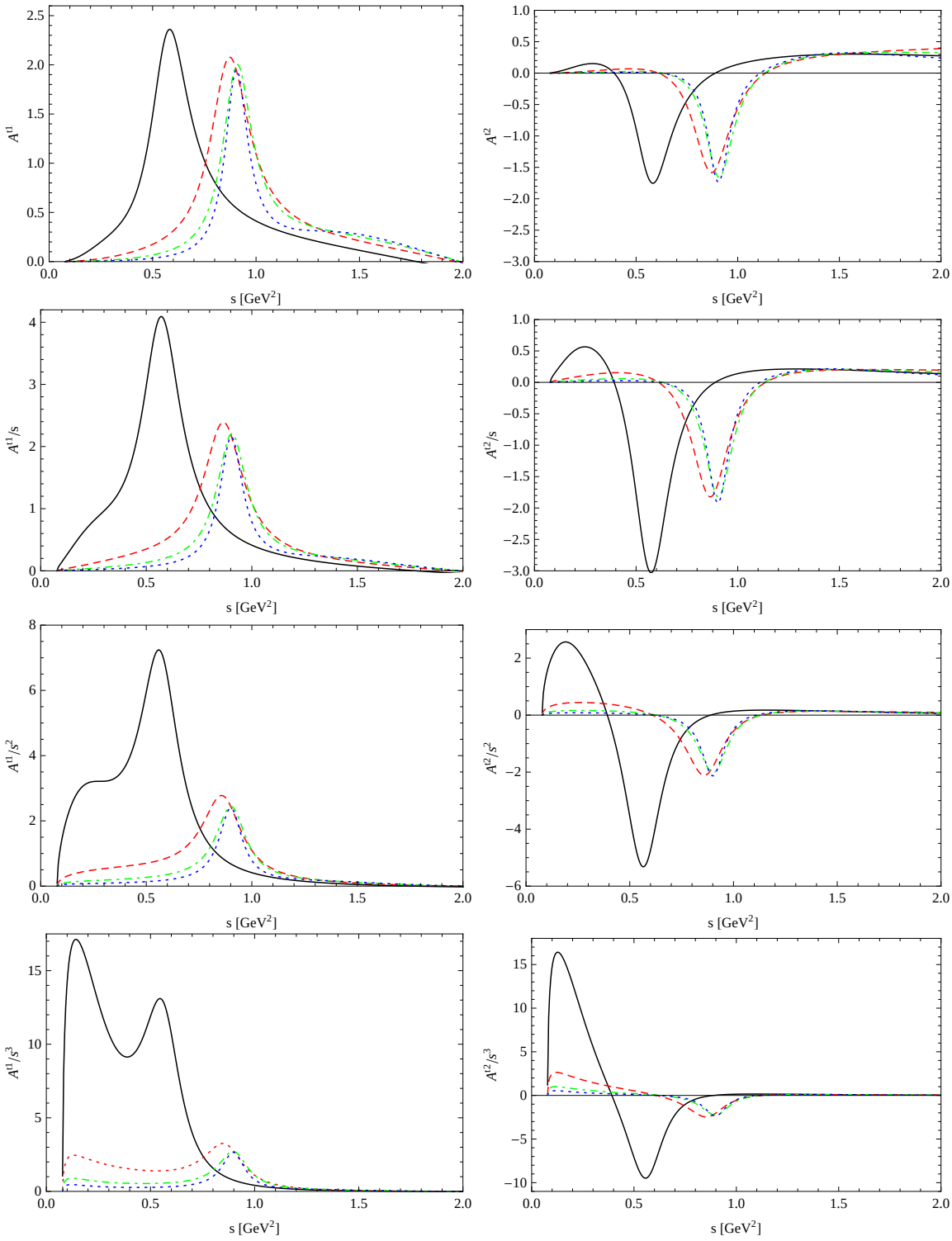

Figure 2.9.: The $\mathrm{Im}A^{tI}(s, t = 4m_\pi^2)/s^n$ amplitudes which form the integrands for the FESR. Black, solid curve $N_c = 3$. Red, Dashed curve $N_c = 6$, Green, Dot-dashed curve $N_c = 9$. Blue, Dotted $N_c = 12$

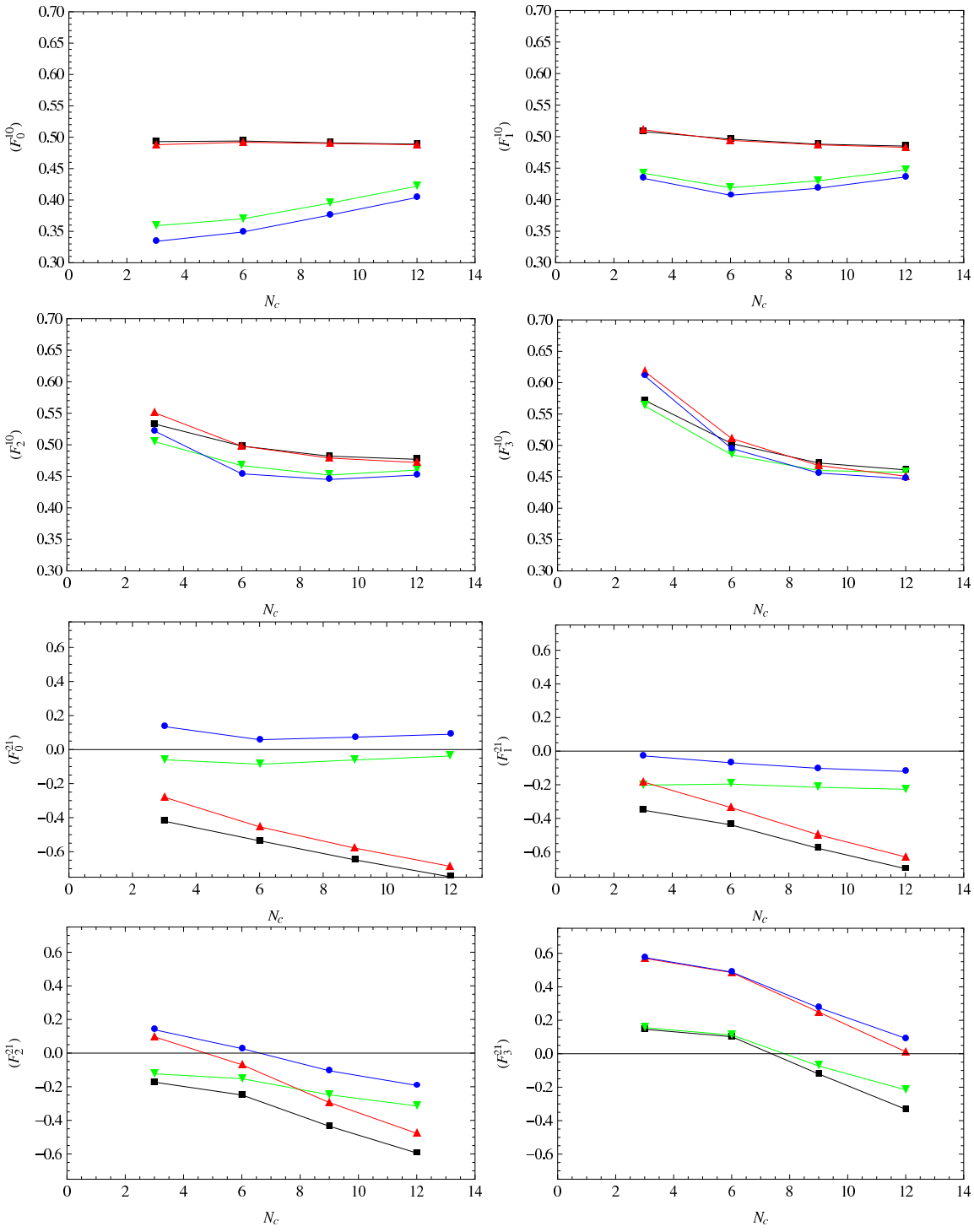

Figure 2.10.: The Ratios F_n^{IJ} at $\mathcal{O}(p^6)$. Black squares: $\nu_{\max} = 1$, $t = 4m_\pi^2$. Red up-triangles: $\nu_{\max} = 1$, $t = 0$. Green down-triangles: $\nu_{\max} = 2$, $t = 4m_\pi^2$. Blue circles: $\nu_{\max} = 2$, $t = 0$

Chapter 3.

The Pole Structure of the $f_0(980)$ Resonance

3.1. Introduction

The $f_0(980)$ is a scalar resonance that lies just above $K\overline{K}$ threshold, whose nature has long been discussed. The most common suggestions for its composition have been a regular $\overline{q}q$ state [39–43], a compact multiquark state [44, 45], a $K\overline{K}$ molecule [46–50], or possibly something else exotic. In fact as we saw in the previous chapter and as noted in [51], the state could be seeded by $\overline{q}q$ and dressed by its strong coupling to hadronic channels. The $f_0(980)$ is seen in $\pi\pi \to \pi\pi$, $\pi\pi \to K\overline{K}$ and $K\overline{K} \to K\overline{K}$ channels. Due to its proximity and coupling to the $K\overline{K}$ threshold the resonance shape is nontrivially distorted from a simple Breit-Wigner by the rapidly varying phase space of this channel.

Recently, Babar has taken extremely precise data on D_s decays. The process $D_s \to \pi f_0(980)$ is of key interest, this is observed as $D_s \to \pi(\pi\pi)$, $D_s \to \pi(\overline{K}^0 K^0)$ and $D_s \to \pi(K^+K^-)$ final states. Crucially for resolving the structure, these data are finely binned and are hoped to constrain the fit more precisely than previous analyses [39, 40, 52].

3.2. Method

Following earlier analyses of this resonance, we make use of an argument due to Weinberg [53–55], that was first applied to determine whether the deuteron was an elementary

state or a composite particle. A similar procedure may be applied to any resonance that fits the following criteria,

(1.) The resonance should lie close to a two-body decay channel with zero angular momentum between decay products.

(2.) The resonance should be stable.

for the $f_0(980)$, condition (1.) is very well fulfilled, and condition (2.) is reasonably well approximated due to the narrow width and rapid rise in phase observed in $\pi\pi$ scattering.[1] The argument of Weinberg is then dependent upon the number of poles of the scattering amplitude. A single pole[2], corresponds to a 'composite' state, which we could interpret here as a bound state of $K\overline{K}$ whilst two poles corresponds to an elementary excitation of QCD which could be a $\overline{q}q$ state, some compact four-quark state, a purely gluonic state, or some other bound combination of quarks and gluons [56].

Normally we consider our amplitudes in s, however, the sheet structure of the complex s-plane is multilayered, and it is simpler to consider instead the complex k_2-plane, which unfolds into a single plane, with the real energy axis running along the positive imaginary axis, around the origin at threshold and then along the positive real axis. There are two definitions that we shall use for k_2, one using a split $K\overline{K}$ threshold where we consider the charged and neutral thresholds separately, and a simpler version using an averaged threshold. These are defined as,

$$k_2^{\text{ave}} = \frac{1}{2}\left(s - (m_{K^\pm} + m_{K^0})^2\right)^{\frac{1}{2}} , \tag{3.1}$$

$$k_2^{\text{split}} = \frac{1}{4}\left\{\left(s - 4m_{K^\pm}^2\right)^{\frac{1}{2}} + \left(s - 4m_{K^0}^2\right)^{\frac{1}{2}}\right\} , \tag{3.2}$$

where m_{K^0} and $m_{K^\pm}$ correspond to the neutral and charged Kaon masses respectively. The key difference is that the physical line for the split case runs around a small quarter-circle at the origin of the k_2 plane, as shown in 3.4. We fit to a narrow region centred on threshold $0.867 < E < 1.11\,\text{GeV}$ to investigate narrow structures. We require our energy region to be centred on our region of interest, and we wish to avoid the added complexity of $\eta\eta$ threshold at $2 \times 0.5478\,\text{GeV}$. The background is not expected to vary rapidly over such a narrow region.

[1] One could argue that the conditions are at odds with each other.
[2] Either in E or k_2 which we define later.

3.2.1. Jost functions, Matrix Elements and matching theory and data

The Jost function [57] representation for the scattering matrix elements is particularly convenient here since it gives precise control over the number and the position of poles in the matrix elements. The Jost function is split into two parts,

$$\phi(k_2) = \phi_{\rm pol}(k_2)\phi_{\rm bg}(k_2), \tag{3.3}$$

where $\phi_{\rm pol}$ represents the part of the Jost function necessary to produce the resonant part of the amplitude. The zeros of this at $k_2^{(np)}$ will correspond to the position of the nth pole in k_2 in the scattering amplitude, we parameterise this as,

$$\phi_{\rm pol}(k_2) = \prod_{n=1}^{N_{poles}} \left(1 - \frac{k_2}{k_2^{(np)}}\right) . \tag{3.4}$$

The $\phi_{\rm bg}$ term is required to produce everything else in the amplitude from the Jost function, primarily the background,

$$\phi_{\rm bg}(k_2) = \exp\left(\sum_{j=0}^{N_\gamma} \gamma_j k_2^j\right) , \tag{3.5}$$

where the γ_i are complex expansion coefficients whose values can be fitted to data. The S-matrix elements may then be related to the Jost function as [40],

$$S_{11} = 1 + 2i\rho_1 T_{11} = \frac{\phi^*(-k_2^*)}{\phi(k_2)} \tag{3.6}$$

$$S_{22} = 1 + 2i\rho_2 T_{22} = \frac{\phi(-k_2)}{\phi(k_2)} \tag{3.7}$$

$$\mathrm{Det}(S) = \frac{\phi^*(k_2^*)}{\phi(k_2)} \tag{3.8}$$

$$S_{12} = 2i\sqrt{\rho_1\rho_2}\, T_{12} = (S_{11}S_{22} - \mathrm{Det}(S))^{\frac{1}{2}} , \tag{3.9}$$

where we now note the importance of the the zeros of $\phi(k_2)$. The ρ_i are phase space factors for the relevant channels. An essential feature of this parameterisation is that it naturally incorporates unitarity which, along with the available data on this channel, provides an important constraint. In this work we consider a wide range of datasets from different experiments and hadronic decay channels, which constrain our T-matrix

elements by relations of the form,

$$A_1 = \alpha_1 T_{11} + \alpha_2 T_{12}, \tag{3.10}$$

$$A_2 = \alpha_1 T_{21} + \alpha_2 T_{22}, \tag{3.11}$$

where A_i is the hadronic decay amplitude, T_{ij} are the T-matrix elements and the α_i are unknown hadronic coupling functions, that are allowed by unitarity. Each distinct process that we consider will require a different set of α coefficients which we parametrise by a linear form in s.

3.2.2. The Flatté form

Flatté [58] originally introduced a modified form of the Breit-Wigner parameterisation to fit the $f_0(980)$ resonance. This has since been generalised [47, 59] in recent studies of this resonance. We perform fits also using this form to check our amplitudes. The Flatté resonance formula is embedded in a general elastic background that is constrained by unitarity [60]. The resonant part is given as,

$$F_{ij}(s) = \frac{g_i g_j}{m_0^2 - s - i g_1^2 \Gamma_1(s) - i g_2^2 \Gamma_2(s)} \ , \tag{3.12}$$

similar to Breit-Wigner fits, where m_0 is a free, wholly real mass parameter, and the g_i's are free parameters that are fitted. Different forms may be used for $\Gamma_i(s)$, the simplest being just the phase space for the given channel, $\Gamma_i(s) = \rho_i(s)$. General unitarity constrains the T-matrix elements to have the form,

$$T_{ij}(s) = \delta_{ij} \frac{\sin\phi_i(s) e^{i\phi_i(s)}}{\rho_i(s)} + e^{i\phi_i(s) + i\phi_j(s)} F_{ij}(s), \tag{3.13}$$

where δ_{ij} is the Kronecker delta-function and the $\phi_i(s)$ are background phases. Physically the Flatté form is similar to the Jost function form since it allows freedom between the positions of the poles such that if the data requires, the sheet 3 pole typically present in a Breit-Wigner can move away into the complex plane. The key difference when performing any analysis is that in the Jost function representation the pole position can be specified directly and thus the behaviour of the fits, the background contribution and the resonant part may all be studied as functions of the position of both poles. Previous studies using this Flatté form have found that the position of the first pole on sheet II is essentially fixed, and the second pole on sheet III is more weakly constrained.

We do not consider this form for our primary analysis since the Jost form is more flexible because we may specify the pole positions in the parameterisation. However, we will check that our amplitudes from the Jost-function paramterisation are consistent with the Flatté parameterisation.

3.2.3. Datasets and Theoretical Parameterisations

The $f_0(980)$ appears in many distinct channels, we supplement direct scattering constraining the $\pi\pi \to \pi\pi$, $\pi\pi \to K\overline{K}$ and $K\overline{K} \to K\overline{K}$ amplitudes with the related hadronic processes $\psi \to \phi\pi\pi$, $\psi \to \phi K\overline{K}$ which come from the BES and Mk3 experiments and also the new data from Babar mentioned previously. We consider additionally data from AFS on $pp \to pp\pi\pi$, $pp \to ppK\overline{K}$, and also $D_s \to 3\pi$ data from the Focus collaboration.

Direct Scattering data

Much of these data have not changed since the previous study but is essential in this analysis. There is an inconsistency in the absolute normalisation of the Etkin, Longacre *et al* [61–63] and Cohen *et al* [64] datasets. There is no problem with the shape or phases, just the normalisation. We fit Etkin *et al* [61] using a free normalisation since this dataset is given in number of events. We also calculate χ^2-fits to Cohen *et al* and Longacre *et al* which have absolute normalisations. These do not alter the fitted solutions particularly, however we will find that one data set is consistent with our other data, whilst the other always returns a large contribution to the total χ^2.

For the direct channel $\pi\pi \to \pi\pi$ there are a range of sources available that concentrate on $\pi^+p \to \pi^+\pi^+n$ and $\pi^-p \to \pi^0\pi^0n$. For the charged channel we use the data from the CERN-Munich collaboration [65–67], these data have been analysed using a variety of methods, we use the version given in ref. [65] which is almost identical to ref. [66] and Solution B of ref. [67], the main difference being the phase at threshold has a much larger error, although the central value is the same.

For the neutral channel there are data available from GAMS and BNL-E852 [68], these both lack absolute phases, only $S-D_0$ is available, and the amplitudes are not normalised. An appropriate analysis that puts these data into a directly usable form is given in ref [69]. The isospin-2 components have to be removed for both S and D_0 amplitudes, along with the isospin-0 D_0 contribution, this allows the inelasticity η_0^0 and the phase δ_0^0 to be

obtained. A problem arises in this dataset beyond the range that we consider in that the amplitudes violate unitarity. In reducing the data to this form multiple solutions arise that have to be carefully considered, it is not clear which best represents physical reality, if any, particularly due to the unitarity violation problem. The authors themselves even question the precision of the method and data to this process. A comparison of the data is shown in figs 3.1 and 3.2. We have assumed this analysis supercedes a previous analysis of Gunter *et al* that gave the $\pi\pi$ phase from a smaller subset of the E852 data [70].

These data directly constrain the scattering amplitude,

$$\begin{aligned} S_{11} =& 1 + 2i\rho_1 T_{11} \\ =& \eta_0^0(s)\, e^{2i\delta_0^0(s)}, \end{aligned} \tag{3.14}$$

which clearly has a simple relation to the Jost-function or Flatté parameterisations. There is however a phase ambiguity in $\delta_0^0(s)$ due to the periodicity in $2\delta_0^0$, if the fitting program finds a discontinuity in phase as it approaches 180° it will add $\pm 180°$ to $\delta_0^0(s)$ in order to keep the phase continuous.

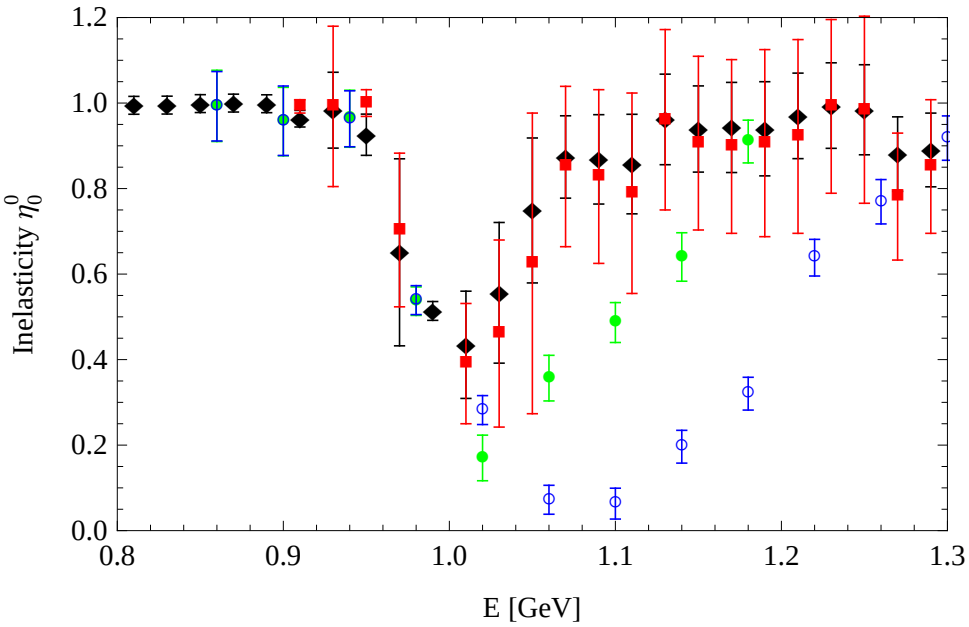

Figure 3.1.: The $\pi\pi$ S-wave inelasticity η_0^0. Red diamonds are Ochs [65], Black squares are Hyams *et al* [66], Green solid circles are the BNL/Achasov *et al* set 1 (fig. 5a from ref. [69]), and the Blue empty circles are the BNL/Achasov *et al* set 2 (fig. 5e from ref. [69])

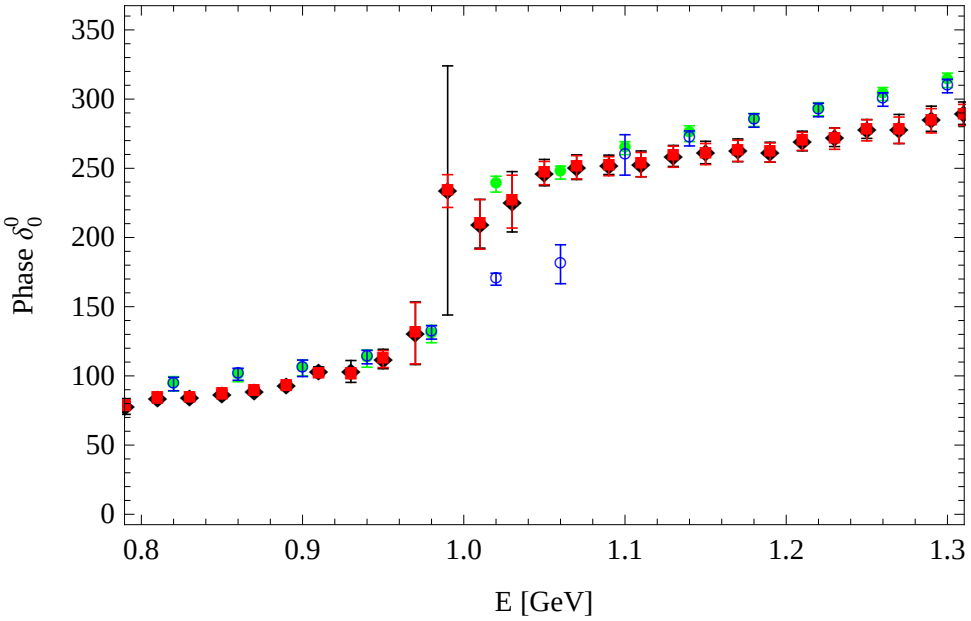

Figure 3.2.: The $\pi\pi$ S-wave phase δ_0^0. Red diamonds are Ochs [65], Black squares are Hyams *et al* [66], Green solid circles are the BNL/Achasov *et al* set 1 (fig. 5b from ref. [69]), and the Blue empty circles are the BNL/Achasov *et al* set 2 (fig. 5f from ref. [69])

$\psi \to \phi(MM)$

In the Mk3 [71] and BES [72] data, the $f_0(980)$ results in a rapid reduction in events in the $\pi\pi$ channel with an associated increase in the $K\overline{K}$ channel. The BES data have particularly high statistics and each point has a small error, but is in 30 MeV bins, whilst the Mk3 data has finer bins and larger errors. We make the connection to theory from these data using eq. (3.11),

$$A_1 = \alpha_1(s)\, T_{11} + \alpha_2(s)\, T_{12}$$
$$A_2 = \alpha_1(s)\, T_{21} + \alpha_2(s)\, T_{22}$$

where we typically use,

$$\alpha_i(s) = \alpha_i^{(0)} + \alpha_i^{(1)} \left(s - (4m_K^2)\right) + \alpha_i^{(2)} \left(s - (4m_K^2)\right)^2 + ..., \tag{3.15}$$

where the $\alpha_i^{(n)}$ are minimised free parameters. The first two terms are sufficient for this narrow region. There are additional factors required to compare to the number of events as given in fig. 3.3.

$$N_i^{\rm events} = C\frac{1}{3}\frac{(s[(m_\psi+m_\phi)^2-s][(m_\psi-m_\phi)^2-s])^{1/2}}{2\pi^2 m_\psi^2}{\rm Re}(\rho_i)|A_i|^2 \qquad (3.16)$$

where C is some normalisation constant, $m_\psi = 3.086$ GeV, is the mass of the J/ψ, $m_\phi = 1.019$ GeV, is the mass of the ϕ meson. An efficiency factor is also required for BES and the normalisation constant C is a relative normalisation between the BES and Mk3 sets since one normalisation may be absorbed into the α_i coefficients that are minimised in the numerical procedure.

$D_s \to \pi(MM)$

The decays $D_s \to \pi\pi\pi$ and $D_s \to \pi KK$ show an enhancement due to the $f_0(980)$ in Dalitz plot analyses. Information on these channels may then be used in a similar fashion to $\psi \to \phi(MM)$ datasets. Excellent new results from D_s decays from Babar [73, 74] have prompted the present reanalysis. There are also data available on the $\pi\pi$ channel from Focus [74,75], which is largely in agreement with the Babar data. We do not include these since they are superceded by the Babar data. The $K\overline{K}$ data is highly constraining, it is in 4 MeV bins with small errors and puts tight constraints on the parameters of our fit. The $\pi\pi$ channel has fewer data points but is still important to constrain the β_i parameters below. Moreover, this dataset has been partial wave analysed which is exactly what we require. The connection between the data and theory is simpler here because the data have been more thoroughly analysed. The magnitude of the $\pi\pi$ data is given as $|A_1|$, whilst the $\overline{K}K$ data is given as $|A_2|^2$, these are the same as given above, and are plotted in fig. 3.3. The coefficients of the T-matrix elements in eq. (3.11) will now be different since this is a different hadronic process, we denote these coefficient functions β_i to avoid confusion later,

$$A_1 = \beta_1(s)\,T_{11} + \beta_2(s)\,T_{12},$$
$$A_2 = \beta_1(s)\,T_{21} + \beta_2(s)\,T_{22}.$$

These are expanded in exactly the same way as before,

$$\beta_i(s) = \beta_i^{(0)} + \beta_i^{(1)}\left(s-4m_K^2\right) + \beta_i^{(2)}\left(s-4m_K^2\right)^2 + ..., \qquad (3.17)$$

where the $\beta_i^{(n)}$ parameters are fitted in order to obtained agreement with the data, and typically the first two orders are sufficient for such a narrow range in energy.

$pp \to pp(MM)$

The $f_0(980)$ is also observed in proton-proton scattering. Data from the AFS collaboration [76] formed an integral part of a previous analysis [40]. These data have now been supplemented by the WA102 experiment, however, neither set has a significant impact on the fits we carry out here.

3.3. Results and analysis

3.3.1. Fitting method

Fits were carried out using the CERNLIB package, *Minuit* [77], primarily using the 'Simplex' and 'Migrad' minimisation options. Fitting was performed using a variety of methods, but one of the most successful for the problem at hand was to begin with a small number of parameters and datasets, then obtaining a minimum and progressively increasing the number of parameters and datasets until a better minimum was found. The one-pole fits are the simplest and the position of the pole on the physical sheet of the k_2-plane is remarkably stable. The two-pole fits were a little more involved for a number of reasons. Firstly, the introduction of the second pole makes the fitting routine less stable and *Minuit* has to work much harder to find a minimum, since moving the second pole slightly requires a readjustment of all of the other parameters in the Jost function. For this reason the second pole is often forced outside the fitting region, where it has little effect and we are essentially dealing with the simpler one-pole case.

3.3.2. One pole vs Two pole fits

The location and residue of a pole in the scattering amplitudes are the key properties we intend to investigate since it is these that will elucidate the particle content in the threshold region. In figure 3.4 we plot the region of interest in our fits. The physical $\sqrt{s}$ scattering energy runs down the imaginary axis $\mathrm{Im}k_2$ and along the positive real axis $\mathrm{Re}k_2$. For a pole to have a significant effect it must lie close to this line. A fit shown

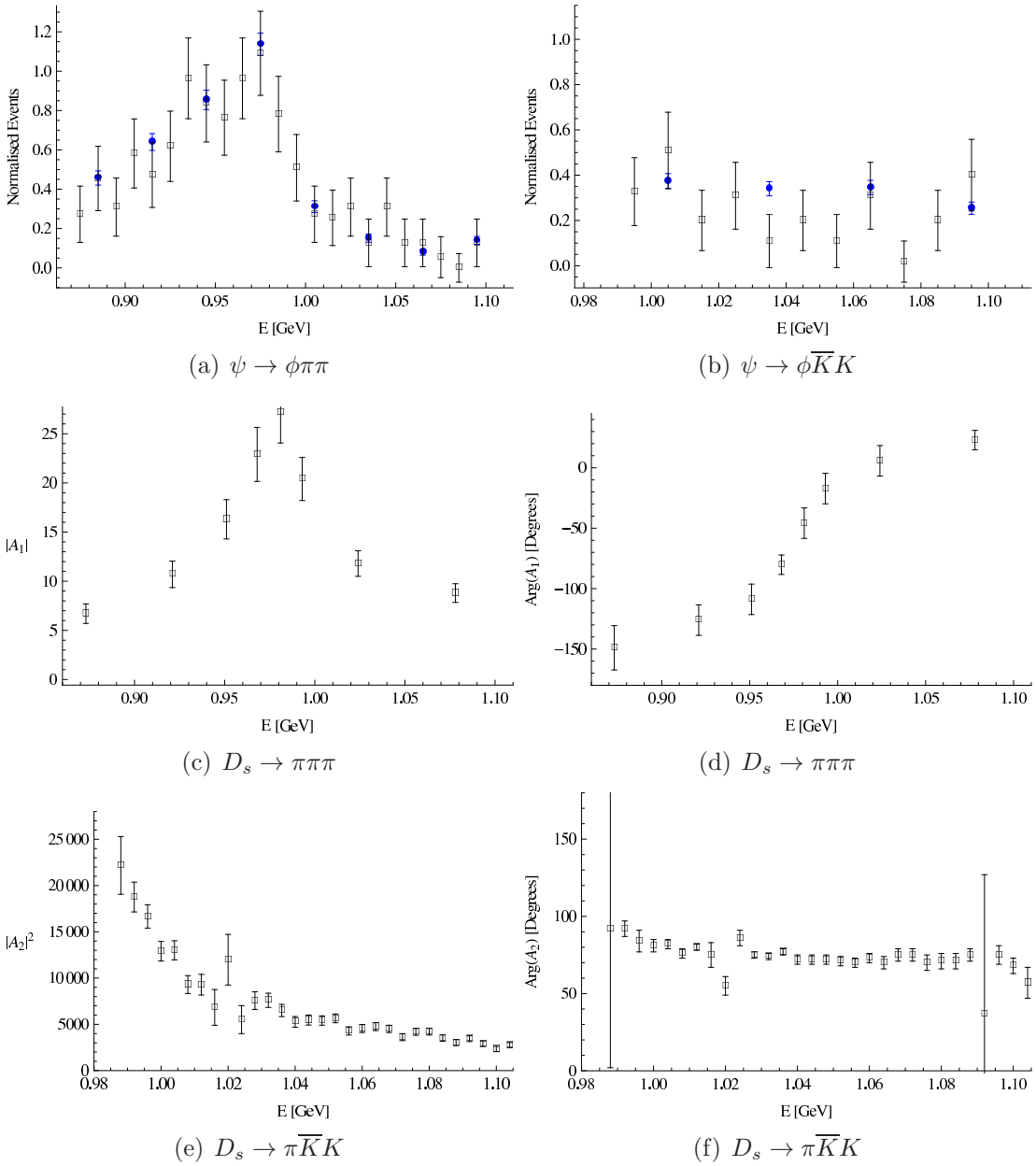

(a) $\psi \to \phi\pi\pi$ (b) $\psi \to \phi\overline{K}K$

(c) $D_s \to \pi\pi\pi$ (d) $D_s \to \pi\pi\pi$

(e) $D_s \to \pi\overline{K}K$ (f) $D_s \to \pi\overline{K}K$

Figure 3.3.: Hadronic Production data. Top: Mk3 and BES, Middle: Babar $\pi\pi$, Bottom: Babar $K\overline{K}$.

by the two black points may be considered a genuine two-pole fit, however as the pole begins to move away, for example the red points in fig. 3.4, then its effect on the real axis is reduced. The residue of the pole is also important; if this vanishes then the pole will also have little effect on the physical amplitude. We bear these properties in mind when investigating our solutions.

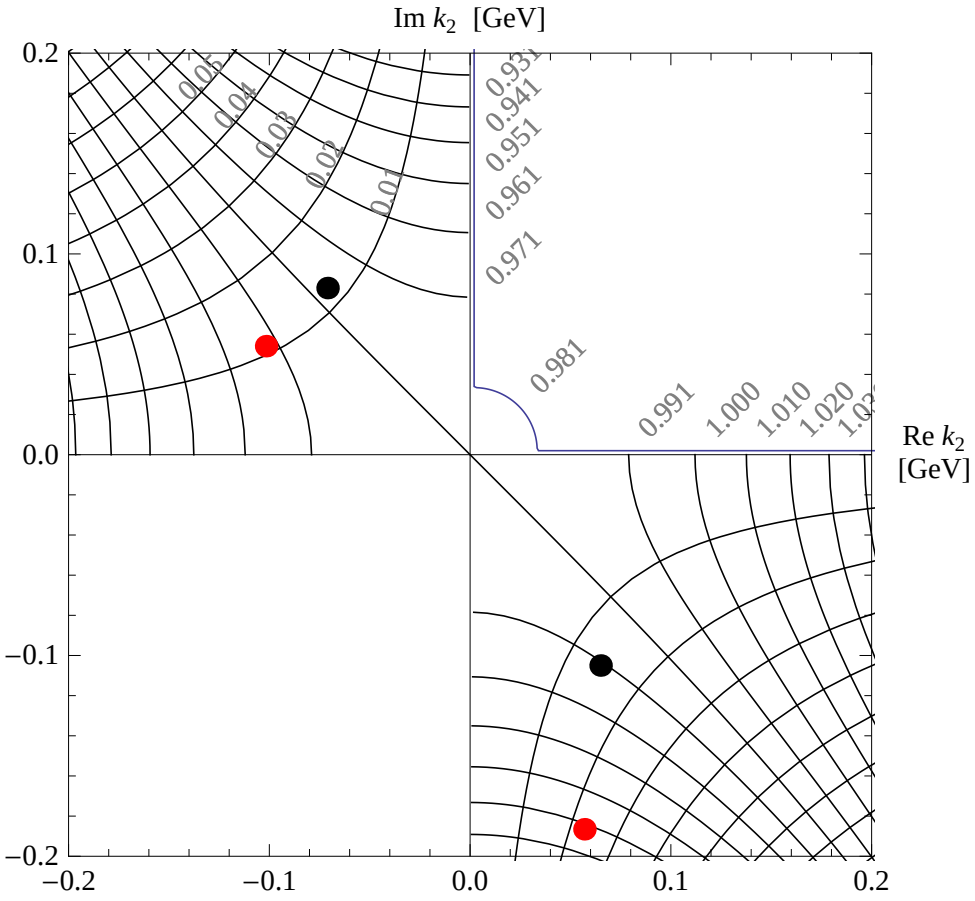

Figure 3.4.: The k_2 plane with contours of Energy and decay width plotted.

3.3.3. Elimination of inconsistent data

As mentioned previously the absolute normalisations of two of the direct $\pi\pi \to K\overline{K}$ datasets are in disagreement, this point has also been covered in ref [40]. There, a free normalisation was applied to bring the data into agreement. In this analysis the three sets have been treated independently. The data of Etkin [61] has a free normalisation, whilst Cohen [64] and Longacre [62] are normalised to $\frac{1}{4}(1-(\eta_0^0)^2)$. It is found that for all fits that satisfy our other data, the Cohen data contributes $\chi^2_{\text{Coh}} \simeq 60$ for only 5 data points, whilst the Longacre data contributes $\chi^2_{\text{Lon}} \simeq 7$ for 4 data points. Hence we neglect the Cohen data from our fits and include the Etkin and Longacre datasets. An example of this is shown in figure 3.5 along with the results of a typical fit.

Also there is a problem related to the $\pi\pi$ scattering data and which analysis of the BNL-E852 data [68,69] is the most appropriate. Performing fits using one or two poles using a minimal set of data we find that in our region of interest, only the first set comes close to

both the other data from the CERN-Munich collaboration and the results of the fitting program. Again, we give an example of a typical fit in fig. 3.6. Hence we use only the data from figures 5a and 5b of ref. [69], which corresponds to the solid green circles in figs. 3.1, 3.2 and 3.6.

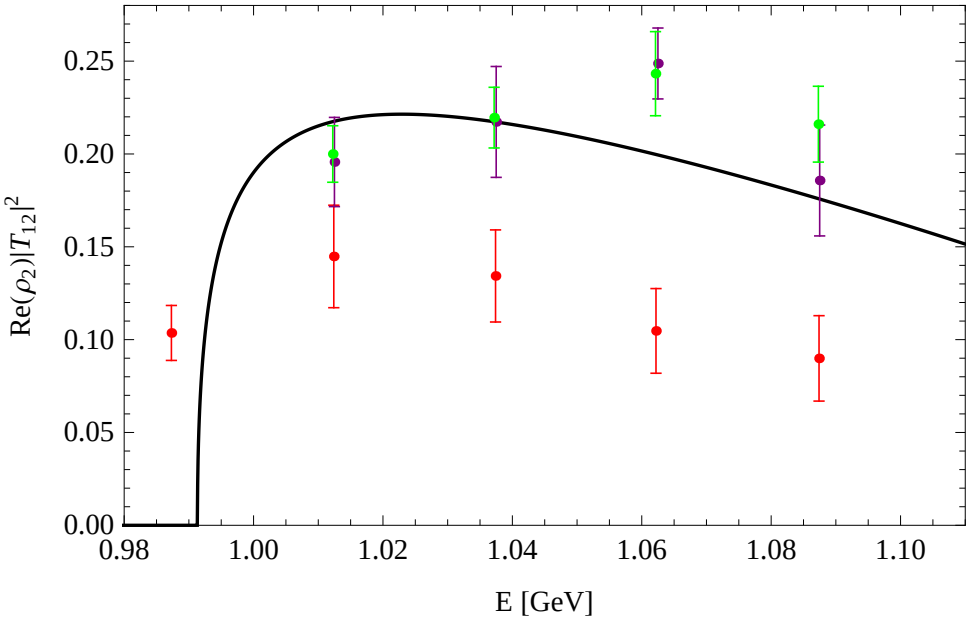

Figure 3.5.: A typical fit to the T_{12} magnitude data. The solid curve is a typical theory fit, Red is Cohen, Violet is Etkin with normalisation included and Green is Longacre. The theory curve is averaged over each experimental bin.

3.3.4. Split Threshold vs Averaged Threshold

Since the $f_0(980)$ lies so close to the $K\overline{K}$ threshold then the choice between k_2^{split} and k_2^{ave} is important, in principle k_2^{split} is the physically correct version, however it is complicated by extra sheets due to the additional square root when going from k_2 to E. This can only be important in the region very close to the threshold and provided the pole does not lie within this region (close to the quarter circle around the origin in fig. 3.4) then the effect can only be small. Since the poles we have found are always well outside of this region then the split threshold does not cause an additional complication. Going from k_2^{ave} to k_2^{split} typically reduces the χ^2 by 2 even without re-minimising the parameters. In the following fits we will primarily use k_2^{split}, this will be clearly visible in the plots that are shown, by two separate kinks in the physical amplitudes as the individual charged and neutral thresholds open.

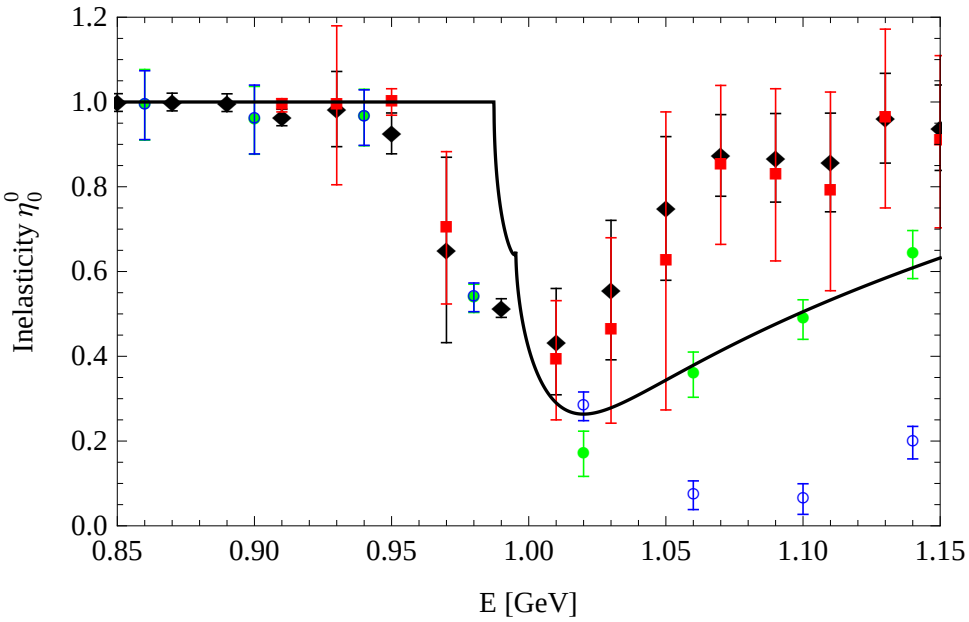

Figure 3.6.: A typical fit to the η_0^0 parameter in $\pi\pi \to \pi\pi$, we reject the data denoted by the blue empty circles (Achasov fig. 5e, [69]) and retain the green filled circles (Achasov fig. 5a, [69])

3.3.5. Second pole position investigation

The initial fits performed suggest that a one-pole parameterisation is sufficient to represent the data selected. However, since the one-pole form is simpler to fit (the extra pole induces some instability in the parameter values), then it is important to investigate the possible positions of the second pole more thoroughly. This is done in three steps of increasing effort. First, the pole position from an earlier analysis are taken as the starting points and how the new datasets affect the positions of these poles are investigated. Second, we slide in the second pole from some asymptotic value using a minimised one-pole solution. In order to do this, the magnitude of the second pole is fixed and the parameters are minimised starting from the previous solution. If small downward steps in the magnitude of the pole are made then the solutions and parameters do not change very much and we can investigate the χ^2 as a function of $|k_2^{(2p)}|$, the magnitude of the second pole. Third, we perform a full parameter scan of the second pole position in the fourth quadrant of the k_2 plane, and plot the total χ^2.

The position of the second pole is important since if it is far from the real axis or if it moves outside of the fitting region then it will have little or no effect on the scattering amplitudes. Also, if the poles are not symmetrically positioned in the k_2 plane as in the

usual Breit-Wigner parameterisation, then it is unlikely that this state may be described as a compact system, and must be molecular in structure.

MP '93 pole positions

The black dot in figure 3.8 corresponds to the solutions given in ref. [40]. We use these pole positions to check our χ^2's and as a potential starting point for minimisation. The values we find are shown in table 3.1. We note that the original solution is now excluded since it is not possible to simultaneously obtain good fits to both channels of the Babar data. When freeing up both poles we note that the second pole moves away from the physical line in k_2 and hence has little effect. Something to note for later is that for these two pole fits the Babar $\pi\pi$ data is sometimes represented poorly. This is due to the β_i coefficients being heavily constrained by the $K\overline{K}$ data, and since there are comparatively fewer points for the $\pi\pi$ data in this channel this is where the discrepancy appears. Nevertheless, it is important to note that the $\pi\pi$ data provides a crucial constraint in order to fix the coefficient functions $\beta_1(s)$ and $\beta_2(s)$.

These pole positions are also heavily excluded when we consider the BNL/Achasov data. This set contributes around $\simeq 90$ to χ^2 for the fixed pole situations, whilst it only contributes $\simeq 32$ when the poles are free. These data did not exist when the analysis of ref. [40] was carried out.

First Pole		Second Pole		χ^2	Note
$E - i\Gamma/2$	$k_2^{(1p)}$	$E - i\Gamma/2$	$k_2^{(2p)}$		
$0.988 - i0.024$	$-0.071 + i0.083$	$0.978 - i0.028$	$0.065 - i0.105$	379.9	Poles fixed
$0.990 - i0.016$	$-0.060 + i0.069$	$0.978 - i0.028$	$0.065 - i0.105$	327.6	$k_2^{(2p)}$ fixed
$1.008 - i0.022$	$-0.104 + i0.053$	$0.915 - i0.053$	$0.060 - i0.202$	190.7	Poles free

Table 3.1.: Pole positions and fits. The fixed pole positions are taken from ref. [40]

Sliding second pole in from good known fit

In investigating the properties of the second pole, a fitting method was used where known good one-pole fits became initial values of the parameters and the second pole was incrementally moved closer to threshold region, from some asymptotic value. Several fits of this type were performed, each with the same behaviour: as the $|k_2|$ value of the second

pole was moved into the 'interesting' region, the value of χ^2 increased significantly. The additional pole allows the amplitude rapid variation over a small energy region, but if it is close to the real axis then a larger phase shift is expected compared to the one pole scenario. If the pole is accompanied by a small residue, or is far from the real axis then the variation offered by the extra parameters may be used in obtaining a better fit, that could also be obtained without the additional pole. This is apparent in the red/solid and orange/dashed curves in figure 3.7 where as the pole approaches the area of interest, for some fits the χ^2 decreases by $\simeq 10$. The pole position at $E = 0.91 - i0.07$ is close to the limit of our region at $E = 0.87$. However, as the pole moves fully into the region of interest, the fits become poorer. It appears the pole is just allowing some extra variation due to the extra parameters, that produces a better fit. This is probably not a physical solution. The paths the poles take in the complex k_2 plane are displayed in figure 3.8. The red and black, dotted curves are at fixed $\mathrm{Arg}(k_2^{(2p)})$ for the second pole whilst the blue dot-dashed curve is restricted to $\mathrm{Arg}(k_2^{(2p)}) > 315^\circ$ and the orange dashed curve is free to move about the whole plane. This demonstrates the common minimisation problem of local minima, since the parameter space of the orange curve includes that of the others, however the χ^2 is at times larger due to the local minima encountered along the path it takes across the parameter space.

Parameter scan

The final method is the most time-consuming numerically but is reasonably conclusive considering the unstable nature of the minimisation parameters. The method is to scan over the fourth quadrant of the k_2-plane in the region of interest. More precisely $\mathrm{Arg}(k_2^{(2p)})$ is scanned in steps of 1° and the $|k_2^{(2p)}|$ is moved into the region of interest in steps of 0.025 GeV, starting from 0.6 GeV and working downwards. The other parameters are left free and the value of χ^2 is plotted in figs. 3.9 and 3.10.

Even making such small steps of $\Delta|k_2^{(2p)}| = 0.025$ GeV, the program occasionally fails to find the absolute minimum and gets stuck in some local minimum. This is seen in fig. 3.9 where the minimisation procedure finds a value of χ^2 larger than those around it and it continues along this path as $|k_2^{(2p)}|$ is reduced. This can be seen as a slightly raised χ^2 at a fixed angle in fig. 3.9. Repeatedly refitting and using different values of the starting parameters does not always alleviate the problem.

There is a global minimum in this plot in a small range of values as can be seen in fig 3.10 with the minimum at $|k_2^{(2p)}| = 0.1950$ and $\mathrm{Arg}(k_2^{(2p)}) = 286^\circ$ with $\chi^2 = 183$.

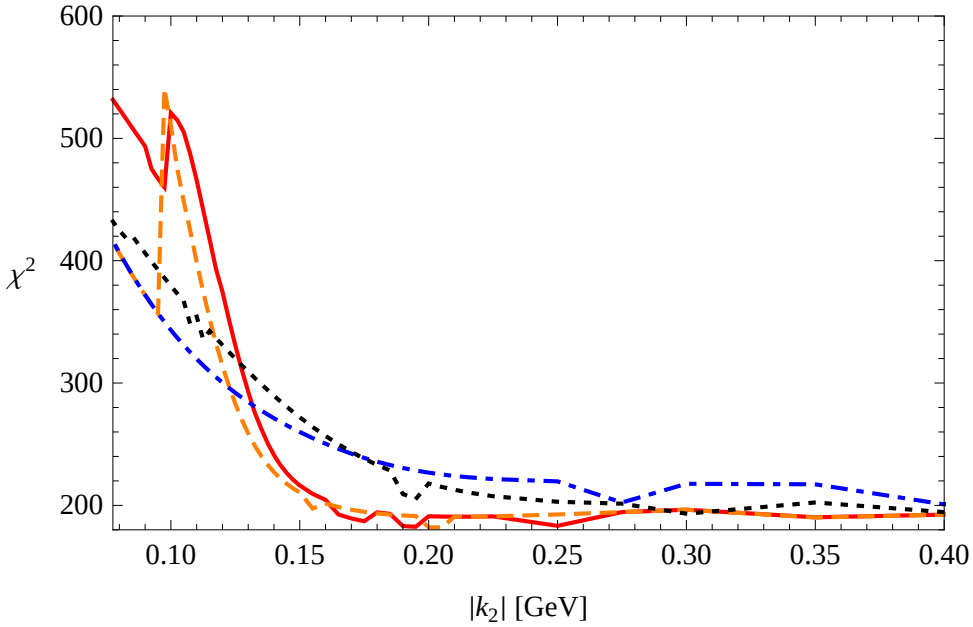

Figure 3.7.: The value of χ^2 as it increases with decreasing $|k_2|$ of the second pole. The red solid curve has Arg $\left(k_2^{(2p)}\right) = 286°$ fixed and passes through the global minimum. The Orange dashed curve has Arg $\left(k_2^{(2p)}\right)$ completely free. The Black dotted curve has Arg $\left(k_2^{(2p)}\right) = 303°$ fixed and the Blue dot-dashed curve is restricted to the part of the plane that has the most effect on the scattering amplitudes, that closest to the real axis, so we enforce the limit Arg$(k_2^{(2p)}) \geq 315°$. These curves also correspond to those shown in figure 3.8.

This is on the edge of the region where the pole can be important and corresponds to $E = 0.9267 - i0.0046$ GeV. Since this pole lies towards the edge of the region of interest and is some distance from the all-important real axis then its effect may be limited. If we consider the residue of this pole in the various amplitudes which we obtain from the Jost functions then its residue is considerably smaller than that for the first pole. For this solution, the first pole residue lies in the range $[-3.4, 4.2]$ and the second pole lies in the range $[-0.4, 0.9]$ however the distance from the real axis is the most important factor: this pole is not required to reproduce the experimental scattering amplitudes.

We now drop the second pole from the analysis since it is an unnecessary complication, and we now investigate how well the data are represented by the Jost function parameterisation using just one pole.

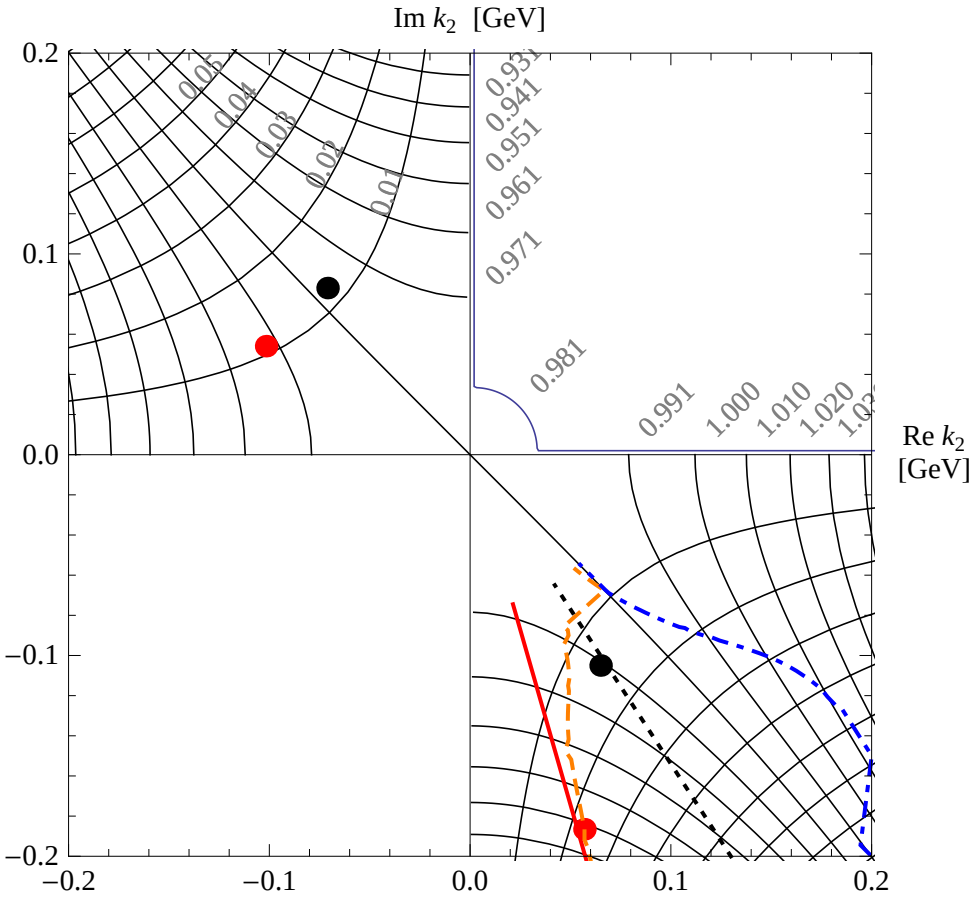

Figure 3.8.: The k_2 plane with contours of Energy and decay width plotted. The red solid curve has $\mathrm{Arg}(k_2^{(2p)}) = 286°$ fixed and passes through the global minimum. The Orange dashed curve has $\mathrm{Arg}(k_2^{(2p)})$ completely free. The Black dotted curve has $\mathrm{Arg}(k_2^{(2p)}) = 303°$ fixed and the Blue dot-dashed curve is restricted to $\mathrm{Arg}(k_2^{(2p)}) \geq 315°$. These curves also correspond to those shown in figure 3.7. The units of k_2 are in GeV.

3.4. Best-fit χ^2 Analysis

It has been found that only a single pole in k_2 is required to reproduce the scattering amplitudes as described by the currently available data. Using the Jost function representation of the threshold region we find a minimum with $\chi^2 \simeq 190$ and a single pole on the second quadrant of k_2 (which corresponds to a sheet 2 pole in E) and this controls the physical amplitude. We summarise in table 3.2 the χ^2 contributions and numbers of data points for each set that we consider.

The row labelled 'Significance' is the output of the CERNLIB routine '*Prob*' [78] given these χ^2's and number of degrees of freedom ($N_{\mathrm{d.o.f}}$), which is defined by the number of

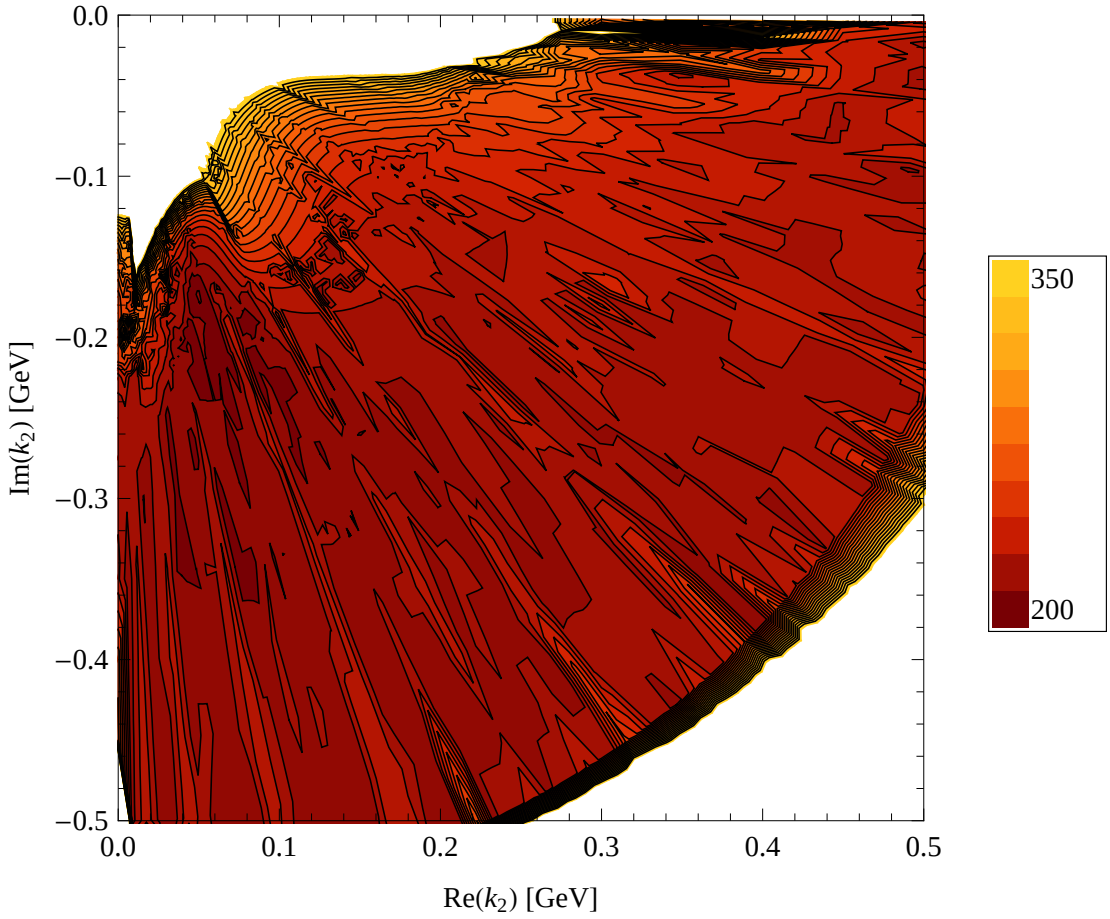

Figure 3.9.: A contour plot of the scanned k_2 plane of the second pole. Note that much of the white region close to the origin has been covered by the scan, however the plot only shows $\chi^2 < 350$. The χ^2 increases rapidly as $|k_2| \to 0$ however there are some small χ^2's around $\mathrm{Im}k_2 \simeq -0.2$, $\mathrm{Re}k_2 \simeq 0.07$.

data points minus the number of fitted parameters. According to statistical folklore, we require this number to be greater than 0.05 in order to have a good fit to the data.

The function '*Prob*' calculates the error integral,

$$Q(\chi^2, N_{\mathrm{d.o.f}}) = \frac{1}{2^{N/2}\,\Gamma(N/2)} \int_{\chi^2}^{\infty} dt\; e^{-t/2}\, t^{N/2-1}. \tag{3.18}$$

If $Q > 0.05$ then the model is considered consistent with the data, if $Q < 0.05$ then there is some statistically significant deviation between model and data.

This is important to assess the relevance of the parameterisation (or model) that we have used to the data. The simplest measure of the quality of a fit is χ^2/d.o.f. which is expected

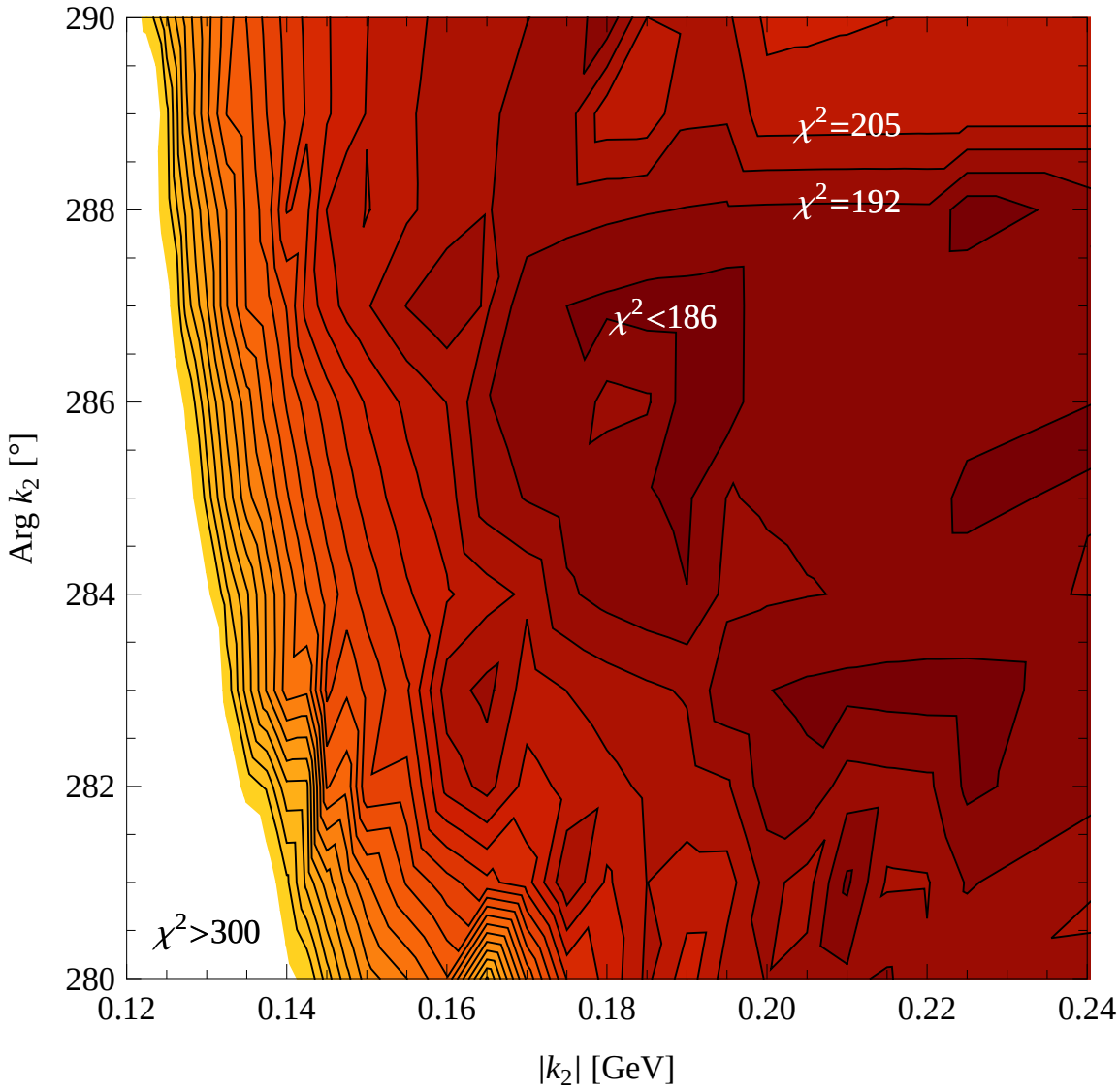

Figure 3.10.: The k_2 plane of the second pole, zoomed. The position of the second pole lies in the dark region labelled $\chi^2 < 186$. The χ^2 increases rapidly as $|k_2| \to 0$.

to be in the region of 1 for a good fit, whilst larger values indicate increasingly poor fits. The values in the first two columns of table 3.2, labelled Fit 1 and 2, indicate a fit that is perhaps not as good as we would hope. The χ^2 contribution of the BNL/Achasov data is always abnormally large, it would be expected that the 12 data points contribute a $\chi^2 \simeq 12$, however they are typically more than double this. The same could be said of the data sets labelled in the table 'Etkin *et al*', this includes the data from Etkin, Longacre and Cohen and the phases from Etkin and Cohen are a little inconsistent with each other. These data are vital and we must be retained in order to constrain the $\pi\pi \to K\overline{K}$ part of the amplitude, however, we may neglect the BNL/Achasov dataset due to the issues

noted by the authors of the paper [69], and the T_{11} matrix element is already constrained by the CERN-Munich data of Ochs *et al.*

The significance of the fits including the Achasov data is less than the required 0.05, which indicates that some of the data is mildly inconsistent. If we drop BNL/Achasov from the fits then we find the results given in last two columns of table 3.2, where the χ^2/d.o.f. values are now close to 1 and the significance values are much improved. This now indicates no significant deviation between the model and the selected data. However, if we investigate the plots and the differences when we include or exclude these data, in the η_0^0 plot we find that the best fit curve always lies between the two sets, regardless of whether the BNL/Achasov is included or not, see fig 3.11.

In order to distinguish between the number poles, ideally the χ^2 analysis would clearly favour one over the other, however, when the same number of free parameters are used, the χ^2's of the Jost function fits are almost identical. There are two situations that we can imagine occuring, first the second pole could be an essential ingredient and the χ^2 is dramatically reduced by its inclusion in the model. Second, the extra pole is not required, but its position and free parameters are utilised by the minimisation routine in order to add some extra variation. Thus comparing a fit with the same free parameters results in a similar χ^2.

In these fits it is the second situation that occurs, the pole is positioned such that its effect is minimal and it gives no improvement over single pole fit. The position of the second pole far from the real axis, its relatively smaller residue and the lack of improvement over the one-pole χ^2 all point to the same conclusion: only one pole is required to produce the experimentally observed scattering amplitude.

In table 3.2 we present the output of the minimisation procedure for a four different fits labelled Fit 1 and 2 for the fits including the BNL/Achasov dataset, and Fit 5 and 6 excluding this dataset. The significance values show an improvement when this dataset is removed. These are the results of one-pole fits and the number of free parameters in the Jost function polynomial is varied between each fit, this is indicated by the total number of free parameters. The minimised values of the parameters are given in table A.1 from appendix A.

In the following figures, we present the results of these four fits for a selection of the data. In fig. 3.11 we present the results of the fits to the $\pi\pi$ scattering data. The green circles correspond to the BNL/Achasov data that is only included in the χ^2 for fits 1 and 2. In fig. 3.12 we show the bins that each data point is averaged over to match from experiment

to theory, this time only for the CERN-Munich data since the BNL/Achasov bins are at different positions. In fig. 3.13 we show the related $\pi\pi \to K\overline{K}$ datasets and the smooth theory curves, that are averaged by the minimisation routine. In fig. 3.14 we present two of the Babar $\pi\pi$ fits, note the unequal bin spacing. The program averages over bins centred on each data point. The final figure for the Jost function fits is that for the Babar $K\overline{K}$ dataset displayed in fig. 3.15.

Data Set	Data Points	$\chi^2_i \quad \mathcal{O}\left(\gamma^{(3)}\right)$ (Jost)	$\chi^2_i \quad \mathcal{O}\left(\gamma^{(4)}\right)$ (Jost)	$\chi^2_i \quad \mathcal{O}\left(\delta^{(1)}\right)$ (Jost)	$\chi^2_i \quad \mathcal{O}\left(\delta^{(2)}\right)$ (Jost)
		Fit 1	Fit 2	Fit 5	Fit 6
Total Parameters	–	22	24	22	24
CERN-Munich	24	20.5	20.5	18.1	19.2
BNL/Achasov A	12	25.2	35.7	–	–
Etkin *et al*	15	27.5	25.9	25.1	21.0
Babar $\pi\pi$	16	15.9	6.7	16.9	5.2
Babar $K\overline{K}$	61	82.2	71.1	75.7	66.7
Mk3	34	21.6	22.1	21.0	22.2
BES	13	5.9	8.0	8.6	11.4
Total	172	199.2	190.3	165.5	144.0
d.o.f.	–	150	148	138	136
χ^2/d.o.f.	–	1.33	1.29	1.10	1.06
Significance	–	4.6×10^{-3}	1.1×10^{-2}	5.5×10^{-2}	0.28
Pole Pos. [GeV]	–	$1.010 - i0.024$	$1.005 - i0.022$	$1.004 - i0.032$	$0.998 - i0.029$

Table 3.2.: Individual χ^2's amongst the datasets for some best-fit amplitudes for the Jost-function fits. Note that Etkin *et al* consists of Etkin, Longacre, Cohen *et al* [61–64].

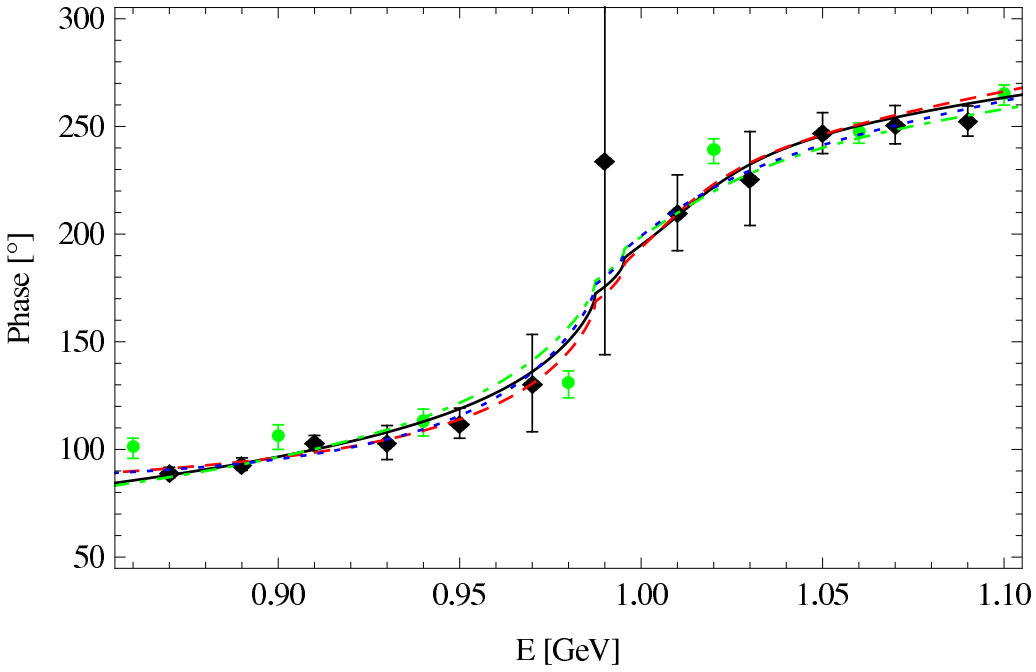

(a) δ_0^0

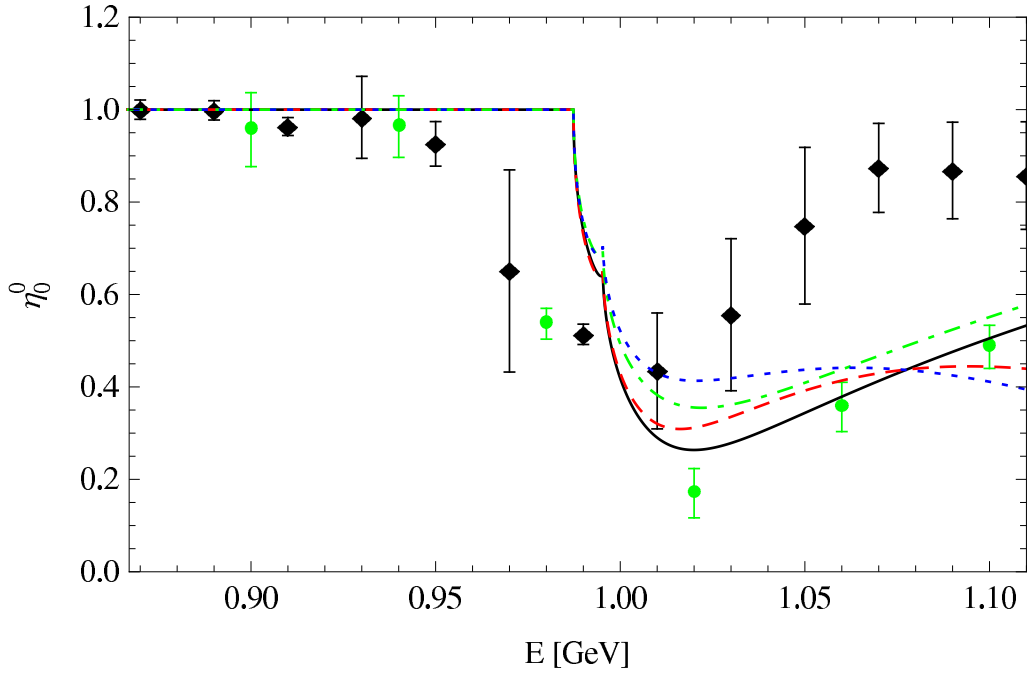

(b) η_0^0

Figure 3.11.: The Jost function fit to the $\pi\pi \to \pi\pi$ data. Fit 1 is Black Solid curve, Fit 2 is the Red dashed curve, Fit 5 is the Green dot-dashed curve and Fit 6 is the Blue dotted curve.

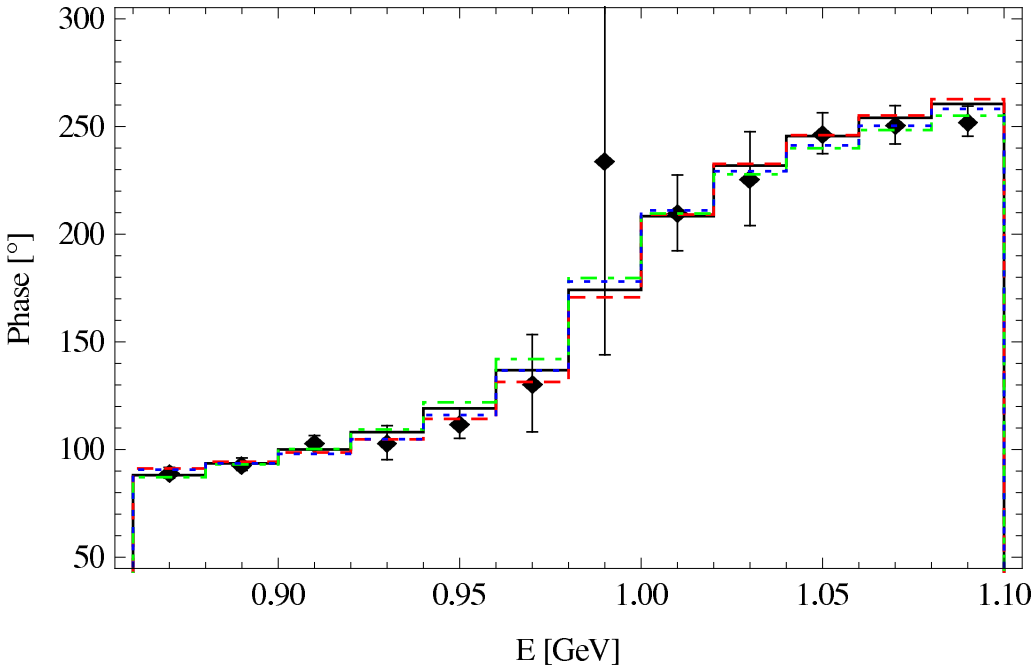

(a) δ_0^0

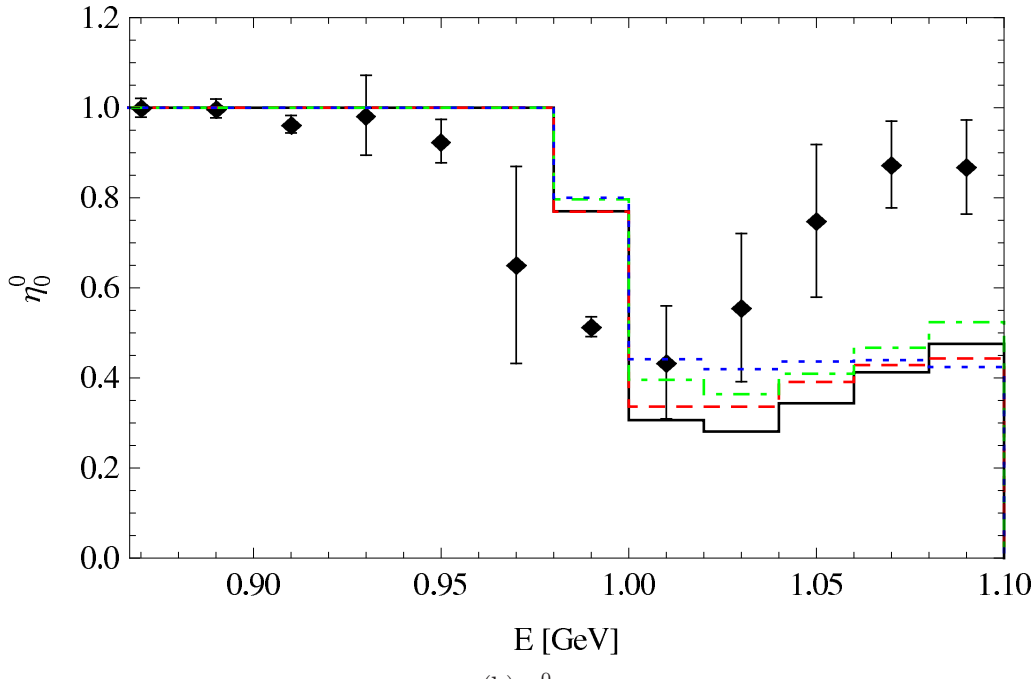

(b) η_0^0

Figure 3.12.: The Jost function fit to the $\pi\pi \to \pi\pi$ data. Fit 1 is Black Solid curve, Fit 2 is the Red dashed curve, Fit 5 is the Green dot-dashed curve and Fit 6 is the Blue dotted curve. The fits depicted by this plot are the same as in fig. 3.11, however here the value for each data bin is shown, this is what is actually fitted.

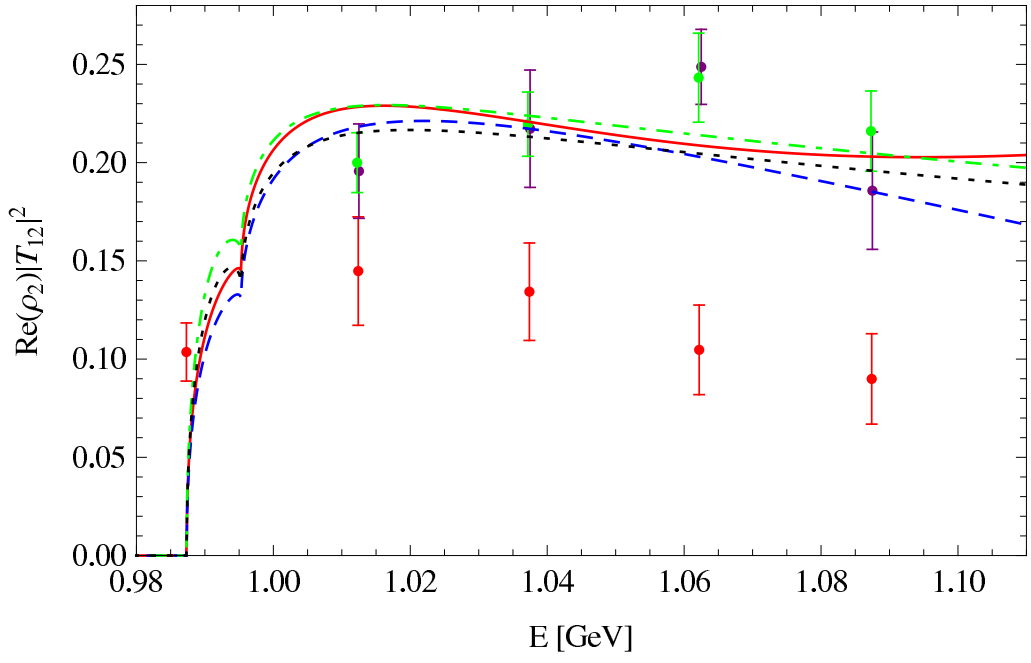

(a) $Re(\rho_2)|T_{12}|^2$

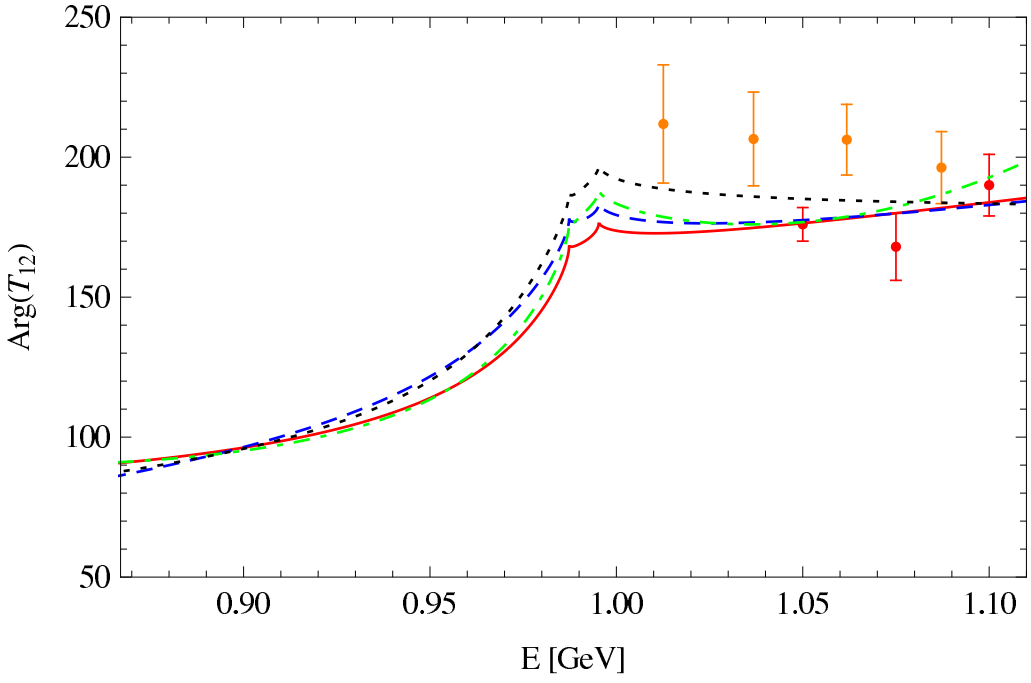

(b) $\mathrm{Arg}(T_{12})$

Figure 3.13.: Some of the fits to the $\pi\pi \to K\overline{K}$ data, using the directly comparable sets with 24 parameters each for both the Jost and Flatté type fits. The phase of T_{12} is the same as $|T_{11}$ below threshold. Fit 2 is Red Solid curve, Fit 3 is the Blue dashed curve, Fit 6 is the Green dot-dashed curve and Fit 7 is the Black dotted curve.

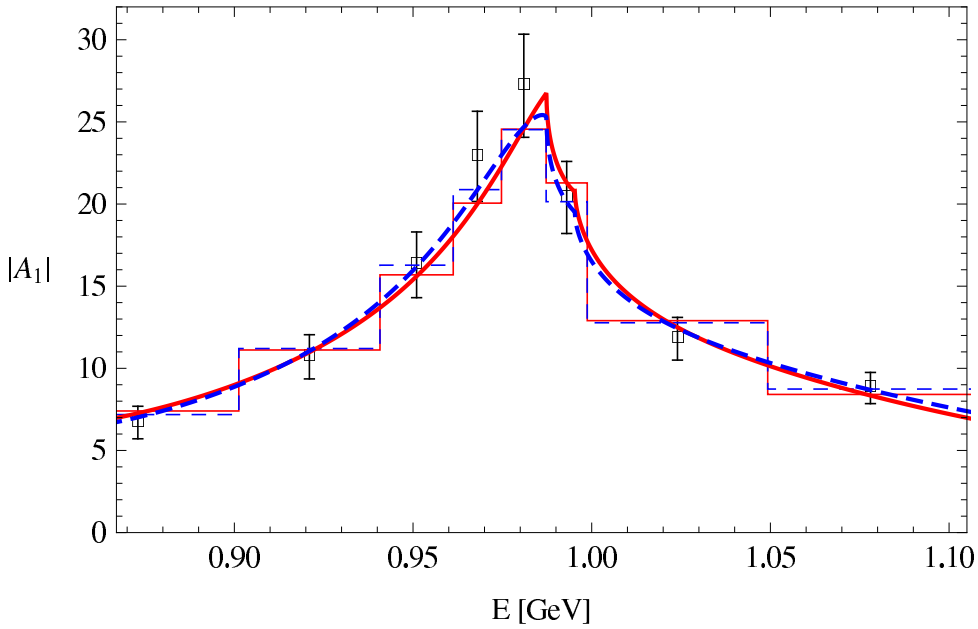

(a) Babar $\pi\pi$ $|A_1|$

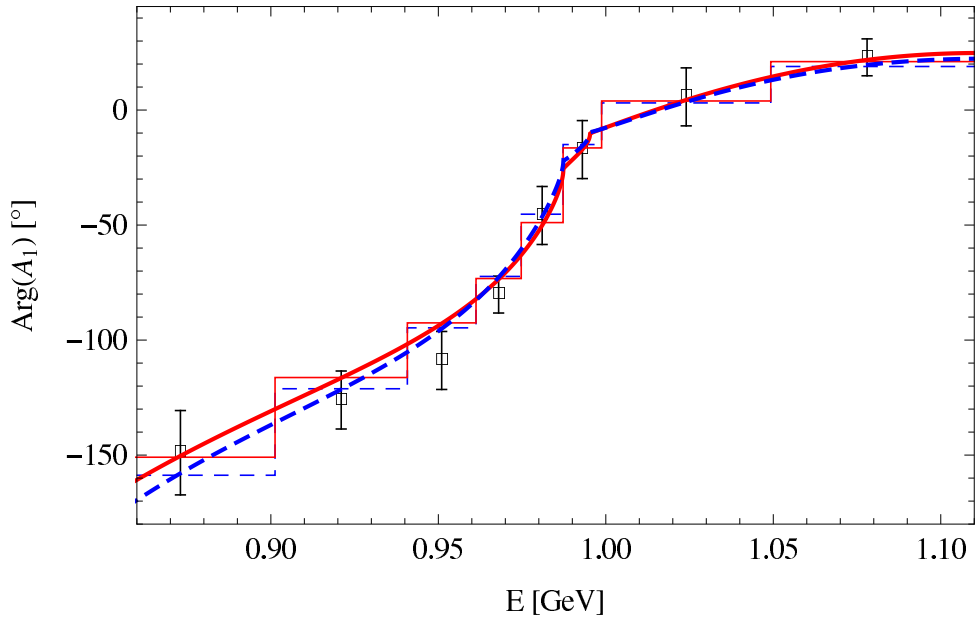

(b) Babar $\pi\pi$ Arg A_1

Figure 3.14.: The fit to the new data from the Babar collaboration, $\pi\pi$ channel. Shown in Red is Fit 2 and the Blue dashed curve is Fit 6. Other fits to these data are much the same. We also show the theoretical fit averaged over each data bin, this is what is actually matched to the experimental data.

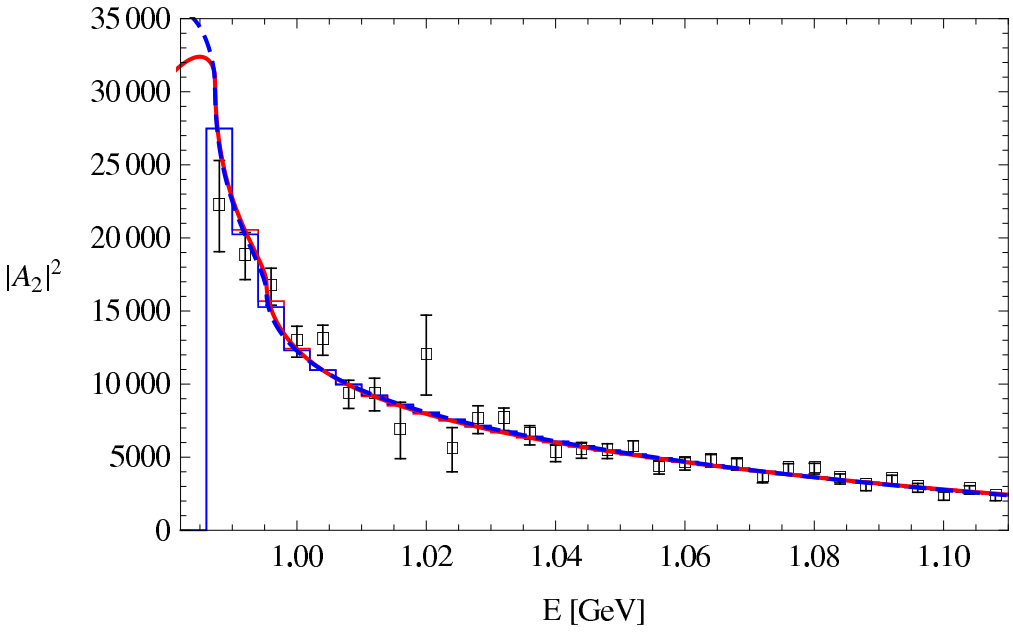

(a) Babar $K\overline{K}$ $|A_2|^2$

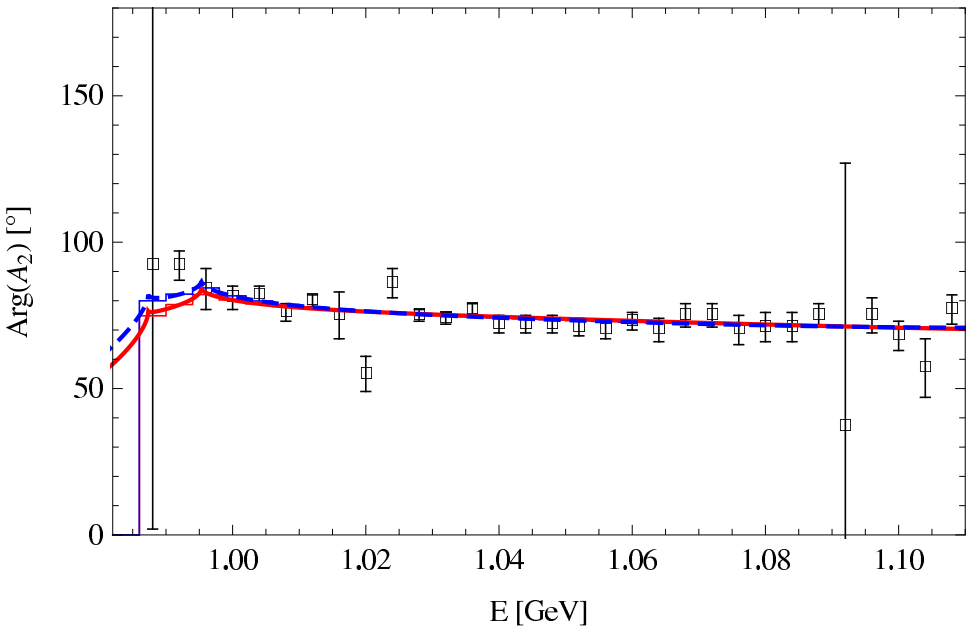

(b) Babar $K\overline{K}$ Arg(A_2)

Figure 3.15.: The fit to the new data from the Babar collaboration, $K\overline{K}$ channel. Shown in Red is Fit 2 and the Blue dashed curve is Fit 6. Other fits to these data are much the same. Again, we also show the theoretical fit averaged over each data bin, this is what is actually matched to the experimental data.

3.5. Flatté Parameterisations

An alternative and popular parameterisation of this resonance is that originally proposed by Flatté [58]. This is an extended form of the standard Breit-Wigner, we use the most general form allowed by unitarity given above in eq. (3.12). The exact form used here is given by [47, 59],

$$F_{ij}(s) = \frac{g_i g_j}{m_0^2 - s - ig_1^2\rho_1(s) - ig_2^2\rho_2(s)} \,, \tag{3.19}$$

$$T_{ij}(s) = \delta_{ij}\frac{\sin\phi_i(s)e^{i\phi_i(s)}}{\rho_i(s)} + e^{i\phi_i(s)+i\phi_j(s)}F_{ij} \,, \tag{3.20}$$

where T_{ij} are the usual T-matrix elements and the terms are defined in eq. (3.12). The first term has the form of an elastic scattering contribution, whilst the second term takes the Flatté resonance formula and gives it an additional phase. This has a different set of parameters compared to the Jost form. The phases $\phi_i(s)$ are parametrised by,

$$\phi_i(s) = \phi_i^{(0)} + \left(\frac{s}{4m_K^2} - 1\right)\phi_i^{(1)} + \left(\frac{s}{4m_K^2} - 1\right)^2\phi_i^{(2)} + ... \tag{3.21}$$

where the coefficients $\phi_i^{(j)}$ are fitted by the minimisation. The remaining parameters, m_0, g_1 and g_2 are also minimised so that the amplitudes fit the data. A similar conclusion may be drawn here regarding the second pole, it does not appear near to the real axis so does not contribute to the scattering amplitude.

The χ^2 values for a similar range of fits as for the Jost analysis are given in table 3.3. The pattern is much the same, including the BNL/Achasov data then the significances indicate mildly inconsistent data and rejecting this dataset results in acceptable values. The relevant pole is found in much the same position as for the Jost function fits to the same datasets. Fits 3 and 4 include the BNL/Achasov data and in fits 7 and 8 this has been excluded. Again, different numbers of parameters are used in the phases ϕ given in the Flatté amplitudes. Fits 3 and 7 are linear in $(1-4m_K^2/s)$ and fits 4 and 8 have phases that vary up to quadratic order. Fits 3 and 7 have the same number of free parameters to the Jost function fits 1 and 5 so the results may be directly compared. Importantly the E pole position is stable given these input data for both types of fit.

An example of the fit to the $\pi\pi \to \pi\pi$ data is given in figure 3.16 and is much the same as the fits using the Jost function.

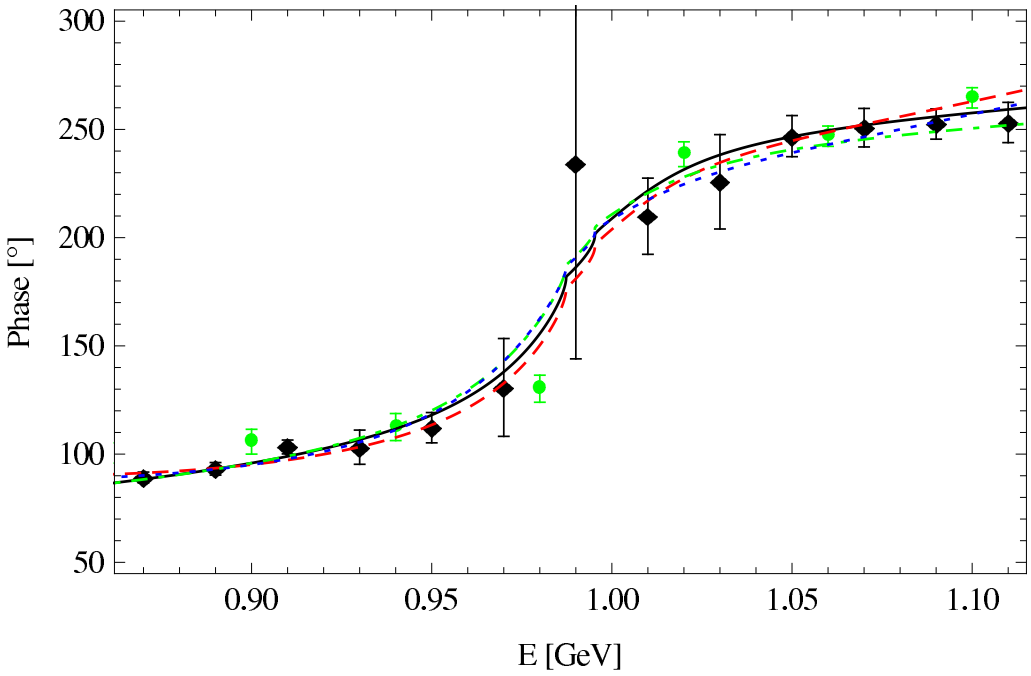

(a) δ_0^0

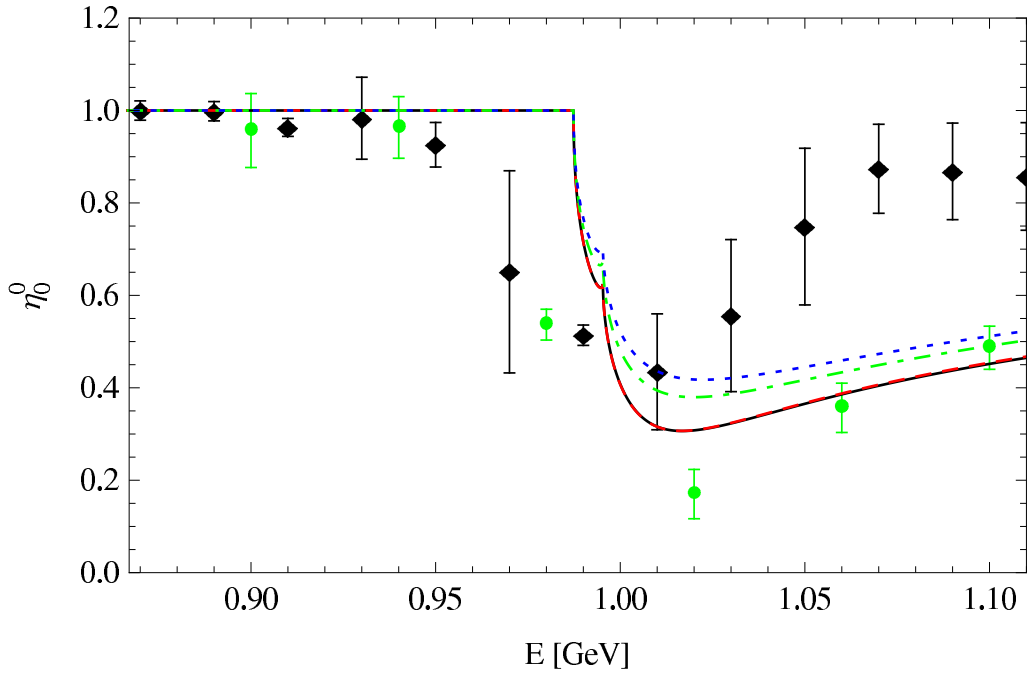

(b) η_0^0

Figure 3.16.: The Flatté fit to the $\pi\pi \to \pi\pi$ data. Fit 3 is Black Solid curve, Fit 4 is the Red dashed curve, Fit 7 is the Green dot-dashed curve and Fit 8 is the Blue dotted curve.

Data Set	Data Points	$\chi_i^2 \quad \mathcal{O}\left(\gamma^{(3)}\right)$ (Flatté)	$\chi_i^2 \quad \mathcal{O}\left(\gamma^{(4)}\right)$ (Flatté)	$\chi_i^2 \quad \mathcal{O}\left(\delta^{(1)}\right)$ (Flatté)	$\chi_i^2 \quad \mathcal{O}\left(\delta^{(2)}\right)$ (Flatté)
		Fit 3	Fit 4	Fit 7	Fit 8
Total Parameters	–	24	26	24	26
CERN-Munich	24	19.8	21.4	18.8	18.1
BNL/Achasov A	12	41.7	20.4	–	–
Etkin *et al*	15	21.4	22.8	20.7	22.1
Babar $\pi\pi$	16	7.1	4.7	7.3	5.8
Babar $K\overline{K}$	61	82.9	73.7	74.8	64.1
Mk3	34	23.8	23.9	22.5	23.0
BES	13	13.5	13.6	11.6	9.3
Total	160	210.3	180.7	155.7	142.6
d.o.f.	–	148	146	136	134
χ^2/d.o.f.	–	1.42	1.24	1.14	1.06
Significance	–	6.1×10^{-4}	2.7×10^{-2}	0.119	0.290
Pole Pos. [GeV]	–	$1.002 - i0.024$	$1.002 - i0.024$	$0.996 - i0.030$	$1.002 - i0.024$

Table 3.3.: Individual χ^2's amongst the datasets for some best-fit amplitudes for the Flatté fits. Note that Etkin *et al* consists of Etkin, Longacre, Cohen *et al* [61–64].

3.6. Mass determination and Error

The fitting procedure naturally returns an error on the given parameters so for the Jost function the determination of the error on the pole is straightforward, using fit 6 from table 3.2 we find that in energy E the pole resides at,

$$E_{\text{pole}} = (1.004 \pm 0.005) - i(0.032 \pm 0.004)\ \text{GeV} \tag{3.22}$$

corresponding to a mass and width given by,

$$M_{f_0(980)} = (1.004 \pm 0.005)\ \text{GeV} \tag{3.23}$$

$$\Gamma_{f_0(980)} = (0.064 \pm 0.008)\ \text{GeV} \tag{3.24}$$

looking at the range of values of E for the different fits given in tables 3.2 and 3.3 the error seems sensible given these fits since all of the fits lie within or very close to the error bound. The value for M is a little higher than that quoted at present by the PDG [20] and

a number of other analyses of this resonance, however given this combination of datasets the position of this pole is very well determined.

3.7. Conclusion

Following an analysis suggested long ago by Weinberg for the deuteron, we have investigated the structure of the $f_0(980)$ resonance observed in meson scattering and decay. By utilising a range of data, including some recently made available by the Babar collaboration we have a firm conclusion that the physical amplitude requires only a single pole to produce the experimental data. A second pole close to the real axis, and therefore physically relevant, is excluded by the data. This conclusion stands well with other related studies of this particle using recent data [47,48] that suggest a single pole is sufficient. Given this pole structure the method dictates that the dominant component of the $f_0(980)$ must be $K\overline{K}$ and this component must dominate all of its physical interactions. However, theoretically, this does not exclude the picture that the state is seeded by a bare $\overline{q}q$ pair, possibly $\overline{s}s$, and is subsequently dressed by strong coupling to $K\overline{K}$ [37,38,43,79].

Chapter 4.

The Schwinger–Dyson Equations of QCD

As we have seen, certain aspects of the QCD Lagrangian may be understood using a perturbative expansion. However, to really understand the inner workings of hadrons it appears we must use some other method since no known expansions are convergent for the region of interest. One method is to go back a step to the fundamental theory and investigate the structure of dressings of bare propagators and vertices. It turns out that the equations lead to strongly coupled non-linear integral equations relating just a few unknown functions, and that these unknown functions can be determined numerically by looking for self-consistent solutions of the integral equations. The method is however not without problems, as we shall find below.

4.1. Introduction

The Schwinger–Dyson equations were first derived for QED [80–82], but exist for any well defined field theory such as QCD that we consider here. The Schwinger–Dyson Equations of QED and QCD form an infinite interconnected series of equations that form the field equations of our theory. They may be expanded in g yielding the familiar series of Feynman diagrams that are found in perturbation theory, or we may attempt to solve them directly using a carefully chosen approximation or truncation. Truncating the infinite series is potentially a dangerous thing to do since it is completely analogous to throwing away diagrams from a perturbative series, which for the gluon propagator can violate transversality, gauge invariance and plague the results with unphysical quadratic

divergences. These problems, that are well understood in perturbative QCD, can also be present in poorly chosen truncations of the Schwinger–Dyson Equations and great care must be taken at all times to retain the physical properties of the underlying theory.

Other than simple curiosity, one of the motivations for studying these equations are that they are necessary inputs for the Bethe–Salpeter Equation for bound state hadronic physics. In pure Yang–Mills theory we may use the Schwinger–Dyson Equations in the Landau Gauge to investigate the behaviour of ghosts and gluons alone without the added complications of quarks and with the additional luxury of precise data from Lattice QCD. Studying these equations contributes to the understanding of confinement and how QCD correlation functions behave at long distances. Confinement is a statement not only about quarks, but also gluons since both are absent asymptotically. In this study we will not consider quarks initially, only the pure SU(3) Yang-Mills theory. Physically this will need rectification later, however mathematically it is a sound approximation and should not introduce additional problems. This naturally links to Lattice QCD where quarks are computationally expensive and more precise data at smaller momenta are available for the pure gauge sector.

We consider the pure Yang–Mills sector of QCD and attempt to construct a minimal, solvable truncation that reproduces perturbation theory in the ultraviolet and produces a manifestly transverse gluon for all momenta. The ultimate intention is to then include quarks and calculate physically observable quantities.

The full derivation of the Schwinger–Dyson equations for QCD is widely available in the literature. In the introductory chapter we showed the form of the generating functional used to give the connected, one-particle-irreducible (1PI) graphs from the fundamental Lagrangian. The SDEs are really just the equations of motion of the theory and may be derived by considering the Euler-Lagrange method originally used in classical mechanics. The structure of the equations and their relation to the perturbative series may also be visualised by considering a summation of the series of all the 1PI graphs. All that is then required is to sum the geometric series of 1PI graphs and we obtain a structure that we shall see many times.

For example, if we consider a simpler theory such as QED we have,

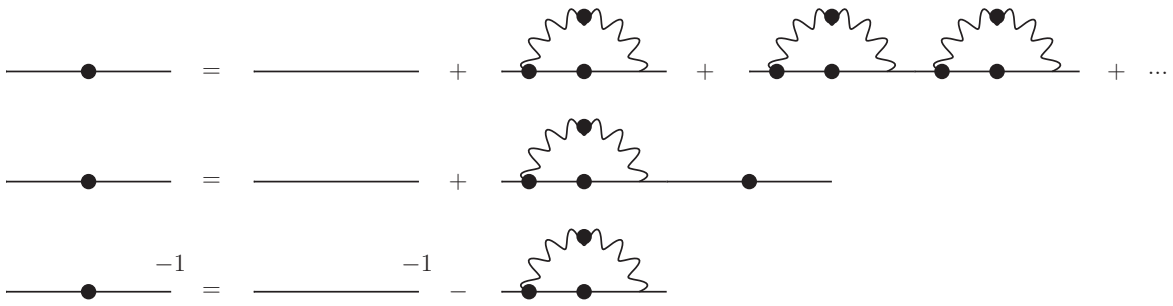

(4.1)

where a heavy dot on a propagator or vertex denotes a fully 'dressed' quantity where all of the infinite loop effects are included. In the second term on the right-hand side of the first line, it can be shown that this combination represents all one-particle-irreducible contributions. The exact same structure will also arise for the ghost propagator in QCD, however the gluon has more terms due to the two self-coupling vertices in the Lagrangian. The dressings of the propagators are neatly restricted by the Ward-Slavnov-Taylor Identities. The simplest WSTI restricts the Gluon propagator dressing in a remarkably simple way,

$$D_{\mu\nu}(p) = \frac{\mathcal{G}l(p^2)}{p^2}\left(g_{\mu\nu} - \frac{p_\mu p_\nu}{p^2}\right) + \xi\frac{p_\mu p_\nu}{p^4} \tag{4.2}$$

so that any dressings from virtual particle effects may be combined into one simple function of momentum-squared, $\mathcal{G}l(p^2)$. This function is known as the gluon propagator dressing function. The gauge parameter ξ is arbitrary and p^2 is the momentum flowing through the propagator. In the Landau gauge, where we perform our calculations, both the bare and dressed gluon propagators are transverse which is an important property that arises when individual gauge–dependent loops are combined; individual loops are not necessarily transverse. A similar relation exists for the Ghost equation,

$$D(p) = -\frac{\mathcal{G}h(p^2)}{p^2} \tag{4.3}$$

where $\mathcal{G}h(p^2)$ is known as the ghost propagator dressing function. In order to learn about the non-perturbative physics of the propagators, in principle, all that is required is to find the correct form that satisfies the Schwinger–Dyson equations. Unfortunately, the problem is complicated by the vertices, which also contain unknown functions and both the ghost and gluon equations depend on these. Some limits are known already though,

for example the perturbative limit, or large-p^2 limit, is straightforwardly calculable order-by-order in g for both propagators. Since the unknown vertex functions depend also on further, higher n-point Greens functions then truncations have to be considered where a vertex dressing is modelled and the propagators are solved self-consistently. A natural first step is to consider the tree-level vertices, further constraints can be found by considering the WSTIs for the vertices, multiplicative renormalisability and the structure of the SDEs for the vertices themselves.

Although they are the simplest Greens Functions in the infinite series of Schwinger–Dyson Equations, the full equations for the Ghost and Gluon propagators have yet to be solved for all momenta. Depicted in figure 4.2 is the full Gluon propagator equation, in the absence of quarks. The truncations considered herein use only relatively simple forms for the vertices. The dressed two-loop terms have never been completely included in any truncations currently in existence, although a significant attempt has been made to include their effects [83] in a scaling type analysis, which refers to a type of solution we discuss below. There are no expansions or power counting schemes for neglecting these terms in general; their effects must be included in order to obtain any reasonable level of precision for the gluon propagator. The reason that these terms are neglected is simply that they are mathematically more difficult and computationally time-consuming to evaluate accurately. However, one must begin somewhere and the inclusion of these diagrams results in sharp increase in complexity and there is little choice but neglect them, at least initially.

Simple truncations observe the presence of two classes of solutions. The 'Type 1' or 'Scaling' solutions denote a Ghost dressing function that is singular in the limit $p^2 \to 0$, or IR limit [84–86] and the 'Type 2' or 'Decoupling' solutions correspond to a Ghost dressing that is finite in the IR limit [86, 87]. These correspond to different solutions of the Ghost equation and it appears both solutions coexist there. The Gluon equation of course couples to the Ghost and extra terms and vertices present complicate matters considerably. The consensus is that a qualitatively similar Gluon dressing which vanishes in the IR limit and reproduces perturbation theory in the UV may simultaneously solve the equations for both types of Ghost solution. This is dependent upon the dressings chosen for the vertices which we will discuss in detail. A comparison of the two types of ghost solution for a fixed gluon input are given in fig. 4.1.

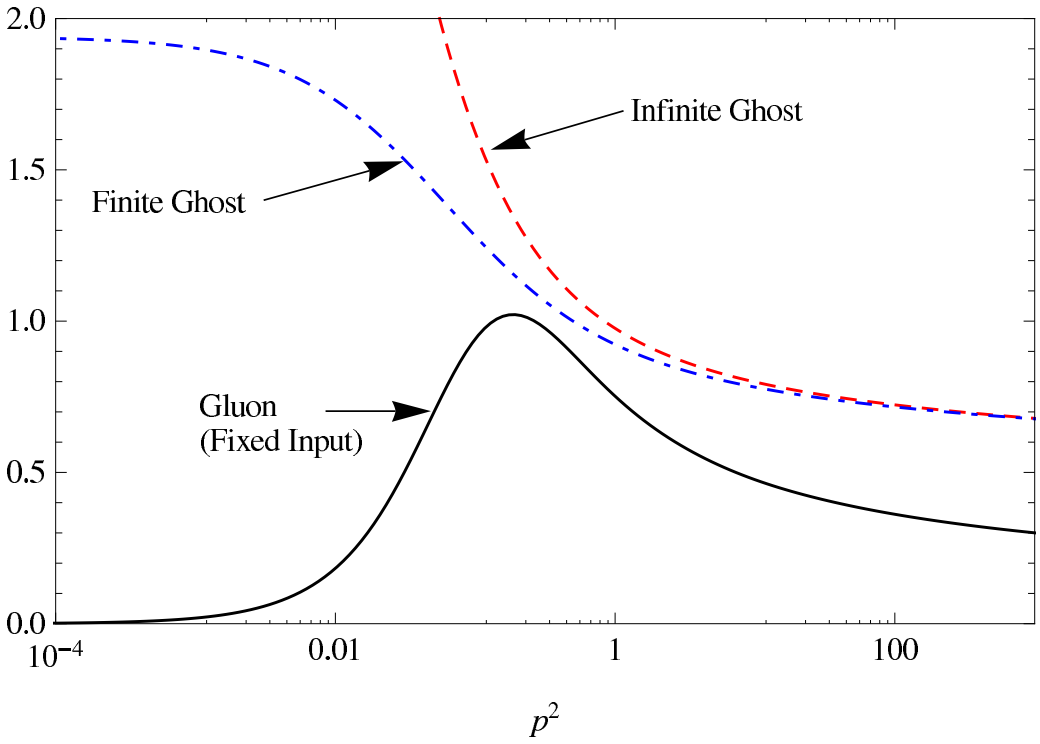

Figure 4.1.: A comparison of typical finite and infinite ghost solutions for a fixed gluon input. The curves depict the the relevant dressing functions $\mathcal{G}h(p^2)$ and $\mathcal{G}l(p^2)$.

The full equation for the ghost propagator represented in figure 4.3, is given by,

$$D^{ab}(p)^{-1} = D^{ab,(0)}(p)^{-1} + \int \frac{d^4\ell}{(2\pi)^4} \Gamma^{acd}_{\mu}(-\ell_-; p, \ell_+) D^{cf}_{\mu\nu}(\ell_-) \Gamma^{bef,(0)}_{\nu}(\ell_-; \ell_+, p) D^{de}(\ell_+), \tag{4.4}$$

where the dressed propagator $D^{ab}(p)$, depends upon its bare counterpart, $D^{ab,(0)}(p)$, and a loop integration containing a ghost and a gluon. The term Γ^{abc}_{μ} is the ghost-gluon vertex and the internal propagator momenta are defined symmetrically using $\ell_{\pm} = \ell \pm p/2$. This will later be renormalised, and models for the ghost-gluon vertex will be inserted. Apart from this vertex, all of the quantities here can be obtained from the equations in a straightforward manner. The full equation for the gluon propagator represented in figure

4.2, with no approximations, is given by,

$$
\begin{aligned}
D^{ab}_{\mu\nu}(p)^{-1} = \; & D^{ab,(0)}_{\mu\nu}(p)^{-1} \\
& + \int \frac{d^4\ell}{(2\pi)^4}\, \Gamma^{acd}_{\mu}(-p;\ell_-,\ell_+) D^{cf}(\ell_+) \Gamma^{bef,(0)}_{\nu}(p;\ell_+,\ell_-) D^{de}(\ell_-) \\
& + \int \frac{d^4\ell}{(2\pi)^4}\, \Gamma^{adeb,(0)}_{\mu\delta\epsilon\nu} D^{de}_{\delta\epsilon}(\ell) \\
& + \int \frac{d^4\ell}{(2\pi)^4}\, \Gamma^{acd}_{\mu\gamma\delta}(p,-\ell_+,\ell_-) D^{cf}_{\gamma\phi}(\ell_+) \Gamma^{bef,(0)}_{\nu\epsilon\phi}(-p,-\ell_-,\ell_+) D^{de}_{\delta\epsilon}(\ell_-) \\
& + \int \frac{d^4\ell_a}{(2\pi)^4} \frac{d^4\ell_b}{(2\pi)^4}\, \Gamma^{acd}_{\mu\gamma\delta}(p,-\ell_2,\ell_4) D^{cg}_{\gamma\zeta}(\ell_2) \Gamma^{befg,(0)}_{\nu\epsilon\phi\zeta} D^{er}_{\epsilon\rho}(\ell_1) D^{ft}_{\phi\tau}(\ell_3) \Gamma^{rst}_{\rho\sigma\tau}(\ell_1,-\ell_4,-\ell_3) D^{ds}_{\delta\sigma}(\ell_4) \\
& + \int \frac{d^4\ell_a}{(2\pi)^4} \frac{d^4\ell_b}{(2\pi)^4}\, \Gamma^{acde}_{\mu\gamma\delta\epsilon}(p,-\ell_1,-\ell_2,-\ell_3) D^{\gamma\psi}_{cj}(\ell_1) D^{dg}_{\delta\zeta}(\ell_2) D^{ef}_{\epsilon\phi}(\ell_3) \Gamma^{bfgj,(0)}_{\nu\phi\zeta\psi}, \qquad (4.5)
\end{aligned}
$$

where latin indices denote colour and greek letters denote the Lorentz indices. The propagators and vertices may be identified by the number of Lorentz indices and are defined in appendix B. Equation 4.5 is represented graphically in fig. 4.2. The momenta are as defined in the figure, the relations between the loop momenta ℓ_a, ℓ_b and the propagator momenta in the two-loop integrals are left undefined, the only restriction is momentum conservation at each vertex.

The integrals in eq. (4.5) contain divergences that may be regulated in a variety of ways. Theoretically, dimensional regularisation is the most appealing since it respects all of the symmetries of the theory, however, numerically a cutoff Λ_{cut} is much simpler to implement so this is chosen for the numerical procedure that is applied to solve these equations. After regularisation, the quantities will typically be of the form, at leading order,

$$
\int^{\Lambda_{\text{cut}}} d^4\ell \frac{\cdots}{\ell^2(\ell+p)^2} \sim 1 + \#g^2 \log\left(\frac{p^2}{\Lambda_{\text{cut}}}\right) + \mathcal{O}(g^4). \qquad (4.6)
$$

The cutoff parameter will appear in the results of the loop integrations and any sensitivity to it is unphysical since is value is arbitrary. The bare equations must be renormalised in order to remove this sensitivity and the method chosen here is a momentum subtraction scheme, sometimes referred to as a MOM scheme. This involves subtracting the result from itself at some value such that the cutoff dependence is cancelled,

$$
\left[\int^{\Lambda_{\text{cut}}} d^4\ell \frac{\cdots}{\ell^2(\ell+p)^2}\right] - \left[\int^{\Lambda_{\text{cut}}} d^4\ell \frac{\cdots}{\ell^2(\ell+p)^2}\Big|_{p^2\to\mu^2}\right] \sim \#g^2 \log\left(\frac{p^2}{\mu^2}\right) + \mathcal{O}(g^4). \qquad (4.7)
$$

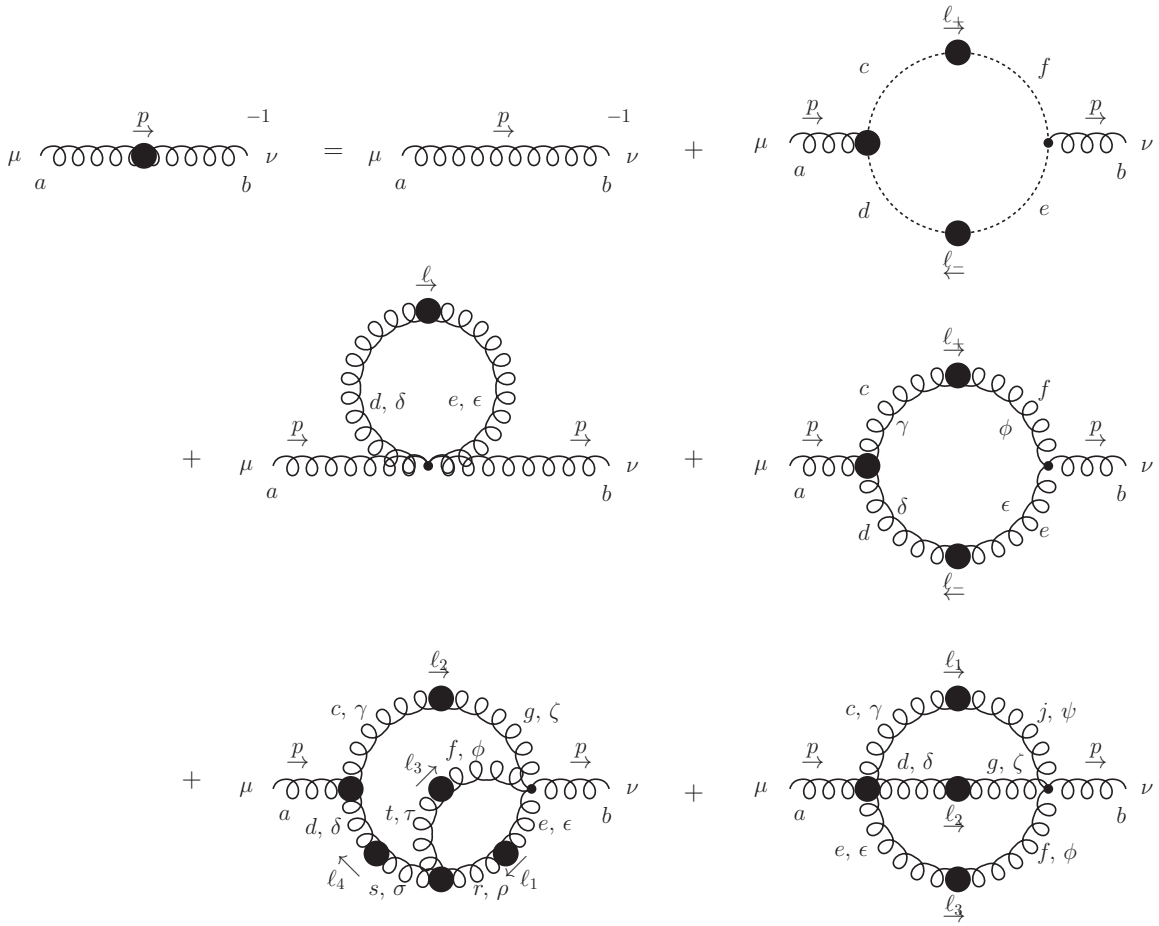

Figure 4.2.: The Schwinger–Dyson Equation for the Gluon in the absence of quarks.

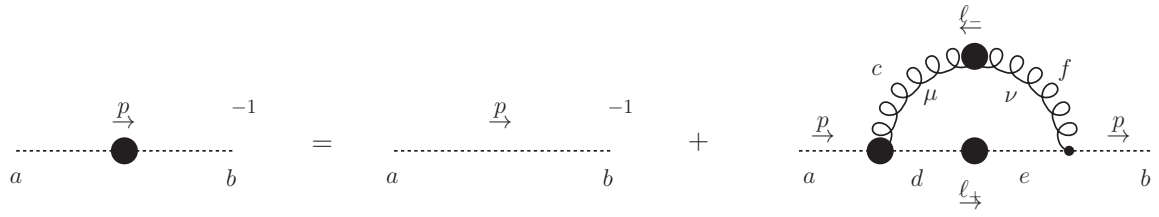

Figure 4.3.: The Schwinger–Dyson Equation for the Ghost.

These subtractions in the SDEs also remove the Z_3 factors that appear in the renormalised ghost and gluon propagator equations, which it must since these are cutoff dependent quantities. The vertices may also receive divergent, as we know from perturbation theory, so these must be renormalised too. The usual method is to replace all of the dressed quantities by their renormalised counterparts in order to remove the cutoff dependence from the quantities that are calculated, a multiplicative method is applied such that,[1]

$$D_{\mu\nu}(p^2,\Lambda^2_{\rm cut}) = D^{(r)}_{\mu\nu}(p^2,\mu^2)Z_3(\mu^2,\Lambda^2_{\rm cut}), \tag{4.8}$$
$$D(p^2,\Lambda^2_{\rm cut}) = D^{(r)}(p^2,\mu^2)\tilde{Z}_3(\mu^2,\Lambda^2_{\rm cut}), \tag{4.9}$$
$$\mathcal{G}l(p^2,\Lambda^2_{\rm cut}) = \mathcal{G}l^{(r)}(p^2,\mu^2)Z_3(\mu^2,\Lambda^2_{\rm cut}), \tag{4.10}$$
$$\mathcal{G}h(p^2,\Lambda^2_{\rm cut}) = \mathcal{G}h^{(r)}(p^2,\mu^2)\tilde{Z}_3(\mu^2,\Lambda^2_{\rm cut}), \tag{4.11}$$
$$\Gamma^{abc}_{\mu}(k^2,p^2,q^2,\Lambda^2_{\rm cut}) = \Gamma^{abc,(r)}_{\mu}(k^2,p^2,q^2,\mu^2)Z_g(\mu^2,\Lambda^2_{\rm cut})\tilde{Z}_1^{-1}(\mu^2,\Lambda^2_{\rm cut}), \tag{4.12}$$
$$\Gamma^{abc}_{\mu\nu\rho}(k^2,p^2,q^2,\Lambda^2_{\rm cut}) = \Gamma^{abc,(r)}_{\mu\nu\rho}(k^2,p^2,q^2,\mu^2)Z_g(\mu^2,\Lambda^2_{\rm cut})Z_1^{-1}(\mu^2,\Lambda^2_{\rm cut}), \tag{4.13}$$
$$g(\Lambda^2_{\rm cut}) = Z_g(\mu^2,\Lambda^2_{\rm cut})g(\mu^2), \tag{4.14}$$

where each Z_i renormalises its respective Green's function and μ^2 is the renormalisation momentum-squared. There are simple relations between some of the renormalisation constants,

$$\tilde{Z}_1 = Z_g Z_3^{1/2}\tilde{Z}_3, \tag{4.15}$$
$$Z_1 = Z_g Z_3^{3/2}, \tag{4.16}$$
$$\frac{Z_1}{Z_3} = \frac{\tilde{Z}_1}{\tilde{Z}_3}. \tag{4.17}$$

The quantities with r-superscripts are now renormalised. Only the dressed Green's functions get renormalised, with the exception of the coupling g which appears in both the dressed and bare vertices. The final ingredient is then to specify some finite value for the dressing functions at the renormalisation point μ^2, for which the most natural choice is,

$$\mathcal{G}l^{(r)}(\mu^2,\mu^2) = 1 \tag{4.18}$$
$$\mathcal{G}h^{(r)}(\mu^2,\mu^2) = 1 \tag{4.19}$$

however other values may be used. The r-superscript, and frequently the parameter μ^2, will be dropped in the notation below. All of the dressed Greens functions considered

[1] This is applied in the Landau gauge where the gauge parameter needs no separate renormalisation constant.

below will be renormalised. We may write down a renormalised version of eq. (4.4),

$$D^{ab}(p,\mu^2)^{-1} = \tilde{Z}_3\left(\mu^2,\Lambda^2_{\rm cut}\right) D^{ab,(0)}(p)^{-1} + \frac{Z_g^2(\Lambda^2_{\rm cut}) Z_3(\mu^2,\Lambda^2_{\rm cut}) \tilde{Z}_3^2(\mu^2,\Lambda^2_{\rm cut})}{\tilde{Z}_1(\mu^2,\Lambda^2_{\rm cut})} \times \int \frac{d^4\ell}{(2\pi)^4}\, \Gamma^{acd}_{\mu}(-\ell_-;p,\ell_+,\mu^2) D^{cf}_{\mu\nu}(\ell_-,\mu^2) \times \Gamma^{bef,(0)}_{\nu}(\ell_-;\ell_+,p,\mu^2) D^{de}(\ell_+,\mu^2). \tag{4.20}$$

This simplifies using eq. (4.15), $f^{acd}f^{bcd} = N_c\delta^{ab}$, the bare ghost-gluon vertex and the Green's function definitions,

$$\mathcal{G}h(p,\mu^2)^{-1} = \tilde{Z}_3\left(\mu^2,\Lambda^2_{\rm cut}\right) - \tilde{Z}_1(\mu^2,\Lambda^2_{\rm cut}) \frac{g^2(\mu^2)N_c}{p^2} \int \frac{d^4\ell}{(2\pi)^4} \left(p.\ell_+ - \frac{p.\ell_-\, \ell_+.\ell_-}{\ell_-^2} \right) \frac{\mathcal{G}h(\ell_+^2,\mu^2)\, \mathcal{G}l(\ell_-^2,\mu^2)}{\ell_-^2\ell_+^2}, \tag{4.21}$$

for other diagrams and extended vertices the momentum factors from the tensor contractions under the integrals lead to lengthy expressions which are usually referred to as a kernel. The kernels here are different to those given in ref. [85] since the loop integration momentum here is symmetric,

$$\mathcal{G}h(p,\mu^2)^{-1} = \tilde{Z}_3\left(\mu^2,\Lambda^2_{\rm cut}\right) + \tilde{Z}_1(\mu^2,\Lambda^2_{\rm cut}) g^2(\mu^2) N_c \int \frac{d^4\ell}{(2\pi)^4}\, \mathcal{K}(p,\ell)\, \mathcal{G}h(\ell_+^2,\mu^2)\, \mathcal{G}l(\ell_-^2,\mu^2), \tag{4.22}$$

which implicitly defines $\mathcal{K}(p,\ell)$,

$$\mathcal{K}(p,\ell) = \frac{-1}{p^2\ell_+^2\ell_-^2} \left(p.\ell_+ - \frac{p.\ell_-\, \ell_+.\ell_-}{\ell_-^2} \right) = -\frac{\ell^2 \sin^2\theta}{\ell_+^2\ell_-^4} \tag{4.23}$$

where θ is the angle between ℓ and p. A vacuum polarisation function is also usually defined,

$$\Pi_{gc}(p^2,\mu^2) = g^2(\mu^2)N_c \int \frac{d^4\ell}{(2\pi)^4}\, \mathcal{K}(p,\ell)\, \mathcal{G}h(\ell_+^2,\mu^2)\, \mathcal{G}l(\ell_-^2,\mu^2)\,. \tag{4.24}$$

The subtraction can then be performed which removes $\tilde{Z}_3$, instead requiring the renormalisation condition to be specified, eq. (4.19),

$$\mathcal{G}h(p^2,\mu^2)^{-1} = \mathcal{G}h(\nu^2,\mu^2)^{-1} + \Pi_{gc}(p^2,\mu^2) - \Pi_{gc}(\nu^2,\mu^2) \tag{4.25}$$

where ν^2 is the point at which the equations are subtracted.

The gluon equation, even without the two-loop diagrams is considerably more complicated than the ghost equation. There is the propagator tensor structure to worry about, and there are many more terms in the two 1-loop integrations, particularly in the gluon loop integration. The Gluon propagator Schwinger–Dyson equation neglecting the two-loop terms is given by the first four lines of eq. (4.5), the first thing we notice is that we have a rank-2 tensor equation to solve when we only wish to solve for the scalar dressing function. We can apply a projector on the propagator, such as,

$$\mathcal{P}^{\mu\nu}(p,\zeta) = \frac{1}{p^2(d-1)}\left(g^{\mu\nu} - \zeta\frac{p^\mu p^\nu}{p^2}\right) \tag{4.26}$$

where d is the number of dimensions that arises from metric contractions and ζ is an abitrary number that will become very important. The projector is normalised such that,

$$\mathcal{P}^{\mu\nu}(p,\zeta)D_{\mu\nu}(p)^{-1} = \frac{1}{\mathcal{G}l(p^2,\mu^2)} \tag{4.27}$$

in principle, the full physical result is independent of the parameter ζ, however in a truncation where terms have been neglected this may not be the case. Should this occur, then it signals a manifest breaking of gauge invariance since the transversality of the gluon propagator must have been lost through truncation. This parameter has two important values, $\zeta = 1$ picks out the function multiplying the $g_{\mu\nu}$ term of the propagator, whilst $\zeta = d$ picks out the term multiplying $p_\mu p_\nu$. Any other value picks out some admixture of the two. Applying the projector eq. (4.26) and following the steps above using the bare vertices leads to,

$$\begin{aligned}\mathcal{G}l(p^2,\mu^2)^{-1} =& Z_3(\mu^2,\Lambda^2_{\rm cut}) \\ &+\tilde{Z}_1(\mu^2,\Lambda^2_{\rm cut})\frac{g^2(\mu^2)N_c}{(d-1)}\int\frac{d^d\ell}{(2\pi)^d}\mathcal{G}h(\ell^2_+,\mu^2)\mathcal{G}h(\ell^2_-,\mu^2)\mathcal{M}(p,\ell,\zeta) \\ &+Z_1(\mu^2,\Lambda^2_{\rm cut})\frac{g^2(\mu^2)N_c}{(d-1)}\int\frac{d^d\ell}{(2\pi)^d}\mathcal{G}l(\ell^2_+,\mu^2)\mathcal{G}l(\ell^2_-,\mu^2)\mathcal{Q}(p,\ell,\zeta).\end{aligned} \tag{4.28}$$

It is important to note that whilst the result *should* be independent of ζ, the integration kernels $\mathcal{M}$ and $\mathcal{Q}$ do depend on it. The tadpole term, the second integral in eq. (4.5) is independent of the external momentum and proportional to $(\zeta - d)$ so does not contribute when $\zeta = d$ and is usually neglected for $\zeta = 1$ since it contains no momentum dependence after integration.

It will become convenient as the kernels become more complex later to collect together the integrals into the polarisation functions Π_{2c} for the ghost loop and Π_{2g} for the gluon loop, we define these implicitly via,

$$\mathcal{G}l(p^2,\mu^2)^{-1} = Z_3(\mu^2,\Lambda^2_{\rm cut}) + \tilde{Z}_1(\mu^2,\Lambda^2_{\rm cut})\Pi_{2c}(p^2,\mu^2) + Z_1(\mu^2,\Lambda^2_{\rm cut})\Pi_{2g}(p^2,\mu^2). \quad (4.29)$$

The functions $\mathcal{M}$ and $\mathcal{Q}$ are found by performing the tensor contractions of the vertices, internal propagators and the projector eq. (4.26), they are given by,

$$\mathcal{M}(p,\ell,\zeta) = (-1)\frac{1}{p^2\ell_+^2\ell_-^2}\left(p^2\left[\ell^2 - \frac{p^2}{4}\right] - \zeta\left[(\ell.p)^2 - \frac{p^4}{4}\right]\right), \quad (4.30)$$

$$\begin{aligned}\mathcal{Q}(p,\ell,\zeta) = \left(\frac{1}{2}\right)\frac{1}{p^2\ell_+^2\ell_-^2}\Big\{ &-2(d-1)\ell^6p^2 + \ell^4\left((7-5d)p^4 + 2(d-1)(\ell.p)^2\zeta\right)\\ &+ (1/8)(\ell.p)^2\left(-16(d-2)(\ell.p)^2\zeta + (d-1)p^4(8+\zeta)\right)\\ &+ (1/8)\ell^2p^2\left(-9(d-1)p^4 + 8(\ell.p)^2\left[-8-3\zeta+d(6+\zeta)\right]\right)\Big\}, \end{aligned} \quad (4.31)$$

where d is the number of dimensions arising from $g_{\mu\nu}g^{\mu\nu}$ terms and ζ is the projection parameter. The factor of (-1) in eq. (4.30) is due to the ghost field being antisymmetric. The factor $(1/2)$ in eq. (4.31) is due to having two identical gluons in the loop.

Part of the renormalisation prescription is to specify some value for the coupling, this is arbitrary but can be fixed with a physically motivated choice or by fitting to some other data, physical or lattice. Since quarks are not considered at present then matching to the physical coupling may not be sensible, however an estimate can be made since in the perturbative region the physics is well understood.

The most precisely measured value of the running coupling is given at the Z-boson mass [20], $\alpha\,(M_Z = 91.1\text{ GeV}) = 0.118$. This is found in the $\overline{\rm MS}$ renormalisation scheme which differs from the MOM scheme used here by finite, momentum dependent terms.

4.1.1. Multiplicative Renormalisability

Multiplicative Renormalisability (MR) is an important property from which all orders constraints can be derived [83, 88–93]. A full MR study is not performed here but it is important to understand how the renormalisation constants arrange themselves and how this can be used to inform the choice of vertex dressing. The standard scheme for renormalisation is as given above where the unrenormalised dressed vertices are renormalised by multiplying an appropriate Z factor. The bare vertices do not receive any renormalisation except for the coupling g which has its own renormalisation factor. In order to check whether MR is satisfied we need to consider eq. (4.10) and eq. (4.11) at two different renormalisation points, leading to,

$$\tilde{Z}_3(\mu^2, \Lambda^2_{\text{cut}})\mathcal{G}h(p^2, \mu^2) = \tilde{Z}_3(\nu^2, \Lambda^2_{\text{cut}})\mathcal{G}h(p^2, \nu^2) \tag{4.32}$$

$$Z_3(\mu^2, \Lambda^2_{\text{cut}})\mathcal{G}l(p^2, \mu^2) = Z_3(\nu^2, \Lambda^2_{\text{cut}})\mathcal{G}l(p^2, \nu^2). \tag{4.33}$$

The next step is to check whether the forms given in eq. (4.22) and eq. (4.28) satisfy this property,

$$\begin{aligned}
\frac{1}{\mathcal{G}h(p^2, \mu^2)} &= \frac{\tilde{Z}_3(\mu^2, \Lambda^2_{\text{cut}})}{\tilde{Z}_3(\nu^2, \Lambda^2_{\text{cut}})}\frac{1}{\mathcal{G}h(p^2, \nu^2)}, \\
&= \frac{\tilde{Z}_3(\mu^2, \Lambda^2_{\text{cut}})}{\tilde{Z}_3(\nu^2, \Lambda^2_{\text{cut}})}\left[\tilde{Z}_3(\nu^2, \Lambda^2_{\text{cut}}) + \tilde{Z}_1(\nu^2, \Lambda^2_{\text{cut}})\Pi_{gc}(p^2, \nu^2)\right], \\
&= \frac{\tilde{Z}_3(\mu^2, \Lambda^2_{\text{cut}})}{\tilde{Z}_3(\nu^2, \Lambda^2_{\text{cut}})}\left[\tilde{Z}_3(\nu^2, \Lambda^2_{\text{cut}}) + \frac{Z_g^2 Z_3 \tilde{Z}_3}{\tilde{Z}_1}\bigg|_{\mu^2}\frac{\tilde{Z}_1^2}{Z_g^2 Z_3 \tilde{Z}_3}\bigg|_{\nu^2}\Pi_{gc}(p^2, \mu^2)\right], \\
&= \tilde{Z}_3(\nu^2, \Lambda^2_{\text{cut}}) + \tilde{Z}_1(\mu^2, \Lambda^2_{\text{cut}})\Pi_{gc}(p^2, \mu^2),
\end{aligned}$$

where we have used the relation in eq. (4.15) twice on the third line, and also the notation $Z_i|_{\mu^2} = Z_i(\mu^2, \Lambda^2_{\text{cut}})$. The factor $\tilde{Z}_1$ is convenient since in Landau gauge we expect this to be 1 [94], since the divergent part of the vertex is proportional to ξ, the gauge parameter. This suggests ghost-gluon vertex dressings of the form $\mathcal{O}\left(\frac{\mathcal{G}h}{\mathcal{G}h}\right)$. The same analysis may also be performed on the gluon equation, there are several versions of this that we may wish to consider with different vertex dressings. Starting with the bare equation eq. (4.28),

we follow the same steps as before,

$$\begin{aligned}
\frac{1}{\mathcal{G}l(p^2,\mu^2)} &= \frac{Z_3(\mu^2,\Lambda^2_{\rm cut})}{Z_3(\nu^2,\Lambda^2_{\rm cut})}\frac{1}{\mathcal{G}l(p^2,\nu^2)},\\
&= \frac{Z_3|_{\mu^2}}{Z_3|_{\nu^2}}\left[Z_3|_{\nu^2} + Z_1(\nu^2,\Lambda^2_{\rm cut})\Pi_{2g}(p^2,\nu^2)\right] + \tilde{Z}_1(\nu^2,\Lambda^2_{\rm cut})\Pi_{2c}(p^2,\nu^2),\\
&= Z_3|_{\mu^2} + \frac{Z_g^2 Z_3^3}{Z_1}\left|_{\mu^2}\frac{Z_1^2}{Z_g^2 Z_3^3}\right|_{\nu^2}\Pi_{2g}(p^2,\mu^2) + \frac{Z_g^2\tilde{Z}_3^2 Z_3}{\tilde{Z}_1}\left|_{\mu^2}\frac{\tilde{Z}_1^2}{Z_g^2\tilde{Z}_3^2 Z_3}\right|_{\nu^2}\Pi_{2c}(p^2,\mu^2),\\
&= Z_3(\mu^2,\Lambda^2_{\rm cut}) + Z_1(\mu^2,\Lambda^2_{\rm cut})\Pi_{2g}(p^2,\mu^2) + \tilde{Z}_1(\mu^2,\Lambda^2_{\rm cut})\Pi_{2c}(p^2,\mu^2),
\end{aligned}$$

as required. The ghost loop term is consistent with $\mathcal{O}(1) \sim \mathcal{O}(\mathcal{G}h/\mathcal{G}h)$ ghost-gluon vertex dressings as in the ghost equation. The gluon loop comes with a factor Z_1 which may be cancelled by a triple-gluon dressing $\mathcal{O}(\mathcal{G}h/\mathcal{G}l)$. Dressings of this form are also suggested by the Ward-Slavnov-Taylor identity for this vertex which we shall consider later. Inserting a term proportional to $\mathcal{G}h/\mathcal{G}l$ in Π_{2g} and using relation eq. (4.17) the Z_1 becomes $\tilde{Z}_1$ which in a carefully chosen subtraction scheme in Landau gauge is remarkably simple, $\tilde{Z}_1 = 1$ [94]. This is particularly convenient since the only renormalisation constants that then appear are Z_3 and $\tilde{Z}_3$ which are be removed by subtraction. It is however straightforward to calculate the Z's, either perturbatively as we do in the next section or from the numerical procedure which we apply later.

4.1.2. Leading Perturbative Behaviour

The truncated SDEs, using tree level vertices, for the ghost and gluon are given in eq. (4.22) and eq. (4.28) respectively. In order to calculate the one-loop perturbative results, we simply insert $\mathcal{G}l(p^2) = 1$ and $\mathcal{G}h(p^2) = 1$ on the right of both equations. The loop integration may then be performed using a variety of methods, using some kind of regulator to control the divergences, either by performing the integrals in $d = 4 - 2\epsilon$ dimensions or by limiting the integration volume to a hypersphere contained within some volume $\ell < \Lambda_{\rm cut}$. Using the latter method, the leading perturbative results for each of the

loops are,

$$\int^{\Lambda_{\rm cut}} d^4\ell\, \mathcal{K}(p,\ell) = -\frac{3\pi}{16}\left(1 - 2\log\frac{p^2}{\Lambda_{\rm cut}^2} + \mathcal{O}(p/\Lambda_{\rm cut})^2\right), \tag{4.34}$$

$$\int^{\Lambda_{\rm cut}} d^4\ell\, \mathcal{M}(p,\ell) = \frac{\pi}{48}\left(13 - 12\log\frac{p^2}{\Lambda_{\rm cut}^2} + \mathcal{O}(p/\Lambda_{\rm cut})^2\right), \tag{4.35}$$

$$\int^{\Lambda_{\rm cut}} d^4\ell\, \mathcal{Q}(p,\ell) = -\frac{7\pi}{24}\left(7 - 12\log\frac{p^2}{\Lambda_{\rm cut}^2} + \mathcal{O}(p/\Lambda_{\rm cut})^2\right). \tag{4.36}$$

At leading order in perturbation theory these are solved to give the unrenormalised dressing functions for the gluon and ghost dressing functions as,

$$\mathcal{G}h(p^2,\Lambda_{\rm cut}^2)^{-1} = 1 - \frac{g^2 N_c}{(2\pi)^3}\frac{3\pi}{16}\left(1 - 2\log\frac{p^2}{\Lambda_{\rm cut}^2}\right), \tag{4.37}$$

$$\mathcal{G}l(p^2,\Lambda_{\rm cut}^2)^{-1} = 1 - \frac{1}{d-1}\frac{g^2 N_c}{(2\pi)^3}\frac{\pi}{48}\left(85 - 156\log\frac{p^2}{\Lambda_{\rm cut}^2}\right). \tag{4.38}$$

Using the momentum subtraction scheme to renormalise, this leads to,

$$\mathcal{G}h(p^2,\mu^2)^{-1} = \mathcal{G}h(\mu^2,\mu^2)^{-1} + \frac{g^2(\mu^2)N_c}{(4\pi)^2}\frac{3}{4}\log\frac{p^2}{\mu^2}, \tag{4.39}$$

$$\mathcal{G}l(p^2,\mu^2)^{-1} = \mathcal{G}l(\mu^2,\mu^2)^{-1} + \frac{g^2(\mu^2)N_c}{(4\pi)^2}\frac{1}{d-1}\frac{13}{2}\log\frac{p^2}{\mu^2}. \tag{4.40}$$

This implicitly defines the renormalisation constants given above, setting the dimensions $d = 4$ and using Taylor's condition, $\tilde{Z}_1 = 1$ [94],

$$Z_3(\mu^2,\Lambda_{\rm cut}^2) = 1 - \frac{N_c g(\mu^2)^2}{(4\pi)^2}\frac{13}{6}\log\left(\frac{\mu^2}{\Lambda_{\rm cut}^2}\right) + \mathcal{O}(g^4), \tag{4.41}$$

$$\tilde{Z}_3(\mu^2,\Lambda_{\rm cut}^2) = 1 - \frac{N_c g(\mu^2)^2}{(4\pi)^2}\frac{3}{4}\log\left(\frac{\mu^2}{\Lambda_{\rm cut}^2}\right) + \mathcal{O}(g^4), \tag{4.42}$$

$$Z_1(\mu^2,\Lambda_{\rm cut}^2) = \frac{Z_3}{\tilde{Z}_3} = 1 - \frac{N_c g(\mu^2)^2}{(4\pi)^2}\frac{17}{12}\log\left(\frac{\mu^2}{\Lambda_{\rm cut}^2}\right) + \mathcal{O}(g^4). \tag{4.43}$$

These results for the propagator dressing functions can be improved by going beyond fixed-order in perturbation theory to resum the leading-logarithms. This is what the SDE solutions should give in the small coupling limit. The general method can be found in ref. [4] and various standard texts. The starting point is the renormalisation group

equation,

$$\frac{d}{d\log\mu}\mathcal{G}l(p^2,\mu^2) = \gamma_0(g)\mathcal{G}l(p^2,\mu^2) \tag{4.44}$$

where γ_0 is the important quantity that may be obtained using the 1-loop results given above and μ is an arbitrary renormalisation point. This equation is solved in a straightforward manner by integrating,

$$\int \frac{d\mathcal{G}l(p^2,\mu^2)}{\mathcal{G}l(p^2,\mu^2)} = \int d\log\mu\,\gamma_0(g). \tag{4.45}$$

The usual method is to use the QCD β function that relates the variation of the coupling with the momentum scale. Typically this is expanded in a series in g, the coefficients β_i are then calculable from perturbation theory,

$$\frac{dg}{d\log\mu} = \beta(g) \tag{4.46}$$

$$= -\beta_0 g^3 - \beta_1 g^5 - \mathcal{O}(g^7). \tag{4.47}$$

Using this, equation eq. (4.45) then becomes,

$$\int \frac{d\mathcal{G}l(p^2,\mu^2)}{\mathcal{G}l(p^2,\mu^2)} = \int dg\,\frac{\gamma_0(g)}{\beta(g)}. \tag{4.48}$$

Performing the integration on the left and exponentiating leads to,

$$\mathcal{G}l(p^2,\mu^2) = \mathcal{G}l(\mu^2,\mu^2)\exp\left(\int_{g(\mu^2)}^{g(p^2)} dg\,\frac{\gamma_0(g)}{\beta(g)}\right), \tag{4.49}$$

which is solvable using the expansion for $\beta(g)$. Since the function $\gamma_0(g)$ may be expanded in the coupling g then this relation goes beyond leading order. The factor $\gamma_0(g)$ may then be found using eq. (4.45),

$$\gamma_0(g) = \frac{1}{\mathcal{G}l(p^2,\mu^2)}\frac{d}{d\log\mu}\mathcal{G}l(p^2,\mu^2) \tag{4.50}$$

$$= 13\frac{g^2(\mu^2)N_c}{(4\pi)^2}\frac{1}{d-1} + \mathcal{O}(g^3) \tag{4.51}$$

inserting into eq. (4.49) gives,

$$\mathcal{G}l(p^2,\mu^2) = \mathcal{G}l(\mu^2,\mu^2)\left(\frac{g^2(p^2)}{g^2(\mu^2)}\right)^{[-\frac{13N_c}{2(4\pi)^2(d-1)\beta_0}]} \tag{4.52}$$

the coefficient β_0 that we require is most straightforwardly calculated using eq. (4.15) using the Landau gauge condition $\tilde{Z} = 1$ and the Z_3 factors as implicitly defined by the renormalisation in eq. (4.40) and eq. (4.39), in the abscence of quarks it is,

$$\beta_0 = \frac{11N_c}{3(4\pi)^2}. \tag{4.53}$$

The ratio of running couplings at different renormalisation points is also required at this order, using $\alpha(\mu^2) = g^2(\mu^2)/4\pi$ then,

$$\frac{\alpha(p^2)}{\alpha(\mu^2)} = \left(1 + \frac{11}{12\pi}N_c\alpha(\mu^2)\log\frac{p^2}{\mu^2}\right)^{-1}. \tag{4.54}$$

Inserting this and replacing the square bracket with the constant γ gives the final expression,

$$\mathcal{G}l(p^2,\mu^2) = \mathcal{G}l(\mu^2,\mu^2)\left(1 + \frac{11}{12\pi}N_c\alpha(\mu^2)\log\frac{p^2}{\mu^2}\right)^{\gamma}. \tag{4.55}$$

Applying the same analysis to the ghost equation where the only real difference are the different factors in eq. (4.39), leads to,

$$\mathcal{G}h(p^2,\mu^2) = \mathcal{G}h(\mu^2,\mu^2)\left(1 + \frac{11}{12\pi}N_c\alpha(\mu^2)\log\frac{p^2}{\mu^2}\right)^{\delta}, \tag{4.56}$$

where δ is the equivalent of the constant γ that arises in the gluon analysis. These are the forms that should match to the full SDE solutions at large momenta. The exponents are sometimes referred to as anomalous dimensions and their values are,

$$\gamma = -13/22, \tag{4.57}$$

$$\delta = -9/44. \tag{4.58}$$

These appear in the next section in the vertex dressings and are used in the numerical procedure when extrapolation is required in the UV.

4.2. Initial Studies

The first full solutions obtained in quarkless QCD using full angular integrations found solutions belonging to the 'Type 1' or 'Scaling' category [84, 85], this followed from a thorough analysis in the infrared region [95] where self-consistent power law solutions were obtained with the form,

$$\lim_{p^2\to 0} \mathcal{G}l\left(p^2\right) = \left(p^2\right)^{2\kappa} \tag{4.59}$$

$$\lim_{p^2\to 0} \mathcal{G}h\left(p^2\right) = \left(p^2\right)^{-\kappa} \tag{4.60}$$

where $\kappa > 0$ and whose value can be restricted by comparing the values simultaneously allowed by the ghost and gluon equations. In order to solve the Schwinger–Dyson equations for the ghost and gluon propagators, and indeed, to do the infrared analysis, some inputs for the vertices are required. Sensible choices for ghost-gluon and triple-gluon vertices are essential since they can dictate whether solutions are present, the type of solutions present, and a poor choice may lead to a lack of solutions or unphysical solutions. In this initial study we will neglect terms containing the four-gluon vertex and consider the triple-gluon and ghost-gluon vertices only. This truncation for the gluon propagator may be represented diagrammatically as shown in figure 4.4.

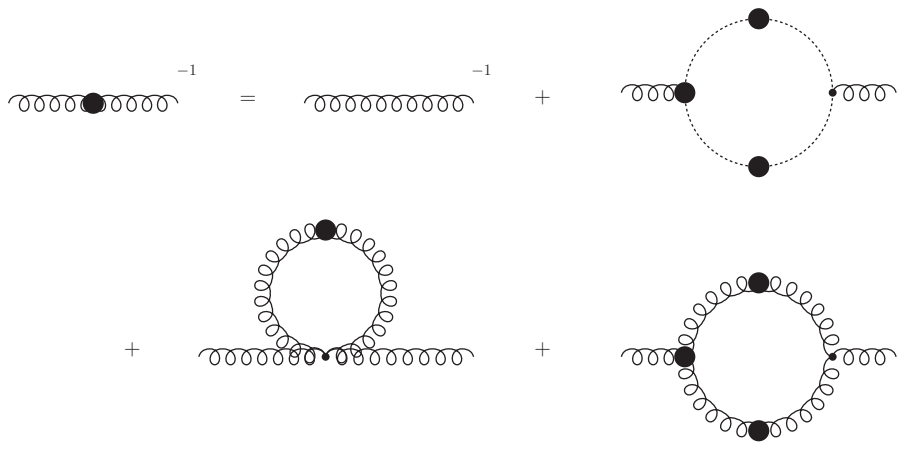

Figure 4.4.: The terms that we consider in the Gluon propagator Schwinger–Dyson Equation.

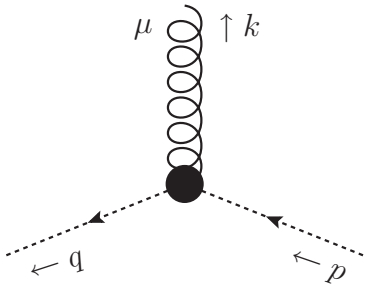

Figure 4.5.: The Ghost-Ghost-Gluon vertex, using a $k = p - q$ momentum definition.

4.2.1. Ghost-Gluon Vertex

This truncation uses the tree-level ghost-gluon vertex,

$$\Gamma^{abc}_{\mu}(k,p,q) \to \Gamma^{(0)\,abc}_{\mu}(k,p,q) = igf^{abc}q_{\mu} \tag{4.61}$$

which at first sight seems like an over-simplification since this cannot be correct even at one-loop level for the vertex [96, 97]. However, it is expected that the ghost-gluon vertex should be relatively simple in the Landau gauge due to a non-renormalisation theorem [94] which is valid in carefully chosen renormalisation schemes [98]. The full vertex is also expected to reduce to its bare form for vanishing incoming ghost momenta [94, 95, 98],

$$\lim_{p\to 0}\Gamma^{abc}_{\mu}(k,p,q) = \Gamma^{(0)\,abc}_{\mu}(k,p,q). \tag{4.62}$$

Reference [95] also suggests that the vertex should be bare in the symmetric limit,

$$\lim_{k^2=p^2=q^2}\Gamma^{abc}_{\mu}(k,p,q) = \Gamma^{(0)\,abc}_{\mu}(k,p,q) \tag{4.63}$$

however this is refuted in ref [98]. The bare vertex appears to be a sensible starting point, so the forms given by eq. (4.22) and eq. (4.23) are used in this initial study, according to ref. [85].

4.2.2. Triple-Gluon Vertex

The triple-gluon vertex does not have any simple restrictions like the ghost-gluon vertex, it does however have a high degree of bose-symmetry due to only gluons being present. In general the loop corrections significantly alter the Lorentz structure compared to the

bare vertex, as can be seen from solutions to the Ward-Slavnov-Taylor Identity [99–101] however initially, we use the simplified form since we wish to study the solutions of refs. [84, 85]. The dressing used in this initial study is motivated by reproducing the resummed one-loop gluon running in the perturbative region and leaving the IR essentially the same[2] as the bare vertex since the dressing returns a constant [85]. The form used is,

$$\Gamma^{abc}_{\mu\nu\rho}(k,p,q) = \frac{1}{Z_1(\mu^2,\Lambda^2_{\rm cut})}\Gamma^{(0)\,abc}_{\mu\nu\rho}(k,p,q)\frac{\mathcal{G}h(p^2)^{1-a/\delta-2a}}{\mathcal{G}l(p^2)^{1+a}}\frac{\mathcal{G}h(q^2)^{1-b/\delta-2b}}{\mathcal{G}l(q^2)^{1+b}}, \tag{4.64}$$

where a and b are arbitrary parameters. The choice $a = b = 3\delta$ with δ the 1-loop ghost anomalous dimension is often applied. Another choice is $a = b = 0$, this is used in other truncations motivated by arguments for multiplicative renormalisability [83]. These can be seen as some sort of minimal dressing that results in the correct one–loop running [85]. Reproduction of the correct running is independent of the arbitrary parameters a and b however the IR behaviour of the solutions is dependent upon their values.

The equation that we then wish to solve is given by eq. (4.28) with an additional factor under the integral,

$$\begin{aligned}\mathcal{G}l(p^2,\mu^2)^{-1} =& Z_3(\mu^2,\Lambda^2_{\rm cut})\\ &+\tilde{Z}_1(\mu^2,\Lambda^2_{\rm cut})\frac{g^2(\mu^2)N_c}{(d-1)}\int\frac{d^d\ell}{(2\pi)^d}\mathcal{G}h(\ell^2_+,\mu^2)\mathcal{G}h(\ell^2_-,\mu^2)\mathcal{M}(p,\ell,\zeta)\\ &+\frac{g^2(\mu^2)N_c}{(d-1)}\int\frac{d^d\ell}{(2\pi)^d}\frac{\mathcal{G}h(\ell^2_+,\mu^2)^{1-a/\delta-2a}}{\mathcal{G}l(\ell^2_+,\mu^2)^a}\frac{\mathcal{G}h(\ell^2_-,\mu^2)^{1-b/\delta-2b}}{\mathcal{G}l(\ell^2_-,\mu^2)^b}\mathcal{Q}(p,\ell,\zeta),\end{aligned} \tag{4.65}$$

where $\mathcal{M}$ and $\mathcal{Q}$ are defined as in eq. (4.30) and eq. (4.31) respectively. It is noted [83], that this form violates multiplicative renormalisability with $a \neq 0 \neq b$,[3] but it does reproduce the one-loop perturbative running for QCD as can be shown by a large-p^2 power matching analysis [85].

4.2.3. Quadratic Divergences

In a perturbative calculation, we sum a series of diagrams that have divergences that cancel between the individual terms only at the end of the calculation. In general, only when all of the diagrams at the relevant order in g have been accounted for, do we have a

[2] However, only for $a = b = 3\delta$.

[3] In [83] multiplicative renormalisability appears to be satisfied but the renormalisation must be done differently since Z_1^2 and $\tilde{Z}_1^2$ factors multiply the bare loops.

physically meaningful result. At intermediate steps, individual diagrams contain quadratic divergences, terms that are like $\frac{\Lambda^2}{p^2}$ if Λ is a cutoff regulator, and these are unphysical. The coefficients of these terms from different diagrams add to zero leaving the leading large-p^2 behaviour logarithmically divergent or possibly even finite, which after renormalisation indicates the presence of terms $\sim \log \frac{p^2}{\mu^2}$ at worst [3].

The same problem also exists in Schwinger–Dyson studies except now there is no simple counting in g to which we can resort. Only in a full treatment, where all diagrams are considered without approximation, can we be certain that the quadratic divergences will be properly cancelled amongst the separate terms. There have been efforts made to restructure the SDEs such that these cancellations are made explicit and an elegant solution has been found [102, 103], however this method is restricted to a different gauge so we do not consider it at present.

There are two broad classes of solution to this problem that exist at present in the literature. The most natural way is to remove the quadratic divergences by using $\zeta = d$ in the projector. This works because the quadratic divergences are always proportional to $g^{\mu\nu}$ and the $p^\mu p^\nu$ term is only logarithmically divergent [83, 104–106]. The other class of solution involves performing the integral and subtracting the piece that goes as $\frac{\Lambda^2}{p^2}$, either by introducing a type of counter-term [84, 85] or by identifying the coefficient of p^{-2} in the polarisation function in the small-p^2 limit and removing this same contribution for all momenta [107]. It is not clear how the second class of solution, using some kind of subtraction of the quadratic divergences, will affect the subleading behaviours of the integrals, particularly since it is performed after integration.

In this initial study we are forced to use $\zeta = 1$ and subtract the quadratic divergences separately in order to reproduce the original scaling solutions [84, 85]. Sensitivitity to ζ is intimately linked with the correct removal of the quadratic divergences and transversality and shall be investigated in the numerical solution of the equations.

4.2.4. Small-p^2 Analyses

A miraculous feature of the SDEs of QCD is that they can be solved exactly when the external momenta p^2 is very small. This is interchangeably referred to as the infrared (IR) limit. A leading power scaling is assumed and self–consistent powers for the Ghost and Gluon dressings may be identified. This happens to work because the integrands are

sharply peaked around the external momentum scale so these scales, and the behaviour of the dressings at these scales, tend to dominate the result.

The assumption usually made is as in eqs. (4.59 and 4.60),

$$\mathcal{G}l(p^2) = A(p^2)^a \tag{4.66}$$

$$\mathcal{G}h(p^2) = B(p^2)^b \tag{4.67}$$

The strongest constraints are obtained from the ghost equation and results in the two types of solution. We first require the integral,

$$\int \frac{d^dq}{(2\pi)^d}\left(\frac{1}{q}\right)^{d/2}\left(\frac{q^2}{k^2}\right)^{\alpha}\left(\frac{k^2}{p^2}\right)^{\beta} = \frac{1}{2^d\pi^{d/2}}\frac{\Gamma(\alpha)\Gamma(\frac{d}{2}-\beta)\Gamma(\beta-\alpha)}{\Gamma(\beta)\Gamma(\frac{d}{2}-\alpha)\Gamma(\frac{d}{2}-\alpha-\beta)}. \tag{4.68}$$

In eq.(4.22), substituting eqs. (4.66 and 4.67), and using eq. (4.68) to perform the integrations, the result is [85],

$$\frac{1}{B(p^2)^b} = \tilde{Z}_3 - (p^2)^{a+b}\frac{g^2N_cAB}{16\pi^2}\frac{3}{2(a+b)(a+b-1)}\frac{\Gamma(2-a-b)\Gamma(1+a)\Gamma(2+b)}{\Gamma(3+a+b)\Gamma(2-a)\Gamma(1-b)}, \tag{4.69}$$

then powers of p^2 are matched, and if the renormalisation constant $\tilde{Z}_3$ is neglected then the requirement that $a = -2b$ is obtained. This forms the basis for searching for the type 1, scaling solutions. A natural consequence of this is that the most natural definition of the non-perturbative running coupling in the IR goes to some finite non-zero value. The most commonly used definition in the ghost-gluon sector is,[4]

$$\alpha(p^2) = \frac{g_0^2}{4\pi}\mathcal{G}h^2(p^2)\mathcal{G}l(p^2), \tag{4.70}$$

this combination of dressings and the requirement $a = -2b$ automatically results in a constant coupling in the IR. A common exponent $a = 2\kappa$ and $b = -\kappa$ is assigned which gives the forms in eqs. (4.59 and 4.60).

A similar procedure can then be carried out on both the gluon and ghost equation simultaneously to restrict the value of κ, except now the coefficients of the leading powers are considered. The coefficients are obtained again by using eq. (4.68) to obtain functions of κ and values where simultaneous solutions to the ghost and gluon may be identified, see

[4] In fact, any of the vertices of the theory may be used to define the running coupling, and whilst perturbatively they all must be identical, non-perturbatively different results can be obtained. It is not clear at present if this is soley due to incomplete truncations.

Refs. [83, 85] for full details. A function $\chi_i(\kappa)$ is identified for each equation and values where these cross in fig. 4.6 correspond to values that simultaneously solve the equations. The results shown do not in fact depend on the gluon loop since in this truncation its contribution vanishes in the $p^2 \to 0$ limit.

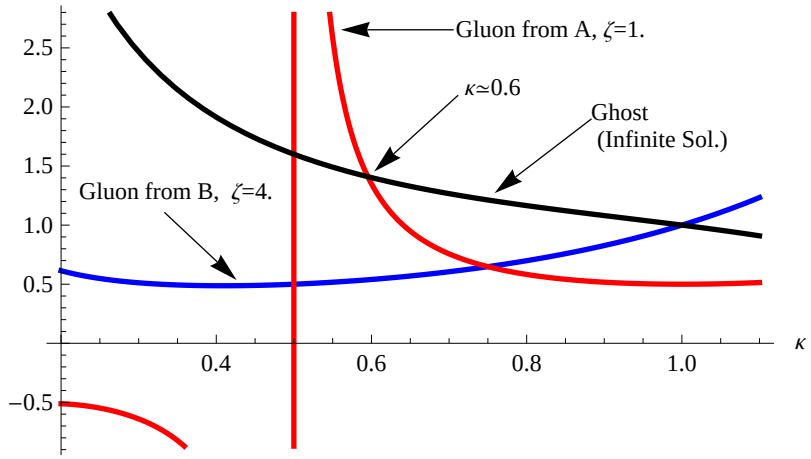

Figure 4.6.: The results of the IR scaling anaysis [83, 84].

Various analyses have come up with a range of values for κ, but we consider in this initial study $\kappa \simeq 0.595$ [84, 85, 95]. In order to remove the quadratic divergence, a counter-term is added to the gluon loop, this is because the IR analysis is dominated by the ghost loop and such a subtraction leaves the ghost loop IR behaviour unaffected.[5]

This is in good agreement with theoretical arguments given by the Kugo-Ojima [108] and Gribov-Zwanziger [109–113] confinement scenarios that predict a singular ghost and a vanishing gluon at vanishing momentum.

4.2.5. Numerical Results and Analysis

It is not possible at present to solve these equations analytically for all momenta for a number of reasons, predominantly due to the products of unknown functions $\mathcal{G}l$ and $\mathcal{G}h$ under the integrals. Therefore we resort to a numerical procedure as outlined in appendix C. The dressing functions are iterated until the inputs and the outputs are consistent with each other. In figure 4.7, we plot the self-consistent solutions found from the $\zeta = 1$

[5] The $\kappa = 1$ IR solution for $\zeta = 4$ has also been investigated, however the numerical procedure has been unable to produce solutions connecting this to the correct perturbative behaviour, it is likely that no solutions exist and this is a solution of the IR equations only.

version of the gluon equation, we also plot the result of using $\zeta = d$, starting from the $\zeta = 1$ solution as input, and iterating just the gluon until convergence.

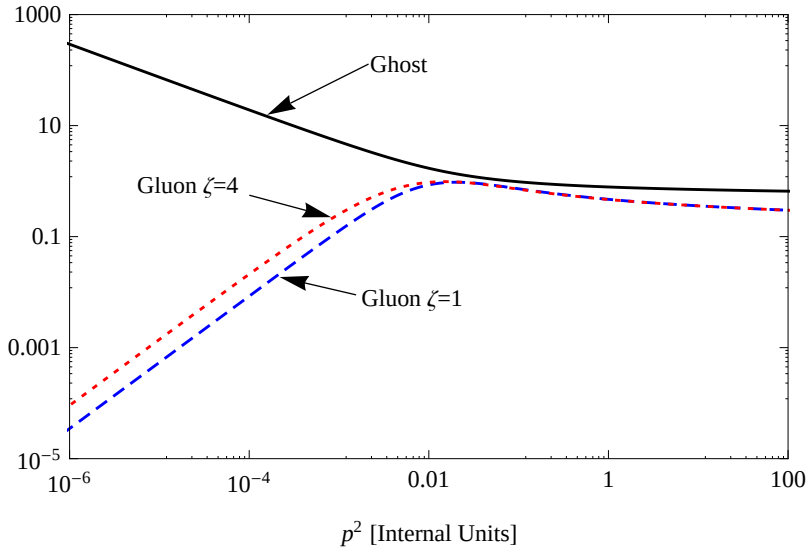

Figure 4.7.: The Scaling Solutions. Black: Ghost dressing consistent with $\zeta = 1$ Gluon. Blue, dashed: Gluon solved using $\zeta = 1$ with additional cancellation of the quadratic divegence. Red, dotted: Gluon solved using $\zeta = d$ which naturally removes the quadratic divergences.

We notice that the gluon is not that different with either $\zeta = 1$ or $\zeta = d$, however, crucially, in this truncation if the $\zeta = d$ projector is used then no solutions can be found that simultaneously satisfy both the ghost and gluon SDEs. The solutions disappear altogether. This difference between $\zeta = 1$ and $\zeta = d$ is of fundamental importance since it points to gauge invariance being broken in these solutions, since the propagator is no longer transverse. This was to be expected, since the IR analysis does not find solutions for $\zeta = d$, this is because there is an improperly cancelled quadratic divergence in the ghost-loop. This is present even as $p^2 \to 0$ and produces a pole at $\kappa = 0.5$ in the gluon IR analysis, this corresponds to a term $\sim p^2$ in the function $\mathcal{G}l$. This pole naturally induces a rapid variation which results in the ghost IR function and gluon IR function having a common IR solution close to $\kappa = 0.5$.

When we do perturbation theory and we calculate the g^2 corrections to the gluon propagator we find that each term from each diagram may be written in the form $Ag_{\mu\nu} + B\frac{p_\mu p_\nu}{p^2}$. Looking a little closer, we find that the A term contains quadratic divergences in the individual contributions that later vanish when we sum the diagrams at this order in the perturbative series. The B term has no such cancellation, the terms simply add together with the expected logarithmic UV divergences. Working in Landau gauge where

the Gluon is transverse, in the end when we take the sum of the diagrams we must find $A = -B$ if transversality is to be upheld. The full inverse Gluon propagator in general covariant gauge in this notation is given by,

$$D^{-1}_{\mu\nu}(p) = A(p^2)p^2 g_{\mu\nu} + \left(B(p^2) + \frac{1}{\xi}\right) p_\mu p_\nu \tag{4.71}$$

since we know that $A = -B$ in a full treatment it would make no difference whether we determined our Gluon propagator dressing from A, B or some admixture of the two. However, since quadratic divergences are present then we must determine our Gluon using the B term since we cannot know *a priori* how these behave in the strongly coupled sector which we are interested in. The A term can be trivially determined from the Gluon dressing that is found from the B term and any difference when this substituted into the Schwinger–Dyson Equation for the A term can be assigned to the quadratic divergences.

We can see that this must be present from the IR analysis of [84], as has been noted previously [83], see figure 4.6. The improperly cancelled quadratic divergence does exactly what would be expected, it gives a pole at $\kappa = 0.5$ resulting from a residual term proportional to p^2 in $\mathcal{G}l(p^2)$, which is just the term from Π_{2c} that goes as $\Lambda_{\rm cut}/p^2$. The difference between the curve A, and the B determined curve is just the quadratic divergence. Moreover, we also know that this cannot be gauge invariant if $A \neq -B$ since in Landau gauge the Gluon propagator has to be transverse. We intend to avoid this problem by determining our Gluon propagator dressing function from the B term, our Gluon propagator is thus,

$$D^{-1}_{\mu\nu}(p) = \frac{p^2}{\mathcal{G}l(p^2)}\left(g_{\mu\nu} - \frac{p_\mu p_\nu}{p^2}\right) + \frac{p_\mu p_\nu}{\xi} \tag{4.72}$$

where $\mathcal{G}l(p^2) = -1/B(p^2)$. This procedure clearly results in a Landau gauge Gluon propagator that is automatically transverse. The relevant Gluon components may then be projected from the general tensor equation by setting the parameter $\zeta = d$, the number of dimensions in which we operate,

$$\mathcal{P}_{\mu\nu}(p, d) = g_{\mu\nu} - d\frac{p_\mu p_\nu}{p^2} \tag{4.73}$$

where p is the external momenta and $d = 4$ is the number of dimensions in which we work. This consistently selects the B term for our iterations, protecting us from the quadratic divergences.

We note that improvements to the scaling solutions have been made by considering the allowed extensions to the vertex structure and using smoothed step functions to switch between desired IR and UV behaviours, however the solutions obtained are identical to those presented here, within numerical tolerances [86]. Since the IR analysis forces the gluon to break transversality, then we do not consider this to be a reliable truncation. We now focus upon producing solutions using $\zeta = d$ only.

4.3. Investigating Vertex Extensions

Our intention is to construct a minimally solvable truncation for the Schwinger–Dyson Equations of QCD, that has a transverse gluon, is gauge invariant and respects the perturbative limit. The aim is to find a simple starting point from which natural extensions, such as the corrections induced from additional diagrams, may be incorporated. Through considerable effort we have been unable to find a transverse gluon solution using bare vertices, those obtained from tree-level perturbation theory. This is not surprising since those vertices do not respect gauge invariance or the Ward-Slavnov-Taylor Identities (WSTI). Our starting point will be to consider simple extensions for the ghost-ghost-gluon and triple-gluon vertices.

4.3.1. Ghost Equation

The Ghost Equation is very simple compared with the Gluon Equation and it is also more robust, likely due to the fact that it requires fewer assumptions. It depends on only three unknown functions, two of which are the Ghost and Gluon dressing functions which we intend to determine. The third is the vertex dressing function which in full generality is given by,

$$\Gamma^{abc}_{\mu}(k,p,q) = igf^{abc}\left(q_{\mu}\alpha(k,p,q) + k_{\mu}\beta(k,p,q)\right) \tag{4.74}$$

however, the β term drops out of the calculation in this loop, and the α term is expected to be $\mathcal{O}(1)$ for the same reasons given in section 4.2. This suggests using a bare form for the vertex with $\beta = 0$ and $\alpha = 1$, however this may be insufficient when included in the gluon equation; the β term can be important there [95]. We postpone discussion of this here since it has no consequences in this equation.

4.3.2. Gluon Equation

In order to keep things simple, we consider only the dressed one-loop diagrams and neglect the contributions from the dressed two-loop diagrams at this time. The one-loop tadpole graph contains a bare four-gluon vertex, but this completely drops out when we use the projector with $\zeta = d$ since it only contributes to the $g_{\mu\nu}$ term in the propagator. It is thought that the three-gluon and ghost-gluon vertices in the remaining one-loop graphs contribute the dominant part of the non-abelian theory in the IR and it is clear that in the UV perturbation theory at leading order requires only the one-loop graphs. The intermediate region is expected to be most affected by these terms, particularly in situations where the gluon dressing becomes large with respect to the ghost. Unfortunately, unless the gluon dressing is heavily suppressed in the IR and the vertices are not enhanced there, then there are no expansions or power counting schemes for dropping these terms; their effects must be included in order to obtain any reliable results the gluon propagator dressings. This approximation is considerably more severe than inserting modelled vertices into the equations since sensitive cancellations can occur between the terms in the SDE itself, for an individual Green's function. This can result in the dressing functions having unphysical properties, for example a sign change or pole, which does not happen when we use a sensibly modelled Green's function. However, the starting point of any analysis must be to address the one-loop diagrams and then, if necessary, the two-loop terms can also be considered.

Triple–Gluon Vertex

The triple-gluon vertex dressing used in the previous section was chosen such that it reproduced the perturbative one-loop running. We would like to go back a step and investigate simple vertices that satisfy the bose symmetry and also forms that are either inspired by, or exact solutions of, the Ward-Slavnov-Taylor identity (WSTI). A completely bare triple-gluon vertex is insufficient, so we only consider dressed vertices that usually include ratios of dressing functions.

The WSTI for the triple-gluon vertex [99, 101, 114–116],

$$ik_\rho\Gamma_{\mu\nu\rho}(k,p,q) = \mathcal{G}h(k^2)\Bigg\{\tilde{\Gamma}_{\mu\nu}(-p;q,k)\left(g_{\mu\rho}-\frac{q_\mu q_\rho}{q^2}\right)\frac{q^2}{\mathcal{G}l(q^2)} \\ -\tilde{\Gamma}_{\mu\rho}(q;-p,k)\left(g_{\nu\mu}-\frac{p_\nu p_\mu}{p^2}\right)\frac{p^2}{\mathcal{G}l(p^2)}\Bigg\}, \tag{4.75}$$

may be used by applying several approximations. The momentum convention for the triple gluon vertex is that all momenta are outgoing, however the ghost-gluon scattering kernel $\tilde{\Gamma}_{\mu\nu}$ is defined from the ghost-gluon vertex which has a different convention ($k = p-q$). In the absence of any ghost corrections, we can set the dressing $\mathcal{G}h \to 1$, and the ghost-gluon scattering kernel $\tilde{\Gamma}_{\mu\nu} = g_{\mu\nu}$. This yields vertex corrections of the form $1/\mathcal{G}l$. Without solving anything exactly, corrections of this form may be applied since the high degree of symmetry for this vertex is already quite restrictive. It is useful to test a variety of forms since the results shouldn't be too sensitive given a range of sensibly chosen vertices and also since the truncation in general does not give good control over the errors. The following forms and their effects on the equations will be tested, the first are two similar symmetric forms we may guess that require little additional work from the bare vertex,

$$\Gamma^{abc}_{\mu\nu\rho}(k,p,q) = \frac{1}{3}\left(\frac{1}{\mathcal{G}l(k^2)}+\frac{1}{\mathcal{G}l(p^2)}+\frac{1}{\mathcal{G}l(q^2)}\right)\Gamma^{(0)abc}_{\mu\nu\rho}(k,p,q), \tag{4.76}$$

$$\Gamma^{abc}_{\mu\nu\rho}(k,p,q) = \frac{1}{3}\left(\frac{\mathcal{G}h(k^2)}{\mathcal{G}l(k^2)}+\frac{\mathcal{G}h(p^2)}{\mathcal{G}l(p^2)}+\frac{\mathcal{G}h(q^2)}{\mathcal{G}l(q^2)}\right)\Gamma^{(0)abc}_{\mu\nu\rho}(k,p,q). \tag{4.77}$$

The second form is a little closer to the full solution, and setting the dressing functions to 1 gives the bare form, which we know works in the perturbative region, various cyclic combinations may be tested provided that they satisfy the symmetry for the vertex. For example,

$$\Gamma^{abc}_{\mu\nu\rho}(k,p,q) = igf^{abc}\times \\ \left(g_{\mu\nu}(k-p)_\rho\frac{\mathcal{G}h(q^2)}{\mathcal{G}l(p^2)}+g_{\nu\rho}(p-q)_\mu\frac{\mathcal{G}h(k^2)}{\mathcal{G}l(q^2)}+g_{\rho\mu}(q-k)_\nu\frac{\mathcal{G}h(p^2)}{\mathcal{G}l(k^2)}\right). \tag{4.78}$$

The full solution at this level of truncation depends additionally on the solution of the WSTI for the ghost-gluon vertex since this tells us something about the ghost-gluon scattering kernel, $\tilde{\Gamma}_{\mu\nu}$.

The vertex used in the initial study eq. (4.64) with the parameters $a = 0$ and $b = 0$ corresponds to a multiplicatively renormalisable form used elsewhere [83]. This leads to the curious property that the gluon equation does not depend on the gluon dressing function directly, the dependence arises only through coupling to the ghost equation via the ghost dressing function. The key property of this vertex is that it should reproduce the correct running for the gluon equation since this is enforced in its derivation by matching powers on either side of the gluon equation in a large-p^2 expansion. A generalisation is considered [86], that is intended for the finite ghost (type 2) solutions,

$$\Gamma^{abc}_{\mu\nu\rho}(k,p,q) = \Gamma^{(0)\,abc}_{\mu\nu\rho}(k,p,q)\left(\frac{\mathcal{G}h(p^2+\Lambda^2_{\rm dec})\mathcal{G}h(q^2+\Lambda^2_{\rm dec})}{\mathcal{G}l(p^2+\Lambda^2_{\rm dec})\mathcal{G}l(q^2+\Lambda^2_{\rm dec})}\right) \tag{4.79}$$

where $\Lambda_{\rm dec}$ is some 'decoupling' scale where the dressings freeze out. Practically, this tames large contributions from the $1/\mathcal{G}l$ terms as the momenta become small. This vertex does not have the bose symmetry between the legs as at the tree level, the momenta corresponding to the dressed terms are meant to be those that participate in the loop integration. This vertex dressing becomes bare in the IR so can be thought of as a minimal dressing required to reproduce the 1-loop results. Whether the bare form in the IR is the correct choice is an open question, however the WSTI solutions suggest otherwise, since these vertices typically give a finite contribution at vanishing momenta.

Ghost–Gluon Vertex

The Ghost–Gluon Vertex is relatively simple in Landau gauge, its renormalisation constant $\tilde{Z}_1$ is always finite and in the $\overline{MS}$ renormalisation scheme or a momentum subtraction scheme where the incoming ghost momentum is set to zero the vertex receives no renormalisation at all, hence $\tilde{Z}_1 = 1$. In other schemes that do not subtract at vanishing incoming ghost momentum, such as a symmetric point ($k^2 = p^2 = q^2$), this may not be the case and the dressing may receive some finite renormalisation [94, 98, 117, 118]. The vertex reduces to its bare form for the vanishing incoming ghost momentum limit. It must also reduce to its bare form at very high energies when the perturbative expansion is valid.

Primarily for these reasons, the bare form has often been used, we find however that this is insufficient, and self-consistent solutions for all momenta do not exist. In general the

full ghost-gluon vertex has the structure,

$$\Gamma^{abc}_{\mu}(k,p,q) = igf^{abc}\left[q_\mu\alpha(k,p,q) + k_\mu\beta(k,p,q)\right] \tag{4.80}$$

where there is a term that is longitudinal in the gluon momentum k_μ that is not present at tree level. We already know from Taylor that in the extreme perturbative limit $\alpha(k,p,q) = 1$ and $\beta(k,p,q) = 0$, as the coupling increases however there may be important effects in both terms that we must try to quantify. An interesting form of the vertex to consider is,

$$\Gamma^{abc}_{\mu}(k,p,q) = igf^{abc}\left[q_\mu\alpha(k,p,q) + k_\mu\left(\gamma(k,p,q) - \alpha(k,p,q)\frac{k.q}{k^2}\right)\right] \tag{4.81}$$

we choose this because it isolates the component constrained by the Ward-Slavnov-Taylor identity, and also explicitly satisfies Taylor's theorem [94, 98] for any choice of $\alpha(k,p,q)$. The truncated WSTI[6] for this vertex reads [101],

$$i\frac{k^\rho}{k^2}\Gamma^{abc}_{\rho}(k,p,q)D(p)D(q) - i\frac{p^\rho}{p^2}\Gamma^{abc}_{\rho}(-p,-k,q)D(k)D(q) = gf^{abc}D(-k)D(p) \tag{4.82}$$

we have already cancelled the momentum conserving δ-functions since they are already factored out of the vertices using the definitions in appendix B. Inserting eq. (4.81) in eq. (4.82) we find that all of the α contributions drop out, which is typical of these relations in both abelian and non-abelian gauge theories where transverse terms are left unconstrained,

$$k^2\gamma(k,p,q)\frac{1}{\mathcal{G}h(k^2)} + p^2\gamma(-p,-k,q)\frac{1}{\mathcal{G}h(p^2)} = -\frac{q^2}{\mathcal{G}h(q^2)}. \tag{4.83}$$

It follows that γ has a simple solution, using conservation of momentum, $k = p - q$,[7]

$$\gamma(k,p,q) = \frac{\mathcal{G}h(k^2)}{\mathcal{G}h(q^2)}\frac{k.q}{k^2}, \tag{4.84}$$

whilst the function α is unconstrained. This is not necessarily a problem, since we know that this term must be $\mathcal{O}(1)$ in the perturbative limit and has some symmetries that

[6] An unknown four-ghost scattering term has been dropped. It is not clear whether this can cause a problem or not [86]. It is completely possible that the neglected term is important.

[7] In deriving this solution, it seems that there may be a sign ambiguity for γ, however since we know that $\alpha \sim 1$ perturbatively then the sign is automatically fixed given this solution for γ

should be satisfied [95, 101]. The vertex this gives is then,

$$\Gamma^{abc}_{\mu}(k,p,q) = igf^{abc}\left[q_\mu\alpha(k,p,q) + k_\mu\frac{k.q}{k^2}\left(\frac{\mathcal{G}h(k^2)}{\mathcal{G}h(q^2)} - \alpha(k,p,q)\right)\right], \tag{4.85}$$

It will be convenient in what follows to factorise this as,

$$\Gamma^{abc}_{\mu}(k,p,q) = igf^{abc}\left[q_\mu\alpha(k,p,q) + k_\mu k.q\,\tilde{\beta}(k,p,q)\right], \tag{4.86}$$

where

$$\tilde{\beta}(k,p,q) = \frac{1}{k^2}\left(\frac{\mathcal{G}h(k^2)}{\mathcal{G}h(q^2)} - \alpha(k,p,q)\right) \tag{4.87}$$

is defined implicitly. A sensible choice for α is to use sums of simple ratios such as,

$$\alpha(k,p,q) = \frac{1}{2}\left(\frac{\mathcal{G}h(q^2)}{\mathcal{G}h(k^2)} + \frac{\mathcal{G}h(p^2)}{\mathcal{G}h(k^2)}\right) \tag{4.88}$$

since in the UV when these functions are all slowly varying logarithms, we protect the perturbative results. There could however be other important non-perturbative terms in $\alpha(k,p,q)$ that need to be understood in order to make exact predictions. The different options available here will be tested in the numerical investigation below, but for now we leave $\alpha(k,p,q)$ an undefined function.

Given this form of the ghost-gluon vertex, we may use it to infer a form for the ghost-gluon scattering kernel that featured in eq. (4.75). The definition of this stems from the ghost-gluon vertex,

$$\Gamma^{abc}_{\mu}(k,p,q) = igf^{abc}\left[q_\mu\alpha(k,p,q) + k_\mu k.q\,\tilde{\beta}(k,p,q)\right], \tag{4.89}$$

$$= igf^{abc}\tilde{\Gamma}_{\nu\mu}(k,p,q)q^\nu, \tag{4.90}$$

this implies the following structure must be present,

$$\tilde{\Gamma}_{\mu\nu}(k,p,q) = \alpha(k,p,q)g_{\mu\nu} + \tilde{\beta}(k,p,q)k_\mu k_\nu, \tag{4.91}$$

this may then be applied to the triple-gluon vertex WSTI.

Simultaneously solving the vertex Ward-Slavnov-Taylor Identities

The full triple gluon vertex WSTI eq. (4.75) and the truncated ghost-gluon vertex WSTI eq. (4.82) have been solved simultaneously [100], however using those solutions, using the $\zeta = d$ UV-safe truncation and full angular integrals does not yield self-consistent solutions in our numerical procedure, which will be explained later. However, the solution to the WSTI may not be unique as noted in the original article so it may be worth considering what alternative forms are possible.

A full decomposition of the ghost-gluon scattering kernel widely used in the literature with all momenta incoming is [87, 99, 115–117],

$$\tilde{\Gamma}_{\nu\mu}(k,p,q) = g_{\mu\nu}a(k,p,q) - p_\mu k_\nu b(k,p,q) + k_\mu q_\nu c(k,p,q) \tag{4.92}$$

$$+ k_\nu q_\mu d(k,p,q) + q_\mu q_\nu e(k,p,q) \tag{4.93}$$

which gives the required ghost-gluon vertex when contracted as in eq. (4.90). This basis is not orthonormal, so may be written in many equivalent ways, to write it in the form for eq. (4.91) we must use the form,

$$\tilde{\Gamma}_{\nu\mu}(k,p,q) = g_{\mu\nu}a(k,p,q) + k_\mu k_\nu b(k,p,q) + k_\mu q_\nu c(k,p,q) + \tag{4.94}$$

$$+ k_\nu q_\mu (b(k,p,q) + d(k,p,q)) + q_\mu q_\nu e(k,p,q) \tag{4.95}$$

where $a = \alpha$, $b = \tilde{\beta}$, $c = 0$, $b = -d$ and $e = 0$ are required to give eq. (4.91). In refs. [99, 115, 116] the triple-gluon WSTI is solved and the following constraint on the the components of $\tilde{\Gamma}_{\mu\nu}$ is found, first they define,

$$a_{kpq} = \frac{\mathcal{G}h(p^2)}{\mathcal{G}l(q^2)} a(k,p,q) \tag{4.96}$$

and similarly for the other scattering kernel functions, then in this notation,

$$(a_{kpq} - a_{pkq}) - k.p\,(b_{kpq} - b_{pkq}) + k.q d_{kpq} - p.q d_{pkq} = 0 \tag{4.97}$$

it can easily be shown that eq. (4.91) does not satify this equation. In ref. [100] a similar problem arises which is then solved by adding a term, however in this solution the term

added would interfere with the form already proposed so it appears it is not possible to find a solution with this choice of scattering kernel.[8]

The von Smekal, Hauck and Alkofer Solution

A simultaneous solution of both WSTI does exist in the literature [100], this uses the same truncated WSTI for the ghost-gluon vertex and the full triple-gluon vertex WSTI as given above. Terms that are added to the ghost-gluon scattering kernel that do not appear in the ghost-gluon vertex itself in order to obtain a simultaneous solution in the triple-gluon vertex WSTI. The vertices that are obtained are,

$$\begin{aligned}
&\Gamma^{\mu\nu\rho}_{3g,abc}(k,p,q) = \\
&igf_{abc}\Bigg[A_+(q,k,p)(k-p)^\rho g^{\mu\nu} + A_-(q,k,p)\left(\frac{1}{2}(k+p)^\rho g^{\mu\nu} + \frac{(k-p)^\rho\,(k.pg^{\mu\nu} - k^\nu p^\mu)}{k^2-p^2}\right) \\
&\quad + A_+(k,p,q)(p-q)^\mu g^{\nu\rho} + A_-(k,p,q)\left(\frac{1}{2}(p+q)^\mu g^{\nu\rho} + \frac{(p-q)^\mu\,(p.qg^{\nu\rho} - p^\rho q^\nu)}{p^2-q^2}\right) \\
&\quad + A_+(p,q,k)(q-k)^\nu g^{\rho\mu} + A_-(p,q,k)\left(\frac{1}{2}(q+k)^\nu g^{\rho\mu} + \frac{(q-k)^\nu\,(q.kg^{\rho\mu} - q^\mu k^\rho)}{q^2-k^2}\right)\Bigg],
\end{aligned} \tag{4.98}$$

where

$$A_\pm(k,p,q) = \frac{\mathcal{G}h(k^2)\mathcal{G}h(q^2)}{\mathcal{G}h(p^2)\mathcal{G}l(p^2)} \pm \frac{\mathcal{G}h(k^2)\mathcal{G}h(p^2)}{\mathcal{G}h(q^2)\mathcal{G}l(q^2)}\,. \tag{4.99}$$

Also, for the ghost-gluon vertex,

$$\Gamma^{abc}_\mu(k,p,q) = igf^{abc}\left[q_\mu\left(\frac{\mathcal{G}h(k^2)}{\mathcal{G}h(q^2)}\right) + k_\mu\left(\frac{\mathcal{G}h(k^2)}{\mathcal{G}h(p^2)} - 1\right)\right]\,. \tag{4.100}$$

Later we shall use these vertices in a numerical procedure and explain why they do not lead to a self-consistent solution in this truncation.

[8] It may be possible that more can be done here by adding extra terms that appear in the ghost-gluon scattering kernel but do not affect the ghost-gluon vertex; terms that are transverse in q_μ, in a similar method as in ref. [100].

An IR-Transverse Ghost-Gluon vertex

A ghost-gluon vertex that is transverse in the IR limit has been suggested on theoretical grounds [95], particularly for the type of projection we apply here. Also, one of the reasons we investigated the form in eq. (4.81) was that recently [86] there has been success in solving the equations using a ghost-gluon vertex that is transverse in the IR. The particular form that is used is,[9]

$$\Gamma_\mu(k,p,q) = ig\left(q_\mu - k_\mu \frac{k.q}{k^2}\mathcal{F}_{\rm IR}(k,p,q,\Lambda_{\rm IR})\right), \tag{4.101}$$

where k is the gluon momentum. This is found by enforcing the relation $k^\mu\Gamma_\mu(k,p,q)=0$ in the IR limit to restrict the vertex functions, α and β. The term $\mathcal{F}_{\rm IR}(k,p,q,\Lambda_{\rm IR})$ is just a smoothed step function that switches this term on roughly below some scale $\Lambda_{\rm IR}$. This allows solutions to be obtained in this truncation and the initial intention when solving the WSTI for eq. (4.81) was that the term $(\frac{Gh(k^2)}{Gh(q^2)}-\alpha)$ would act somehow similarly to this step function, unfortunately this does not work since the dressing function ratio is always less than 1 under the ghost-loop integration in the IR and this prevents solutions from being obtained, since it induces an unphysical change in sign of the dressing function, for a range of sensible choices for α.

Typical choices for the smoothed step function are,

$$\mathcal{F}_{\rm IR}(k,p,q,\Lambda_{\rm IR}) = \frac{\Lambda_{\rm IR}^2}{(k^2+p^2+q^2+\Lambda_{\rm IR}^2)}, \tag{4.102}$$

$$\mathcal{F}_{\rm IR}(k,p,q,\Lambda_{\rm IR}) = \frac{\Lambda_{\rm IR}^6}{(k^2+\Lambda_{\rm IR}^2)\,(p^2+\Lambda_{\rm IR}^2)\,(q^2+\Lambda_{\rm IR}^2)}, \tag{4.103}$$

the first of which has a spherical boundary and the second is cubic, both result in qualitatively similar solutions. The expectation is that $\Lambda_{\rm IR}\simeq\Lambda_{\rm QCD}$, which in the momentum subtraction scheme is expected to be roughly $5\times$ that of the $\overline{\rm MS}$ scheme [96]. We will use the version given by eq. (4.102) unless stated otherwise.

The reason that this form works so differently to the others is the presence of the $1/k^2$ term in the second term in eq. (4.101). This becomes large and positive in the IR limit of the ghost loop in the gluon equation, similar to the ghost in the original scaling solutions. In the decoupling solutions this new singular factor essentially replaces the one lost when

[9] In ref [86] additional terms are present in the suggested vertex since they have the additional problem of the removal of quadratic divergences from using the $\zeta=1$ projection.

the ghost dressing becomes finite, mathematically then the contributions of the ghost loop and gluon loop are qualitatively similar in each set of solutions. Physically, this term could be justified if the ghost loop were the only term that contributes in the deep infrared region since this diagram would have to be transverse alone, in order to obtain a transverse gluon. Whether or not this is the case depends on the choice of triple-gluon vertex and will be investigated using the numerical procedure. However, if this diagram does dominate, then transversality of the gluon should happen automatically since the correct logarithms should be selected by using $\zeta = d$. The real reason that this term could be a important, if this is a sensible choice for the ghost-gluon vertex, must then be that important longitudinal loop corrections occur either non-perturbatively or at higher orders, and that these are required to obtain self-consistent solutions.

4.3.3. Numerical Solutions of the Ghost Equation

It is a useful exercise to attempt to solve the equation for the ghost dressing function alone, for a fixed gluon input. There are two classes of solution possible [87] for a wide range of choices for the ghost-gluon vertex and the input gluon propagator dressing. The first problem is always to obtain self-consistent solutions, and second, to check the physical properties.

In the majority of the truncations considered in recent years where calculations have been performed in the Landau gauge with ghosts included, the gluon propagator dressing has been found to vanish. We consider first the type 1, scaling solutions that satisfy relations eq. (4.60) and eq. (4.59). In order to produce a divergent ghost propagator we subtract at zero momentum, and set $\mathcal{G}h(\nu^2)^{-1} = 0$ in the SDE where ν^2 is the subtraction point for the ghost equation which is in principle, different to the renormalisation point μ^2.

We consider the following inputs for the gluon propagator,

$$\mathcal{G}l(p^2) = \left(\frac{p^2}{p^2 + \lambda^2}\right)^{2\kappa} \tag{4.104}$$

this is the form of a bare massive propagator for $\kappa = 1/2$, for other values it may be used to test the IR condition. The idea of a dynamically generated gluon mass term has become popular recently, partially due to results obtained by lattice QCD, a form with a

mass term and UV running is,

$$\mathcal{G}l(p^2) = \frac{p^2}{m^2 + p^2\left[1 + \frac{13}{2}\frac{g^2 N_c}{12\times 4\pi^2}\log\left(\frac{p^2+m^2}{\mu^2}\right)\right]}, \tag{4.105}$$

where strictly speaking, m should be a function of p^2 that can only be nonzero in the non-perturbative region. Both the type 1, scaling solutions and the type 2, decoupling solutions can be obtained with minimal effort using the bare ghost-gluon vertex. In order to obtain both sets of solutions we input eq. (4.104) and a ghost dressing that has the desired form we wish to obtain. For the type 1 solutions we input,

$$\mathcal{G}h(p^2) = \left(\frac{p^2}{p^2+\lambda^2}\right)^{-\kappa} \tag{4.106}$$

and for the type 2 solutions, the tree level value $\mathcal{G}h(p^2) = 1$ may be used. In figure 4.8 we show the results for a fixed gluon input and the consistent ghost output. The power law behaviour is reproduced in the IR such that eq. (4.60) and eq. (4.59) are satisfied for a wide range of values of κ. The same analysis can be performed for the type 2 solutions.

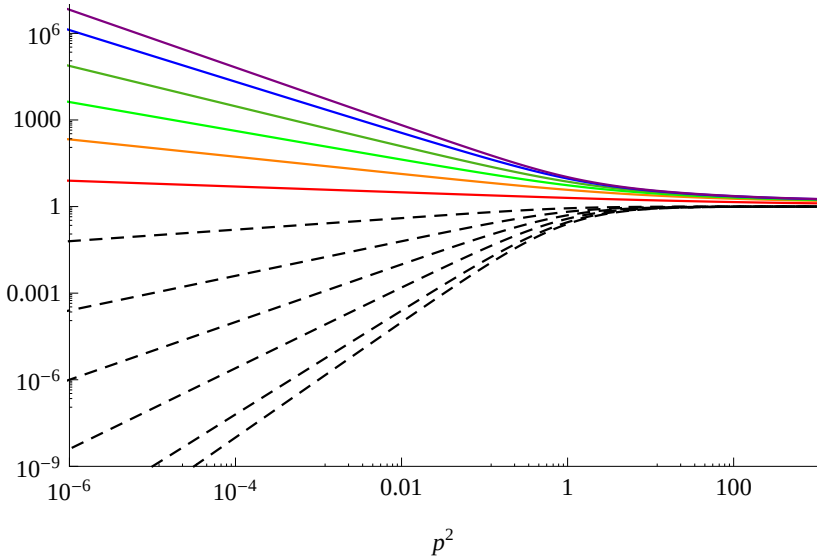

Figure 4.8.: Gluon inputs and consistent ghost outputs for Type 1 solutions. Each curve corresponds to its 'mirror' about $y = 1$. Gluon inputs eq. (4.104), from bottom to top (Black, dashed), $\kappa = 1.0, 0.9, 0.7, 0.5, 0.3, 0.1$. Numerical Ghost outputs from top to bottom (Colours, Solid), $\kappa = 1.0, 0.9, 0.7, 0.5, 0.3, 0.1$.

Here we renormalise and subtract in the most natural way, using the same perturbative point $\mu^2 = 100$ and $\alpha(\mu^2) = 0.15$. We see that the ghost equation is highly solvable for a range of gluon inputs. Using perturbative renormalisation conditions automatically

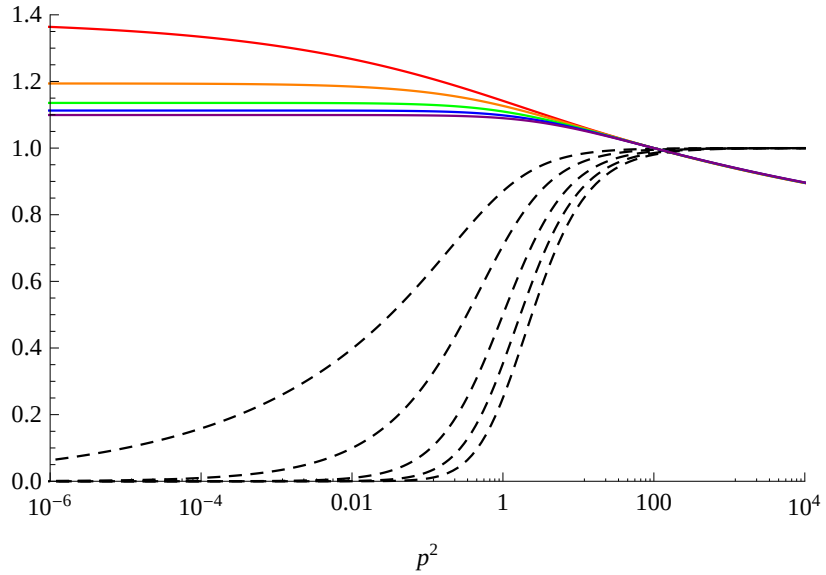

Figure 4.9.: Gluon inputs and consistent ghost outputs for the Type 2 Solutions. Gluons from left to right (in IR region), κ=0.1, 0.25, 0.5, 0.75 and 1 (Dashed, Black). Ghosts from top to bottom in IR region, κ=0.1, 0.25, 0.5, 0.75 and 1 (Solid, Colours).

gives rise to the type 2 solutions, however the type 1 solutions are readily obtained by subtracting at zero momentum. We now turn to simultaneous analyses of both equations.

4.3.4. Full Numerical Studies and Analysis

In the numerical study, we follow the methods used before as outlined in appendix C. The vertices listed above give rise to new and extended kernels in addition to those of section 4.2, these are given below. The tensor contractions for the gluon loop lead to long expressions in the intermediate steps and the derivation can be lengthy. The solutions obtained will be dependent upon the vertex choice. There are also free parameters that must be sensibly fixed in order to obtain physically meaningful solutions. We begin with a known working set of vertices and produce a set of solutions. These are then used to investigate the reasons why some vertices lead to consistent solutions and others do not.

Solution Set 1

The first set of solutions we present are built from the vertex dressings given in equations (4.77, 4.101) which is the transverse ghost-gluon vertex and the simplest bose-symmetric triple-gluon vertex, using the parameter valuess listed in table 4.1. The integral equations

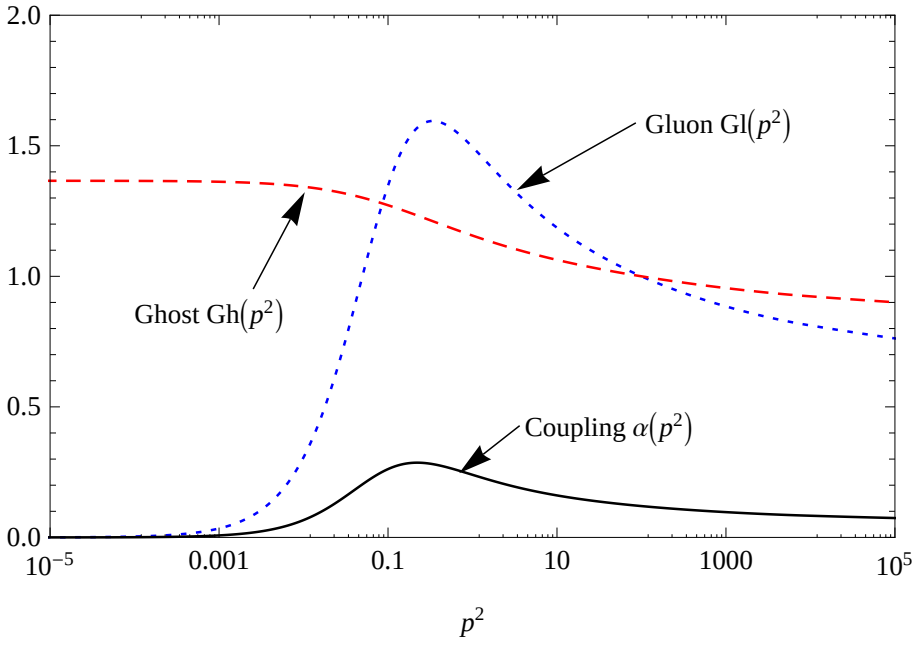

Figure 4.10.: Solution Set 1, showing the Gluon dressing (Blue, dotted), the Ghost dressing (Red, dashed) and the running coupling (Black).

that are solved require a slight generalisation compared to those used in section 4.2, since we now use the vertex defined by eq. (4.101) which contains an additional tensor structure. We write this using the generic form from eq. (4.80) where in this specific case $\alpha(-p;\ell_-,\ell_+)=1$ and $\beta(-p;\ell_-,\ell_+)=+\frac{p.\ell_+}{p^2}\mathcal{F}_{\rm IR}(p,\ell_+,\ell_-,\Lambda_{\rm IR})$. The Gluon SDE with polarisation functions is given in eq. (4.29), with the new vertices these become,

$$\begin{aligned}\Pi_{2c}(p^2,\mu^2)=&\frac{g^2(\mu^2)N_c}{(d-1)}\int\frac{d^d\ell}{(2\pi)^d}\mathcal{G}h(\ell_+^2,\mu^2)\mathcal{G}h(\ell_-^2,\mu^2)\times\\&\Big(\alpha(-p;\ell_-,\ell_+)\mathcal{M}(p,\ell,\zeta)+\beta(-p;\ell_-,\ell_+)\mathcal{M}_\beta(p,\ell,\zeta)\Big),\end{aligned}\tag{4.107}$$

$$\begin{aligned}\Pi_{2g}(p^2,\mu^2)=&\frac{g^2(\mu^2)N_c}{(d-1)}\int\frac{d^d\ell}{(2\pi)^d}\mathcal{G}l(\ell_+^2,\mu^2)\mathcal{G}l(\ell_-^2,\mu^2)\times\\&\frac{1}{3}\left(\frac{\mathcal{G}h(p^2,\mu^2)}{\mathcal{G}l(p^2,\mu^2)}+\frac{\mathcal{G}h(\ell_-^2,\mu^2)}{\mathcal{G}l(\ell_-^2,\mu^2)}+\frac{\mathcal{G}h(\ell_+^2,\mu^2)}{\mathcal{G}l(\ell_+^2,\mu^2)}\right)\mathcal{Q}(p,\ell,\zeta),\end{aligned}\tag{4.108}$$

where $\mathcal{M}$ and $\mathcal{Q}$ are as given in eqs. (4.30 and 4.31) respectively and,

$$\mathcal{M}_\beta(p,\ell,\zeta)=(-1)\frac{(\zeta-1)\,p.\ell_-}{p^2\ell_+^2\ell_-^2}.\tag{4.109}$$

Although we give a physical unit in GeV this is not to be taken too seriously, since without quarks matching to a physical scale is not entirely meaningful, however we do expect Λ_{IR} to be in the region of 1 GeV, given the arguments above. The solutions obtained from the numerical procedure are shown in figure 4.10. The first thing to note is that we have obtained what appears to be 'type 2' or 'decoupling' solutions where the ghost is IR finite. 'Scaling' or 'type 1' solutions have not been found in this truncation and likely do not exist. A perturbative renormalisation point is chosen and the one-loop running for each dressing is verified numerically, by taking the derivative to find the coefficient of the logarithm. The renormalisation constants are also calculated and checked against their one-loop perturbative counterparts, this is a 3% and a 0.5% error respectively for

Parameter	Value
μ^2	1000 GeV^2
ν^2	1000 GeV^2
$\alpha(\mu^2)$	0.1
$\mathcal{G}l(\mu^2)$	1
$\mathcal{G}h(\nu^2)$	1
Λ^2_{IR}	5 GeV^2

Table 4.1.: The parameters used for Solution Set 1.

Quantity	One-loop Perturbative	All orders Numerical
Ghost log coeff.	-9/4	-2.26
Gluon log coeff.	-13/2	-6.69
Z_3	1.119	1.153
$\tilde{Z}_3$	1.041	1.049

Table 4.2.: Numerical and perturbative values for solution Set 1.

the gluon and ghost, which is in reasonable agreement. We also find that these vertices automatically produce a Gluon dressing that goes exactly as p^2 as p becomes small.

The subtracted gluon equation that we solve for numerically is,

$$\mathcal{G}l^{-1}(p^2) = \mathcal{G}l^{-1}(\mu^2) + \big(\Pi_{2c}(p^2) - \Pi_{2c}(\mu^2)\big) + \big(\Pi_{2g}(p^2) - \Pi_{2g}(\mu^2)\big) \tag{4.110}$$

where we have dropped the second argument of the dressing and polarisation functions for simplicity. The reason for choosing a subtracted polarisation function is to remove the renormalisation constant Z_3. Throughout this section we will enforce the most basic momentum subtraction condition that $\mathcal{G}l(\mu^2, \mu^2) = 1$. The Gluon dressing function must always be positive and any sign change will lead to a breakdown of the iterative procedure. A minimal constraint then for a solvable system is,

$$1 + \Pi_{2c}^{(\mathrm{sub})}(p^2, \mu^2) + \Pi_{2g}^{(\mathrm{sub})}(p^2, \mu^2) > 0 \quad , \tag{4.111}$$

where $\Pi_i^{(\mathrm{sub})}(p^2, \mu^2) = \Pi_i(p^2) - \Pi_i(\mu^2)$. For the full gluon equation there are more contributions and the condition then would be,

$$1 + \Pi_{2c}^{(\mathrm{sub})}(p^2, \mu^2) + \Pi_{2g}^{(\mathrm{sub})}(p^2, \mu^2) + \Pi_{3g}^{(\mathrm{sub})}(p^2, \mu^2) + \Pi_{4g}^{(\mathrm{sub})}(p^2, \mu^2) > 0 \quad , \tag{4.112}$$

this is where the uncertainty arises regarding the statements we make about the ghost-gluon vertex.

For the Set 1 solutions we find that both of these polarisation functions are both at leading order in the infrared, contrary to the solutions in section 4.2 where the ghost loop dominates and the gluon loop contribution is negligible. In fact they both have a pole in p^2 in the IR which when inverted becomes the p^2 behaviour that is shown in figure 4.10. Since they are of opposite sign, to compare the behaviours of these it makes sense to include an additional p^2 factor, so we plot the components of eq. (4.111) multiplied by p^2 in figure 4.11, where we still require the sum to be greater than zero at any given p^2. We find that the leading IR component of the ghost loop is $0.140/p^2$ and that of the gluon loop is $-0.0516/p^2$. In the UV however the situation is reversed, as is known from perturbation theory, the gluon loop gives the larger of the two contributions and both are significant. The fact that both loops are at leading order has been found elsewhere [83]. This undermines the choice of using an infrared transverse ghost-gluon vertex,[10] since there is no reason why that loop should be transverse on its own when the gluon-loop contributes at the same numerical order.

[10] An IR transverse vertex and an IR transverse ghost-loop in the gluon equation are identical in the constraint bewteen the vertex functions

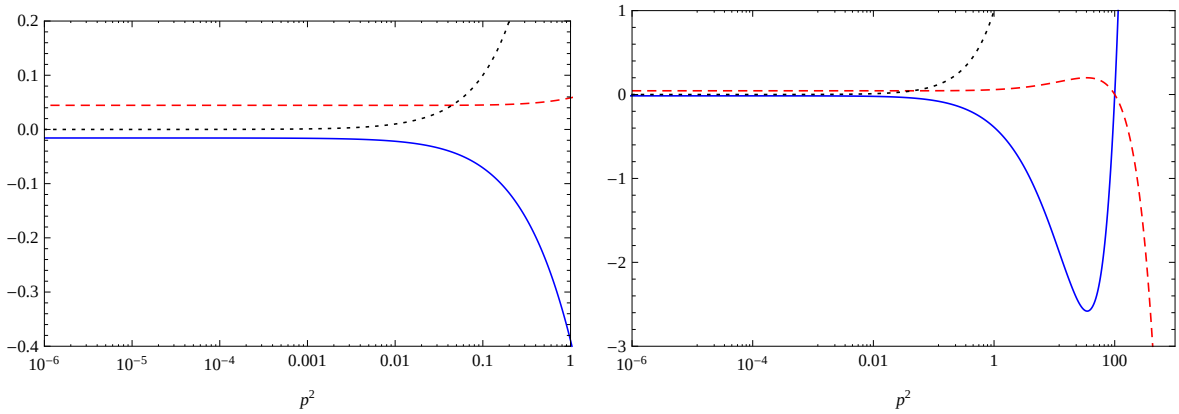

Figure 4.11.: Gluon polarisation contributions for the Solution Set 1. Left: Full Region, Right: IR Region. These show $p^2\Pi_{2g}^{(\mathrm{sub})}(p^2)$ (Blue, Solid), $p^2\Pi_{2c}^{(\mathrm{sub})}(p^2)$ (Red, Dashed) and p^2 (Black, Dotted).

Gluon UV running and subleading components

One problem that becomes apparent when solving this truncation for the vertices given above is how the UV subleading components of the gluon propagator drop off as p^2 becomes large. The gluon is expected to have some distinct intermediate momentum behaviour but to tend to the simple resummed logarithm from perturbation theory as g^2 becomes small as p^2 becomes larger. How these subleading components slowly die away is something we may consider analytically [85, 90] or numerically.

It is noted in refs. [83, 85] that a dressing like $\mathcal{G}h^2/\mathcal{G}l^2$ in the large-p^2 limit gives the correct running for the gluon loop. Some of the vertices here do not correctly reproduce the logarithmic running by some small amount, this can make the results ambiguous because the matching point between the SDE loop and perturbative running then has a small kink which introduces and unphysical depdendence on this point. When using these vertices, we use a procedure where we always match at the renormalisation point. The extrapolation is required since the momentum in the dressing functions under the integrals sample momenta beyond the cutoff. The exact procedure is defined in appendix C.3, along with details regarding the effects of using these vertices.

Truncations with other vertices

In this study we have found that many of the vertices used elsewhere do not give self-consistent solutions in our numerical procedure. It is worth checking exactly why this

is since it will inform our choices for improving the truncation. There are many reasons why a truncation could fail. They could of course fail due to neglecting the dressed two-loop graphs which we do not consider at present. Provided that the neglected terms are subleading in the IR[11] then we require eq. (4.111) to be satisfied. In all of the triple-gluon vertices that we have considered we have found that,

$$\lim_{p^2\to 0} \Pi_{2g}^{(\mathrm{sub})}(p^2,\mu^2) \leq 0\,. \tag{4.113}$$

Although this list of vertices is not exhaustive, and presumably some vertex could be contrived that would violate this condition, we are led to the requirement on the ghost loop term that,

$$\lim_{p^2\to 0} \Pi_{2c}^{(\mathrm{sub})}(p^2,\mu^2) > 0\,. \tag{4.114}$$

Some triple-gluon vertices that lead to non-zero IR contributions in that loop would require the even stronger condition,

$$\lim_{p^2\to 0} \Pi_{2c}^{(\mathrm{sub})}(p^2,\mu^2) > \left|\lim_{p^2\to 0} \Pi_{2g}^{(\mathrm{sub})}(p^2,\mu^2)\right|, \tag{4.115}$$

for a truncation without the two-loop terms. Obtaining a ghost-gluon vertex that satisfies this condition will be our primary concern. This is not a guarantee that solutions will exist, eq. (4.111) must be satisfied everywhere. First we must calculate the new integrands that result from the new tensor contractions. The required ingredients for the ghost loop are already given by eq. (4.107), we choose to compare four ghost-gluon vertices, the transverse vertex eq. (4.101), the bare vertex, the WSTI solution eq. (4.100) and an additional dressed form closely related to the transverse vertex. Since ratios of dressing functions should result from the WSTI analysis we choose the term multiplying the tree level term from eq. (4.100) to multiply the whole transverse vertex from eq. (4.101),

$$\Gamma_\mu(k,p,q) = ig\frac{\mathcal{G}h(k^2)}{\mathcal{G}h(q^2)}\left(q_\mu - k_\mu\frac{k.q}{k^2}\mathcal{F}_{\mathrm{IR}}(k,p,q,\Lambda_{\mathrm{IR}})\right)\,. \tag{4.116}$$

In order to perform the same study on the gluon loop term, we must calculate the resulting kernels for the generalised triple-gluon dressing eq. (4.78) which we choose to write now

[11] This is an unverified assumption that should be checked by explicit evaluation of the two loop graphs, with a careful choice of dressed vertices.

a more generic way,

$$\Gamma^{\mu\nu\rho}_{3g,abc}(k,p,q) = igf_{abc}\Big[\Gamma_{3g}(q^2,k^2,p^2)g^{\mu\nu}(k-p)^\rho + \Gamma_{3g}(k^2,p^2,q^2)g^{\nu\rho}(p-q)^\mu + \Gamma_{3g}(p^2,q^2,k^2)g^{\rho\mu}(q-k)^\nu\Big] \tag{4.117}$$

where typically we choose something like, $\Gamma_{3g}(k^2,p^2,q^2) = \mathcal{G}h(k^2)/\mathcal{G}l(p^2)$. If we perform the tedious but straightforward tensor contractions, projecting the tensor structure using $\mathcal{P}_{\mu\nu}(p^2,\zeta)$ we find,

$$\begin{aligned}\Pi_{2g}(p^2) = \left(\frac{1}{2}\right)\frac{N_c g^2(\mu^2)}{(d-1)(2\pi)^4}\int d^4\ell \frac{\mathcal{G}l(\ell_+^2)\mathcal{G}l(\ell_-^2)}{4\,(p^2\ell_+^2\ell_-^2)^2}\times \\ \Big\{\Gamma_{3g}(p^2,\ell_-^2,\ell_+^2)\,[\,-32\zeta(\ell.p)^4 + (3\zeta-4)p^4(\ell.p)^2 \\ - 48\ell^6p^2 + 24\ell^4(2\zeta\ell.p^2 - p^4) + \ell^2p^2(8(\zeta+6)\ell.p^2 + p^4)\,] \\ +\Gamma_{3g}(\ell_-^2,\ell_+^2,p^2)2(\ell.p^2 - l^2p^2)\left[4\ell^2(5p^2+2\zeta\ell.p) + p^2(7p^2 - 2(\zeta-12)\ell.p)\right] \\ +\Gamma_{3g}(\ell_+^2,p^2,\ell_-^2)2(\ell.p^2 - l^2p^2)\left[4\ell^2(5p^2-2\zeta\ell.p) + p^2(7p^2 + 2(\zeta-12)\ell.p)\right]\Big\}.\end{aligned} \tag{4.118}$$

We also calculate the triple-gluon WSTI solution given in eq. (4.98) using the above result eq. (4.118), with the substitution $\Gamma_{3g}(k^2,p^2,q^2) \to A_+(k^2,p^2,q^2)$, defined in eq. (4.99), the

new terms from this extended vertex simply add to the previous result,

$$\begin{aligned}
\Pi_{2g}(p^2) &= \Pi_{2g}(p^2)^{(\text{eq. (4.118)})} + \\
&\frac{N_c g^2(\mu^2)}{2\,(d-1)(2\pi)^4}\int d^4\ell \frac{\mathcal{G}l(\ell_+^2)\mathcal{G}l(\ell_-^2)}{4\,(p^2\ell_+^2\ell_-^2)^2}\Bigg\{\Bigg(32\,\ell.p\,p^2\,(\ell.p^2-\ell^2p^2)\times \\
&\Big[A_-(\ell_+^2,p^2,\ell_-^2)(4(\ell^2+\ell.p)-3p^2)(4(\ell^2-\ell.p)+p^2)(4\ell^2-8\ell.p+7p^2) \\
&-A_-(\ell_-^2,\ell_+^2,p^2)(4(\ell^2-\ell.p)-3p^2)(4(\ell^2+\ell.p)+p^2)(4\ell^2+8\ell.p+7p^2)\Big]\Bigg) \\
&-\Bigg(A_-(p^2,\ell_-^2,\ell_+^2)\left(4(\ell^2-3p^2)^2-16\,\ell.p^2\right)\times \\
&\Big[\ell^2\left(192\zeta\ell.p^4+4(7\zeta-16)p^4\ell.p^2+p^8\right)+(9\zeta-10)\ell.p^2p^6+16(8-7\zeta)\ell.p^4p^2 \\
&+192p^2\ell^8+16\ell^6\left(7p^4-12\zeta\ell.p^2\right)+4p^2\ell^4\left(4(3\zeta-22)\ell.p^2+5p^4\right)\Big]\Bigg)\Bigg\}. \qquad (4.119)
\end{aligned}$$

Using the ghost-gluon vertices listed above, and the integrands calculated above along with the bare triple-gluon vertex and the simply dressed form from eq. (4.77), we use solution Set 1 as input, then calculate the subtracted polarisation functions and plot them in fig. 4.12. There are no iterations here so the results do not represent the quantities that may be produced by self-consistent solutions, however this gives some measure of the properties of the vertices with respect to each other. It is from this plot we learn why some of the other vertices do not work.

At first glance the ghost-gluon vertices are all very similar and in the UV all have roughly the correct running. The bare ghost-gluon vertex is vanishing in the IR and too small to give self-consistent solutions, as is the vertex from the simultaneous WSTI solution eq. (4.100), although it gives a slightly different intermediate behaviour.

The result from the triple-gluon vertex given by eq. (4.78) is not that different to the one already used in obtaining the first set of solutions and self-consistent solutions may be found using it. The triple-gluon vertex given by the full WSTI solution eq. (4.98) is quite large in the IR and also does not give the correct running in the UV. For this vertex to work, it requires a larger cancelling contribution in the IR, using the transverse vertex eq. (4.101), which is the largest considered so far, it is not possible to obtain self-consistent solutions with this set of parameters. Solutions may be found but require very small bare couplings.

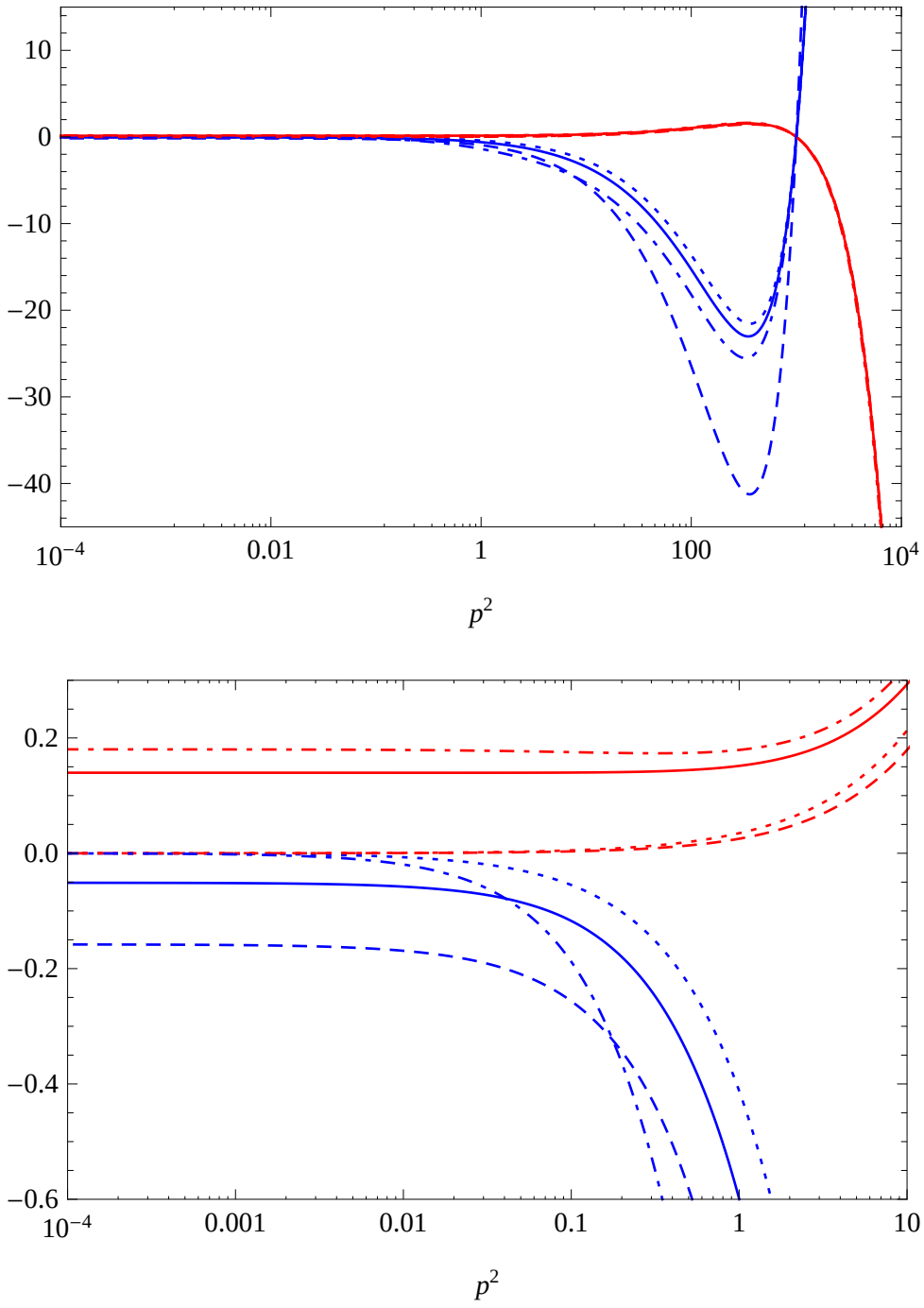

Figure 4.12.: Gluon polarisation contributions for the vertices that are considered, these show $p^2\Pi_{2g}^{(\mathrm{sub})}(p^2)$ and $p^2\Pi_{2c}^{(\mathrm{sub})}(p^2)$. Top: Full Region, Bottom: IR Region. The upper curves are the ghost loop contributions (Red) and the lower curves are the gluon loop contributions (Blue). Solid lines: Set 1 polarisation functions, Dotted lines: tree level vertices, Dashed lines: Alkofer *et al* WSTI vertices eq. (4.100) and eq. (4.98), Dot-dashed ghost loop is the dressed Fischer *et al* vertex with a WSTI type ratio of dressings, the Dot-dashed gluon loop uses individually dressed terms as in eq. (4.78).

It is also useful to consider the UV running of the different vertices since this should be correct and is often considered a problem. In figure 4.13 we zoom on the UV region from figure 4.12. We add a black solid curve that shows correct gluon loop contribution in order to obtain the correct perturbative one-loop running. We find that the individually dressed vertex, eq. (4.78), is a little way off, and the full WSTI triple-gluon vertex, eq. (4.98), gives a very different answer to that obtained from one-loop perturbation theory. The simplest symmetric dressing eq. (4.77) and the vertex like $\mathcal{G}h^2/\mathcal{G}l^2$ gives UV running contributions that are very close. However, neither of these satify the WSTI for this vertex which is an outstanding problem.

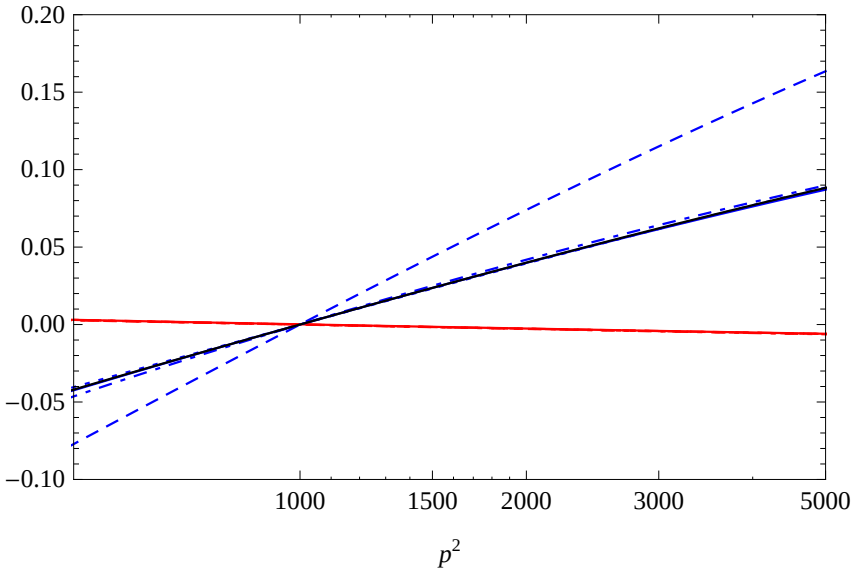

Figure 4.13.: Gluon polarisation contributions for the vertices that are considered, for the details of each curve see the caption of fig. 4.12 except now we drop the p^2 and plot $\Pi_i^{(\mathrm{sub})}(p^2)$. In the perturbative region shown here the ghost loop contributions are almost identical amongst the vertices. The black solid curve is the correct contribution we expect from using the vertex given by a $\mathcal{G}h^2/\mathcal{G}l^2$ dressing, for example eq. (4.79). This lies almost exactly on top of the simplest symmetric dressed triple-gluon vertex eq. (4.77). The individually dressed vertex, eq. (4.78), is a little way off (blue dot-dashed curve), and the full WSTI triple-gluon vertex, eq. (4.98) (the blue dashed curve), gives a very different answer to that obtained from one-loop perturbation theory.

Solution Set 2

Using the triple-gluon vertex in eq. (4.78) that has an individual dressing for each momentum term similar to the full WSTI solution, we solve the Schwinger–Dyson Equations

again and obtain self–consistent solutions. The parameters used are much the same as for the set 1 solutions, the range of values of $\Lambda_{\rm IR}$ is a smaller for this vertex, the numbers are as in table 4.1. The reason for this reduction can be correctly guessed from fig. 4.12, the dressing given by eq. (4.78) (the blue, solid curve) relative to eq. (4.76) (the black, dotted curve) is larger and in the changeover region around 1 GeV where the largest contribution switches from being the ghost in the IR to the gluon in the UV then a larger ghost contribution is required to keep the polarisation function positive.

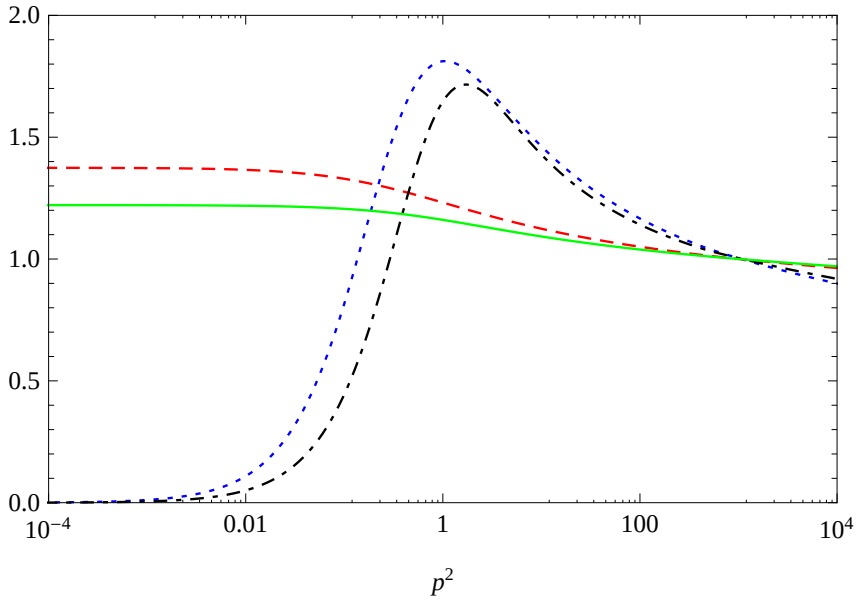

Figure 4.14.: The Set 2 Solutions with Set 1 also shown for comparison. Set 1 Gluon (Blue, Dotted), Set 1 Ghost (Red, Dashed), Set 2 Gluon (Black, Dot-dashed), Set 2 Ghost (Green, Solid). The different running given by this triple-gluon vertex is clearly visible in the UV.

4.3.5. The Running Coupling

The running coupling in quarkless non-perturbative QCD is more often than not defined by the quantity [119],

$$\alpha(p^2) = \alpha(\mu^2)\mathcal{G}h^2(p^2)\mathcal{G}l(p^2), \tag{4.120}$$

where $\alpha(\mu^2) = g^2(\mu^2)/4\pi$ is what we refer to as the running coupling. There are other definitions that may also be used, some of which may be obtained from the definitions of the renormalisation factors and the multiplicative renormalisation conditions. When studying the fundamental physics of mesons, then the quark-gluon vertex may be a more natural

starting point. To derive the above equation we require Eqs. (4.10, 4.11, 4.12, 4.14 and 4.15). The derivation generalises from a perturbative one by considering the dressing functions and using these to relate the coupling at different scales,

$$\alpha(\mu^2) = \alpha(\Lambda^2_{\rm cut})\frac{\tilde{Z}_3^2(\mu^2,\Lambda^2_{\rm cut})\, Z_3(\mu^2,\Lambda^2_{\rm cut})}{\tilde{Z}_1^2(\mu^2,\Lambda^2_{\rm cut})} \tag{4.121}$$

where the presence of $\Lambda_{\rm cut}$ denotes a bare Green's function and we have used the defintion $\alpha(\mu^2) = g^2(\mu^2)/(4\pi)$. Substituting the MR conditions we obtain,

$$\alpha(\mu^2)\mathcal{G}h^2(p^2,\mu^2)\mathcal{G}l(p^2,\mu^2) = \alpha(\Lambda^2_{\rm cut})\mathcal{G}h^2(p^2,\Lambda^2_{\rm cut})\,\mathcal{G}l(p^2,\Lambda^2_{\rm cut})\frac{1}{\tilde{Z}_1^2(\mu^2,\Lambda^2_{\rm cut})}\,. \tag{4.122}$$

In order to obtain the usual relation the Taylor condition is invoked, setting $\tilde{Z}_1 = 1$. We then notice that the LHS is independent of $\Lambda_{\rm cut}$ and the RHS is independent of μ^2 so we can eliminate the $\Lambda_{\rm cut}$ by evaluating at two different renormalisation points μ^2 and ν^2 and dividing the resulting expressions,

$$\alpha(\mu^2)\mathcal{G}h^2(p^2,\mu^2)\mathcal{G}l(p^2,\mu^2) = \alpha(\nu^2)\mathcal{G}h^2(p^2,\nu^2)\mathcal{G}l(p^2,\nu^2)\,. \tag{4.123}$$

Then we simply set $p^2 = \nu^2$ and apply the perturbative renormalisation conditions $\mathcal{G}l(\nu^2,\nu^2) = 1$ and $\mathcal{G}h(\nu^2,\nu^2) = 1$ and find,

$$\alpha(\nu^2) = \alpha(\mu^2)\mathcal{G}l(\nu^2,\mu^2)\mathcal{G}h^2(\nu^2,\mu^2)\,, \tag{4.124}$$

which is valid for a general renormalisation point μ^2. Subtleties can be missed by blindly applying the Taylor condition, so we propose to explicitly include the vertex dressing. Returning to eq. (4.122) we use relation eq. (4.12),

$$\alpha(\mu^2)\frac{\mathcal{G}l(\ell^2,\mu^2)\mathcal{G}h^2(\ell^2,\mu^2)}{\Gamma^2_\rho(k,p,q,\mu^2)} = \alpha(\Lambda^2_{\rm cut})\frac{\mathcal{G}h^2(\ell^2,\Lambda^2_{\rm cut})\,\mathcal{G}l(\ell^2,\Lambda^2_{\rm cut})}{\Gamma^2_\rho(k,p,q,\Lambda^2_{\rm cut})}\,. \tag{4.125}$$

The next issue is the precise definition of how the vertex is renormalised in a momentum subtraction scheme. Various conditions have been applied in the literature [95, 98, 117, 118, 120], either using a symmetric point (where $k^2 = p^2 = q^2$), or the point where either the gluon momentum vanishes ($k^2 = 0$, and $p^2 = q^2$), or the incoming ghost momentum vanishes ($k^2 = q^2$ and $p^2 = 0$). This final condition is the one that leads to Taylor's theorem, and hence a vertex that is bare in this limit. The first and second differ from this by some finite amount, even as $\Lambda_{\rm cut} \to \infty$ in Landau gauge.

We choose the Taylor point where $p = 0$ where the general ghost-gluon vertex eq. (4.80) becomes[12],

$$\Gamma_\rho(-q;0,q,\Lambda^2_{\rm cut}) = Z_g(\mu^2,\Lambda^2_{\rm cut})g(\mu^2)\,\tilde{Z}_1(\mu^2,\Lambda^2_{\rm cut})\,iq_\rho\left(\alpha(-q;0,q,\mu^2)-\beta(-q;0,q,\mu^2)\right). \tag{4.126}$$

The renormalisation condition then requires,

$$\alpha(-q,0,q,\mu^2)-\beta(-q,0,q,\mu^2)=1 \tag{4.127}$$

at a *perturbative* momentum q, in the region of μ. Taylor's condition however, states that this should be valid for all q but the ghost-gluon vertex we have applied using eq. (4.101) violates this condition away from the perturbative region. We can then cancel some factors in eq. (4.125), apply the renormalisation conditions (assuming a perturbative point), and relabel, we then find,

$$\alpha(p^2)=\alpha(\mu^2)\frac{\mathcal{G}l(p^2,\mu^2)\mathcal{G}h^2(p^2,\mu^2)}{\left(\alpha(-p,0,p,\mu^2)-\beta(-p,0,p,\mu^2)\right)^2} \tag{4.128}$$

which for the ghost-gluon vertex in eq. (4.101) gives,

$$\alpha(p^2)=\alpha(\mu^2)\frac{\mathcal{G}l(p^2,\mu^2)\mathcal{G}h^2(p^2,\mu^2)}{\left(1-\mathcal{F}_{\rm IR}(p^2,0,p^2,\Lambda_{\rm IR})\right)^2}. \tag{4.129}$$

Note that the denominator vanishes in the IR and the relative powers of this and the gluon vanishing determine the behaviour of the IR running coupling. Since $\mathcal{F}_{\rm IR}$ is arbitrary then this cannot be a firm prediction of the truncation. However, using the definition used in the two solution sets given above then this would lead to an IR divergent running coupling. A form could be chosen whose limiting behaviour is as p in the IR which would result in a finite IR coupling.

This redefinition does not get around the problem that Taylor's theorem is broken by this choice of vertex. A different approach would be supplement the ghost-gluon vertex functions $\alpha(k,p,q)$ and $\beta(k,p,q)$ by additional terms that protect Taylor's theorem, this we consider next.

[12]Note that often the Taylor condition is quoted with a + between the two components of the vertex, this is just due to differences in the definition of the vertex momentum.

4.3.6. A Singular Ghost-Gluon Vertex?

The only ghost-gluon vertex that we have so far that produces self-consistent solutions is the infrared transverse form eq. (4.101). This essentially has something like a $1/p^2$ term, in the term in the vertex proportional to the gluon momentum. This enters under the integral but gives a strong enhancement in Π_{2c} as $p^2 \to 0$ that is required for a vanishing gluon at small momentum.[13] This term does not contribute in the ghost equation or the SDE projected with the $\zeta = 1$, but is important in the $\zeta = 4$ version of the equations. Several other forms are suggested that introduce some sort of singularity in the vertex [86,95,98,121], however the nature of this singularity will of course be dependent upon the other factors from the loop integration and vertex dressing. Numerical investigations have shown that a singularity is necessary to drive the Gluon dressing to zero (at least in the one-loop-only truncation), which appears to be the most natural way of simultaneously obtaining solutions like those found on the lattice. This may appear unnatural at first and unexpected from related studies in QED [88,115,116], but seems to be necessary here. We set aside these concerns for now and investigate some simple forms. The question is how best to inform our choice of dressing. We have used eq. (4.101) [86,95] to obtain our solutions so far but other forms may be possible and we would ideally prefer something derived from the fundamental theory.

In a different truncation that uses pinch-technique and background field method rearrangements [122, 123], where the Green's functions are elegantly rearranged into manifestly transverse groups, [121], the following dressing is used, along with a similar form for the triple-gluon vertex,

$$\Gamma_\mu(k,p,q) = \Gamma^{(0)}_\mu(k,p,q) + \frac{k_\mu}{k^2}\left(\frac{p^2}{\mathcal{G}h(p^2)} - \frac{q^2}{\mathcal{G}h(q^2)}\right) \tag{4.130}$$

this is chosen so that the Schwinger mechanism is reproduced [123]. This corresponds to, in the above notation,

$$\alpha(k,p,q) = 1 \tag{4.131}$$

$$\beta(k,p,q) = \frac{1}{k^2}\left(\frac{p^2}{\mathcal{G}h(p^2)} - \frac{q^2}{\mathcal{G}h(q^2)}\right). \tag{4.132}$$

[13] In the transverse vertex there is not actually a singularity since it is cancelled by the numerator in the appropriate limit, however the result is that $\Pi_{2c}(p^2)$ goes as p^{-2} in the IR.

The Green's functions from this related method do not coincide with the Landau gauge version exactly [124], because of the pinch-technique rearrangements, however we may use this form and investigate its effect on our solutions. Clearly the $1/k^2$ in the external gluon momentum may dominate in the small momentum region, as $k \to 0$, if no cancelling factors arise in the numerator. In this truncation, this vertex does not appear to give sensible results.

A third dressing is inferred [98], by careful consideration of Schwinger–Dyson, Perturbative and Lattice QCD results to restrict the deep IR powers of the propagators and vertices. The conclusions there favour an IR divergent ghost-gluon vertex which has a particular form that clarifies the structure of any singular term such that Taylor's theorem [94] is satisfied. Taylor's theorem is often referred to as the 'non-renormalisation' theorem for the ghost-gluon vertex. The actual statement, in the notation and momentum definition used in eq. (4.80) is,

$$\alpha(-q, 0, q, \mu^2) - \beta(-q, 0, q, \mu^2) = 1. \tag{4.133}$$

The ghost-gluon vertex functions α and β may be written in terms of the ghost-gluon scattering kernel function defined as a–e, and used earlier in eq. (4.90). The decompositions for the vertex functions α and β are [98],

$$\alpha(k, p, q) = a(k, p, q) + [b(k, p, q) + d(k, p, q)]\, k.q + q^2 e(k, p, q) \tag{4.134}$$

$$\beta(k, p, q) = b(k, p, q) k.q + c(k, p, q) q^2 \tag{4.135}$$

where it is noted that since only $b(k, p, q)$ appears in both terms, then if any term is singular when $p^2 \to 0$, in order to satisfy Taylor's theorem then it may occur only in b since it will automatically cancel in eq. (4.133). The authors of [98] consider terms such as $q^{-2} \times$ (regular fn.) or $p^{-2} \times$ (regular fn.). In the numerical procedure, we have not found any working forms with singularities such as these. However, the vertex already considered eq. (4.101), may be put into this form if we take,

$$b(k, p, q) = -\frac{1}{k^2} \mathcal{F}_{\rm IR}(k, p, q, \Lambda_{\rm IR}). \tag{4.136}$$

This would lead to the natural extension of the transverse vertex, eq. (4.101),

$$\alpha(k, p, q) = 1 - \frac{k.q}{k^2} \mathcal{F}_{\rm IR}(k, p, q, \Lambda_{\rm IR}). \tag{4.137}$$

This new vertex can be most simply written as the bare vertex plus a term proportional to the incoming ghost momentum,

$$\Gamma^{abc}_{\mu}(k,p,q) = igf^{abc}\left(q_\mu + p_\mu \frac{k.q}{k^2}\mathcal{F}_{\rm IR}(k,p,q,\Lambda_{\rm IR})\right), \tag{4.138}$$

in this form it is clear that the additional term vanishes as p vanishes and the vertex reduces to its bare form. We now solve the equations using this vertex and compare with the previous sets.

Solution Set 3

Using the above expressions for the ghost-gluon vertex, we find the solutions shown in figure 4.15. They are plotted with the Set 1 solutions for comparison. We notice that this extra term in the ghost-gluon dressing hardly affects the result for the gluon equation, but significantly changes the low momentum behaviour of the ghost dressing function. It appears that there is a compensating effect in the gluon equation that counteracts the increase in the ghost dressing since in the previous truncation with the transverse ghost-gluon vertex if the ghost dressing increased by this amount then it would have a much larger effect on the gluon equation.

The input parameters are as given for the Set 1 solutions in table 4.1 and the triple-gluon vertex is also as used for Set 1 given by eq. (4.77), the simple symmetric dressing. Although the solutions do not look that different, this vertex is much more restrictive in the solutions that can be obtained, whilst for the Set 1 and Set 2 there are other solutions for a wide range of parameters.

4.3.7. Using the Ghost-Gluon Vertex WSTI solution

Choosing a form for $\alpha(k,p,q)$ in the WSTI vertex eq. (4.81) from fundamental methods is currently a problem. Appealing to the forms that have currently been found to work, for example in eq. (4.101) and eq. (4.138) we can arrange a form that allows for self-consistent solutions, utilising again the function $\mathcal{F}_{\rm IR}(k,p,q,\Lambda_{\rm IR})$ since it is otherwise difficult to arrange the limits that are required by perturbation theory,

$$\alpha(k,p,q) = 1 + N\mathcal{F}_{\rm IR}(k,p,q,\Lambda_{\rm IR}) \tag{4.139}$$

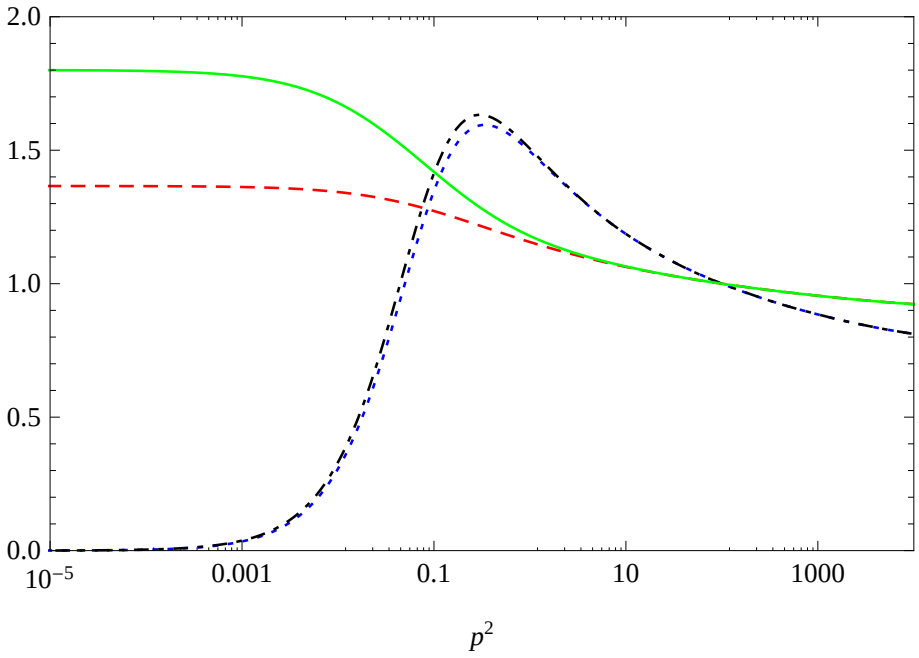

Figure 4.15.: The Set 3 Solutions, shown with Set 1 for comparison. The Ghost dressing is quite different in the IR, but gluon dressing is almost identical. Set 1 Gluon (Blue, Dotted), Set 1 Ghost (Red, Dashed), Set 3 Gluon (Black, Dot-dashed), Set 3 Ghost (Green, Solid).

where N is a normalisation parameter that is selected so that solutions may be obtained. We can also consider dressings to $\alpha(k,p,q)$ suggested by comparisons to eq. (4.100). The full vertex is then,

$$\Gamma^{abc}_{\mu}(k,p,q) = igf^{abc}\Bigg[q_\mu\Big(1+N\mathcal{F}_{\rm IR}(k,p,q,\Lambda_{\rm IR})\Big) + k_\mu\frac{k.q}{k^2}\left\{\frac{\mathcal{G}h(k^2)}{\mathcal{G}h(q^2)} - \Big(1+N\mathcal{F}_{\rm IR}(k,p,q,\Lambda_{\rm IR})\Big)\right\}\Bigg]. \qquad (4.140)$$

When solving the equations using this input we find that the range of solutions is similarly restricted as found for Set 3. The additional term in $\alpha(k,p,q)$ causes an enhancement in the ghost equation in the IR region compared to the bare vertex, for large couplings the relation given by eq. (4.115) is not satisfied, the ghost-loop contribution can even become negative. In order to find solutions we begin with very small couplings ($\alpha(\mu^2) = 0.01$) and find self-consistent solutions. The coupling is then increased adjusting the new parameter N in eq. (4.140) such that we have solutions. The effects are non-trivial since N appears in both the ghost equation and the ghost-loop term of the gluon equation. The non-

linear nature of the equations makes it difficult to predict *a priori* which values of N lead to solutions, however making small steps in the parameter values, re-solving for the ghost and gluon equations self-consistently at each step and checking the behaviour of the polarisation functions in the IR leads us to the parameters given in table 4.3 which correspond to the solutions depicted in figure 4.16.

Parameter	Value
μ^2	1000 GeV^2
ν^2	1000 GeV^2
$\alpha(\mu^2)$	0.065
$\mathcal{G}l(\mu^2)$	1
$\mathcal{G}h(\nu^2)$	1
Λ^2_{IR}	1 GeV^2
N	6.5

Table 4.3.: The parameters used for Solution Set 4.

The form of the ghost-gluon vertex from eq. (4.140) is unfortunately not particularly useful in this truncation. This leads to a number of possible conclusions, either the solution of the WSTI is not a sensible one, that the terms neglected from the four-ghost term are important. Alternatively, these ghost-gluon vertex dressings could be sensible and it is the one-loop-only truncation that is at fault and the additional diagrams in the gluon equation give important contributions. Finally it is even possible that some complex unforeseen structures arise in the triple-gluon vertex dressings conspire to make the gluon polarisation positive in the IR region at larger couplings.

4.4. Lattice QCD

In recent years a complementary technique where the equations of QCD are solved on a four-dimensional lattice using discretised Euclidean spacetimes and a a finite number of spacetime points, have achieved impressive results using increasingly improved algorithms and improved computers. The lattice technique is not presently computationally practical for the light quarks observed in nature and often lattice results are calculated for the pure gauge part of QCD as we have done here. Furthermore, the calculations they perform should be directly comparable to our own since they are usually carried out in Landau

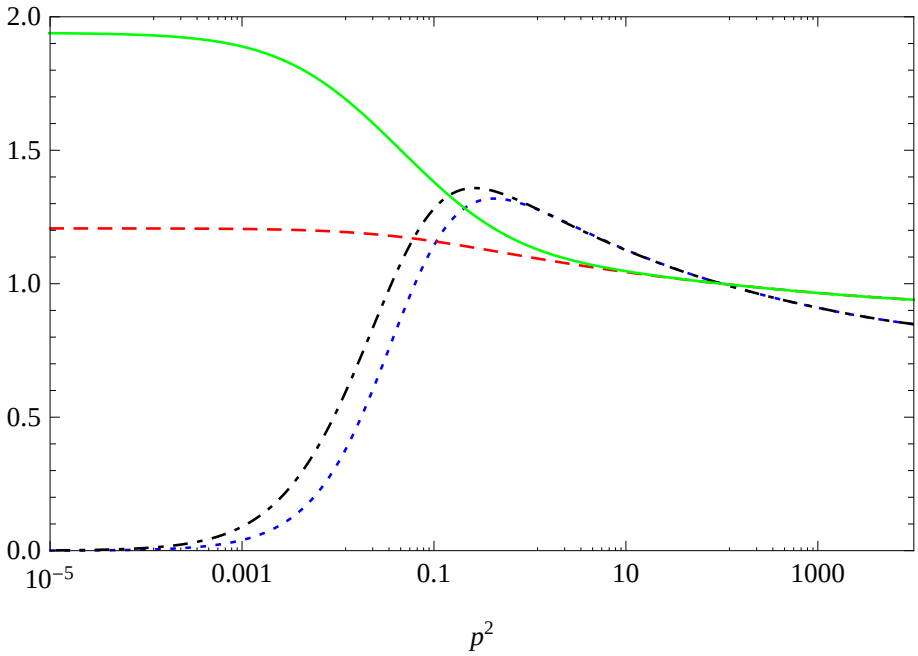

Figure 4.16.: The Set 4 Solutions. Also shown with a new version of Set 1, denoted Set 1*, where $\alpha(\mu^2) = 0.09$ has been used for direct comparison. Similarly to Set 3 we notice a large enhancement of the ghost dressing in the IR caused by the additional term in the function $\alpha(k, p, q)$. Set 1* Gluon (Blue, Dotted), Set 1* Ghost (Red, Dashed), Set 3 Gluon (Black, Dot-dashed), Set 3 Ghost (Green, Solid).

gauge and in Euclidean space. There are many differences also, some rather technical related to the existence of Gribov copies and how this could have different effects in different methods. The lattice can potentially suffer from finite volume effects and finite spacing effects that do not vanish after the calculation when the continuum limit is taken. The lattice should in principle include effects that would be contained within the two-loop dressed graphs, which we have deliberately neglected. However, this does not stop us comparing results.

The lattice solutions given in [125,126] are taken and fitted with a smooth curve. Starting from solution Set 1, using eq. (4.101) for the ghost-gluon vertex and eq. (4.76) for the triple-gluon vertex. We then tune a set of parameters, (see table 4.4) such that we obtain something close to that given by the lattice. The subtraction and renormalisation point is set to a point where both of the lattice dressing functions are roughly 1, doing a simple logarithmic extrapolation we find a value of $\mu^2 \simeq 650$ GeV^2 the position of the peak of the gluon propagator roughly fixes the value of $\Lambda_{\rm IR}$ and the coupling can be fixed by choosing a value that best matches the data overall or fixing at some specific point on the dressing functions. We will often use the latter option and fix the coupling by tuning the IR value of the ghost dressing. There are two ways to present the gluon propagator dressing function. In this work and most SDE studies it is the function multiplying the bare propagator that is given, $\mathcal{G}l(p^2)$ however in many lattice studies the quantity $\mathcal{G}l(p^2)/p^2$ is given which is usually finite for vanishing p^2.

The functions are fitted manually by adjusting the free parameters in order to get the best agreement with the data. The gluon data is considered twice, once with $\mathcal{G}l(p^2)$ which emphasises the UV points and once with $\mathcal{G}l(p^2)/p^2$ which puts emphasis on the IR. This is repeated for all of the combinations of vertices tested above. Many of these are discarded because only very poor fits can be obtained.

We now consider three combinations of vertices in the standard one-loop-only truncation. First we attempt to tune the parameters for the Set 1 vertices, using the triple gluon-vertex given by eq. (4.77) and the ghost-gluon vertex given by eq. (4.101). For the solution sets B-D we use the triple gluon-vertex given by eq. (4.77) and the ghost-gluon vertex given by eq. (4.138), and for solution sets E and F we use the triple gluon-vertex given by eq. (4.79) and the ghost-gluon vertex given by eq. (4.101). We find qualitative agreement over a range of parameters as shown in table 4.4.

Parameter	Sol A.	Sol. B	Sol. C	Sol. D	Sol. E	Sol. F
μ^2 [GeV^2]	650	650	650	650	650	650
ν^2 [GeV^2]	650	650	650	650	650	650
$\alpha(\mu^2)$	0.1347	0.1253	0.1257	0.1363	0.1603	0.1665
$\mathcal{G}l(\mu^2)$	1	1	1	1	1	1
$\mathcal{G}h(\nu^2)$	1	1	1	1	1	1
$\Lambda^2_{\rm IR}$ [GeV^2]	12	7	12	24	2.75	4

Table 4.4.: The parameters used for the lattice solutions.

Unfortunately none of the solutions presented here naturally reproduce all of the lattice data to any degree of precision. The triple-gluon vertex used for solutions E and F, given by eq. (4.79) allows the gluon peak, when plotted as $\mathcal{G}l(p^2)$, to be most accurately reproduced however when comparing with the actual lattice data plotted as $\mathcal{G}l(p^2)/p^2$ the behaviour in the transition to the IR has a strange peak, see fig 4.19. Similar effects have been seen elsewhere using this form of vertex [83, 85]. This is a good reason, along with the lack of symmetry between legs, and having a different form to that given by any of the WSTI solutions, to reject this form vertex, however the correct reproduction of the perturbative one-loop running is appealing. There may also be a problem with all of the ghost-gluon vertices used. The value of $\Lambda_{\rm IR}$ used is always larger than would be expected if it is to be associated with $\Lambda_{\rm QCD}$ which in a MOM scheme is always less than 1 GeV^2. The lattice solutions are not necessarily matched to a physical scale, any matching would still be questionable due to the lack of quarks in these treatments, however they are solved at $\beta = 6/g^2 = 5.7$, which corresponds to a smaller coupling than used here. This could be due to the extrapolation that we have applied, or it could be due to finite spacing effects giving an incorrect log running in the UV. The gluon naturally matches the one-loop resummed form in the lattice solutions, but the ghost does not match completely smoothly. There have been many discussions on finite volume, finite spacing and gauge fixing effects [85, 127–129], and the indications are that the lattice should find solutions of this qualitative form, regardless of whether the corresponding infinite volume SDEs have a finite or divergent IR behaviour.

We must also bear in mind that these equations are coupled and any effects that lead to one equation not matching will lead to a corresponding effect in the other equation, so in order to unravel the differences it may be important to consider the equations individually. At present this isn't necessary because the ghost is always fairly well reproduced (except for solution A).

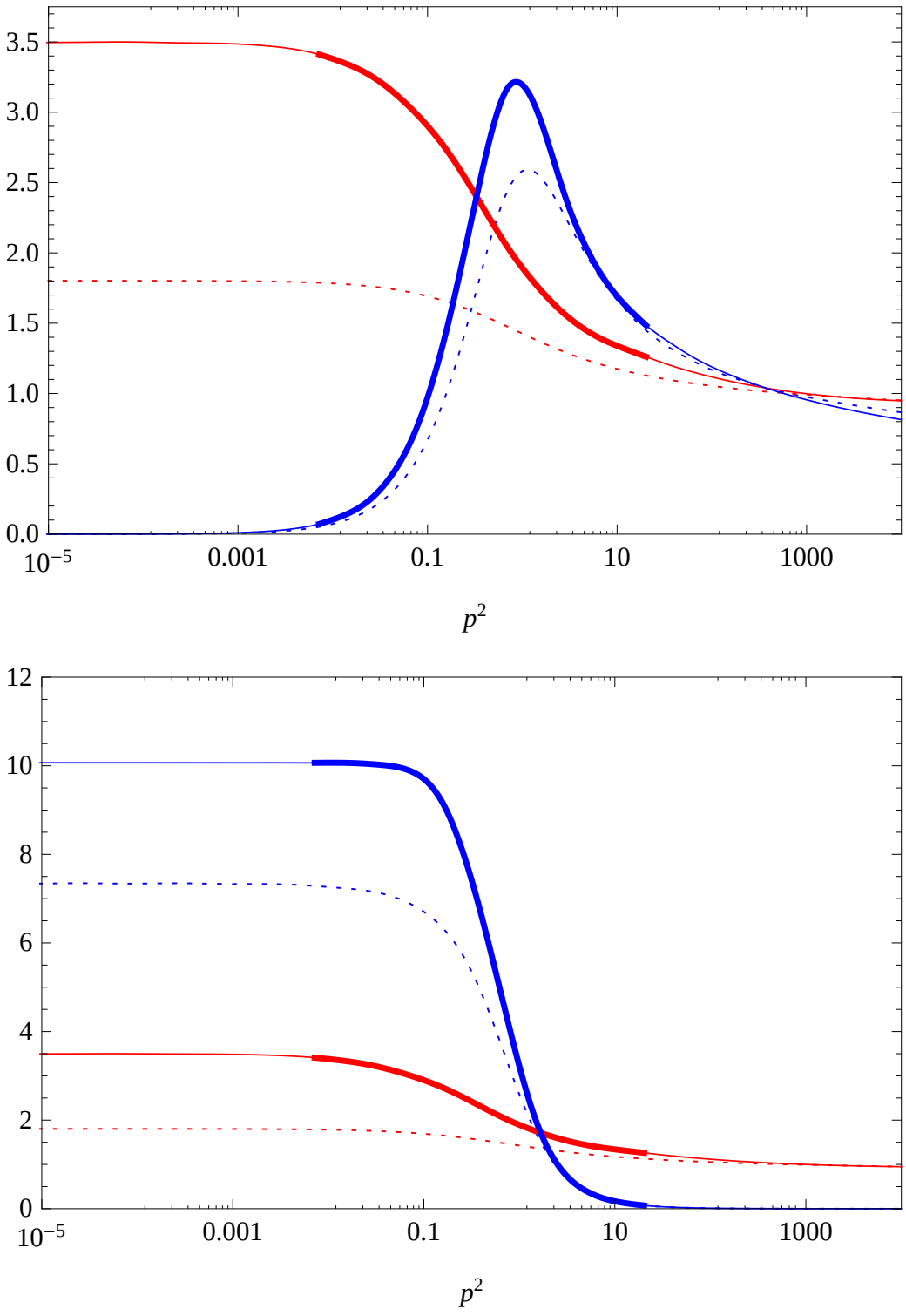

Figure 4.17.: Lattice Fits using the triple gluon-vertex given by eq. (4.77) and the ghost-gluon vertex given by eq. (4.101). The heavy solid lines represent the lattice data, the feint lines are extrapolations. Dotted curve is Set A. (Blue: Gluon, top plot $\mathcal{G}l(p^2)$, bottom plot $\mathcal{G}l(p^2)/p^2$, Red, both plots IR $\simeq 3.5$ curves: Ghost $\mathcal{G}h(p^2)$.)

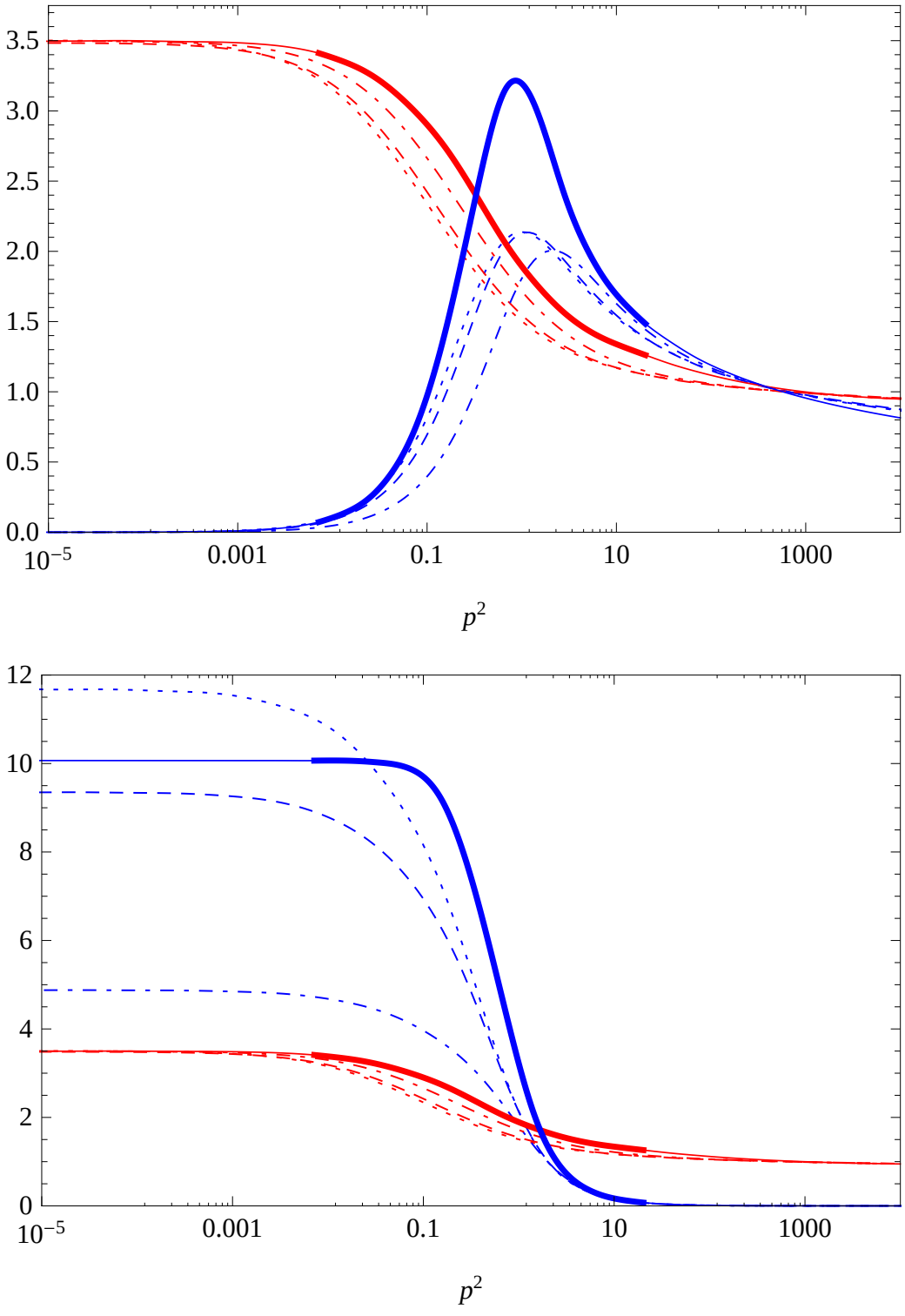

Figure 4.18.: Lattice Fits using the triple gluon-vertex given by eq. (4.77) and the ghost-gluon vertex given by eq. (4.138). The heavy solid lines represent the lattice data, the feint lines are extrapolations. Dotted Set B, Dashed Set C, Dot-dashed Set D. (Blue: Gluon, top plot $\mathcal{G}l(p^2)$, bottom plot $\mathcal{G}l(p^2)/p^2$, Red, both plots IR $\simeq 3.5$ curves: Ghost $\mathcal{G}h(p^2)$.)

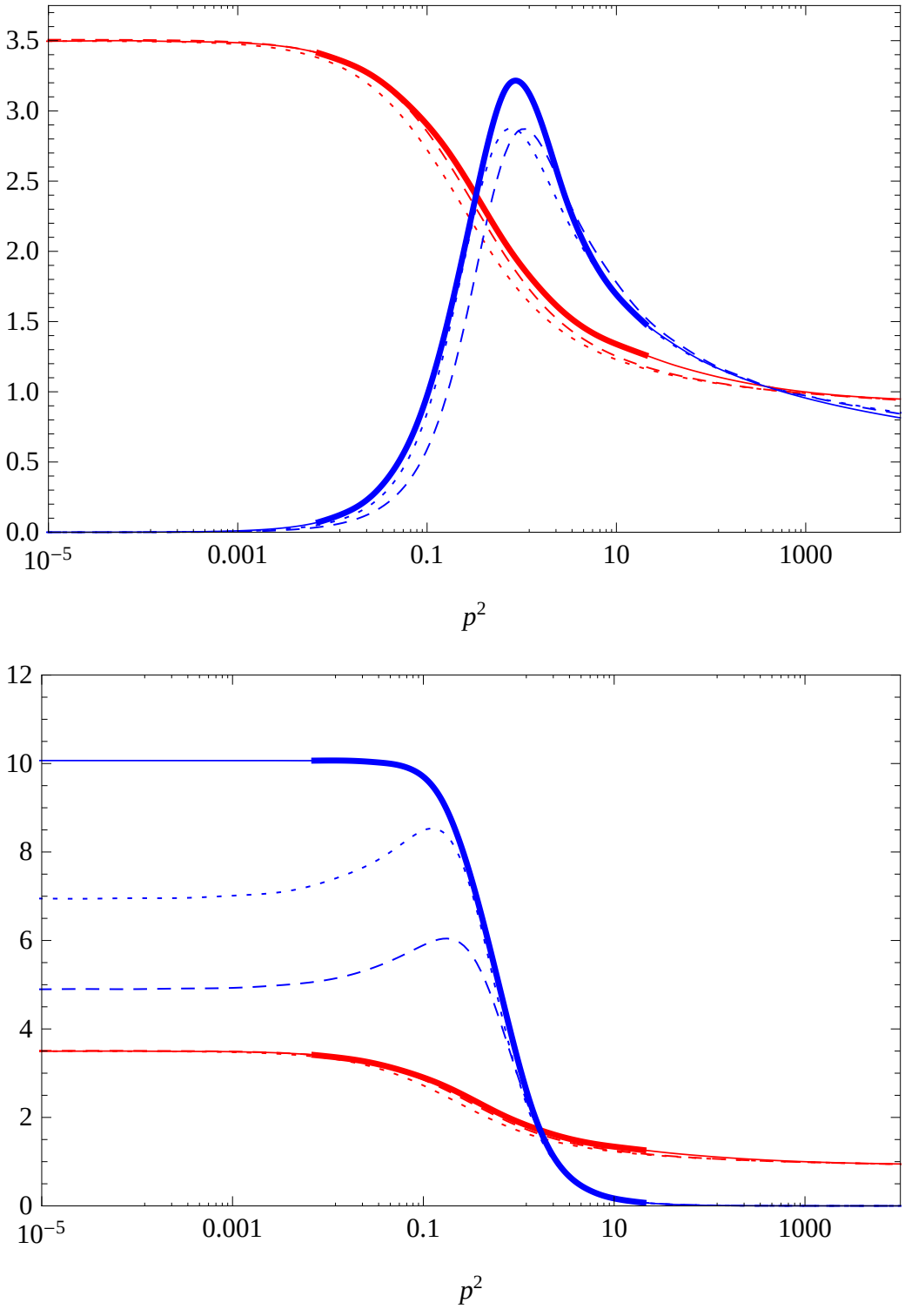

Figure 4.19.: Lattice Fits using the triple gluon-vertex given by eq. (4.79) and the ghost-gluon vertex given by eq. (4.101). The heavy solid lines represent the lattice data, the feint lines are extrapolations. Dotted Set E, Dashed Set F. (Blue: Gluon, top plot $\mathcal{G}l(p^2)$, bottom plot $\mathcal{G}l(p^2)/p^2$, Red, both plots IR $\simeq$ 3.5 curves: Ghost $\mathcal{G}h(p^2)$.)

4.5. Conclusion

In solving the SDEs of QCD we encountered many questions, new and old, which we have yet to find clear conclusions for. In all likelihood the issues that we give below are interconnected and many will only be resolved by performing a much more complete treatment of the Schwinger–Dyson equation for the gluon propagator dressing function.

4.5.1. Triple-Gluon Vertex dressing

Two forms were considered for the triple-gluon vertex dressing,

1. Vertex proportional to $\mathcal{G}h/\mathcal{G}l$
   - Naturally arises in WSTI studies.
   - Satisfies Multiplicative Renormalisability and removes vertex renormalisation constant Z_1 in Landau gauge.
   - Incorrect resummed logarithmic running when used in Gluon loop.
2. Vertex proportional to $\mathcal{G}h^2/\mathcal{G}l^2$
   - Leads to a logarithmic running consistent with the ghost-loop in the gluon equation, the ghost equation and 1-loop perturbation theory, if considered alone.
   - If combined with the WSTI then this is not the case since it implies that the ghost-gluon scattering kernel must have dressings of the form,

     $$\tilde{\Gamma}_{\mu\nu} \sim \mathcal{G}h/\mathcal{G}l\, g_{\mu\nu} + \dots , \tag{4.141}$$

     which in turn implies ghost-gluon vertex dressings of the same form. If these vertices are then used in the ghost-loop and the ghost equation then the one-loop running becomes inconsistent.
   - Leads to additional renormalisation factors to cancel the dressings in the gluon loop.
   - Vertices of this type with Bose symmetry have not been found to lead to self-consistent solutions.

A fair conclusion appears to be that $\mathcal{G}h/\mathcal{G}l$ is the preferred dressing, but more work is needed to resolve the one-loop running issue.

4.5.2. Ghost-Gluon Vertex dressing

We considered a range of forms for this vertex, driven by practical reasons (are solutions obtainable?) and theoretical reasons (WSTI, the running coupling, Taylor's Theorem). The results again are not conclusive but are step forward. In this study, considering forms already in existence in the literature, we have used this vertex to drive the gluon propagator dressing as p^2 in the IR limit. This arises naturally if the ghost loop digram alone is transverse in the IR, which only occurs if all other terms are vanishing. This was found not to be the case for any of the triple-gluon dressings informed by WSTIs, both terms are found to be of similar order so the ghost loop diagram does not need to be transverse alone. Extensions are considered with additional terms that ensure Taylor's theorem ($\alpha - \beta = 1$) is satisfied. This is driven by the practical reason that solutions should be obtainable in this, one-loop-only, truncation. This may not be the case, it is entirely possible, and even likely, that large contributions of leading order in the IR limit arise from the two-loop diagrams. This serves as a caveat to many of the conclusions regarding this vertex.

1. Bare or minimally dressed vertex with no singularities.
    - Solutions are not obtainable
    - Preferred by WSTI.
    - Allows for a simpler definition of the running coupling, with no or little contribution from the vertex dressing.
2. Transverse dressing
    - Solutions are obtainable.
    - Violates Taylor's Theorem.
    - Running coupling not well defined, particularly sensitive to vertex modelling with $\mathcal{F}_{\mathrm{IR}}$.
    - Scale Λ_{IR} often too large to be compared with Λ_{QCD}

3. Modified Transverse dressing

   - Solutions are obtainable for a limited range of parameters.
   - Respects Taylor's Theorem.
   - Running coupling particularly sensitive to vertex modelling with $\mathcal{F}_{\mathrm{IR}}$.
   - Scale Λ_{IR} often too large to be compared with Λ_{QCD}
   - Singular structure is not expected, and may be unphysical. It would not be allowed in QED.

4.5.3. Final Words

The Schwinger–Dyson Equations of QCD were investigated using a minimal truncation that ensures the solutions do not manifestly break gauge invariance. We find a ghost propagator dressing function that is finite in the vanishing momentum limit and a gluon propagator dressing function that vanishes like p^2 as $p^2 \to 0$. We do not find an infinite ghost type solution.

Significant effort has been devoted to this one-loop only truncation and whether solutions are obtainable became an important consideration. A number of forms for the ghost-gluon vertex have been investigated that provide solutions but have the unexpected property of containing a singular term. This is necessary to provide the p^2 behaviour that is required by the ghost equation and in order to obtain solutions similar to those found on the lattice. The main limitation and source of uncertainty in this study is the lack of two-loop terms in the equation for gluon propagator, these could easily provide the required contributions that have here been attributed to the ghost-gluon vertex. A study of these terms has begun and some preliminary details are given in the following chapter.

Chapter 5.

Outlook for Landau Gauge SDE studies in QCD

In this study of the SDEs of QCD, it was found that the ghost-gluon vertex in the one-loop-only truncation is a very important object. This is the most natural place where large positive contributions can arise to make the gluon equation solvable. In the infinite-ghost solutions this is what happens, however in the finite solutions that appear to be favoured by the lattice we require a similar contribution to be produced by the ghost-gluon vertex, that becomes large as the gluon momentum vanishes.

It is not clear if this requirement is due to physical reality or a by-product of dropping the two-loop diagrams; a full analysis of both contributions is necessary to fully understand the structure of the gluon equation.

5.1. Ghost-Gluon Vertex

The ghost-gluon vertex in the Landau gauge was always supposed to be simple, and compared to other gauges it almost certainly is due to it only receiving finite renormalisations. However, if the one-loop-only truncations are meant to be taken seriously then significant non-perturbative effects must arise. Taking into consideration Taylor's Theorem [94] and the truncated Ward-Slavnov-Taylor Identity [94,100,130] then the solutions found for the ghost-gluon vertex have not been found to permit solutions at non-perturbative couplings. This could be due to either the truncation of the WSTI by neglecting the four-ghost scattering terms thus invalidating the solution, or alternatively, it could be that this is not the correct place to generate the large positive contribution required in the gluon-equation,

and the required contribution must then be due to the dressed two-loop diagrams whose solution has all but been neglected in SDE studies to date due to their high numerical complexity [83].

A natural place to turn to shed light on this vertex is the Schwinger-Dyson equation for the vertex itself. This may be truncated to obtain a relatively simple form that should be solvable numerically, and preliminary studies of this quantity have shown that significant non-zero contributions can arise in the longitudinal terms after just one natural iteration, using dressed propagator inputs [131]. This has been investigated only using the infinite-ghost scaling solutions at present and no fully self-consistent solutions have been obtained. There are numerous difficulties that are present and some of the problems found here are the same as those found in attempts to solve the two-loop diagrams.

5.2. Two-loop diagrams

The two-loop diagrams have never been fully included in the gluon propagator. Attempts have been made to quantify their effects [83] but a full numerical analysis has never been performed. Neglecting these terms is quite a severe approximation since there are no power-counting or expansion schemes that suggest why they are subleading. Indeed, we know that their inclusion is mandatory in order to correctly reproduce the NNLO ($\mathcal{O}(g^4)$) perturbative behaviour. The integration kernels are straightforward to calculate, either by hand or making use of some algebraic system. Following ref. [83], we refer to the polarisation contribution due the the sunset diagram as $\Pi_{3g}(p^2)$ and that due to the crescent diagram as $\Pi_{4g}(p^2)$. The propagator momenta and diagram notation are as defined in the relevant terms of figure 4.2. We leave the relation of the loop momenta to the propagator momenta undefined, the only restriction is to conserve momentum but the specific choice can simplify a numerical procedure. We begin with the sunset diagram and for simplicity we use only bare lorentz structures in the vertices. This diagram turns out to be relatively simple since the bare four-gluon vertex has no momentum dependence and the kernel function is symmetric on interchange of any pair of gluon propagator momenta. The bare vertices may be improved in the usual manner by multiplying sensible ratios of

propagator dressings,

$$\begin{aligned}\Pi_{3g}(p^2) =& 2\frac{g^4 N_c^4}{(2\pi)^8}\int d^d\ell_a \int d^d\ell_b \frac{\mathcal{G}l(\ell_1^2)\mathcal{G}l(\ell_2^2)\mathcal{G}l(\ell_3^2)}{p^2\ell_1^2\ell_2^2\ell_3^2}\times \\ &\Big\{3\ell_1.\ell_2\,\ell_2.\ell_3\,\ell_3.\ell_1 + 3((d-8)d+17)p^2\ell_1^2\,\ell_2^2\,\ell_3^2 \\ &+ 4(d-5)\left[\ell_1.p^2\,\ell_2^2\,\ell_3^2 + \ell_2.p^2\,\ell_3^2\,\ell_1^2 + \ell_3.p^2\,\ell_1^2\,\ell_2^2\right] \\ &+ \left(4(p.\ell_1)^2 + (d-8)\ell_1^2p^2\right)(\ell_3.\ell_2)^2 - 4\ell_1.p\ell_2.p\left[\ell_2.\ell_3\,\ell_1.\ell_3 - 3\ell_1.\ell_2\,\ell_3^2\right] \\ &+ \left(4(p.\ell_2)^2 + (d-8)\ell_2^2p^2\right)(\ell_1.\ell_3)^2 - 4\ell_2.p\ell_3.p\left[\ell_3.\ell_1\,\ell_2.\ell_1 - 3\ell_2.\ell_3\,\ell_1^2\right] \\ &+ \left(4(p.\ell_3)^2 + (d-8)\ell_3^2p^2\right)(\ell_2.\ell_1)^2 - 4\ell_3.p\ell_1.p\left[\ell_1.\ell_2\,\ell_3.\ell_2 - 3\ell_3.\ell_1\,\ell_2^2\right]\Big\}. \end{aligned} \tag{5.1}$$

The crescent diagram cannot be written in such a simple form which is just due to the asymmetric structure, there should however be a symmetry between ℓ_1 and $-\ell_3$ so we divide the momentum external to this loop equally between each propagator, $\ell_1 = \ell_a - \frac{\ell_4}{2}$

and $\ell_3 = \ell_a + \frac{\ell_4}{2}$,

$$
\begin{aligned}
\Pi_{4g}(p^2) = \frac{g^4 N_c^2}{(2\pi)^8}\frac{3}{4}\int d^d\ell_a \int d^d\ell_b \frac{\mathcal{G}l(\ell_1^2)\mathcal{G}l(\ell_2^2)\mathcal{G}l(\ell_3^2)\mathcal{G}l(\ell_4^2)}{p^2\ell_1^4\ell_2^4\ell_3^4\ell_4^4}\times \\
\Bigg\{ \ell_4^2(\ell_4^2-4\ell_a^2)(\ell_4^2p^2-\zeta\ell_4.p^2)\ell_2.\ell_a^2 + 2\ell_4^2(\ell_4^2-4\ell_a^2)\ell_2.\ell_a\times \\
\Big[p.\ell_2\ell_4.\ell_a\left(\zeta p.\ell_4-(d-2)p^2\right)+\ell_2.\ell_4\left(\zeta p.\ell_4 p.\ell_a+(d-\zeta-3)\ell_4.\ell_a p^2\right)-(d-2)\ell_2^2\ell_4.\ell_a p^2\Big] \\
+\Bigg[\left\{\zeta p.\ell_a^2+2\ell_a^2p^2(\zeta+2-2d)\right\}\ell_4^6+\Bigg\{(2d-5)\zeta\ell_a^2p.\ell_4^2 \\
+\left(2(d-4)\zeta\ell_4.\ell_a p.\ell_a+(2d-1)\ell_a^2p^2\right)p.\ell_4+8\ell_a^4p^2(4+\zeta-2d) \\
+2\ell_4.\ell_a p^2\left((2d-\zeta-2)\ell_4.\ell_a+(d-2)p.\ell_a\right)+\ell_a^2\left((1-2d)\ell_2.\ell_4p^2-4\zeta p.\ell_a^2\right)\Bigg\}\ell_4^4 \\
+\Bigg\{\left[4\zeta(3-d)p.\ell_4^2+(5-4d)p^2\,p.\ell_4+p^2\left\{(4d-5)\ell_2.\ell_4+8\ell_a^2(2d-\zeta-4)\right\}\right]\ell_4.\ell_a^2 \\
-8\ell_a^2p.\ell_a\,\ell_a.\ell_4\left((d-4)\zeta p.\ell_4+(d-2)p^2\right)+4\ell_a^4\left[(2d-7)\zeta p.\ell_4^2+(2d-3)(p.\ell_4-\ell_2.\ell_4)p^2\right]\Bigg\}\ell_4^2 \\
+\zeta p.\ell_2\Bigg\{\left[(2d-1)p.\ell_4\ell_a^2+2(d-2)\ell_a.\ell_4p.\ell_a\right]\ell_4^4-\left[4\ell_4.\ell_a^2p.\ell_4\ell_a^2\right] \\
+\left[(5-4d)p.\ell_4\,\ell_4.\ell_a^2-8(d-2)\ell_a^2\,p.\ell_a\,\ell_4.\ell_a+4(2d-3)p.\ell_4\ell_a^4\right]\ell_4^2\Bigg\}+4\ell_4.\ell_a^2p^2\ell_a^2(\ell_2.\ell_4-p.\ell_4)\Bigg] \\
+\ell_2.\ell_4\Bigg[p.\ell_2\Bigg\{\left(4\zeta p.\ell_4\ell_a^2+(1-2d)p^2\ell_a^2+2\zeta\ell_4.\ell_a p.\ell_a\right)\ell_4^4+4\ell_4.\ell_a^2\ell_a^2p^2\Bigg\} \\
-\ell_2.\ell_4\ell_4^2\left\{\ell_4^2\left[\zeta p.\ell_a^2+(2\zeta-2d+3)\ell_a^2p^2\right]\right. \\
\left.+\,4\left[(d-\zeta-2)p^2\ell_4.\ell_a^2-\zeta\ell_a^2\,p.\ell_a^2+(2\zeta-2d+5)\ell_a^4p^2\right]\right\}\Bigg]\Bigg\}. \qquad (5.2)
\end{aligned}
$$

Preliminary analyses performed using an extended version of our numerical program have shown that these diagrams although subleading in the UV can have an important contribution in the IR. There are some singularities in certain kinematic regions that need to be dealt with and there is also the problem of nested logarithmic divergences that must be considered carefully. A simple resolution of these issues is still required.

Chapter 6.

Conclusion

In chapters 2 and 3 we investigated the behaviour of two light scalar resonances, the $\sigma(600)$ and the $f_0(980)$, both observed in low energy QCD in $\pi\pi$ scattering. There are many scalars in QCD, many more in fact than might initially be expected, but dynamical models suggest [37,79] that the $\overline{q}q$ *seeds* for the scalars lie around 1.4 GeV [30–32,37] and coupling to decay channels pulls their pole masses towards the relevant threshold. In chapter 2 we found that the dominant four–quark component of the $\sigma(600)$ at $N_c = 3$ [31, 44, 45] gives way to a pole above 1.2 GeV and that this is neccessary for semi-local duality to be upheld for $N_c > 3$. In chapter 3 we found that the dominant component of the $f_0(980)$ is that of a molecular $K\overline{K}$ bound state due to only a single pole being required for its scattering amplitude. This does not neccessarily exclude the possibility of the state being *seeded* by some higher pole and being pulled towards $K\overline{K}$ threshold by a stong coupling to the decay channel. However, its composition at N_c is clear, and that is that it is governed by a long-range force between two compact K mesons.

In chapter 4 we began a study to investigate the properties of QCD from the fundamental Lagrangian utilising a truncated Schwinger–Dyson Equation. The main conclusions drawn were that previous truncations may be at fault since transversality of the gluon propagator has been violated which may be observed by the different solutions (or lack of) obtained when solving the equations for the $g_{\mu\nu}$ term in the propagator or the $p_\mu p_\nu$ term. It was also observed that the effects of both the ghost-gluon and triple-gluon vertices are highly non-trivial and the bare vertices are insufficient. Firm conclusions await an analysis of the two–loop diagrams in the gluon propagator Schwinger–Dyson equation.

Appendix A.

Parameters for the $f_0(980)$ fits

A.1. Jost

The best fit Jost-function parameters for the various fits are given in table A.1 below.

Parameter	Fit 1.	Fit 2.	Fit 3.	Fit 4.
$\lvert k_2^{(1p)}\rvert$	0.12298	0.11395	0.13109	0.12052
$\mathrm{Arg}(k_2^{(1p)})$	153.86	151.06	145.85	140.85
$\lvert k_2^{(2p)}\rvert$	–	–	–	–
$\mathrm{Arg}(k_2^{(2p)})$	–	–	–	–
$\mathrm{Re}(\gamma_0)$	–	–	–	–
$\mathrm{Im}(\gamma_0)$	3.1962	3.1661	3.2330	3.2188
$\mathrm{Re}(\gamma_1)$	0.26139	0.50813	0.28270	0.47542
$\mathrm{Im}(\gamma_1)$	-0.30590	-0.09956	-0.21554	-0.00909
$\mathrm{Re}(\gamma_2)$	–	–	–	–
$\mathrm{Im}(\gamma_2)$	3.1227	4.3910	3.1517	4.5415
$\mathrm{Re}(\gamma_3)$	–	-8.5979	–	-11.254
$\mathrm{Im}(\gamma_3)$	–	-3.3223	–	-0.90109

Table A.1.: Pole positions and fits. Any dimensionful quantites are in GeV.

A.2. Flatté

The best fit Flatté parameters corresponding to fit 7 are given in table A.2.

Parameter	Fit 7.
m_0	0.750 GeV
g_1^2	0.555 GeV^2
g_2^2	2.74 GeV^2
$\phi_1^{(0)}$	73.9°
$\phi_1^{(1)}$	37.5°
$\phi_2^{(0)}$	2.78°
$\phi_2^{(1)}$	−53.1°

Table A.2.: The Flatté parameters.

A.3. Amplitude Argand Plot

A useful representation of the amplitudes is to plot the path taken by T_{ij} in the complex plane. We give an example of this in figure A.1.

The curve begins at the lower limit of our fitting region where $E \simeq 0.87$ GeV, around $\mathrm{Arg}(T_{11}) = \pi/2$ and $|T_{11}| = 1$ at the top of figure A.1 and the phase increases to $\mathrm{Arg}(T_{11}) = \pi$ in the region of $K\overline{K}$ threshold which is visible by the first sharp kink from the unitarity circle.

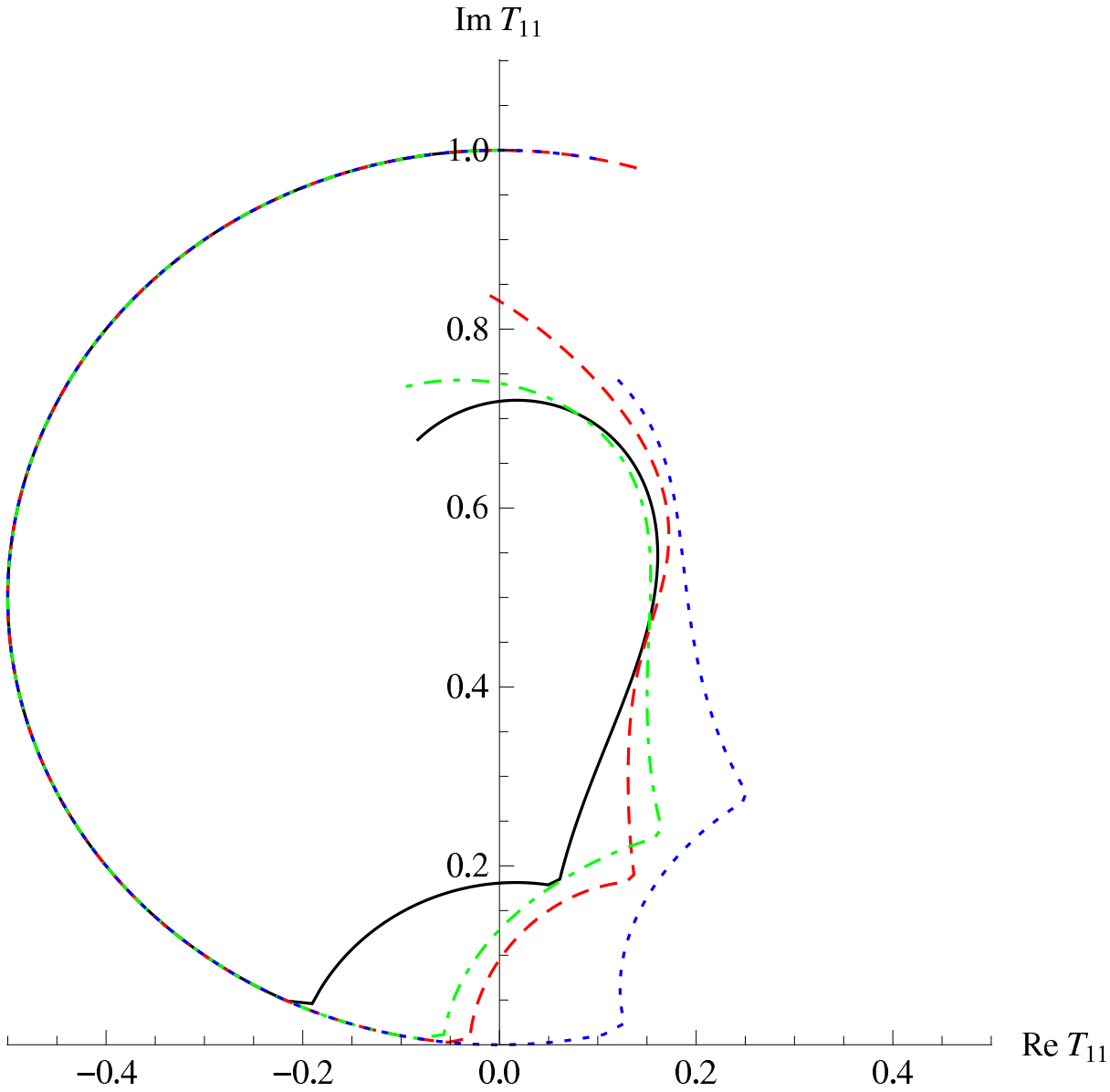

Figure A.1.: Argand plots of T_{11}, for Fit 1 (Black), Fit 2 (Red, Dashed), Fit 5 (Green, Dot-dashed), Fit 6 (Blue, Dotted).

Appendix B.

Feynman Rules and Notation

B.1. Bare Propagators and Vertices

The following definitions are used for the Feynman rules throughout this thesis, delta functions on the momenta of the vertices are implicit,

$$D^{(0)}_{\mu\nu}(p) = \frac{1}{p^2}\left(g_{\mu\nu} - \frac{p_\mu p_\nu}{p^2}\right) + \xi\frac{p_\mu p_\nu}{p^4} \tag{B.1}$$

$$D^{(0)}(p) = \frac{-1}{p^2} \tag{B.2}$$

$$\Gamma^{(0)abc}_{\mu\nu\rho}(k,p,q) = igf^{abc}\left(g_{\mu\nu}(k-p)_\rho + g_{\nu\rho}(p-q)_\mu + g_{\rho\mu}(q-k)_\nu\right) \tag{B.3}$$

$$\Gamma^{(0)abc}_{\mu}(k,p,q) = igf^{abc}q_\mu \tag{B.4}$$

In some truncations, a factorised dressing is applied where the bare Lorentz structure for the triple-gluon vertex, is used but multiplied by some propagator dressings. It is useful to define the quantity,

$$\Gamma_{\mu\nu\rho}(k,p,q) = g_{\mu\nu}(k-p)_\rho + g_{\nu\rho}(p-q)_\mu + g_{\rho\mu}(q-k)_\nu. \tag{B.5}$$

The bare four-gluon vertex is very simple, the bare form contains no momentum dependence and we have not considered any dressed forms,

$$\begin{aligned}\Gamma^{(0)abcd}_{\mu\nu\rho\sigma} = g^2\,[\, & f^{abe}f^{cde}\left(g_{\mu\rho}g_{\nu\sigma} - g_{\mu\sigma}g_{\nu\rho}\right) + \\ & f^{ace}f^{bde}\left(g_{\mu\nu}g_{\rho\sigma} - g_{\mu\sigma}g_{\nu\rho}\right) + \\ & f^{ade}f^{bce}\left(g_{\mu\nu}g_{\rho\sigma} - g_{\mu\rho}g_{\nu\sigma}\right)\,].\end{aligned} \tag{B.6}$$

Appendix C.

Numerical Procedure

There are two largely separater numerical problems to solve, the first is the integration and the second the iterative procedure. We integrate numerically upto some momentum cutoff $\ell^2 = \kappa^2$. This is a safe thing to do with the subtracted equations, our loop integration becomes,

$$\int d^4\ell \to \frac{1}{2\pi} \int_0^{\kappa^2} d\ell^2 \, \ell^2 \int_0^{\pi} d\theta \sin^2\theta \tag{C.1}$$

this may be performed using standard quadrature techniques using a small linear piece in the IR region, and a logarithmic scale for the rest, with a break at $l^2 = p^2/4$ where some of the angular integrands have a kink which would result in lost accuracy from a numerical quadrature method.

The iterative procedure we use is the Newton-Raphson method. We represent our functions using Chebychev polynomials and some appropriate mapping for our momentum region. We then do the usual Taylor expansion and calculate corrections to our coeffiecients using the first derivative and neglecting higher terms. This results in a stable iterative procedure that works well from a wide range of starting functions. These solutions however are particularly stable and may be obtained using a natural iterative procedure also, the Newton-Raphson procedure however works reliably for a wider range of starting functions. Typical starting forms we have used are the lattice solutions or the form,

$$\mathcal{G}l(p^2) = \left(\frac{p^2}{p^2 + \lambda^2} \right)^a \tag{C.2}$$

for the gluon and a constant for the ghost. For $0 < a \leq 1$ we find that $a = 1$ is returned from the iterative procedure. For other values the iterative procedure does not always converge. The equations naturally reproduce the logarithmic running in the large momentum limit, provided self-consistent solutions are found.

C.1. Integrations

C.1.1. Volume Integrals

The volume integral for closed loops is,

$$\int \frac{d^d\ell}{(2\pi)^d} \tag{C.3}$$

we typically work in 4-dimensional Euclidean space which allows the insertion,

$$\int \frac{d^d\ell}{(2\pi)^d} \to \frac{1}{(2\pi)^4}\frac{1}{2}\int_0^\infty d\ell^2\ell^2 \int_0^\pi d\psi\, \sin^2\psi \int_0^\pi d\theta\, \sin\theta \int_0^{2\pi} d\phi \tag{C.4}$$

For propagator integrals, there is a dependence on only one angle, hence both θ and ϕ are symmetric so this reduces to,

$$\int \frac{d^d\ell}{(2\pi)^d} \to \frac{1}{(2\pi)^3}\int_0^\infty d\ell^2\ell^2 \int_0^\pi d\psi\, \sin^2\psi \tag{C.5}$$

the angle ψ is defined by the angle between the external momenta p^μ, and the loop momenta ℓ^μ, $\ell.p = (\ell^2 p^2)^{1/2}\cos\psi$. In order to perform vertex integrals and the inner parts of the propagator integrals a second angle is required,

$$\int \frac{d^d\ell}{(2\pi)^d} \to \frac{1}{(2\pi)^3}\frac{1}{2}\int_0^\infty d\ell^2\ell^2 \int_0^\pi d\psi\, \sin^2\psi \int_0^\pi d\theta\, \sin\theta \tag{C.6}$$

we now choose our external momenta as k^μ and q^μ, we define,

$$k.q = (k^2 q^2)^{1/2}\cos\gamma, \tag{C.7}$$

the following choice is arbitrary, but it follows that,

$$\ell.k = (k^2\ell^2)^{1/2}\cos\psi, \tag{C.8}$$

$$\ell.q = (q^2\ell^2)^{1/2}\left(\cos\psi\cos\gamma + \sin\psi\sin\gamma\cos\theta\right), \tag{C.9}$$

this is applicable either in the vertex integrations where only a single loop integration is necessary or when nested in the two-loop terms where then either q or k would be replaced by the integration variable.

C.1.2. Numerical Integration

We integrate up to some momentum-squared cutoff κ^2 in Euclidean space. The subtraction of the integrals helps with the convergence of the expressions, we always test that the results are insensitive to the cutoff. We first split the integration into two regions, $[0, \epsilon^2]$ and $[\epsilon^2, \kappa^2]$. Usually we will choose something in the region of $\epsilon^2 = 10^{-8}$ and $\kappa^2 = 10^4$. The small momentum region we perform the angular integration numerically, nested inside the momentum integration, and perform the momentum integration on a linear scale. All integrations are performed using a standard one-dimensional Gauss-Legendre quadrature method [132]. The region $[\epsilon^2, \kappa^2]$ is treated similarly except the scale is logarithmically stretched such that we make the replacement,

$$\int_{\epsilon^2}^{\kappa^2} d\ell^2 \mathcal{F}(p^2, \ell^2) \to \int_{\log\epsilon^2}^{\log\kappa^2} du\, u\, \mathcal{F}(p^2, e^u) \tag{C.10}$$

where $u = \log\ell^2$. The integration method we use works well for smooth functions however, due to the angular integrations, the momentum integration is kinked at $\ell^2 = p^2/4.d0$ due to the propagators. We choose to split the integration at this point so that we have two smooth integrals, which is numerically more efficient. Typical requirements for the number of integration points are 30 for the angular integrals which are nested inside the momentum integrals, and 5 points for the $[0, \epsilon^2]$ region and 30 for $[\epsilon^2, \kappa^2]$ region. These numbers can be increased or reduced depending on the specific problem.

C.2. Numerical Representations

The functions $\mathcal{G}l(p^2)$ and $\mathcal{G}h(p^2)$ are fortunately only functions of a single variable, for which there are many simple ways of representing them. It is important to have a smooth representation for all momenta, we choose to split the function at two points and represent the function differently in the three regions defined similarly to the integrations, $[0, \epsilon^2]$, $[\epsilon^2, \kappa^2]$ and $[\kappa^2, \infty]$. In the IR region $[0, \epsilon^2]$, the function is represented by a power law $\sim A(p^2)^a$ where $a = 0$ is a valid choice. In the intermediate region $[\epsilon^2, \kappa^2]$ the functions are represented using Chebychev polynomials that are logarithmically mapped onto the momentum region, $[-1, 1] \to [\log \epsilon^2, \log \kappa^2]$ [133, 134]. Chebychev polynomials form an orthogonal set that can be defined via,

$$T_j(s) = \cos\left(j \arccos(s)\right) \tag{C.11}$$

A truncated Chebychev expansion gives a smooth interpolation and is exact at the zeroes of the $n+1$ polynomial if we truncate the series at n. The Chebychev expansion is given as,

$$f(s) = \sum_{i=0}^{\infty} c_i T_i(s) \tag{C.12}$$

where $f(s)$ is defined on the region $[-1, 1]$, c_i are the coefficients and T_i are the Chebychev polynomials, the mapping we use is,

$$s(p^2) = \frac{1}{2} \frac{2 \log p^2 - (\log \epsilon^2 + \log \kappa^2)}{\log \kappa^2 - \log \epsilon^2}. \tag{C.13}$$

The Chebychev representation is preferred over using some other procedure, for example splines, due to the orthogonality of the representation, which allows,

$$\frac{\partial f(s)}{\partial c_j} = \frac{\partial}{\partial c_j} \sum_{i=0}^{\infty} c_i T_i(s) = T_j(s) \tag{C.14}$$

this relation will be very useful when constructing our iterative procedure.

The Chebychevs are most accurate for a flat function (for which $n = 1$ is perfectly adequate!), so it can help the convergence of the Chebychev series if we factorise some of the functional dependence, ideally we want to eliminate any rapid variation. There are two variants of this that have been applied here, both produce numerically consistent

results with $n \simeq 30$,

$$\mathcal{G}l(p^2) = \left(\frac{p^2}{p^2+\lambda_a^2}\right)^a \sum_{i=0}^{n} c_i^{(\mathcal{G}l)} T_i(s(p^2)) \tag{C.15}$$

$$\mathcal{G}h(p^2) = \left(\frac{p^2}{p^2+\lambda_b^2}\right)^b \sum_{i=0}^{n} c_i^{(\mathcal{G}h)} T_i(s(p^2)) \tag{C.16}$$

and also,

$$\mathcal{G}l(p^2) = \log\left(\sum_{i=0}^{n} c_i^{(\mathcal{G}l)} T_i(s(p^2))\right) \tag{C.17}$$

$$\mathcal{G}h(p^2) = \log\left(\sum_{i=0}^{n} c_i^{(\mathcal{G}h)} T_i(s(p^2))\right) \tag{C.18}$$

where a and b can be chosen as the require exponent for the required solution type and the λ's can be chosen around the region where the variation of the function is most rapid.

Although the integrations only run to $\ell^2 = \kappa^2$, the propagator momenta $\ell_\pm^2$ sample values greater than κ^2 so some UV extrapolation is required. For this the most natural choice is the 1-loop resummed running and this is smoothly matched at some point ν^2, in the region of κ^2 using the following formulae [85],

$$\mathcal{G}l(p^2) = \mathcal{G}l(\nu^2)\left(1 + \frac{11N_c\alpha(\nu^2)}{12\pi}\log\left(\frac{p^2}{\nu^2}\right)\right)^\gamma \tag{C.19}$$

$$\mathcal{G}h(p^2) = \mathcal{G}h(\nu^2)\left(1 + \frac{11N_c\alpha(\nu^2)}{12\pi}\log\left(\frac{p^2}{\nu^2}\right)\right)^\delta \tag{C.20}$$

where $\delta = -9/44$ and $\gamma = -1 - 2\delta$ are found from the 1-loop integrations.

C.3. Subleading components in the UV

Depending on where the functions are matched to their perturbative running, an ambiguity can be introduced that gives an additional dependence on the matching point. Typical choices for the matching point are the UV cutoff or the renormalisation point. The renormalisation point is perhaps the best choice if the running is a little off since the $\log p^2/\mu^2$ term in the running is automatically zero. If the cutoff is used and the running

is a little off, then working down from the cutoff Λ^2_{cut} to the renormalisation point μ^2, can result in different solutions since the intermediate behaviours differ.

An illustration of this is given in figure C.1 which is the case for solution Set 1 using the $\mathcal{G}h/\mathcal{G}l$ vertex, given by eq. (4.77) that approximates the WSTI solution. There are several ways to match to the one loop results, the numerical procedure benefits from having completely smooth functions so matching the derivative over a small region can also be beneficial. If the one-loop running is reproduced exactly then this is of course not a problem. This can be particularly important when solutions are not allowed for specific regions of parameter space because different choices may lead to different solutions being obtainable. An ambition for future studies will be to find solutions that simulaneously satisfy the WSTI and correctly reproduce the leading resummed perturbative results.

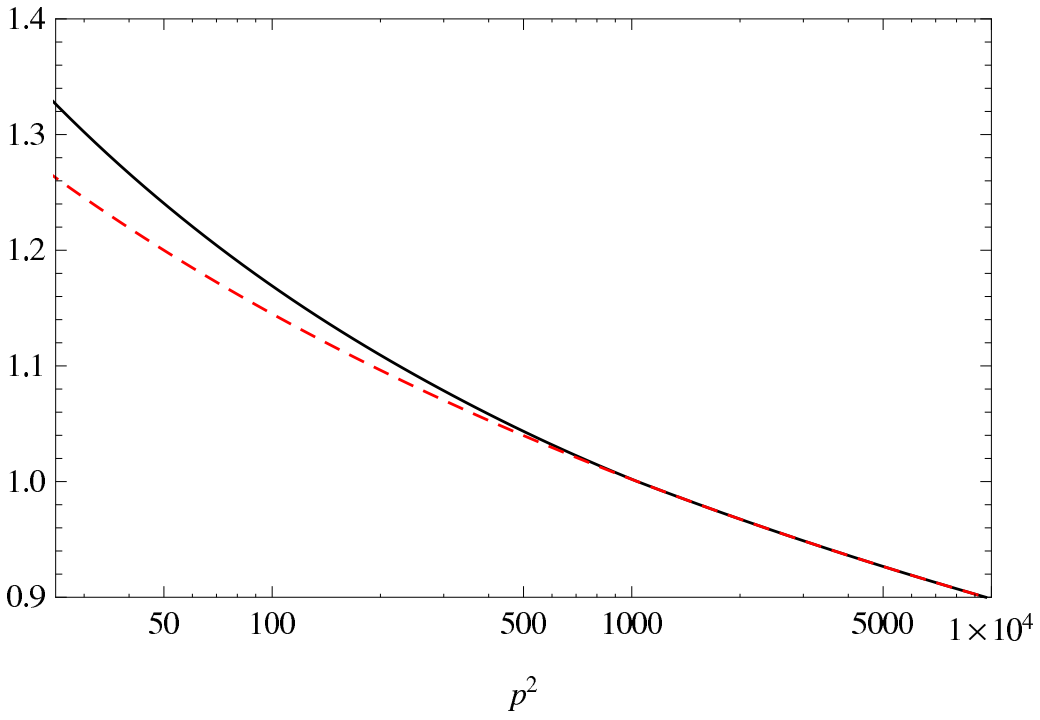

Figure C.1.: The gluon running in the UV matched at 1000 GeV^2 for the Set 1 solutions showing the one-loop behaviour (red, dashed), and the numerical SDE solution (black, solid).

C.4. Iterative Procedure

Several iterative procedures work when solving these equations. The most comprehensive used here is using a Newton-Raphson technique, but natural iterative procedures work also in some cases and can also be more efficient computationally.

C.4.1. Natural Iterative Procedure

The natural iterative procedure has no guarantee of convergence whether a solution exists or not, or whether the initial function is close or far from any given solution. It is however, rather fast to compute subsequent steps and for independent equations (as opposed to coupled equations), it actually works here reasonably well. The iterative procedure would be defined via, eg for the truncated gluon,

$$\mathcal{G}l_{i+1}(p^2) = \mathcal{G}l_i(\mu^2) + \Pi^{(\mathrm{sub})}_{2c,i}(p^2,\mu^2) + \Pi^{(\mathrm{sub})}_{2g,i}(p^2,\mu^2) \tag{C.21}$$

where on the right we substitute the current guess $\mathcal{G}l_i$ where it is required. An obvious alternative may be used that can sometimes stabilise an oscillatory iterative procedure,

$$\mathcal{G}l_{i+1}(p^2) = \frac{1}{2}\left(\mathcal{G}l_i(p^2) + \left[\mathcal{G}l_i(\mu^2) + \Pi^{(\mathrm{sub})}_{2c,i}(p^2,\mu^2) + \Pi^{(\mathrm{sub})}_{2g,i}(p^2,\mu^2)\right]\right). \tag{C.22}$$

The iterative procedure may be applied to each equation in turn in a coupled problem, provided that this coupling is not too strong between the equations and the initial guess is reasonably good. For equations that are strongly coupled, numerically sensitive or we have no idea about what solutions there may be, then we have no choice but to resort to a more advanced procedure such as a Newton-Raphson method.

C.4.2. Newton-Raphson Iterative Procedure

The method we apply here considers a function represented by a truncated Chebychev expansion to order n, tabulated at the zeroes of the $n+1$ Chebychev polynomial, x_i.[1] In order to derive this, we arrange our equations such that,

$$\mathcal{F}_i(p^2,\mathbf{c}_i) = \mathcal{G}l_i(p^2,\mathbf{c}_i)^{-1} - \mathcal{G}l_i(\mu^2,\mathbf{c}_i)^{-1} + \Pi_i(p^2,\mathbf{c}_i) - \Pi_i(\mu^2,\mathbf{c}_i) \tag{C.23}$$

[1] For more general discussions of the same procedure see [132, 133].

where $\mathbf{c}_i = (c_{0,i}, ..., c_{n,i})$ is the vector of the Chebychev coefficients for the ith iteration. For a good initial guess then $\mathcal{F}_i \simeq 0$, and for convergence we require $\mathcal{F}_i = 0$, we can Taylor expand to find the required correction,

$$\mathcal{F}_{i+1}(p^2, \mathbf{c}_i + \delta\mathbf{c}_i) = \mathcal{F}_i(p^2, \mathbf{c}_i) + \sum_{j=0}^{n} \frac{\partial \mathcal{F}_i(p^2, \mathbf{c}_i)}{\partial c_{j,i}} \delta c_{j,i} + \mathcal{O}(\delta c_{j,i})^2 = 0, \tag{C.24}$$

where i denotes the relative iteration number, j is the Chebychev polynomial degree, $\delta\mathbf{c}_i = (\delta c_{0,i}, ..., \delta c_{n,i})$, and the higher order terms are neglected. The iterative procedure is then defined via $\mathbf{c}_{i+1} = \mathbf{c}_i + \delta\mathbf{c}_i$ which requires us to find the quantity $\delta c_{j,i}$. The functions are numerically tabulated at the zeroes of the $n+1$ polynomial (via the mapping) which we donte p_k^2,

$$\mathcal{F}_i(p_k^2, \mathbf{c}_i) = -\sum_{j=0}^{n} \frac{\partial \mathcal{F}_i(p_k^2, \mathbf{c}_i)}{\partial c_{j,i}} \delta c_{j,i} \tag{C.25}$$

we then identify this as a matrix diagonalisation problem where we have,

$$\begin{pmatrix} \mathcal{F}_i(p_0^2, \mathbf{c}_i) \\ \vdots \\ \mathcal{F}_i(p_k^2, \mathbf{c}_i) \\ \vdots \\ \mathcal{F}_i(p_n^2, \mathbf{c}_i) \end{pmatrix} = - \begin{pmatrix} \frac{\partial \mathcal{F}_i(p_0^2, \mathbf{c}_i)}{\partial c_{0,i}} & \cdots & \frac{\partial \mathcal{F}_i(p_0^2, \mathbf{c}_i)}{\partial c_{j,i}} & \cdots & \frac{\partial \mathcal{F}_i(p_0^2, \mathbf{c}_i)}{\partial c_{n,i}} \\ \vdots & \ddots & \vdots & & \vdots \\ \frac{\partial \mathcal{F}_i(p_k^2, \mathbf{c}_i)}{\partial c_{0,i}} & \cdots & \frac{\partial \mathcal{F}_i(p_k^2, \mathbf{c}_i)}{\partial c_{j,i}} & \cdots & \frac{\partial \mathcal{F}_i(p_k^2, \mathbf{c}_i)}{\partial c_{n,i}} \\ \vdots & & \vdots & \ddots & \vdots \\ \frac{\partial \mathcal{F}_i(p_n^2, \mathbf{c}_i)}{\partial c_{0,i}} & \cdots & \frac{\partial \mathcal{F}_i(p_n^2, \mathbf{c}_i)}{\partial c_{j,i}} & \cdots & \frac{\partial \mathcal{F}_i(p_n^2, \mathbf{c}_i)}{\partial c_{n,i}} \end{pmatrix} \begin{pmatrix} \delta c_{0,i} \\ \vdots \\ \delta c_{j,i} \\ \vdots \\ \delta c_{n,i} \end{pmatrix} \tag{C.26}$$

all that is required then is to invert this relation which is a simple numerical problem for which we can use various techniques, for example LU decomposition [132]. Any sufficiently precise procedure may be used since the diagonalisation takes several orders of magnitude less time than the calculation of the matrix elements.

In order to derive this quantity we make repeated use of eq. (C.14). Calculation of the matrix $\partial \mathcal{F}_i(p_k^2, \mathbf{c}_i)/\partial c_{j,i}$ is time consuming, particularly for more complicated vertex dressings since they involve repeated calls to the interpolation and extrapolation routines for the dressing functions.

This method naturally generalises to coupled equations and this is where its real usefulness lies since it takes into account correlations in the derivatives of the Chebychev coefficients

between the equations, we can simply expand the matrix and vectors in the following way,

$$\begin{pmatrix} \mathcal{F}^{(1)} \\ \mathcal{F}^{(2)} \end{pmatrix} = - \begin{pmatrix} \frac{\partial \mathcal{F}^{(1)}}{\partial c_j^{(1)}} & \frac{\partial \mathcal{F}^{(1)}}{\partial c_j^{(2)}} \\ \frac{\partial \mathcal{F}^{(2)}}{\partial c_j^{(1)}} & \frac{\partial \mathcal{F}^{(2)}}{\partial c_j^{(2)}} \end{pmatrix} \begin{pmatrix} \delta c_j^{(1)} \\ \delta c_j^{(2)} \end{pmatrix} \tag{C.27}$$

where the two coupled equations $\mathcal{F}^{(1)}$ and $\mathcal{F}^{(2)}$ are solved simulaneously by diagonalisation of the matrix in eq. (C.27). This method may be generalised to several coupled equations, however the additional time spent computing the off-diagonal elements increases such that this method can become too costly [133].

Bibliography

[1] R. P. Feynman *The Principle of Least Action in Quantum Mechanics, Ph.D Thesis* (1942).

[2] C. Itzykson and J. B. Zuber, *Quantum Field Theory*, . New York, USA: McGraw-Hill (1980) 705 P. (International Series In Pure and Applied Physics).

[3] M. E. Peskin and D. V. Schroeder, *An Introduction to quantum field theory*, . Reading, USA: Addison-Wesley (1995) 842 p.

[4] T. Muta, *Foundations of quantum chromodynamics. Second edition*, *World Sci. Lect. Notes Phys.* **57** (1998) 1–409.

[5] E. J. Eichten, K. Lane and C. Quigg, *Charmonium levels near threshold and the narrow state $X(3872) \to \pi^+\pi^- J/\psi$*, *Phys. Rev.* **D69** (2004) 094019 [hep-ph/0401210].

[6] E. J. Eichten, K. Lane and C. Quigg, *New states above charm threshold*, *Phys. Rev.* **D73** (2006) 014014 [hep-ph/0511179].

[7] M. R. Pennington and D. J. Wilson, *Decay channels and charmonium mass-shifts*, *Phys. Rev.* **D76** (2007) 077502 [0704.3384].

[8] E. S. Swanson, *Hadron Spectroscopy – Theory*, 0910.3704.

[9] I. V. Danilkin and Y. A. Simonov, *Channel coupling in heavy quarkonia: energy levels, mixing, widths and new states*, *Phys. Rev.* **D81** (2010) 074027 [0907.1088].

[10] A. Gomez Nicola and J. R. Pelaez, *Meson meson scattering within one loop chiral perturbation theory and its unitarization*, *Phys. Rev.* **D65** (2002) 054009 [hep-ph/0109056].

[11] J. Bijnens, G. Colangelo, G. Ecker, J. Gasser and M. E. Sainio, *Pion pion scattering at low energy*, *Nucl. Phys.* **B508** (1997) 263–310 [hep-ph/9707291].

[12] T. N. Truong, *Chiral Perturbation Theory and Final State Theorem*, *Phys. Rev. Lett.* **61** (1988) 2526.

[13] A. Dobado and J. R. Pelaez, *The inverse amplitude method in Chiral Perturbation Theory*, *Phys. Rev.* **D56** (1997) 3057–3073 [hep-ph/9604416].

[14] G. Veneziano, *Construction of a crossing - symmetric, Regge behaved amplitude for linearly rising trajectories*, *Nuovo. Cim.* **A57** (1968) 190–197.

[15] M. Ademollo, H. R. Rubinstein, G. Veneziano and M. A. Virasoro, *Bootstrap of meson trajectories from superconvergence*, *Phys. Rev.* **176** (1968) 1904–1925.

[16] R. Dolen, D. Horn and C. Schmid, *Finite energy sum rules and their application to pi N charge exchange*, *Phys. Rev.* **166** (1968) 1768–1781.

[17] R. Dolen, D. Horn and C. Schmid, *Prediction of Regge Parameters of rho Poles from Low- Energy pi N Data*, *Phys. Rev. Lett.* **19** (1967) 402–407.

[18] M. R. Pennington, *What a Dominating rho and Weak Exotics Can Do for pi pi Scattering Near Threshold*, *Nuovo Cim.* **A25** (1975) 149.

[19] R. Kaminski, J. R. Pelaez and F. J. Yndurain, *The pion-pion scattering amplitude. III: Improving the analysis with forward dispersion relations and Roy equations*, *Phys. Rev.* **D77** (2008) 054015 [0710.1150].

[20] **Particle Data Group** Collaboration, C. Amsler *et. al.*, *Review of particle physics*, *Phys. Lett.* **B667** (2008) 1.

[21] A. Donnachie and P. V. Landshoff, *Dynamics of Elastic Scattering*, *Nucl. Phys.* **B267** (1986) 690.

[22] G. 't Hooft, *A planar diagram theory for strong interactions*, *Nucl. Phys.* **B72** (1974) 461.

[23] E. Witten, *Large N Chiral Dynamics*, *Ann. Phys.* **128** (1980) 363.

[24] J. R. Pelaez, *Light scalars as tetraquarks or two-meson states from large Nc and unitarized Chiral Perturbation Theory*, *Mod. Phys. Lett.* **A19** (2004) 2879–2894 [hep-ph/0411107].

[25] J. R. Pelaez and G. Rios, *Nature of the f0(600) from its N(c) dependence at two loops in unitarized chiral perturbation theory*, *Phys. Rev. Lett.* **97** (2006) 242002 [hep-ph/0610397].

[26] J. R. de Elvira, J. R. Pelaez, M. R. Pennington and D. J. Wilson, *Structure of the lightest scalar meson from the 1/Nc expansion of Unitarized Chiral Perturbation Theory and Regge Theory*, *AIP Conf. Proc.* **1257** (2010) 467–471 [1001.2746].

[27] J. R. de Elvira, J. R. Pelaez, M. R. Pennington and D. J. Wilson, *Chiral Perturbation Theory, the $1/N_c$ expansion and Regge behaviour determine the structure of the lightest scalar meson*, 1009.6204.

[28] J. R. Pelaez, *On the nature of light scalar mesons from their large N(c) behavior*, *Phys. Rev. Lett.* **92** (2004) 102001 [hep-ph/0309292].

[29] N. A. Tornqvist, *Understanding the scalar meson $q\bar{q}$ nonet*, *Z. Phys.* **C68** (1995) 647–660 [hep-ph/9504372].

[30] J. A. Oller and E. Oset, *N/D Description of Two Meson Amplitudes and Chiral Symmetry*, *Phys. Rev.* **D60** (1999) 074023 [hep-ph/9809337].

[31] D. Black, A. H. Fariborz, F. Sannino and J. Schechter, *Putative Light Scalar Nonet*, *Phys. Rev.* **D59** (1999) 074026 [hep-ph/9808415].

[32] F. E. Close and N. A. Tornqvist, *Scalar mesons above and below 1 GeV*, *J. Phys.* **G28** (2002) R249–R267 [hep-ph/0204205].

[33] E. van Beveren and G. Rupp, *Scalar mesons within a model for all non-exotic mesons*, hep-ph/0201006.

[34] M. Harada, F. Sannino and J. Schechter, *Large N(c) and chiral dynamics*, *Phys. Rev.* **D69** (2004) 034005 [hep-ph/0309206].

[35] L. Maiani, F. Piccinini, A. D. Polosa and V. Riquer, *A new look at scalar mesons*, *Phys. Rev. Lett.* **93** (2004) 212002 [hep-ph/0407017].

[36] F. Giacosa, *Mixing of scalar tetraquark and quarkonia states in a chiral approach*, *Phys. Rev.* **D75** (2007) 054007 [hep-ph/0611388].

[37] E. van Beveren *et. al.*, *A low-lying scalar meson nonet in a unitarized meson model*, *Z. Phys.* **C30** (1986) 615–620 [0710.4067].

[38] M. R. Pennington, *Light O^{++} Mesons: Scalargators in Florida*, 1003.2549.

[39] D. Morgan and M. R. Pennington, *f0 (s*): Molecule or quark state?*, *Phys. Lett.* **B258** (1991) 444–450.

[40] D. Morgan and M. R. Pennington, *New data on the k anti-k threshold region and the nature of the f0 (s*)*, *Phys. Rev.* **D48** (1993) 1185–1204.

[41] C.-H. Chen, *Evidence for two-quark content of $f_0(980)$ in exclusive $b \to c$ decays*, *Phys. Rev.* **D67** (2003) 094011 [hep-ph/0302059].

[42] N. A. Tornqvist and M. Roos, *Resurrection of the Sigma Meson*, *Phys. Rev. Lett.* **76** (1996) 1575–1578 [hep-ph/9511210].

[43] E. van Beveren, G. Rupp and M. D. Scadron, *Why the f(0)(980) is mostly ssbar*, *Phys. Lett.* **B495** (2000) 300–302 [hep-ph/0009265].

[44] R. L. Jaffe, *Multi-Quark Hadrons. 1. The Phenomenology of (2 Quark 2 anti-Quark) Mesons*, *Phys. Rev.* **D15** (1977) 267.

[45] R. L. Jaffe, *Multi-Quark Hadrons. 2. Methods*, *Phys. Rev.* **D15** (1977) 281.

[46] J. D. Weinstein and N. Isgur, *K anti-K Molecules*, *Phys. Rev.* **D41** (1990) 2236.

[47] R. Escribano, A. Gallegos, J. L. Lucio M, G. Moreno and J. Pestieau, *On the mass, width and coupling constants of the f0(980)*, *Eur. Phys. J.* **C28** (2003) 107–114 [hep-ph/0204338].

[48] V. Baru, J. Haidenbauer, C. Hanhart, Y. Kalashnikova and A. E. Kudryavtsev, *Evidence that the a0(980) and f0(980) are not elementary particles*, *Phys. Lett.* **B586** (2004) 53–61 [hep-ph/0308129].

[49] Y.-J. Zhang, H.-C. Chiang, P.-N. Shen and B.-S. Zou, *Possible S-wave bound-states of two pseudoscalar mesons*, *Phys. Rev.* **D74** (2006) 014013 [hep-ph/0604271].

[50] Y. S. Kalashnikova, *f0(980) and a0(980) as hadronic molecules*, *AIP Conf. Proc.* **1030** (2008) 112–117.

[51] F. De Fazio and M. R. Pennington, *Probing the structure of $f_0(980)$ through radiative ϕ decays*, *Phys. Lett.* **B521** (2001) 15–21 [hep-ph/0104289].

[52] K. L. Au, D. Morgan and M. R. Pennington, *Meson dynamics beyond the quark model: A study of final state interactions*, *Phys. Rev.* **D35** (1987) 1633.

[53] S. Weinberg, *Elementary particle theory of composite particles*, *Phys. Rev.* **130** (1963) 776–783.

[54] S. Weinberg, *Quasiparticles and the Born Series*, *Phys. Rev.* **131** (1963) 440–460.

[55] S. Weinberg, *Evidence That the Deuteron Is Not an Elementary Particle*, *Phys. Rev.* **137** (1965) B672–B678.

[56] D. Morgan, *Pole counting and resonance classification*, *Nucl. Phys.* **A543** (1992) 632–644.

[57] R. Jost *Helv. Phys. Acta* **20** (1947) 256.

[58] S. M. Flatte, *Coupled - Channel Analysis of the pi eta and K anti-K Systems Near K anti-K Threshold*, *Phys. Lett.* **B63** (1976) 224.

[59] V. Baru, J. Haidenbauer, C. Hanhart, A. E. Kudryavtsev and U.-G. Meissner, *Flatte-like distributions and the a0(980) / f0(980) mesons*, *Eur. Phys. J.* **A23** (2005) 523–533 [`nucl-th/0410099`].

[60] A. M. Badalian, L. P. Kok, M. I. Polikarpov and Y. A. Simonov, *Resonances in Coupled Channels in Nuclear and Particle Physics*, *Phys. Rept.* **82** (1982) 31.

[61] A. Etkin *et. al.*, *Amplitude Analysis of the K0(s) K0(s) System Produced in the Reaction pi- p → K0(s) K0(s) n at 23-GeV/c*, *Phys. Rev.* **D25** (1982) 1786.

[62] R. S. Longacre *et. al.*, *A measurement of pi- p → K0(s) K0(s) n at 22-gev/c and a systematic study of the 2++ meson spectrum*, *Phys. Lett.* **B177** (1986) 223.

[63] R. S. Longacre *et. al.*, $\pi^- p \to K0(s)K0(s)n$ *at 22-gev/c and a systematic study of the 2++ and 0++ meson spectrum*, . Submitted to 2nd Int. Conf. on Hadron Spectroscopy, Tsukuba, Japan, Apr 16-18, 1987.

[64] D. H. Cohen *et. al.*, *Amplitude Analysis of the K- K+ System Produced in the Reactions pi- p → K- K+ n and pi+ n → K- K+ p at 6- GeV/c*, *Phys. Rev.* **D22** (1980) 2595.

[65] W. Ochs *University of Munich, Ph.D Thesis* (1973).

[66] B. Hyams *et. al.*, *pi pi Phase Shift Analysis from 600-MeV to 1900-MeV*, *Nucl. Phys.* **B64** (1973) 134–162.

[67] G. Grayer *et. al.*, *High Statistics Study of the Reaction pi- p → pi- pi+ n: Apparatus, Method of Analysis, and General Features of Results at 17-GeV/c*, *Nucl. Phys.* **B75** (1974) 189.

[68] **E852** Collaboration, J. Gunter *et. al.*, *A partial wave analysis of the pi0 pi0 system produced in pi- p charge exchange collisions*, *Phys. Rev.* **D64** (2001) 072003

[hep-ex/0001038].

[69] N. N. Achasov and G. N. Shestakov, *$\pi\pi$ scattering S wave from the data on the reaction $pi^- p^+ \to \pi^0\pi^0 n$*, *Phys. Rev.* **D67** (2003) 114018 [hep-ph/0302220].

[70] **E852** Collaboration, J. Gunter *et. al.*, *Analysis of the pi0 pi0 final state in the pi-p reactions at 18.3-GeV/c*, hep-ex/9609010.

[71] **MARK-III** Collaboration, W. S. Lockman, *production of the f0 (975) meson in j / psi decays*, . Presented at 3rd Int. Conf. on Hadron Spectroscopy, Ajaccio, France, Sep 23-27, 1989.

[72] **BES** Collaboration, M. Ablikim *et. al.*, *Resonances in $J/\psi \to \phi\pi^+\pi^-$ and $\phi K^+ K^-$*, *Phys. Lett.* **B607** (2005) 243–253 [hep-ex/0411001].

[73] **BABAR** Collaboration, B. Aubert *et. al.*, *Dalitz Plot Analysis of $D_s \to \pi^+\pi^-\pi^+$*, *Phys. Rev.* **D79** (2009) 032003 [0808.0971].

[74] **BABAR** Collaboration, M. Pappagallo *et. al.*, *Studies of D_s decays at Babar*, *Talk presented at 35th International Conference on High Energy Physics, Paris.* (2010).

[75] **FOCUS** Collaboration, J. M. Link *et. al.*, *Dalitz plot analysis of D/s+ and D+ decay to pi+ pi- pi+ using the K-matrix formalism*, *Phys. Lett.* **B585** (2004) 200–212 [hep-ex/0312040].

[76] **Axial Field Spectrometer** Collaboration, T. Akesson *et. al.*, *A search for glueballs and a study of double pomeron exchange at the cern intersecting storage rings*, *Nucl. Phys.* **B264** (1986) 154.

[77] F. James, *MINUIT Function Minimization and Error Analysis*, *CERN Program Library Long Writeup D506* (1994).

[78] G. Folger *et. al.*, *Upper Tail Probability of Chi-Squared Distribution*, *CERN Program Library Short Writeup G100* (1971).

[79] N. A. Tornqvist, *Scalar Mesons in the Unitarized Quark Model*, *Phys. Rev. Lett.* **49** (1982) 624–627.

[80] F. J. Dyson, *The S matrix in quantum electrodynamics*, *Phys. Rev.* **75** (1949) 1736–1755.

[81] J. S. Schwinger, *On the Green's functions of quantized fields. 1*, *Proc. Nat. Acad. Sci.* **37** (1951) 452–455.

[82] J. S. Schwinger, *On the Green's functions of quantized fields. 2*, *Proc. Nat. Acad. Sci.* **37** (1951) 455–459.

[83] J. C. R. Bloch, *Two-loop improved truncation of the ghost-gluon Dyson- Schwinger equations: Multiplicatively renormalizable propagators and nonperturbative running coupling*, *Few Body Syst.* **33** (2003) 111–152 [hep-ph/0303125].

[84] R. Alkofer, C. S. Fischer, H. Reinhardt and L. von Smekal, *On the infrared behaviour of gluons and ghosts in ghost- antighost symmetric gauges*, *Phys. Rev.* **D68** (2003) 045003 [hep-th/0304134].

[85] C. S. Fischer, *Non-perturbative propagators, running coupling and dynamical mass generation in ghost - antighost symmetric gauges in QCD*, hep-ph/0304233.

[86] C. S. Fischer, A. Maas and J. M. Pawlowski, *On the infrared behavior of Landau gauge Yang-Mills theory*, *Annals Phys.* **324** (2009) 2408–2437 [0810.1987].

[87] P. Boucaud *et. al.*, *On the IR behaviour of the Landau-gauge ghost propagator*, *JHEP* **06** (2008) 099 [0803.2161].

[88] D. C. Curtis and M. R. Pennington, *Truncating the Schwinger-Dyson equations: How multiplicative renormalizability and the Ward identity restrict the three point vertex in QED*, *Phys. Rev.* **D42** (1990) 4165–4169.

[89] A. Kizilersu, M. Reenders and M. R. Pennington, *One loop QED vertex in any covariant gauge: Its complete analytic form*, *Phys. Rev.* **D52** (1995) 1242–1259 [hep-ph/9503238].

[90] D. Atkinson and J. C. R. Bloch, *Running coupling in non-perturbative QCD. I: Bare vertices and y-max approximation*, *Phys. Rev.* **D58** (1998) 094036 [hep-ph/9712459].

[91] A. Bashir, A. Kizilersu and M. R. Pennington, *The non-perturbative three-point vertex in massless quenched QED and perturbation theory constraints*, *Phys. Rev.* **D57** (1998) 1242–1249 [hep-ph/9707421].

[92] J. C. R. Bloch, *Multiplicative renormalizability of gluon and ghost propagators in QCD*, *Phys. Rev.* **D64** (2001) 116011 [hep-ph/0106031].

[93] A. Kizilersu and M. R. Pennington, *Building the Full Fermion-Photon Vertex of QED by Imposing Multiplicative Renormalizability of the Schwinger-Dyson Equations for the Fermion and Photon Propagators*, *Phys. Rev.* **D79** (2009)

125020 [0904.3483].

[94] J. C. Taylor, *Ward Identities and Charge Renormalization of the Yang- Mills Field*, *Nucl. Phys.* **B33** (1971) 436–444.

[95] C. Lerche and L. von Smekal, *On the infrared exponent for gluon and ghost propagation in Landau gauge QCD*, *Phys. Rev.* **D65** (2002) 125006 [hep-ph/0202194].

[96] W. Celmaster and R. J. Gonsalves, *The Renormalization Prescription Dependence of the QCD Coupling Constant*, *Phys. Rev.* **D20** (1979) 1420.

[97] A. I. Davydychev, P. Osland and O. V. Tarasov, *Three-gluon vertex in arbitrary gauge and dimension*, *Phys. Rev.* **D54** (1996) 4087–4113 [hep-ph/9605348].

[98] P. Boucaud *et. al.*, *The infrared behaviour of the pure Yang-Mills Green functions*, hep-ph/0507104.

[99] S. K. Kim and M. Baker, *Consequences of gauge invariance for the interacting vertices in nonabelian gauge theories*, *Nucl. Phys.* **B164** (1980) 152.

[100] L. von Smekal, R. Alkofer and A. Hauck, *The infrared behavior of gluon and ghost propagators in Landau gauge QCD*, *Phys. Rev. Lett.* **79** (1997) 3591–3594 [hep-ph/9705242].

[101] L. von Smekal, A. Hauck and R. Alkofer, *A solution to coupled Dyson-Schwinger equations for gluons and ghosts in Landau gauge*, *Ann. Phys.* **267** (1998) 1 [hep-ph/9707327].

[102] D. Binosi and J. Papavassiliou, *The pinch technique to all orders*, *Phys. Rev.* **D66** (2002) 111901 [hep-ph/0208189].

[103] D. Binosi and J. Papavassiliou, *Gauge-invariant truncation scheme for the Schwinger-Dyson equations of QCD*, *Phys. Rev.* **D77** (2008) 061702 [0712.2707].

[104] N. Brown and M. R. Pennington, *Studies of confinement: how quarks and gluons propagate*, *Phys. Rev.* **D38** (1988) 2266.

[105] N. Brown and M. R. Pennington, *Studies of Confinement: How the Gluon Propagates*, *Phys. Rev.* **D39** (1989) 2723.

[106] J. C. R. Bloch and M. R. Pennington, *Numerical cancellation of photon quadratic divergence in the study of the Schwinger-Dyson equations in strong coupling QED*,

Mod. Phys. Lett. **A10** (1995) 1225–1233 [hep-ph/9501411].

[107] C. S. Fischer, P. Watson and W. Cassing, *Probing unquenching effects in the gluon polarisation in light mesons*, *Phys. Rev.* **D72** (2005) 094025 [hep-ph/0509213].

[108] T. Kugo and I. Ojima, *Local Covariant Operator Formalism of Nonabelian Gauge Theories and Quark Confinement Problem*, *Prog. Theor. Phys. Suppl.* **66** (1979) 1.

[109] V. N. Gribov, *Quantization of non-Abelian gauge theories*, *Nucl. Phys.* **B139** (1978) 1.

[110] D. Zwanziger, *Vanishing of zero momentum lattice gluon propagator and color confinement*, *Nucl. Phys.* **B364** (1991) 127–161.

[111] D. Zwanziger, *Renormalizability of the critical limit of lattice gauge theory by BRS invariance*, *Nucl. Phys.* **B399** (1993) 477–513.

[112] D. Zwanziger, *Fundamental modular region, Boltzmann factor and area law in lattice gauge theory*, *Nucl. Phys.* **B412** (1994) 657–730.

[113] D. Zwanziger, *Time-independent stochastic quantization, DS equations, and infrared critical exponents in QCD*, *Phys. Rev.* **D67** (2003) 105001 [hep-th/0206053].

[114] U. Bar-Gadda, *Infrared behavior of the effective coupling in quantum chromodynamics: a nonperturbative approach*, *Nucl. Phys.* **B163** (1980) 312–332.

[115] J. S. Ball and T.-W. Chiu, *Analytic Properties of the Vertex Function in Gauge Theories. 2*, *Phys. Rev.* **D22** (1980) 2550.

[116] J. S. Ball and T.-W. Chiu, *Analytic Properties of the Vertex Function in Gauge Theories. 1*, *Phys. Rev.* **D22** (1980) 2542.

[117] K. G. Chetyrkin and A. Retey, *Three-loop three-linear vertices and four-loop MOM beta functions in massless QCD*, hep-ph/0007088.

[118] P. Boucaud *et. al.*, *Non-perturbative power corrections to ghost and gluon propagators*, *JHEP* **01** (2006) 037 [hep-lat/0507005].

[119] R. Alkofer, C. S. Fischer and F. J. Llanes-Estrada, *Vertex functions and infrared fixed point in Landau gauge SU(N) Yang-Mills theory*, *Phys. Lett.* **B611** (2005) 279–288 [hep-th/0412330].

[120] L. von Smekal, K. Maltman and A. Sternbeck, *The strong coupling and its running to four loops in a minimal MOM scheme*, *Phys. Lett.* **B681** (2009) 336–342 [0903.1696].

[121] A. C. Aguilar and J. Papavassiliou, *Gluon mass generation without seagull divergences*, *Phys. Rev.* **D81** (2010) 034003 [0910.4142].

[122] D. Binosi and J. Papavassiliou, *Non-perturbative pinch technique*, *JHEP* **03** (2007) 041 [hep-ph/0611354].

[123] D. Binosi and J. Papavassiliou, *Pinch Technique: Theory and Applications*, *Phys. Rept.* **479** (2009) 1–152 [0909.2536].

[124] A. C. Aguilar, D. Binosi and J. Papavassiliou, *QCD effective charges from lattice data*, 1004.1105.

[125] I. L. Bogolubsky, E. M. Ilgenfritz, M. Muller-Preussker and A. Sternbeck, *Lattice gluodynamics computation of Landau gauge Green's functions in the deep infrared*, *Phys. Lett.* **B676** (2009) 69–73 [0901.0736].

[126] O. Pene *et. al.*, *A Ghost Story: Ghosts and Gluons in the IR regime of QCD*, 0911.0468.

[127] C. S. Fischer, B. Gruter and R. Alkofer, *Solving coupled Dyson-Schwinger equations on a compact manifold*, *Ann. Phys.* **321** (2006) 1918–1938 [hep-ph/0506053].

[128] C. S. Fischer, *Infrared properties of QCD from Dyson-Schwinger equations*, *J. Phys.* **G32** (2006) R253–R291 [hep-ph/0605173].

[129] C. S. Fischer, A. Maas, J. M. Pawlowski and L. von Smekal, *Large volume behaviour of Yang-Mills propagators*, *Annals Phys.* **322** (2007) 2916–2944 [hep-ph/0701050].

[130] A. A. Slavnov, *Ward Identities in Gauge Theories*, *Theor. Math. Phys.* **10** (1972) 99–107.

[131] W. Schleifenbaum, A. Maas, J. Wambach and R. Alkofer, *Infrared behaviour of the ghost gluon vertex in Landau gauge Yang-Mills theory*, *Phys. Rev.* **D72** (2005) 014017 [hep-ph/0411052].

[132] Press, William H. and Teukolsky, Saul A. and Vetterling, William T. and

Flannery, Brian P., *Numerical Recipes in C: The Art of Scientific Computing.* Cambridge University Press, New York, NY, USA, 1992.

[133] J. C. R. Bloch, *Numerical investigation of fermion mass generation in QED*, `hep-ph/0208074`.

[134] R. Williams *Schwinger-Dyson equations in QED and QCD: The Calculation of fermion-antifermion condensates, Ph.D Thesis* (2007).